Studies of Elementary Collision Processes Under Single Collision Conditions

A thesis submitted in partial fulfulment of
the requirements for the degree of

Doctor of Philosophy in Chemistry

at the
University of Canterbury
Christchurch
New Zealand

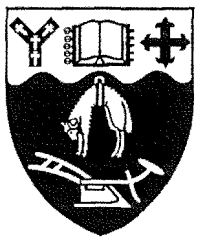

Claire Vallance
1999

If at first you don't succeed

What did you expect?

— from 'Ode to Frustration'

by Frederick Reines

ABSTRACT

Absolute electron impact ionization cross sections have been measured for CH_4 and the methyl halides CH_3F, CH_3Cl, CH_3Br and CH_3I. A theoretical model has been developed which predicts absolute maximum cross sections in good agreement with these measurements and also with results published in the literature for a range of small molecules. In addition, the model is able to qualitatively reproduce the recently observed orientation dependence of the electron impact ionization process. The dependence of the ionization cross section on molecular polarizability has been investigated and general expressions for the calculation of maximum electron impact ionization cross sections have been deduced.

State specific cross sections have been measured for collisional attenuation of upper Stark state selected beams of CH_3F with a range of scattering gases inside a hexapole collision chamber. Cross sections are found to lie in the range between 246 and 654 Å. This corresponds to a long range interaction involving the transfer of tiny amounts of energy, consistent with $\Delta M_J = \pm 1$ rotational transitions.

The parameters affecting orientation of upper Stark state selected beams have been investigated. The minimum uniform electric fields required to maintain spatial orientation for beams of CH_3F, CH_3Cl, CH_3Br and CH_3I have been measured and rationalised in terms of the hyperfine interaction between the rotational angular momentum and nuclear spin of the beam molecules. The time for which orientation is retained under field free conditions has been considered.

A crossed beam ion imaging experiment has been designed and constructed for the investigation of collisions between electrons or ions and spatially oriented molecules. Software for analysing the data obtained from these experiments has been developed and tested on simulated images.

ACKNOWLEDGEMENTS

I would firstly like to thank my supervisor, Professor Peter Harland, for his advice, encouragement, and friendship both inside and outside of the lab over the past three years. His calm(ish) response to news of floods, fires and suicidal gate valves has also been greatly appreciated.

Thank you to Professor John Simons for the opportunity to spend time in the Physical and Theoretical Chemistry Laboratory at Oxford University during the early part of my Ph.D., and to Dr Mark Brouard, for his guidance and support while I was there. Thanks to Simon, Gavin, Sam, Dave, Dom, Matt, Kostas, Evan and Andy for making my stay in room 13.13 an enjoyable one.

I am very very grateful to the chemistry department technical staff for their invaluable assistance in keeping the molecular beam machine alive and expanding, and for providing emergency CPR during the odd minor catastrophe. In the mechanical workshop special thanks go to Danny Leonard for turning my drawings of an ion source into the genuine article, to Russell Gillard, for help with design work on a number of occasions and for not strangling me on a number of others, and to Geoff Speer, for managing to sneak the odd jobs past Russell's infamous white forms. Thanks also to Wayne Mackay for dealing with electrical problems on the spot, and for his neverending supply of heat shrink. Thank you to Sandy in Electronics for his willingness (!) to troubleshoot troublesome mass spectrometers, and Steve, Roger and Mike for designing and building electronic instrumentation, and suffering through the multiple modifications that nearly always seemed to follow. I am also grateful to John Davis for help with computer problems, and especially for fixing the C drive meltdown which happened with impeccable timing during the last week of writing my thesis.

I would like to acknowledge Professor Egon Vietzke, of the Institut für Chemie der Kernforschungsanlage Jülich, Germany, for his willingness to supply detailed information on his negative halogen ion source, on which the ion source described in Chapter 7 is based. Thanks also to Andy Pratt and Ted Rafferty for many interesting (and sometimes maddening) dis-

cussions and for offering new perspectives on my research. To Sunny Hu, for her help in the lab over the last three years, and especially for her sterling work in aligning the molecular beam machine on the occasions when I managed to find some other very pressing job to do. Thank you to Sean Harris, for being there to sort out my blunders during the first year of my Ph.D. The observation that ion gauge controllers work much better if you switch them on will stand me in good stead for the future. Financial support from a University of Canterbury Doctoral Scholarship is gratefully acknowledged.

Finally, thank you to my family, without whom I would never have made it this far.

LIST OF PUBLICATIONS

1. Claire Vallance, Robert G. A. R Maclagan and Leon F. Phillips, 'Numerical study of the reaction of CN with O_2', *Chem. Phys. Lett.*, **250(1)** 59-65 (1996)

2. Claire Vallance, Peter W. Harland and Robert G. A. R. Maclagan, 'Quantum mechanical calculation of maximum electron impact single ionization cross sections for the inert gases and small molecules', *J. Phys. Chem.*, **100(37)** 15021-15026 (1996)

3. Claire Vallance, Robert G. A. R. Maclagan and Peter W. Harland, 'Ionization surfaces for small molecules', *J. Phys. Chem. A*, **101(19)** 3505-3508 (1997)

4. Claire Vallance, Sean A. Harris, James E. Hudson and Peter W. Harland, 'Absolute electron impact ionization cross sections for CH_3X, where X = H, F, Cl, Br and I', *J. Phys. B*, **30(10)** 2465-2475 (1997)

5. Peter W. Harland and Claire Vallance, 'Ionization cross sections and ionization efficiency curves from polarizability volumes and ionization potentials', *Int. J. Mass Spectr. Ion Proc.*, **171** 173-181 (1997)

6. Peter W. Harland and Claire Vallance, 'Positive ion - electron impact ionization cross sections: theory and experiment' in *Advances in Gas Phase Ion Chemistry Volume 3*, Ed. Nigel G. Adams and Lucia M. Babcock (*J. A. I. Press Inc.* 1998)

7. Mark Brouard, Itomar Burak, Gavin A. J. Markillie, Katrina McGrath and Claire Vallance, 'The $H+H_2O \rightarrow OH + H_2$ reaction: OH state resolved differential cross sections and H_2 internal energy disposal' *Chem. Phys. Lett.*, **281** 97-104 (1997)

8. Craig P. Butts, I. Eberson, R. Gonzales Luque, Christopher M. Hartshorn, Michael P. Hartshorn, M. Merchan, Ward T. Robinson, B. O. Roos, Claire Vallance and Brian R. Wood, 'Photochemical nitration by tetranitromethane 40. Regiochemistry of trinitromethyl attachment in the photolysis of benzofuran with tetranitromethane', *Acta. Chem. Scand.*, **51(10)** 984-999 (1997)

9. Claire Vallance, Sunny Wan-Ping Hu and Peter W. Harland, 'Upper Stark state collisional relaxation cross sections for single rotational states of CH_3F'. *J. Phys. Chem.*, **103(6)** 665-670 (1999).

10. David C. Bull, Peter W. Harland, Claire Vallance and Garry J. Foran 'EXAFS study of chromated copper arsenate timber preservative in wood', submitted to *Dalton Transactions*, February 1999.

11. Peter W. Harland, Sunny Wan-Ping Hu, Claire Vallance and Philip R. Brooks, 'Spatial deorientation lifetimes for upper Stark state selected beams of CH_3F, CH_3Cl, CH_3Br and CH_3I in field free space', in preparation.

12. Mark Brouard, Simon D. Gatenby, Gavin J. Markillie and Claire Vallance, 'OH State resolved polarization dependent differential cross sections for the reaction $H+H_2O \rightarrow OH+H_2$', in preparation.

13. Mark Brouard, Simon D. Gatenby, Gavin J. Markillie and Claire Vallance, 'OH State resolved polarization dependent differential cross sections for the reaction $H+N_2O \rightarrow OH+N_2$', in preparation.

CONTENTS

Part I Electron impact ionization cross sections – experiment and theory 2

1. Experimental determination of electron impact ionization cross sections 5

1.1 Experimental requirements 5

1.2 Literature review: Experimental techniques for the measurement of electron impact ionization cross sections 6

1.2.1 The condenser plate method 6

1.2.2 The Lozier tube 8

1.2.3 The summation method 9

1.2.4 Other experimental methods 11

1.3 Experimental measurement of absolute electron impact ionization cross sections for CH_4, CH_3F, CH_3Cl, CH_3Br and CH_3I 12

2. Theoretical determination of electron impact ionization cross sections 18

2.1 Literature Review: Theoretical methods for the calculation of electron impact ionization cross sections 18

2.1.1 Introduction 18

2.1.2 Quantum mechanical calculations and the partial wave approximation 19

Exchange 20

Resonances 21

Correlation 22

2.1.3 Semi-empirical and semi-classical calculations 23

The Lotz equation 24

The Bell equation 25

Kistemaker's modified additivity rule 26

The Deutsch-Märk (DM) method 27

The Binary-encounter Bethe (BEB) method 29

The Jain-Khare model 32
2.2 A simple electrostatic *ab initio* model for calculation of maximum ionization cross sections 33
2.2.1 The correlation between molecular polarizability volume and electron impact ionization cross section 35
The calculation of molecular ionization efficiency curves 40
2.3 Results 44
2.3.1 *Ab Initio* Calculations based on the electrostatic model 44
Inert Gases 44
Molecules 47
2.3.2 Comparison of theories 49
2.3.3 The effect of orientation on the electron impact ionization cross section 52

Part II Design and Characterisation of an electron/ion–molecule crossed beam machine for future studies 58

3. Molecular beam machine 62
3.1 Introduction 62
3.2 Nozzle source chamber 65
3.2.1 Alignment rods 66
3.2.2 Supersonic nozzle source and carriage assembly 67
3.3 Buffer chamber 69
3.3.1 Skimmers 69
3.3.2 Rotating chopper 69
3.4 Hexapole and C field chambers 69
3.4.1 Hexapoles 71
3.4.2 Radiofrequency resonance cell 71
3.5 Ion source chamber 72
3.6 Scattering chamber 73
3.7 Gas handling and liquid nitrogen system 74
3.8 Computer interfacing 75

4. Theory of Rotationally state selected and spatially oriented molecular beams . . . 76
4.1 Molecular beam sources . . . 76
4.1.1 Effusive sources . . . 76
4.1.2 Supersonic sources . . . 78
Structure of the supersonic expansion . . . 78
Skimmers . . . 79
Beam characteristics . . . 81
Seeded beams . . . 82
4.2 Rotation of symmetric top molecules . . . 83
4.2.1 The rotational Hamiltonian . . . 83
4.3 Trajectories of symmetric top molecules through a hexapole electrostatic field - upper Stark state selection . . . 89
4.4 Conditions for successful transmission through the hexapole . . . 93
4.5 Selection of $|JKM_J>$ states . . . 95
4.6 Orientation . . . 96

5. Molecular beam characterisation . . . 97
5.1 Nozzle source . . . 97
5.2 Beam profile . . . 97
5.3 Parallel velocity distribution . . . 98
5.4 Rotational quantum state populations . . . 102
5.5 Orientation properties of symmetric top molecules . . . 107
5.5.1 Beam attenuation due to dipole scrambling . . . 109
5.5.2 Hyperfine coupling . . . 110
Weak field case . . . 111
Strong field case . . . 112
5.5.3 Orienting field requirements . . . 112
5.5.4 Mean deorientation lifetimes . . . 115

6. Upper Stark state collisional relaxation cross sections . . . 119
6.1 Introduction . . . 119
6.2 Experimental . . . 120
6.3 Results and discussion . . . 123

7. Ion source . . . 127

7.1 Ion production on a heated LaB_6 surface . . . 127

7.2 Ion source design . . . 131

7.2.1 Electrostatic lens system . . . 134

7.3 Characterisation . . . 136

7.3.1 Temperature profile of the tip . . . 136

Electron emission . . . 138

Ion emission . . . 140

8. Ion imaging and data analysis techniques . . . 143

8.1 Literature review: the ion imaging technique . . . 143

8.2 Image reconstruction and data analysis . . . 147

8.2.1 The Abel inversion method . . . 148

8.2.2 Forward simulation method . . . 149

8.3 Data analysis methods . . . 150

8.3.1 Monte Carlo simulation methods . . . 150

Convergence and variance reduction methods . . . 151

Random number generators . . . 152

8.3.2 Fitting algorithms . . . 155

Least squares fitting . . . 156

Genetic algorithms . . . 158

9. Dynamics of the $H+H_2O \rightarrow OH+H_2$ reaction . . . 163

9.1 Experimental: Laser pump–probe experiments and Döppler resolved laser induced fluorescence spectroscopy . . . 163

9.1.1 Background collision theory . . . 167

9.1.2 Analysis . . . 169

Data fitting . . . 174

Monte-Carlo Error Analysis . . . 176

9.1.3 Results . . . 177

Simulated Data . . . 177

Experimental data . . . 180

9.2 Discussion . . . 189

9.2.1 Previous work on the H+H_2O reaction . . . 189
Theoretical studies . . . 189
Experimental studies . . . 190
9.2.2 Present work . . . 192
The differential cross section and translational energy distribution . . 192
Rotational polarization of the products . . . 193

10. Experimental design and analysis software . . . 196
10.1 Systems to be studied . . . 196
10.1.1 K^++CH_3X reactions . . . 196
10.1.2 X^-+CH_3Y reactions . . . 198
S_N2 reactions . . . 198
Other reaction channels . . . 201
Planned experiments . . . 204
10.2 Experiment design . . . 205
10.2.1 Neutral beam . . . 205
10.2.2 Ion / electron beam . . . 205
Ion source . . . 205
Pierce electron gun . . . 206
Phosphor screen detector . . . 208
10.2.3 Beam crossing region . . . 209
10.2.4 Scattering chamber lid . . . 211
10.2.5 Pulse sequences and electronics . . . 212
10.2.6 Product ion detection . . . 214
Ion imaging system . . . 214
Time of flight detection . . . 214
10.2.7 Data analysis software . . . 215
Analysis package 1 . . . 215
Analysis package 2 . . . 217
10.2.8 Preliminary experiments and future work . . . 220

Appendices 241

A. Theoretical data for calculation of electron impact ionization cross sections 241

A.1 Data for *ab initio* calculations 241

A.2 Data for DM calculations 246

B. Solution of the Schrodinger equation for a symmetric top molecule 261

C. Theory of photoinitiated bimolecular reaction dynamics 265

C.1 Vector correlations 266

C.1.1 The CM frame $\mathbf{k} - \mathbf{k}' - \mathbf{j}'$ distribution 266

C.1.2 Consequences of reflection symmetry in the scattering plane 269

C.1.3 The moments of the $\mathbf{k} - \mathbf{k}'$ distribution 270

C.1.4 The moments of the $\mathbf{k} - \mathbf{j}'$ distribution 271

C.1.5 The moments of the $\mathbf{k}' - \mathbf{j}'$ distribution 273

C.1.6 Other moments 274

C.2 The lab frame angular distribution 275

C.2.1 The reagent velocity distributions 281

D. Composite Doppler Profiles 283

E. The saga of the copper lens 286

F. Computer Programs 289

F.1 Programs used in beam characterisation experiments 289

F.1.1 `beamvel` - Beam velocity fitting program 289

F.1.2 `enhance` - Monte Carlo simulation of hexapole enhancements 291

F.2 Analysis software for ion imaging experiments 297

F.2.1 `imagebas` - Basis function program 297

F.2.2 `imagefit` - non-linear least squares fitting program 301

F.2.3 `eisim` - Image simulation program for electron impact ionization experiments 308

F.2.4 `ionsim` - Image simulation program for ion–molecule experiments . . . 316

LIST OF FIGURES

1.1 Tate and Smith ion source 7

1.2 Lozier tube 8

1.3 Electron impact ionization cell used for measuring ionization efficiency curves for methane and the methyl halides 13

1.4 Measurement of an electron impact ionization cross section. 15

1.5 Experimentally measured ionization efficiency curves for methane and the methyl halides. 17

2.1 Correlation of atomic maximum electron impact ionization cross sections with polarizability volume. 37

2.2 Correlation of atomic maximum electron impact ionization cross sections with $\left(\frac{\alpha}{E_0}\right)^{1/2}$ 38

2.3 Correlation between molecular maximum electron impact ionization cross section and polarizability volume 39

2.4 Correlation between molecular electron impact ionization cross section and $\left(\frac{\alpha}{E_0}\right)^{1/2}$ 40

2.5 The dependence of the position of the peak in the ionization efficiency curve on the rms molecular diameter. 42

2.6 Comparison of the performance of the electrostatic, BEB and DM models. . . 51

2.7 Comparison of the polarization model, DM and BEB calculations and experimental results. 52

2.8 Electron impact ionization surfaces for a series of small molecules 54

2.9 View from either end of the molecular dipole of the electron impact ionization surfaces for NH_3 and CH_3Cl. 55

2.10 Steric ratio for CH_3Cl and CH_3Br (DM calculations). 56

3.1 Schematic of the molecular beam machine. 64

3.2 Internal componenet of the molecular beam machine. 65
3.3 The aligment rod and hexapole assemblies. 66
3.4 Nozzle source assembly. 68
3.5 RF resonance cells 72

4.1 Structure of a supersonic expansion. 80
4.2 Euler's angles relating the set of molecule fixed axes xyz to a set of space fixed axes XYZ for a symmetric top molecule 84
4.3 Precessional motion of a symmetric top molecule. 88
4.4 Hexapole state selection and orientation of symmetric top molecules. 90

5.1 Intensity profiles for focused and unfocused beams of CH_3F. 98
5.2 Effect of $T_{\|}$ on the parallel velocity distribution and detected decay signal of a chopped supersonic molecular beam. 100
5.3 Experimental and simulated time of flight profiles and extracted velocity distributions for supersonic molecular beams of symmetric top molecules. 101
5.4 Comparison of two RF cell geometries. 104
5.5 Effect of hexapole voltage and seeding on RF resonance spectra of CH_3F. . . 106
5.6 Hexapole transmission curves for beams of CH_3F, CH_3Cl, CH_3Br and CH_3I for C fields of 20 and 0 Vcm^{-1}. 109
5.7 Rise in signal with increasing C field. 114
5.8 Ratio of upper to lower Stark states as a function of homogeneous field strength E and $\mu E < \cos\theta >$ for CH_3I. 115
5.9 Dip in the CH_3F beam signal observed on pulsing the C field to ground. . . . 116
5.10 Experimental arrangement required for the measurement of deorientation lifetimes for a beam of oriented symmetric top molecules in field free space. . . . 117

6.1 Effect of RF amplitude on the resonance signal measured for the $|21>$ peak of a 10% CH_3F/Ar beam at a hexapole voltage of 3000 V and RF frequency of 2 MHz. 121
6.2 Ion gauge calibration curves for He, Ne, Ar, Xe, CO_2, CH_4, CH_3F and SF_6. . 122
6.3 Resonance spectrum and hexapole transmission curves for the rotational states present in a seeded beam of CH_3F. 123

6.4 A typical data set used in determination of the cross section for collisional attenuation of the $|111>$ state of CH_3F by Ar. 125

7.1 Cutaway view of the halide ion source. 132
7.2 Graphite components of the ion source tip. 133
7.3 Standard calibration curve for a C type thermocouple. 134
7.4 Electrostatic lens system used for extraction and focusing of a low energy ion beam. 135
7.5 Dependence of ionizer temperature on heating power. 137
7.6 a) Temperature differential between inner graphite tube and porous graphite tip; b) Calibration curve for C type thermocouple used to measure temperature of ion source tip 138
7.7 Ion emission curves 141

8.1 Schematic of an ion imaging detector. 145
8.2 Illustration of the Abel transform image reconstruction technique. 149
8.3 Flow diagram representation of a generalised genetic algorithm. 159

9.1 Schematic of the experimental apparatus 164
9.2 Laser aligments used in photoinitiated bimolecular reaction studies. 166
9.3 Newton diagram for A+BC reaction. $\mathbf{k}$ is the relative velocity vector, $\mathbf{v}_{CM}$ is the CM velocity, $\mathbf{v}'$ and $\mathbf{w}'$ are the lab and CM frame product velocities and θ_t is the CM frame scattering angle. 168
9.4 Basis set for a) β_{sp} and b) β_{kv} profiles in the $H+H_2O \rightarrow OH(v=0,J=1)+H_2$ reaction. 171
9.5 Basis set for $\beta_{kj'}$, $\beta_{vj'}$ and $\beta_{kvj'}$ composite Döppler profiles in the $H+H_2O \rightarrow OH(v=0,J=5,A')+H_2$ reaction. 174
9.6 Simulated data and fits for forward scattering 178
9.7 Simulated data and fits for backward scattering 178
9.8 Simulated data and fits for forward–backward scattering. 179
9.9 Simulated data and fits for sideways scattering. 179
9.10 Simulated data and fits for isotropic scattering. 180
9.11 Experimental and best fit composite Döppler profiles for $OH(v = 0, J = 1)$ using uncontracted f_T basis functions. 181

9.12 Experimental and best fit composite Döppler profiles for OH($v = 0, J = 1$) using contracted f_t basis functions. 182
9.13 As for Figure 9.11 but for the A' Λ–doublet level of OH($v = 0, J = 5$). 182
9.14 As for Figure 9.12 but for the A' Λ–doublet level of OH($v = 0, J = 5$). 183
9.15 As for Figure 9.11 but for the A'' Λ–doublet level of OH($v = 0, J = 5$). 183
9.16 As for Figure 9.12 but for the A'' Λ–doublet level of OH($v = 0, J = 5$). 184
9.17 Experimental and best fit $\beta_{kj'}$, $\beta_{vj'}$ and $\beta_{kvj'}$ composite Döppler profiles and returned PDDCS's for the A' Λ–doublet of OH($v = 0, J = 5$). 185
9.18 As for Figure 9.17 but for the A'' Λ doublet component. 186
9.19 Polar plot of the rotational polarization of the OH($v = 0, J = 5, A''$) product of the H+H_2O reaction. 187
9.20 As for Figure 9.19 but for the A'' Λ doublet component. 187
9.21 Polar plot of the rotational polarization in the scattering plane of the OH($v = 0, J = 5, A'$) product of the H+H_2O reaction. 188
9.22 As for Figure 9.21 but for the A'' Λ doublet component. 188

10.1 Relative energies of accessible product channels for the Br^-+CH_3Cl reaction. 202
10.2 Dependence of interaction potential on direction for approach of a) Br^- to CH_3Cl and b) Cl^- to CH_3Br. 204
10.3 Electron gun for use in crossed beam electron impact ionization experiments. 206
10.4 Pierce electron gun characteristics 208
10.5 Phosphor screen detector designed for electron beam imaging. 209
10.6 Field plate assembly designed for the beam crossing region. 210
10.7 New scattering chamber lid 211
10.8 Pulse sequence for crossed beam ion/electron–molecule experiments. 213
10.9 3 × 3 basis set of ion images 216
10.10 Simulated and fitted ion images. 217
10.11 Simulated ion images 219
10.12 Images of a 1 eV Cl^- ion beam as a function of the potential applied to the electrostatic mirror. 221
10.13 Time of flight signal of background ions. 222

C.1 Centre of mass frame coordinate system 266

C.2 Coordinates involved in the CM to v_1 frame transformation 276

C.3 Definition of the Euler angles for the CM to v_1 frame transformation 277

LIST OF TABLES

1.1 Comparison of measured maximum electron impact ionization cross sections with literature values. 16

2.1 Relationships for the calculation of maximum electron impact ionization cross sections. 41

2.2 Maximum electron impact ionization cross sections for the inert gases calculated using the electrostatic model. 45

2.3 Comparison of experimental and calculated positions of the peak in the ionization efficiency curves for the inert gases. 47

2.4 'Cartesian averaged' maximum electron impact ionization cross sections for small molecules calculated using the electrostatic model. 49

2.5 Effect of level of theory and basis set on electron impact ionization cross section of CO calculated using the electrostatic model. 50

2.6 Effect of level of theory and basis set on electron impact ionization cross section of H_2O calculated using the electrostatic model. 50

4.1 Statistical weighting factors for symmetric top molecules. 95

4.2 Average orientation angles θ for some rotational states of symmetric top molecules 96

5.1 Optimised values of mean flow velocity u and parallel translational temperature $T_{\parallel}$ for continuous molecular beams. 100

5.2 Measured and calculated ratios of hexapole enhancements with zero C field to those with non-zero C field. 110

5.3 Estimate of the hyperfine interaction energy for the methyl halides based on the spin–rotation matrix elements. 113

6.1 Collisional attenuation cross sections for individual rotational states of a seeded beam of 10% CH_3F with a range of scatterers at a hexapole voltage of 5200 V. 124

7.1 Thermodynamic data for the species involved in ionization of CsCl on a lanthanum hexaboride surface. 130
7.2 Measured electron currents reaching each electrostatic lens element. 138

10.1 Reaction exoergicities for halide transfer and association reactions of K^+ ions with CH_3Cl, CH_3Br and CH_3I. 197
10.2 Geometries of CH_3X and $K^+.CH_3X$ association complexes calculated at HF/LanL2DZ level. 198
10.3 Optimum electrostatic lens potentials for Pierce electron gun determined from SIMION6.0 simulations. 207
10.4 Electrostatic lens potentials used for the Pierce electron gun. 207

A.1 Data for electrostatic model calculations of maximum electron impact ionization cross sections. 241
A.2 Maximum electron impact ionization cross sections for small molecules calculated using the *ab initio* method. 242
A.3 Maximum electron impact ionization cross sections for CX_3Y molecules calculated using the *ab initio* method. 243
A.4 Effect of basis set and level of theory on the maximum electron impact ionization cross section of CO. 244
A.5 Effect of basis set and level of theory on the maximum electron impact ionization cross section of H_2O. 244
A.6 Data for DM calculations on H_2. 246
A.7 Data for DM calculations on N_2. 246
A.8 Data for DM calculations on O_2. 247
A.9 Data for DM calculations on CO. 248
A.10 Data for DM calculations on NO. 249
A.11 Data for DM calculations on H_2O. 250
A.12 Data for DM calculations on CO_2. 251
A.13 Data for DM calculations on NO_2. 252
A.14 Data for DM calculations on NH_3. 254
A.15 Data for DM calculations on CH_4. 255
A.16 Data for DM calculations on CH_3F. 255

A.17 Data for DM calculations on CH_3Cl. 256
A.18 Data for DM calculations on CH_3Br. 258

D.1 The relationship between commonly determined 3D v_1 frame bipolar moments and the PDDCS's. 284
D.2 Construction of composite Doppler profiles by summing Doppler profiles according to rotational branch and experimental geometry 285

INTRODUCTION

The work described in this thesis falls into two sections. The first part, reported in Chapters 1 and 2, concerns experimental and theoretical studies into the process of electron impact ionization. Chapters 3 to 10 involve the design and characterisation of a crossed molecular beam ion imaging experiment for the study of electron and ion collisions with spatially oriented molecules. A brief introduction and chapter summary is included at the front of each section.

Part I

ELECTRON IMPACT IONIZATION CROSS SECTIONS – EXPERIMENT AND THEORY

INTRODUCTION

Electron impact ionization plays a major role in many areas of physics and chemistry. Electron bombardment is one of the most commonly used methods for ion production in mass spectrometry, having first been used for this purpose by Dempster in 1918.[1] The majority of ionization thresholds reported in thermochemical databases were determined through electron impact ionization studies.[2–4] The process is also widely used to produce ions for use in chemical dynamics studies, perhaps most notably in selected ion flow tube (SIFT) studies of ion–molecule reactions.[5] In addition to providing insight into the mechanism of the ionization process, accurate ionization cross sections are widely used in modelling studies involving a diverse range of systems, from fusion plasmas to radiation effects in medical and materials science.

While a great deal of data is available on ionization thresholds for electron impact ionization, the number of measurements of absolute cross sections for the process remains relatively small, and there is as yet no single theoretical model which can accurately reproduce cross sections for every class of molecule. Measurements of cross sections are almost exclusively 'bulb' type experiments, involving passage of an electron beam through a gas filled collision chamber, so that the result obtained is always an average over molecular orientation. In a recent series of electron–oriented molecule crossed beam experiments carried out in this group,[6–8] electron impact ionization of symmetric top molecules in a spatially oriented molecular beam demonstrated the orientation dependence of the ionization cross section for the first time.

The following two chapters each begin with a literature review of currently available techniques. Chapter 1 is concerned with experimental measurement of cross sections, while Chapter 2 concentrates on theoretical models for predicting these quantities. Original research in each of these areas is presented in the second part of each chapter.

The crossed beam experiments mentioned above are only able to determine relative ionization cross sections; absolute cross sections for the molecules studied have not previously

been measured. In Chapter 1 beam–gas measurements of absolute cross sections for methane and the methyl halides are presented. The development of a theoretical model for calculation of the maximum electron impact ionization cross section is detailed in Chapter 2. This model, based on a simple electrostatic treatment of the interaction between an electron and a target molecule, allows the orientation dependence of the cross section to be investigated, one of the objectives being to rationalise the results of the oriented beam experiments. A second model, based on the observed dependence of the electron impact ionization cross section on the molecular polarizability, is also discussed. The results of these calculations are compared with two of the major current theories available in the literature for the calculation of electron impact ionization cross sections.

1. EXPERIMENTAL DETERMINATION OF ELECTRON IMPACT IONIZATION CROSS SECTIONS

1.1 Experimental requirements

The experimental determination of a total electron impact ionization cross section requires the measurement of four quantities:[9]

1. the electron current I^- of the ionizing electron beam of known energy;
2. the ion current I^+ produced through collisions of the electron beam with the target gas;
3. the number density n of the gas;
4. the path length l over which the ions are collected.

Such an experiment generally consists of passing a beam of electrons of known energy through a collision cell containing a gas sample of known temperature and pressure and detecting the resulting ion and electron currents.[10]

If the ion detection is mass selective then partial ionization cross sections σ_i may be determined, corresponding to the production of i electrons and an ion or ions having total charge $+ie$. Some systems allow the counting cross section $\sigma_c = \sum_i \sigma_i$, also known as the ion production cross section, to be obtained, but in general the measured quantity is the total, gross, or electron production cross section $\sigma_t = \sum_i i\sigma_i$. The total cross section is determined from the listed quantities using the Beer-Lambert law.

$$\frac{(I^- - I^+)}{I^-} = e^{-n\sigma_t l} \tag{1.1}$$

in which I^- is the electron beam current incident on the collision cell, I^+ is the positive ion current resulting from electron impact ionization processes within the cell, n is the number density of the sample gas inside the cell and l is the path length over which ions are formed. The quantity $(I^- - I^+)$ is the electron beam current transmitted through the collision cell.

Since $n\sigma_t l$ is much less than unity the exponential may be approximated by the first two terms of its Taylor expansion, leading to the more commonly used expression:

$$\frac{I^+}{I^-} = nl\sigma_t \tag{1.2}$$

There are several criteria which must be fulfilled for any measuring apparatus in order to ensure that accurate ionization cross sections are obtained.[11]

1. The gas pressure must be kept low enough to preclude scattering of the electron beam. This requires a pressure of less than 10^{-3} Torr.

2. To prevent space-charge effects in the electron beam the beam current should be kept to below 10^{-6} A.

3. The electron current to all electrostatic elements apart from the electron collector must be minimised. The electron current collected must be independent of the potential applied to the collector, again to guarantee complete collection of the electron beam.

4. In order to ensure that all the ions produced are recorded, the potential on the ion collector must be large enough so that the measured ion current has become independent of the collector potential. If a magnetic field is used to constrain the electron beam to an axial flow the ratio of ion to electron currents must be independent of the magnetic field strength. Inclusion of a magnetic field for confinement of electrons to the beam axis has the added advantage of preventing further ionization of the target gas by high energy secondary electrons produced in the primary ionizing collisions: the primary ion is accelerated away from the collision region to the collector plate with minimal risk of further encounters with primary or secondary electrons.

1.2 *Literature review: Experimental techniques for the measurement of electron impact ionization cross sections*

1.2.1 The condenser plate method

The condenser plate method is the most commonly used technique for measuring the electron impact ionization cross section of a static gas target. One of the earliest designs was that of Compton and Van Voorhis.[12] Electrons were produced at a molybdenum filament in the source chamber and focused into a gas filled scattering chamber through a metal tube

separating the two chambers. The resulting ions were collected on a set of five wires in a circular arrangement around the outside of the scattering chamber, while the electrons were detected on a further set of wires at the far end of the chamber. The pressure was measured using a McLeod gauge. Attempts at wire wrapping the chamber in order to produce an axial magnetic field to constrain the electron beam were unsuccessful, making it necessary to apply a large negative potential to the ion collector and leading to poor resolution of the electron energy. This problem was overcome by setting up an integral equation to represent the observations and solving it by differentiating the experimental curve.

Tate and Smith[13] improved the above design, surrounding the instrument with a solenoid to provide a magnetic field which helped to define the electron beam and also facilitated the separation of the electrons and ions for ion collection, without introducing a large uncertainty into the electron energy. A schematic diagram is shown in Figure 1.1

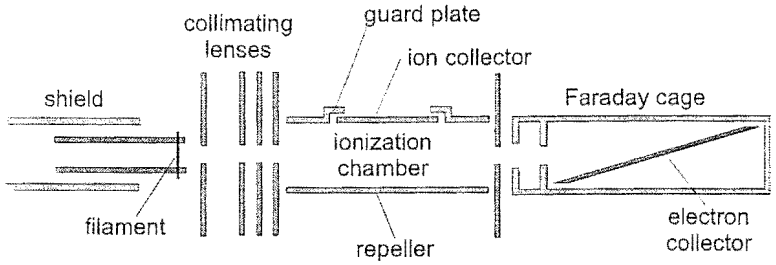

Figure 1.1: Tate and Smith ion source

Electrons are emitted from a resistively heated tungsten filament and pass through a set of collimating lenses which accelerate and focus the beam before it enters the ionization chamber. A field of around 5 Vcm^{-1} is maintained between the repeller and ion collector plates to accelerate positive ions formed in the ionization chamber towards the collector. Guard plates situated on either side of the collector ensure homogeneity of the electric field in the region of ion collection. At the end of the ionization chamber the unscattered portion of the electron beam passes through a final collimating lens and strikes the electron collector. The ion and electron currents are measured using sensitive ammeters attached to the ion and electron collector plates respectively. It is important that the electron collector is kept at a high positive potential with respect to the Faraday cage to ensure that all the electrons are collected on the plate and not lost to the chamber walls.

Tate and Smith used this apparatus to measure cross sections for helium, neon, argon, and mercury[14] and later molecular targets.[15] These results achieved much higher accuracy than

any previous measurements due to the well defined path length and more accurate knowledge of the electron energy for the Tate and Smith ion source.

Over thirty years later Rapp and Golden[16] made a series of measurements of atomic and molecular electron impact ionization cross sections using an essentially unchanged Tate and Smith type design. Two different kinds of measurements were possible. Total ionization cross sections could be measured by maintaining an electric field between the repeller and collector sufficient to collect all the positive ions formed in the fixed path length on the ion collector. The device could also be used to study dissociative ionization by reversing the field so that ions were collected on the positive plate. Becuse the ions had to move against a retarding field to reach the plate, only dissociated ions, which had gained kinetic energy during the dissociation process, could reach the detector.

The electron impact ion source designed by Tate and Smith has a great deal of versatility. It has been used in many subsequent experiments and the basic design is still used today; the results of recent measurements are still in good agreement with the original values determined by Tate and Smith in their work carried out during the 1930's.

1.2.2 The Lozier tube

This type of device has been used by several groups for a variety of different studies, including the determination of appearance energies and kinetic energies of ion fragments produced in electron impact induced dissociation processes[10,17] as well as the measurement of total ionization cross sections. The basic system is shown in Figure 1.2.

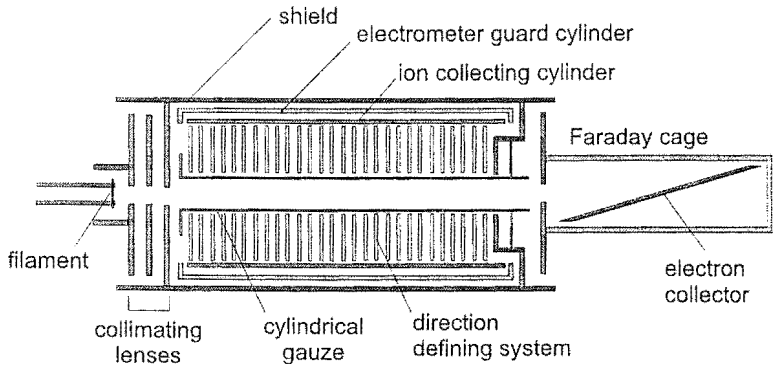

Figure 1.2: Lozier tube

The electron beam is treated in the same way as in the Tate and Smith source. Electrons are formed at a heated filament and accelerated through a series of three lenses into the

ionization chamber. A magnetic field supplied by an external solenoid constrains the electrons to move along the axis, and they are detected on a Faraday plate. As it passes through the ionization chamber the electron beam is contained within a cylindrical gauze. Surrounding the gauze is a direction defining system consisting of a series of thin cylindrical disks, supported on three slotted bars. This in turn is enclosed by an ion collecting cylinder, electrometer guard cylinder, and shield.

Ions formed in collisions of the target gas with the electron beam pass through the gauze and a small proportion, whose direction of motion is almost perpendicular to the electron beam, pass through the defining system towards the ion collector. To measure the kinetic energy of the ions a radial electric field is applied between the disks of the direction defining system and the collector. The gauze is present so that an electric field may be applied between this and the defining system, if required, to prevent negative ionic products of dissociation processes from reaching the detector.

Tate and Lozier[18] first used the device to measure quantities such as the kinetic energy distribution of the ions produced at a specified electron energy, the minimum energy required to produce ions of a specified energy, and the relative efficiencies of production of ions of a specified energy as a function of incident electron energy. This final measurement is effectively a determination of a relative electron impact ionization cross section. Absolute cross sections cannot be measured using the Lozier tube since the collection efficiency for the ions is less than 100%, and is in fact unknown in practice. In order to obtain the true cross section the data has to be normalised to the results of a previous measurement made using some other technique. Even after normalization the anisotropy of the angular distribution of the dissociated products leads to significant errors in the determination of total electron impact ionization cross sections using this method. Also, Tozer[19] noted that for polyatomic molecules it is likely that different dissociation products will have different collection efficiencies, so that the method of normalization employed may not be particularly reliable in these cases.

1.2.3 The summation method

In the summation method a mass spectrometer is used to detect the ions in place of the simple Faraday plate–electrometer arrangements used in the systems discussed so far. The measured quantities are partial ionization cross sections rather than gross cross sections, since each type of ion fragment resulting from an electron impact has a different mass to charge ratio and is

therefore detected separately. Since the detection efficiency is not unity, only relative cross sections may be measured in this way, as for the Lozier tube experiments, and the results must be normalized against a known measured value of the absolute cross section. Care must be taken to ensure that the ion collection efficiency inside the mass spectrometer is independent of the mass to charge ratio of the ion, and also of the energy of the ionizing electron. If these requirements are satisfied then the resulting partial ionization cross sections are all on the same scale and differ from the absolute values only by a common constant factor determined by the collection efficiency of the mass spectrometer. The unnormalized total cross section is determined from

$$\sigma = \sum_i i\sigma_i \tag{1.3}$$

This quantity can be compared to a known value of the cross section determined by some other method, often the condenser plate method, in order to obtain the normalization factor required for correction of the measured partial ionization cross sections. If a value for the absolute cross section is unavailable it is often acceptable to assume that the normalization factor is the same as that for some other target molecule for which the partial cross sections have been measured and the total cross section is known, as shown by Märk and Egger,[20] who normalized the cross section for PH_3 using the normalization constant determined from measurements on argon. This constant had been calculated as the ratio of the total cross section measured by the summation method to that obtained by Rapp and Englander-Golden[21] using the condenser plate method.

One of the first studies using the summation method was that of Kistemaker *et al*,[22] who measured the electron impact ionization cross section of H_2O using a special cycloidal mass spectrometer with an extremely high ion extraction efficiency in order to avoid mass discrimination effects. The data was normalized against measurements made in the same laboratory using a condenser plate source. The same study was repeated by Märk and Egger[23] with a few improvements to the method, giving results in fairly good agreement with Kistemaker. The summation method of determining electron impact ionization cross sections has since been applied to a wide range of atomic and molecular targets.

1.2.4 Other experimental methods

In addition to the methods described above, there are several other techniques which have been successfully used in the experimental determination of electron impact ionization cross sections.

Nottingham and Bell[24,25] developed a method specifically for the purpose of accurately determining the absolute electron impact ionization cross section of mercury. A semicircular electron velocity analyser included in their design allowed very high energy resolution, since only electrons of the required velocity emerged from the analyser into the ionization chamber. Other aspects of the experiment were similar to the condenser plate method.

Another type of measurement uses so called 'gas filled counters'.[9] This method has mainly been used to determine electron impact ionization cross sections at fairly high energies of greater than 100 eV and is therefore well suited for making measurements for comparison with the predictions of the Bethe theory[26] (see Chapter 2). The method was first suggested by Graf[27] and measurements have since been carried out by McClure[28] and more recently by Rieke and Prerejchal.[29] The electrons are produced from a beta emitter and velocity selected in a magnetic analyser. The analysis is based on the application of Poisson statistics to the collision process. The probability P that an electron passes through the ionization chamber without ionizing a target molecule is measured and can then be used to determine the cross section σ via the relation

$$-\ln(P) = nl\sigma \tag{1.4}$$

where n is the number density of the target gas and l is the path length through the chamber.

The method of crossed beams was originally introduced into this field by Boyd and Green[30] and Fite and Brackman[31] to enable cross section measurements to be carried out on species that are unstable at ordinary temperatures and pressures. The method has both advantages and disadvantages over the techniques described so far. The much lower number density and smaller collision region compared to other methods translates into low signal levels, which generally makes modulation of the signal necessary in order to separate it from the background. Because the target can no longer be treated as stationary with respect to the incoming electron beam, the cross section is no longer given by the simple relation

$$\frac{I^+}{I^-} = nl\sigma \tag{1.5}$$

and the correct expression is

$$\frac{I^+}{I^-} = \frac{(v_e^2 + v_t^2)^{1/2}}{v_t v_e}\sigma(E)RF \tag{1.6}$$

where v_e and v_t are the electron and target beam velocities (assumed to be perpendicular), R is the number of target molecules per second arriving at the target detector. E is the energy of relative motion of the target and electron, and F is a measure of the beam overlap. Because of the difficulty in determining R experimentally, cross sections determined via crossed beam experiments often need to be normalized against a known value, as described above for the Lozier tube and summation methods.

The stability of species in a molecular beam makes it possible to measure cross sections for many species which would be impossible to obtain by any other method. The development of oriented beam techniques has also allowed an orientation effect on the ionization cross section to be demonstrated for the first time. Experiments carried out on oriented molecular beams of a series of symmetric top molecules[6–8] showed that a distinct preference for ionization exists when the electron approaches the positive end of the molecular dipole. One of the advantages of the crossed beam technique is that the initial velocities of the collision partners are well defined. If a moveable time-of-flight or ion imaging detection system is used products may be detected as a function of scattering angle and velocity, creating the possibility of investigating the dynamics of the ionization process in ways which are inaccessible by other methods. A system designed to carry out these experiments is described in Chapter 10.

1.3 *Experimental measurement of absolute electron impact ionization cross sections for CH_4, CH_3F, CH_3Cl, CH_3Br and CH_3I*

As mentioned previously, research has recently been carried out into the orientation dependence of electron impact ionization cross sections for a series of methyl halides.[6–8] Following these experiments a simple model was developed which allows total electron impact ionization cross sections to be calculated as a function of molecular orientation. The model was found to qualitatively reproduce the orientation dependence observed experimentally, but there were no published measurements of the absolute cross sections for the methyl halides against which to judge the values predicted by the model. A decision was made to make measurements of these cross sections using a condenser plate type ionization cell.

The ionization cell used for these measurements is a modified version of the condenser

plate type ion source used by Tate and Smith and described in Section 1.2.1. The cell was designed by Sean Harris, a previous doctoral student, and had previously been used to make preliminary measurements of the maximum electron impact ionization cross sections for the inert gases and several small molecules, though it had not been extensively characterised or used to determine the energy dependence of the cross section. The cell is shown in Figure 1.3.

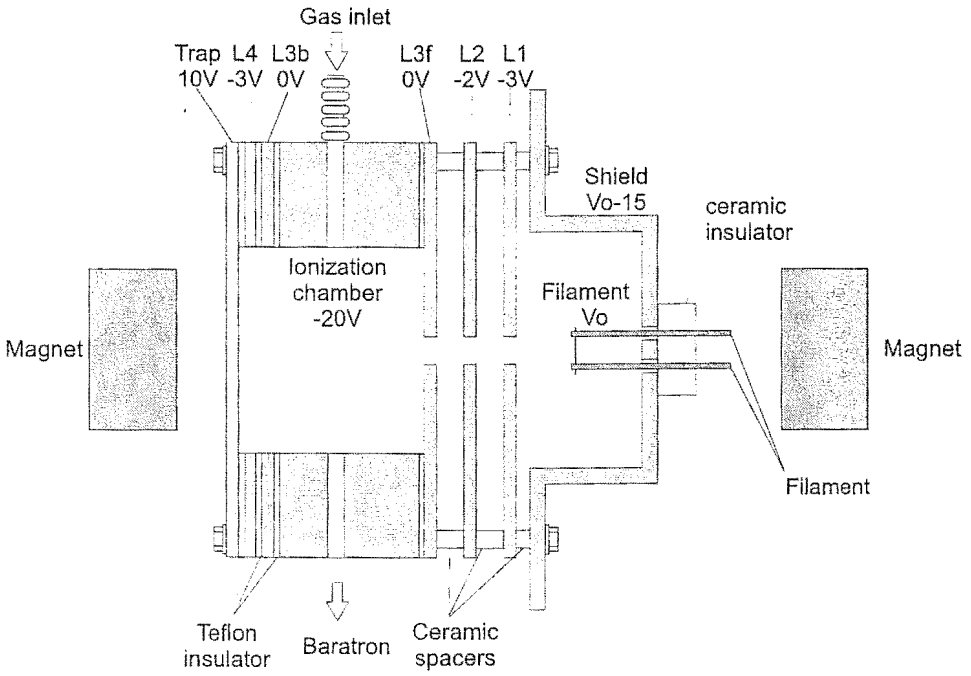

Figure 1.3: Electron impact ionization cell used for measuring ionization efficiency curves for methane and the methyl halides

The device is housed inside a vacuum chamber with a typical background pressure of around 10^{-6} Torr. Electrons are formed at a resistively heated rhenium filament. A shield held at a potential of -15 V relative to the filament serves to repel the electrons towards a set of three stainless steel lens elements which collimate the beam. The lenses each have a 1 mm aperture in the centre for the beam to pass through and are spaced 2 mm apart. The electron energy is controlled through variation of the potential of the filament relative to the ground potential of the collision region. The beam enters the collision cell through the third lens element, which is insulated from the cell and maintained at ground potential. A magnetic field generated by 20 mm diameter rare earth cobalt permanent magnets situated at each

end of the beam path constrains the electron beam to the axis*. The magnets are rated at 8200 Gauss at the pole face, and the magnetic field strength at the centre of the collision cell was measured with a Hall probe to be 700 Gauss.

The collision cell is cylindrical, with a radius of 5 mm and a length of 11 mm and is machined from stainless steel. The inside surfaces are coated with colloidal graphite to prevent surface scattering of charged particles; this is important since the walls of the collision cell also serve as the ion collector. Two diametrically opposed 3 mm diameter apertures are drilled through the wall of the collision cell. The gaseous sample is admitted through one aperture via a Leybold-Hearaeus needle valve, while the other is a port for a high accuracy 0.05 Torr full scale MKS baratron used for monitoring the pressure in the cell. The temperature of the gas sample is assumed to be the same as that of the collision cell wall, and is measured using a chromel-alumel thermocouple attached to the outer surface of the collision chamber and read by a Doric digital pyrometer.

After traversing the collision cell, the electron beam passes through two further lens elements before being collected on a Faraday plate. The ion currents from the collision cell wall and electron current from the Faraday plate are recorded using Keithley Model 486 picoammeters.

Ion trajectories through the system were simulated using Simion6.0.[32] There were two main objectives to this modelling exercise:

1. the electrostatic lens potentials could be optimised for production of a well focused electron beam. The optimised potentials used in the experiments are shown in Figure 1.3;

2. the distance over which newly formed ions reached the detector, i.e. the path length l of Equation 1.2, could be determined. This was found to be 13.3 mm and was independent of the mass of the ion used in the simulations within the uncertainty of the calculation method.

The effect of the collision cell and Faraday plate potentials on the ion and electron currents was measured. As expected, the signal levels increased with increasing detector potentials, leveling off at a collision cell (positive ion collector) potential of -10 V and a Faraday cup

* Cross sections measured in the absence of the magnetic field were identical to those measured with the magnets installed, within the limits of experimental reproducibility.

(electron collector) potential of +3 V for an electron energy of 70 eV. Further increases in the magnitudes of these potentials had no effect on the collection efficiency. The values of these thresholds for maximum ion and electron collection were found to scale with the square root of the electron energy i.e. linearly with the electron velocity. For the experiments described, the ion collector was set at a potential of -20 V and the electron collector at +10 V. With these potentials the ratio of the ion current to electron current using argon as a test gas was independent of the cell pressure over the range 5×10^{-6} to 1×10^{-3} Torr. All cross section measurements were made at a cell pressure of between 2 and 6×10^{-4} Torr. Electron currents were kept below 100 nA to exclude space charge effects, and typical ion currents were in the range 1 to 100 pA.

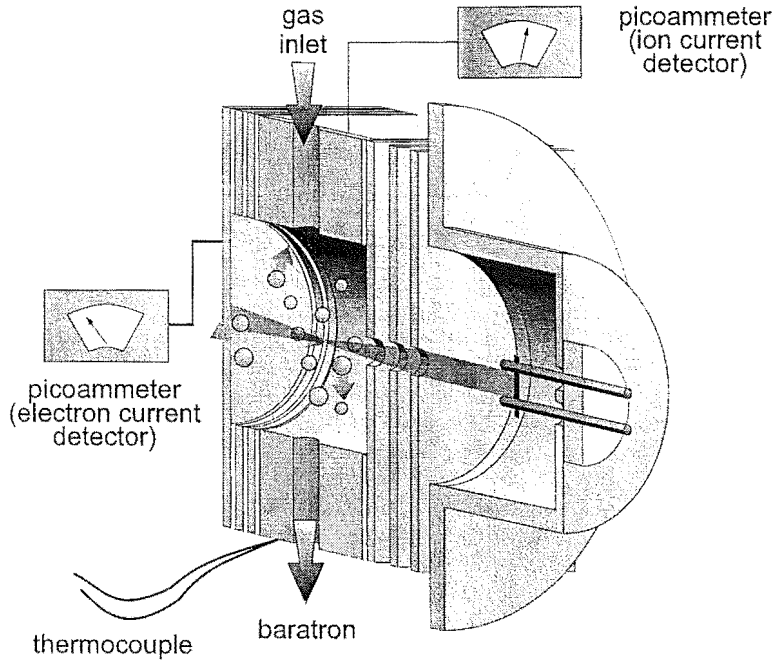

Figure 1.4: Measurement of an electron impact ionization cross section. Test gas is admitted to the chamber and ionized by the electron beam. The pressure and temperature of the test gas, and the electron and ion currents are measured and used to calculate the ionization cross section from Equation 1.9.

The experiment is illustrated in Figure 1.4. In practice, the measurement of an ionization efficiency curve proceeds as follows. The cathode potential is adjusted to set the electron energy to the desired value, usually close to the ionization threshold. After zeroing the picoammeter used to detect the electron current to the Faraday plate, a current of aroumd 2.6-2.7 A is passed through the filament and the electron current allowed to stabilize. The

Table 1.1: Comparison of maximum electron impact ionization cross sections measured with the ionization cell shown in Figure 1.3 for the inert gases with literature values.

	σ_t (this work)	σ_t (literature)
He	0.39±0.05	0.37,[16,33,34] 0.38[35]
Ne	0.63±0.03	0.72,[33] 0.74,[35] 0.78[16]
Ar	2.81±0.03	2.54,[33] 2.70,[35,36] 2.86[16]
Kr	3.50±0.10	3.70,[35] 3.72,[33] 4.26[16]
Xe	5.10±0.13	4.59,[37] 4.98,[35] 5.46[16]

filament current is kept fairly low to generate an electron current which does not exceed 100 nA as the electron energy is increased, preventing any significant space charge effects. The picoammeter monitoring the current to the ion collector is zeroed and the target gas admitted to a pressure of around 3×10^{-4} Torr. Once the ion current has stabilized the electron current, ion current, gas temperature and pressure are recorded. Usually several measurements are made and the results averaged. These steps are repeated as the electron energy is increased.

The ideal gas law is assumed, so that the number density n for the gaseous sample may be determined from the measured temperature T and pressure P.

$$n = \frac{P}{k_B T} \tag{1.7}$$

where k_B is Boltzmann's constant. The ionization cross section at each electron energy may then be determined by rearranging Equation 1.2

$$\sigma = \frac{I^+}{I^-}\frac{1}{nl} \tag{1.8}$$

Using the path length of 13.3 mm determined from the trajectory simulations described earlier, and carrying out the required unit conversions, the electron impact ionization cross section may be determined from the numerical expression

$$\sigma = (7.788 \times 10^{-4})\frac{I^+}{I^-}\frac{T}{P} \tag{1.9}$$

in which I^+ and I^- are measured in nA, T in Kelvin and P in Torr.

As a test of the experimental setup, the first cross sections to be measured with the ionization cell were those of the inert gases. These cross sections have been measured previously by several groups[16,33–35,37] and make good standards for comparison. Ionization cross

sections were measured for He, Ne, Ar, Kr and Xe at an electron energy of 80 eV, near the maximum in the ionization efficiency curves. These cross sections were in close agreement with previously recorded values and are shown in Table 1.1. The standard deviations shown were calculated over 15–20 repeated determinations of the maximum ionization cross section. This data will be compared with the results of theoretical calculations in Chapter 2.

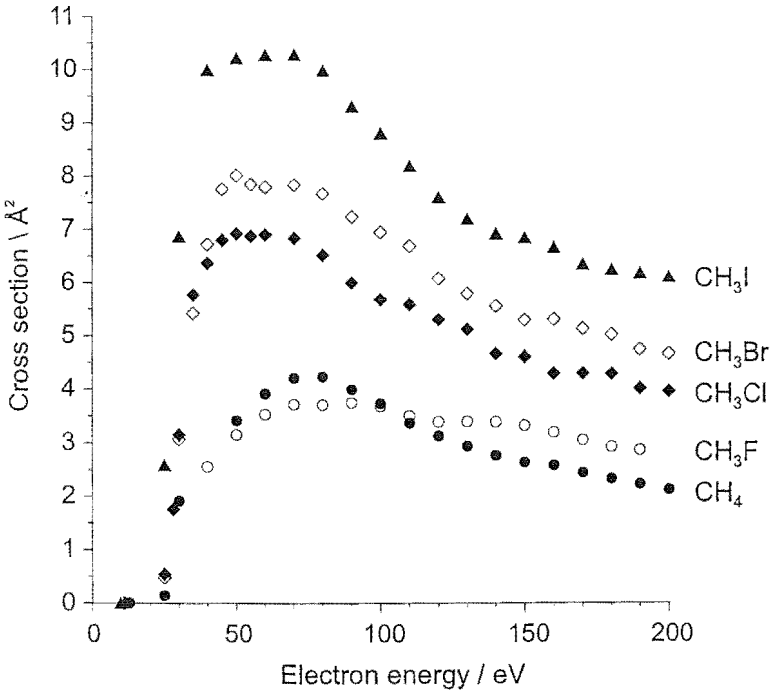

Figure 1.5: Experimentally measured ionization efficiency curves for methane and the methyl halides.

The ionization efficiency curves determined by this method for methane and the methyl halides are shown in Figure 1.5. The maximum in the ionization efficiency curve moves to lower electron energy as the molecular mass increases, with a shift of around 20 eV between CH_3F and CH_3I. This effect has also been observed previously in both experimental and theoretical data on the series of inert gases, and a possible reason for the shift will be explored in Section 2.2.1. Methyl fluoride has a somewhat broader peak than the other methyl halides, but otherwise the curves all exhibit a similar shape. The maximum cross section for CH_3Cl of 6.92 Å^2 is significantly lower than the previously published value of around 9.4 Å^2, but the results for CH_4 are in good agreement with literature values. Literature values were not available for comparison in the cases of the remaining methyl halides. These cross sections will be compared with theoretical results in the following chapter.

2. THEORETICAL DETERMINATION OF ELECTRON IMPACT IONIZATION CROSS SECTIONS

2.1 Literature Review: Theoretical methods for the calculation of electron impact ionization cross sections

2.1.1 Introduction

Electron impact ionization is a difficult problem to treat rigorously using quantum mechanical methods, one of the main reasons being that the exit channel, consisting of two free electrons in the field of an ionized atom or molecule, constitutes a complex quantum many body system.[9] In addition, there are also the usual considerations of coupling effects, target polarization and other factors which are involved in all electron–atom scattering calculations. For these reasons attention has been focused on the development of approximate methods which, while physically reasonable, are manageable for use in numerical calculations. The result is a wide range of semi-empirical and semi-classical methods for calculating the ionization cross section, in addition to the more rigorous quantum mechanical approaches.

Quantum mechanical methods, while only applicable to a small number of systems, can give very detailed information. They are able to take into account quantum phenomena such as resonance effects, exchange and electron correlation, which cannot be treated using semi-empirical and semi-classical theories but can have a significant effect on the experimentally measured cross section. Though quantum scattering calculations have not been carried out on the systems studied in this work, a brief description of the quantum mechanical treatment of electron impact ionization has been included both to show the current state of knowledge in this area, and also to illustrate some of the difficulties which have led to the widespread interest in semi–classical and semi–empirical treatments of the electron impact ionization process.

2.1.2 Quantum mechanical calculations and the partial wave approximation

The many body problem is now fairly easy to deal with for bound systems, and can also be extended to the case of a bound system in the presence of a single free electron. However, so far it has not been possible to apply similar methods to a system containing two free electrons, for which the exit channel of the electron impact ionization process provides an example. Several groups[38] have applied perturbation methods in an attempt to solve this problem. Fadeev[39] used a different approach and reformulated the three body problem in terms of an infinite number of two body problems. While these are no longer difficult to solve in theory, in practice they are still computationally unmanageable. So far these kinds of approaches have only been applied to very light atoms such as hydrogen or helium. Almost all calculations on many electron systems use some variation on the partial wave approximation.

In partial wave theory, free electrons are treated as waves. An electron with momentum $\mathbf{k}$ has a wavefunction $\psi(\mathbf{k}, r)$, which is expressed as a linear combination of angular functions—the spherical harmonics $Y_{lm}(\theta, \phi)$—and radial functions $R_l(\mathbf{k}, r)$.

$$\psi(\mathbf{k}, r) = \sum_{lm} c_{lm} Y_{lm}(\theta, \phi) R_l(\mathbf{k}, r) \tag{2.1}$$

The radial function is a solution to the associated radial Schrödinger equation.

$$\left[-\frac{1}{2}\frac{d^2}{dr^2} + \frac{l(l+1)}{2r^2} + V(r) \right] R_l(\mathbf{k}, r) = \frac{\mathbf{k}^2}{2} R_l(\mathbf{k}, r) \tag{2.2}$$

in which $V(r)$ is the potential experienced by the free electron and largely determines the functional form of $R_l(\mathbf{k}, r)$. There are several variants of the partial wave approximation, differing in the functional form used for the potential $V(r)$. In the simplest treatment, known as the plane wave Born approximation, the potential is set to zero. The target atom has no interaction with the electron, and the resulting radial functions are the spherical Bessel functions. Because of its relative simplicity this method has been widely applied.[40–46] The first improvement to this treatment is to assume that the free electron undergoes a Coulomb interaction with an effective nuclear charge Z centred on the ionized target atom, i.e. $V(r) = -\frac{Z}{r}$. In this case the $R_l(\mathbf{k}, r)$ are Coulomb functions, and this treatment is therefore known as the Coulomb approximation. Nussbaumer and Moores[47,48] have used this form to carry out calculations for several ionic targets. A further improvement is to include a term describing the potential due to the electrons of the atomic target—the so called 'distorted wave approximation'—so that $V(r) = -\frac{Z}{r} + V_{\text{elec}}$. This type of potential has been used in the study of both atomic and ionic targets.[49–56]

During the scattering process the incident electron approaches the target with energy E, interacting via the Coulomb potential $V_{12}(r_1, r_2)$ with the electrons of the target. An inelastic transition scatters the free electron into a final state of energy E_f, at the same time as a bound electron is ejected into a state of energy E_e. Considering only the first order perturbation, the matrix element describing this direct interaction is

$$M_d = \left\langle \psi_b \psi_i \left| \frac{1}{r_{12}} \right| \psi_e \psi_f \right\rangle \tag{2.3}$$

where the wavefunctions ψ_b, ψ_i, ψ_e and ψ_f describe the bound, incident, ejected and final scattered electrons respectively.

The state to state transition probability, or probability of ionization, is proportional to the square of this matrix element.

$$P(bi, ef) \propto |M_d|^2 \tag{2.4}$$

Incorporating the required kinematic factors transforms the transition probability into a cross section.

$$\sigma(E, E_e, E_f) = \frac{16a_0^2}{E} \sum_L (2L+1)|M_d|^2 \tag{2.5}$$

where L is the total angular momentum of the electron–target system. The total cross section is obtained by integrating over the final states of the electrons.

$$\sigma(E) = \int_0^{E_{\max}} \sigma(E, E_e, E_f) dE_e \tag{2.6}$$

According to the so called 'half range Born' approximation, the upper limit is given by $E_{\max} = \frac{1}{2}(E - E_0)$, where E_0 is the ionization potential of the target.

When treating the electron impact process quantum mechanically there are several phenomena which should be taken into account. Resonances in the cross section, electron correlation between the various electrons involved in the process, and also exchange due to the indistinguishability of the electrons can all contribute to the cross section and have not been included in the treatment so far.

Exchange

There are two types of exchange to be considered. Potential exchange between a free electron and a bound target electron is analagous to the type of exhange encountered in Hartree–Fock

calculations on bound state systems, and can easily be included in a frozen core aproximation by incorporating non-local terms in V_{elec}. Scattering exchange between the two final state free electrons is much more difficult to deal with. The exchange scattering matrix element is

$$M_{\text{ex}} = \left\langle \psi_b \psi_i \left| \frac{1}{r_{12}} \right| \psi_f \psi_e \right\rangle \tag{2.7}$$

so that the total ionization probability including exchange is

$$P(bi, ef) \propto |M_d + M_{\text{ex}}|^2 = |M_d|^2 + |M_{\text{ex}}|^2 - \lambda |M_d||M_{\text{ex}}| \tag{2.8}$$

The first two terms are the direct and exchange ionization terms, while the remaining term is an interference term. λ is a phase factor related to the relative phases of the two matrix elements and depends on the interaction between the two electrons. There are several commonly used choices for λ. In the Born-Oppenheimer approximation $\lambda = 0$, the interference term is ignored, and since the exchange cross section is often comparable to the direct cross section the total cross sections obtained are usually far too large. A more realistic approximation is the Born–exchange approximation, of which there are two variants. In the Peterkop formulation[57] λ is set equal to unity, maximising the interference term and minimising the total exchange contribution. In the Rudge and Schwartz formulation[58] λ is chosen to cancel the imaginary part of the scattering matrix element. For both methods the cross section calculated including exchange is not too different from the direct cross section, and both give comparable results.

In the Born-Oppenheimer approximation the same final state orbitals are used to calculate both matrix elements. In the Born-exchange approximation overlapping orbitals in a matrix element must be calculated in the same potential so that orbitals on opposite sides of the scattering matrix remain orthogonal. In practice the fast final state partial wave is calculated using the potential of the ion (an $N-1$ electron system) and the slow ejected electron wave in the potential of the initial target (an N electron system). This choice gives total electron impact ionization cross sections in good agreement with experiment for light atoms and ions.

Resonances

Resonances arise when the energy of the bound target system is the same as that of the ionized state in the presence of a free electron, and can occur in either the entrance or exit channels of the electron impact scattering process. Resonances involving the incoming electron lead

to spikes in the total cross section at specific incident electron energies corresponding to the resonance state, while resonances involving the ejected electron appear as spikes in the energy differential cross section $\sigma(E, E_e, E_f)$. Since an exit channel resonance will contribute to the total cross section at all incident electron energies above its threshold, it leads to sharp steps in the total cross section at the corresponding threshold energy. These resonances can be considered as excitation into a configuration which is autoionizing and are often called 'excitation–autoionization' resonances.

Usually a cross section is first calculated ignoring resonances and the cross sections corresponding to excitation of autoionization resonances involving the ejected electron are then added. This assumes that all atoms excited to the resonance state will autoionize, which is not true for highly charged ions; as the ionic charge increases, the rate of relaxation to a true bound state of the N electron system through photon emission becomes faster than the rate of autoionization from the resonance state. In these cases the contribution from excitations must be modified by multiplying the resonance cross section by an effective branching ratio for autoionization versus stabilization. Accounting for resonances can make quantum mechanical calculations of electron impact ionization cross sections very complicated and various different approaches have been attempted to simplify the problem.[59,60]

Correlation

Correlation generally has only a minor effect on electron impact ionization cross sections due to the two body nature of the Coulomb operator $\frac{1}{r_{12}}$ which governs the interaction. The most important correlation corrections to a Hartree–Fock ground state wavefunction usually involve doubly excited determinants or 'pair correlations'. Since $\frac{1}{r_{12}}$ is a two body operator, the total wavefunctions on either side of an interacton matrix element can only differ by a maximum of two electrons. One of these electrons is the scattered electron undergoing a transition from the incident to the final scattered state, while the other is the orbital corresponding to the bound electron, which becomes the ejected electron wave. If a double excitation is included in the wavefunction for the entrance channel the initial and final total wavefunctions differ by too many electrons and the matrix element disappears. If the double excitation is included in both the entrance and exit channels the matrix element no longer disappears, but the contribution to the cross section is usually still small since the 'excited' matrix element does not generally add in phase to the ground state matrix element. It is

much more difficult to treat electron correlation between the two final state free electrons, and so far the effects of such correlations have not been included in calculations.

Partial wave methods have been widely used and tested on a variety of systems (see[9] and references therein). They are usually accurate to better than 50% for total ionization cross sections of light atoms. Very heavy atoms have been less successfully treated due to the increasing contributions of resonances and electron correlation effects, although cross sections accurate to within a factor of two have been obtained in some cases.[46] At present quantum mechanical calculations using the partial wave method are limited to atomic or ionic targets.

2.1.3 Semi-empirical and semi-classical calculations

Due to the complexity of a quantum mechanical treatment of electron impact ionization for all but relatively simple systems, a large number of semi-empirical and semi-classical models have been developed. A common shortfalling of these treatments is that they often make basic assumptions which can limit their range of validity to fairly small classes of atomic or molecular targets. However, the more successful of such theories apply to broad classes of species, and can be extremely useful for generating cross sections in the absence of good experimental data. Comparing the results of these calculations with experiment also gives some insight into the validity of the approximations and assumptions on which the models are based.

Semi-empirical treatments of the electron impact process attempt to formulate fairly simple equations containing parameters determined experimentally in order to reproduce the measured cross section and possibly determine cross sections for systems which have not been studied experimentally. Semi-classical treatments make classical approximations to simplify the full quantum mechanical scattering problem. They commonly contain empirical adjustable parameters determined from a best fit to known experimental data. Several fairly major approximations must be made in going from the quantum mechanical to the semi-classical treatment,[61] in which the collision must be treated according to classical laws of motion. The initial state of the bound electron must be described classically in terms of some kind of classical orbit. Various approaches have assumed this electron to be either at rest, orbiting at a constant velocity, or to have some predetermined velocity distribution.[62] Because the three body problem is difficult to deal with, the binary-encounter approximation is often used to simplify the electron impact process to a two body problem. This simplification

was first introduced by Thomson,[63] who treated the ionization process as a simple two body collision between the incident electron and an atomic or molecular electron in the target.

Ionizing collisions may be classified as either fast or slow depending on the relative magnitudes of the incoming electron velocity and the mean orbital velocity of the atomic or molecular electron in the target. Different approximations can be made for the two cases. The Born approximation is often applied to fast collisions,[26,64] while classical scattering theories such as the binary encounter approximation[63] may be used for slow collisions.

A point to bear in mind when using these semi-empirical and semi-classical approaches is that they can generally only give either partial cross sections σ_i, the cross section for production of an ion of charge i in a collision, or counting cross sections $\sum_i \sigma_i$, the sum of all partial cross sections. Most experiments measure the total ion current produced by all ionization processes, and the cross sections derived from such measurements will usually always be greater than the counting cross section. For example, a doubly charged ion will contribute twice the current of a singly charged ion, so that unless the number of ionization events can be measured, the quantity measured experimentally is $\sum_i i\sigma_i$.

The Lotz equation

One of the most widely used empirical expressions for the electron impact ionization efficiency curve was that proposed by Lotz.[65–67] His equation was designed to reproduce cross sections for single ionization of atoms and ions from the ground state, and could be used to fit nearly all available experimental results from threshold to 10 keV to within 10%.

An atomic electron contributes an individual cross section σ_{ei} to the total ionization cross section σ whenever the incident electron energy E is greater than the binding energy E_i of the electronic shell to which the atomic electron belongs.

$$\sigma = \sum_{i=1}^{N} \sigma_i \tag{2.9}$$

where $\sigma_i = n_i\sigma_{ei}$, n_i is the number of equivalent electrons in subshell i, and N is the number of subshells present. According to Bethe[64] and Rudge and Schwartz,[58] the cross section for subshell i is given by

$$\sigma_i(E) = a_i n_i \frac{\ln(E/E_i)}{EE_i} \tag{2.10}$$

where a_i is a constant between 2.6 and 4.5×10^{-14} cm^{2}eV^2. Extensive trials for fitting the cross section yielded a relatively simple expression with three adjustable parameters a_i, b_i

and c_i.

$$\sigma_i(E) = a_i n_i \frac{\ln(E/E_i)}{EE_i}[1 - b_i e^{-c_i(\frac{E}{E_i}-1)}] \tag{2.11}$$

The total electron impact ionization cross section is then

$$\sigma(E) = \sum_{i=1}^{N} a_i n_i \frac{\ln(E/E_i)}{EE_i}[1 - b_i e^{-c_i(\frac{E}{E_i}-1)}] \tag{2.12}$$

In the above sum the $i = 1$ term corresponds to the outermost electronic shell, the $i = 2$ term to the next inner subshell, and so on. Near threshold when the incident electron energy E is approximately equal to the ionization potential E_1, Equation (2.12) reduces to

$$\sigma(E) = a_1 n_1 \frac{E/E_1 - 1}{E_1^2}(1 - b_1) \tag{2.13}$$

so that the cross section is proportional to $\frac{E}{E_1} - 1$. For large electron energies $E >> E_i$ it is found that

$$\begin{aligned} \sigma_i(E) &= a_i n_i \frac{\ln(E/E_i)}{EE_i} \\ &= a_i n_i \frac{\ln E - \ln(E_i)}{EE_i} \\ &\approx a_i n_i \frac{\ln(E)}{EE_i} \\ &\propto \frac{\ln E}{E} \end{aligned} \tag{2.14}$$

The Lotz equation therefore has the correct functional energy dependence for both small and large energies of the colliding electron.

Lotz also showed that in most cases Equation 2.12 could be substituted for the simpler form

$$\sigma(E) = a[1 - be^{-c(\frac{E}{E_1}-1)}] \sum_{i=1}^{N} n_i \frac{\ln(E/E_i)}{EE_i} \tag{2.15}$$

in which $N = 2$ or 3 usually gave good results.

The Bell equation

Bell and coworkers[68] surveyed a wide range of experimental data on electron impact ionization of light atoms and ions and found that the cross sections could all be fitted to the same simple analytic expression.

$$\sigma(E) = \frac{1}{IE}[A \ln(\frac{E}{I}) + \sum_{i=1}^{N} B_i(1 - \frac{i}{E})^{\,i}] \tag{2.16}$$

in which E is the incident electron energy, I is the ionization potential of the atom or ion, and N is the number of subshells. The coefficients B_i are determined by a least squares fit to the experimental data, with two or three coefficients being sufficient to reproduce the cross section in many cases. The coefficient A is a Bethe coefficient which may be calculated either by fitting the equation

$$\sigma(E) = \frac{1}{IE}[A \ln(E) + B] \tag{2.17}$$

to the high energy form of the Born approximation, or from the equation

$$A = \frac{1}{\pi\alpha} \int_I^\infty \frac{\sigma_{\text{ph}}}{E} dE \tag{2.18}$$

in which σ_{ph} is the photoionization cross section, and α is the fine structure constant.

The Bell equation gives the correct behaviour for the ionization cross section at both high and low impact energies. In cases where autoionization is important it is not always possible to reproduce the cross section from the single equation above, but if the equation is used in two separate fits, one from the ionization threshold to the autoionization threshold, and the second above the autoionization threshold, a good fit to the cross section may be obtained over the entire range.

Both the Lotz and Bell equations have been used with great success to obtain analytical expressions for atomic and molecular cross sections from experimental data. However, since they are based on a well chosen parameterised function, rather than on a physical model of the ionization process, their application is limited to fitting experimental data and neither gives any great insight into the physical process of electron impact ionization process. Calculation of ionization cross sections from first principles for comparison with experiment requires rather more sophisticated theories.

Kistemaker's modified additivity rule

The original additivity rule put forward by Otvos and Stevenson,[69] according to which a molecular ionization cross section is given by the sum of the cross sections of the constituent atoms, was based on Bethe's observation[64] that the probability of ionization of an atomic electron in the n, l atomic orbital is approximately proportional to the mean square radius of the orbital. They showed that the rule is generally valid for hydrocarbons, but tends to overestimate the cross section in a significant number of cases.

Kistemaker *et al*[70] suggested that the model could be improved by taking into account the orientation dependence of the cross section. In the case of a long chain hydrocarbon it seems reasonable to assume that the cross section for an electron approaching the molecule 'head on' will be very different from that for one approaching side on due to the vastly different cross sectional areas which the target presents to the electron in the two orientations. Kistemaker used the additivity rule to determine 'parallel' and 'perpendicular' cross sections by summing known cross sections of atoms or molecular fragments. When considering the long chain hydrocarbon $CH_3(CH_2)_nCH_3$ for example, the parallel cross section $\sigma_{||}$ would be taken as the cross section for a methyl fragment, while the perpendicular cross section $\sigma_{\perp}$ is the sum $2\sigma_{CH_3} + n\sigma_{CH_2}$. The measured cross section is an average over all orientations and is given approximately by

$$\sigma = \frac{1}{3}(\sigma_{||} + 2\sigma_{\perp}) \tag{2.19}$$

Using this approach gives a significant improvement over the original additivity method for large hydrocarbons. This method is limited by the fact that either experimental or theoretical electron impact ionization cross sections for the various molecular fragments must be known, but in cases where these quantities are available it provides a simple method for approximating cross sections for large molecules, which may or may not be known, from previously existing data on smaller species.

The Deutsch-Märk (DM) method

This formalism was originally devised to describe single ionization of ground state atoms, but has since been successfully applied to the calculation of electron impact ionization cross sections for a range of molecules, radicals, clusters and excited state atoms. Like many of the semi-empirical and semi-classical methods used to describe the electron impact process, the theory has its roots in work carried out by J. J. Thomson,[63] who used classical mechanics to derive an expression for the atomic electron impact ionization cross section.

$$\sigma = \sum_n 4\pi a_0^2 N_n \left(\frac{E_i^H}{E_{in}}\right)^2 \frac{u-1}{u^2} \tag{2.20}$$

in which a_0 is the Bohr radius; N_n is the number of electrons in the nth subshell; E_i^H is the ionization potential of hydrogen; and $u = \frac{E}{E_{in}}$, where E is the energy of the incident electron.

Grysinski improved the model by assuming a continuous velocity distribution for the atomic electrons,[71] leading to the following expression.

$$\sigma = \sum_n 4\pi a_0^2 N_n \left(\frac{E_i^H}{E_{in}}\right)^2 f(u) \tag{2.21}$$

where

$$f(u) = \frac{1}{u}\left(\frac{u-1}{u+1}\right)^{3/2}\left(1 + \frac{2}{3}(1-\frac{1}{2u})\ln[2.7 + (u-1)^{1/2}]\right) \tag{2.22}$$

A further improvement is the incorporation of quantum mechanical considerations, such as exchange effects,[72] but the theory still fails to predict the correct magnitude of the ionization cross section for several fairly simple atoms such as neon, nitrogen and fluorine. Deutsch and Märk compared the classical model with the theory developed by Bethe.[64] Bethe's calculations showed that the ionization cross section for an atomic electron is approximately proportional to the mean square radius $\langle r_{nl}^2 \rangle$ of the n, l electronic shell to which the electron belongs. Experiment had also shown a correlation between the maximum in the atomic cross section and the sum of the mean square radii of all outer electrons. This led to the replacement of the Bohr radius with the radius of the corresponding subshell, so that the ionization cross section was now given by

$$\sigma = \sum_{n,l} g_{nl}\pi r_{nl}^2 N_{nl} f(u) \tag{2.23}$$

where r_{nl}^2 is the mean square radius of the n, l shell[73] and the quantities g_{nl} are empirically determined weighting factors. This equation gives improved agreement with experimental results except in cases involving strong autoionization channels, where additional corrections are necessary.[74]

The weighting factors g_{nl} were initially calculated by Bethe as a function of n and l using hydrogenic wavefunctions. Deutsch and Märk determined these generalised factors via a fitting procedure using the inert gases and uranium as test cases. Later, when a more sophiticated fitting procedure was used, it was found that the product of the weighting factor and the binding energy for a specific set of n, l and N_{nl} values is independent of the atomic number.[75] This allowed a weighting factor matrix, with elements $g_{nl}E_{nl}$, to be constructed, from which weighting factors can be extracted for any atomic orbital once the binding energy of an electron occupying the orbital is known. Using the weighting factor matrix, inner atomic orbitals tend to receive a much lower weight than previously. These orbitals, having a large

binding energy, would not be expected to contribute much to the cross section except in the case of very high energy collisions, requiring incident electron energies of hundreds or even thousands of electron volts. There are also significant changes in the weighting factors for valence orbitals, so that using the new set of g_{nl} values leads to considerable changes in the calculated cross section.

The DM method may be extended to allow calculation of molecular ionization cross sections using a modified form of Otvos and Stevenson's additivity rule.[69] which assumes that the molecular ionization cross section is equal to the sum of contributions from the constituent atoms. The sum over atomic energy levels is now replaced by a sum over the molecular orbitals. The core orbitals, having large binding energies, contribute very little to the cross section and may be omitted from the sum. In the calculations reported here the ionization cross sections were only determined up to an energy of 200 eV, so that only molecular orbitals with a binding energy less than this value were included in the sum.

$$\sigma = \sum_{i,nl} \pi r_{i,nl}^2 \sum_j g_{i,nl}^j N_{i,nl}^j f(u_j) \tag{2.24}$$

where $u_j = \frac{E}{E_j}$.

In order to use the DM method a population analysis must be carried out to determine $N_{i,nl}^j$, the contribution of each atomic orbital to the molecular orbitals considered. For this series of calculations a Mulliken population analysis at Hartree–Fock level was chosen. The minimal STO-3G basis set was used in these calculations since larger basis sets would have made the analysis prohibitively time consuming. According to a Mulliken analysis[76] the orbital population is given by

$$N_{i,nl}^j = n_i(c_{ji}^2 + \sum_k c_{ji} S_{jk} c_{ki}) \tag{2.25}$$

where n_i is the occupation number of molecular orbital i, c_{ji} and c_{ki} are the molecular orbital coefficients of atomic orbitals j and k in molecular orbital i, and S_{jk} is the overlap integral between atomic orbitals j and k.

The Binary-encounter Bethe (BEB) method

The BEB theory is a simplified version of the binary-encounter dipole (BED) model developed by the same authors.[77] It is based on a combination of two earlier theories known to accurately describe high and low energy collisions respectively. Collisions occuring at low

incident electron energies are described well by the Mött theory,[78] originally developed for collisions between two electrons. High energy collisions, occuring at high impact parameters, were shown by Bethe[64] to occur mainly through the dipole interactions between the atom and the electron. The Mött theory for low energy collisions may be augmented by the symmetric form of the binary-encounter theory,[79] which assigns a velocity distribution to a target electron instead of a wave function. However, because the dipole contribution is still lacking, the cross section is not well described at high energies, when the majority of collisions are distant and the dipole interaction dominates.

The BED model combines this augmented form of the Mött cross section with the Bethe cross section to give an expression which describes the electron impact ionization process over the entire energy range. The ratio between the binary-encounter and Bethe theories is set by requiring the form of the binary-encounter theory in the high electron energy limit to match that of the Bethe theory, both in the predicted cross section and in the so called 'stopping cross section' *. The BED model leads to an expression for the energy distribution of the ejected electron's energy differential cross section $\frac{d\sigma}{dW}$ for each atomic or molecular orbital. The total cross section is found by integrating $\frac{d\sigma}{dW}$ over the allowed range of W i.e. from 0 to $\frac{1}{2}(T-B)$, where T is the energy of the incident electron and B is the binding energy of the atomic electron, and is given by

$$\sigma_i(t) = \frac{S}{t+u+1}\left[D(t)\ln t + (2+\frac{N_i}{N})(\frac{t-1}{t} - \frac{\ln t}{t+1})\right] \tag{2.26}$$

where $t = \frac{T}{B}$ is the reduced incident electron energy; $u = \frac{U}{B}$ is the reduced orbital kinetic energy; $S = \frac{4\pi a_0^2 N R^2}{B^2}$ in which $R = 13.6$ eV is the ionization potential of the 1s orbital of hydrogen; $D(t) = \frac{1}{N}\int_0^{\frac{t-1}{2}} \frac{1}{w+1}\frac{df(w)}{dw}dw$ with $w = \frac{W}{B}$; and $N_i = \int_0^{\infty} \frac{df(w)}{dw}dw$.

The quantities required for each orbital in order to carry out a BED calculation are therefore the binding energy B, average orbital kinetic energy U, orbital occupation number N and dipole oscillator strength $\frac{df}{dw}$. The parameters U and B are easily calculated using any atomic or molecular wavefunction package. The average orbital kinetic energy U is a theoretical quantity which cannot be directly measured, but if available experimental values of the binding energy B may be used. This is especially useful in the case of the lowest

* The stopping cross section describes the efficiency of a collision of a heavy particle and an electron in causing a loss of kinetic energy of the heavy particle.[80] It is used to evaluate the 'stopping power' of the target medium for electrons and is given by the integral of the product of the energy loss cross section and the energy loss of the incident electron.

binding energy in order to ensure the correct threshold is obtained, though according to Hwang *et al*[81] using theoretical values of B leads to better agreement near the peak in the ionization efficiency curve. It is not so straightforward to obtain the dipole oscillator strength $\frac{df}{dw}$. The calculation of this quantity requires that the wavefunctions of both the initial and continuum states are known, and the calculation of excited state wavefunctions is difficult. In consequence, values for this parameter are only available for a fairly small number of atomic and molecular species.

The BEB model was developed to overcome this problem. The dipole oscillator strength is assumed to have a simple form based on the approximate shape of the function for ionization of ground state hydrogen.

$$\frac{df}{dw} = \frac{N}{(w+1)^2} \tag{2.27}$$

The integrated cross section per orbital is then given by

$$\sigma_{\mathrm{BEB}} = \frac{S}{t+u+1}\left[\frac{\ln(t)}{2}(1-\frac{1}{t^2})+1-\frac{1}{t}-\frac{\ln(t)}{t+1}\right] \tag{2.28}$$

In the expressions for the BED and BEB cross sections for each orbital the first log term represents large impact parameter collisions dominated by the dipole interaction. The remaining terms represent low impact parameter collisions, described by the augmented Mött cross section. The second log function describes interference between direct and exchange scattering which is included in the Mött cross section.

For molecules containing heavy atoms, i.e. atoms with electrons occupying shells with principal quantum number n greater than two, the cross sections obtained using this expression are often significantly smaller than experiment. This is largely due to the fact that the atomic orbitals with these higher principal quantum numbers tend to have very large orbital kinetic energies, and a molecular orbital which essentially has the character of one of these atomic orbitals will contribute little to the ionization cross section since the quantity U appears in the denominator of Equation (2.28). This problem can be rectified[82] once a Mulliken analysis has been carried out to determine the composition of each molecular orbital. If a molecular orbital has more than a 90% contribution from an atomic orbital (or orbitals) with $n \geq 3$ then the orbital kinetic energy is divided by the principal quantum number n before being substituted into Equation (2.28). While this is a purely empirical correction, it can led to a great improvement in the agreement of the BEB cross section with experiment.

The Jain-Khare model

In a similar approach to that used in deriving the BED theory described above, Jain and Khare[83,84] divided ionizing collisions into two categories: soft or glancing collisions involving a small energy transfer between the incident electron and the target molecule, and hard collisions with a large amount of energy transfer. For high energy incident electrons and a small energy transfer the Born-Bethe approximation is valid and $\sigma(E,\epsilon)$, where E and ϵ are the energies of the incident and ejected electrons respectively, is proportional to the differential oscillator strength. For hard collisions the cross section is described by Mött scattering theory. The Born-Bethe and Mött cross sections are given by

$$\begin{aligned} \sigma_{BB}(E,\epsilon) &= \frac{4\pi a_0^2 R^2}{E}\frac{1}{W}\frac{df}{dW}\ln(CE) \\ \sigma_M(E,\epsilon) &= \frac{4\pi a_0^2 R^2}{E}S\left[\frac{1}{\epsilon^2}-\frac{1}{\epsilon(E-\epsilon)}+\frac{1}{(E-\epsilon)^2}\right] \end{aligned} \tag{2.29}$$

where W is the energy loss suffered by the incident electron during the collision, R is the Rydberg constant, S is the number of electrons which can participate in hard collisions, $\frac{df}{dW}$ is the differential oscillator strength, and C is a collisional parameter defined by Miller and Platzman.[85]

For ionization of a molecule by an incident electron of energy E, with production of a secondary electron of energy ϵ, Khare[86] proposed the following semi-empirical relations.

$$\begin{aligned} \sigma(E,\epsilon) &= \sigma(E,W) = f_1(E,\epsilon)\sigma_{BB}(E,\epsilon) \qquad \text{for } \mathrm{I} \le \mathrm{W} \le \mathrm{W_0} \\ \sigma(E,\epsilon) &= \sigma(E,W) = f_2(E,\epsilon)\sigma_M(E,\epsilon) \qquad \text{for } \mathrm{W_0} \le \mathrm{W} \le \frac{\mathrm{E}+\mathrm{I}}{2} \end{aligned} \tag{2.30}$$

where I is the ionization potential and W_0 is the threshold in the energy loss between the secondary electron being formed by soft and hard collisions. A suggested value was (I+60) eV. The functions f_1 and f_2 are introduced to extrapolate the cross sections to the low energy region where the Born-Bethe and Mött cross sections are expected to give results which are too high.

$$\begin{aligned} f_1 &= \left(1-\frac{2W-1}{E}\right)\frac{\ln(1+C(E-I)}{\ln(CE)} \\ f_2 &= 1-\frac{2W-I}{E} \end{aligned} \tag{2.31}$$

These expressions for the cross section give a discontinuity at $W = W_0$. To rectify this the two expressions for $W < W_0$ and $W > W_0$ were combined to give a single relation to

describe the cross section over the entire energy range.

$$\sigma(E.\epsilon) = \sigma(E, W) = f_1'(E, \epsilon)\sigma_{BB}(E, \epsilon) + f_2'(E.\epsilon)\sigma_M(E.\epsilon) \tag{2.32}$$

where f_1' and f_2' extrapolate to low energies as before and also control the mixing of the Born-Bethe and Mött cross sections.

$$\begin{aligned} f_1' &= \frac{1}{1+1/E}\left(1 - \frac{\epsilon}{E-I}\frac{\ln(1+C(E-I)}{\ln(CE)}\right) \\ f_2' &= \frac{\epsilon^3}{\epsilon^3+\epsilon_0^3}\left(1-\frac{I}{E}\right) \end{aligned} \tag{2.33}$$

The parameter ϵ_0 was chosen for best agreement with the experimental data of Opal *et al*[87] at an incident electron energy of 500 eV.

Jain and Khare applied this expression to the calculation of ionization cross sections for CO_2, CO, H_2O, CH_4 and NH_3 and achieved fairly good agreement with experiment for all cases apart from CO, where the cross section was too low, though the ionization efficiency curve still had the correct functional form. However, as in the case of the BED theory the requirement of knowing differential oscillator strengths for the target molecule severely limits the number of systems to which the Jain-Khare theory can be applied.

2.2 *A simple electrostatic* ab initio *model for calculation of maximum ionization cross sections*

The new model is based on a very simple analysis which considers the electron impact event in terms of an electrostatic interaction[6] between the target and the incoming electron. During the electron impact process, the target atom or molecule experiences the Coulomb electrostatic field of the approaching electron. The electrostatic model supposes that when the resulting interaction potential exceeds the ionization potential of the target, ionization can occur as the atom or molecule absorbs energy from the field. For the purpose of the calculations a 'threshold separation', $r_{\rm th}$ is defined. This is the separation between the electron and the molecular centre of mass at which the interaction potential is equal to the ionization potential of the molecule. As the electron–molecule separation decreases the Coulomb potential experienced by the target will increase, so that $r_{\rm th}$ represents the maximum distance at which ionization may occur. A molecular orbital package such as GAUSSIAN94[88] may be used to determine the value of $r_{\rm th}$, and conversion of this quantity into a cross section yields the maximum in the ionization efficiency curve. A useful property of these calculations is

the fact that, because the z-matrix input to the electronic structure calculations specifies a relative orientation of the electron and the molecule, the method can be used to calculate the dependence of the maximum cross section on the direction of approach of the incident electron, effectively allowing the 'shape' of the ionization cross section to be investigated.

The first step in calculating an electron impact ionization cross section using the electrostatic model is to optimise the molecular geometry. The vertical ionizaion potential is calculated by taking the difference in the energy of the positive ion at the neutral geometry and the zero point energy of the neutral molecule. Alternatively, an experimentally determined ionization potential may be used. A 'threshold energy' E_{th}, the energy of the system at which the model predicts ionization will occur, must now be determined. This is simply the neutral energy E_0 plus the Coulomb potential due to the electron at the threshold impact parameter r_{th}, or, since the Coulomb potential at ionization is equal to the ionization potential I of the molecule,

$$E_{\mathrm{th}} = E_0 - I \tag{2.34}$$

Next, a series of single point energy calculations is carried out on the neutral molecule in the presence of a charge distribution consisting of a single electron. The initial guess electron–molecule separation is modified in an iterative procedure until the energy of the system converges to the threshold energy, at which point the electron–molecule separation is equal to r_{th}. When the threshold separation has been determined the maximum electron impact ionization cross section for the orientation under consideration is given by

$$\sigma = \pi r_{\mathrm{th}}^2 \tag{2.35}$$

In general, measurements of electron impact ionization cross sections are carried out on randomly oriented molecules, so that the total ionization cross section is given by the average over all possible orientations of the molecule with respect to the incoming electron. Because the input for the GAUSSIAN calculations requires that the charge distribution be entered in Cartesian coordinates, a convenient approximate total cross section can be found using the present method by averaging the cross sections for approach along each of the positive and negative Cartesian axes. Including a larger number of approach directions in the average would improve the value of the total cross section, but information concerning the effect of orientation on the electron impact ionization process is lost in the averaging process.

The model has been tested on the inert gases and a range of small molecules, and gives good agreement with experimental results, where available, in almost all cases.[89] The method will be discussed further in relation to the orientation dependence of the electron impact ionization cross section in Section 2.3.3.

While the electrostatic model is almost unique in its ability to predict orientation effects for electron impact ionization, it also has a number of limitations. The method does not take into account the actual trajectory of an approaching electron; the calculations are on a static system of a molecule and a stationary charge. The model can therefore provide no information on the electron energy dependence of the cross section, yielding only the maximum in the ionization efficiency curve.

2.2.1 *The correlation between molecular polarizability volume and electron impact ionization cross section*

The polarizability α_p of an atom or molecule describes the ease with which an electric field can induce a dipole in the system. The relationship between the electric field vector $\mathbf{E}$ and the induced dipole vector μ^* is

$$\mu^* = \alpha_p \mathbf{E} \tag{2.36}$$

Polarizability should strictly be described by a second rank tensor. However, in practice the term 'polarizability' usually refers to an average over all orientations, and it is this scalar quantity rather than the polarizability tensor which is more commonly used to describe the response of an atom or molecule to an electric field. The average polarizability is generally converted to units of $Å^3$ and expressed as a polarizability volume α.

The relationship between the maximum in the electron impact ionization efficiency curve and the polarizability of the ionized atom or molecule was first noted by Franklin, Field and Lampe[90] in 1957. The observation was rationalised in terms of the dependence of both atomic polarizability and atomic electron impact ionization cross section on the dipole matrix. The correlation was next reported for several series of organic molecules by Bartmess and Georgiadis,[91] and has more recently been noted by Nishimura and Tawara,[92] who reasoned that for a given electron energy the electron impact ionization cross section should correlate strongly with the total number of electrons present and also with the molecular dipole polarizability. This was shown to be the case for a range of simple hydrocarbons, suggesting

that the incident electron recognises not only all the electrons in a molecule, but also to some degree the structure of its electron cloud as reflected by the polarizability

A literature study of atomic and molecular electron impact ionization cross sections and polarizabilities has shown that for both atomic and molecular species there is a clear linear relationship between the maximum electron impact ionization cross section and the polarizability volume α. A linear relationship has also been shown to exist[93] between the maximum cross section and the quantity $(\frac{\alpha}{E_0})^{1/2}$, where E_0 is the ionization potential.

For atomic species the proportionality constants depend on the position of the element in the periodic table, with group I and II metals, main group elements and transition metals lying on separate curves. Plots of the two correlations are shown in Figures 2.1 and 2.2. The dependence of the maximum cross section on α has been explained previously by Lampe and coworkers.[90] The dependence on $(\frac{\alpha}{E_0})^{1/2}$ may be explained qualitatively from simple electrostatic arguments as follows:

For an atom with polarizability α the approach of an electron will induce a dipole moment

$$\mu^* = \alpha E \tag{2.37}$$

where E is the field experienced by the atom due to the presence of the electronic charge. The electrostatic potential associated with a dipole field has the form

$$\phi = \frac{\mu \cos\theta}{4\pi\epsilon_0 r^2} \tag{2.38}$$

where θ is the angle from the dipole axis. The potential energy of the electron in the induced dipole field is therefore

$$\begin{aligned} V &= -\phi e \\ &= -\frac{\mu^* e \cos\theta}{4\pi\epsilon_0 r^2} \\ &= -\frac{\alpha e E}{4\pi\epsilon_0 r^2} \end{aligned} \tag{2.39}$$

in which e is the electronic charge and $\theta = 0$ since the induced dipole is along the vector connecting the atom and approaching electron. The Coulomb field E which the electron exerts on the molecule is

$$E = -\frac{e}{4\pi\epsilon_0 r^2} \tag{2.40}$$

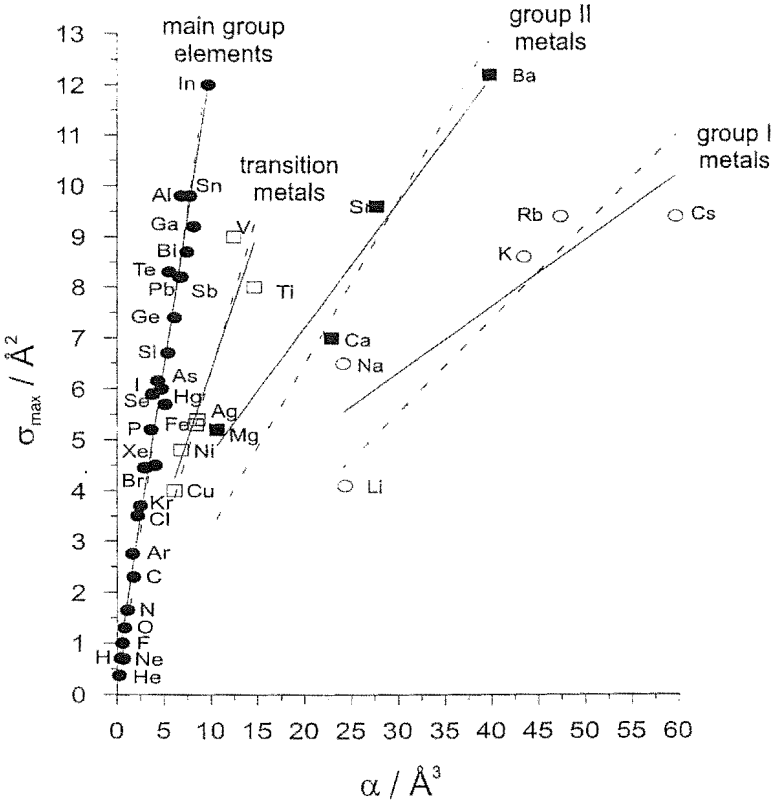

Figure 2.1: Correlation of atomic maximum electron impact ionization cross sections (See[75] and references therein) with polarizability volume α.[94] r^2 values for linear fits and linear fits through the origin (solid and dashed lines respectively) are as follows: Main group elements: 0.9692 and 0.9900, Transition metals: 0.8608 and 0.9870, Group I Metals: 0.7776 and 0.9751, Group II Metals: 0.9577 and 0.9870

and substituting this into Equation (2.39) gives

$$V = \frac{e^2\alpha}{(4\pi\epsilon_0 r^2)^2} \tag{2.41}$$

If it is assumed that when this potential exceeds the atomic ionization potential then the atom can absorb energy from the field and be ionized, then the maximum impact parameter $b_{\max}$ can be related to the ionization potential E_0. Under this assumption the maximum impact parameter for which ionization can occur corresponds to the case in which the Coulomb potential is equal to the ionization potential, giving

$$E_0 = \frac{e^2\alpha}{(4\pi\epsilon_0 b_{\max}^2)^2} \tag{2.42}$$

and therefore

$$b_{\max}^2 = \left[\frac{e^2\alpha}{(4\pi\epsilon_0)^2 E_0}\right]^{1/2} \tag{2.43}$$

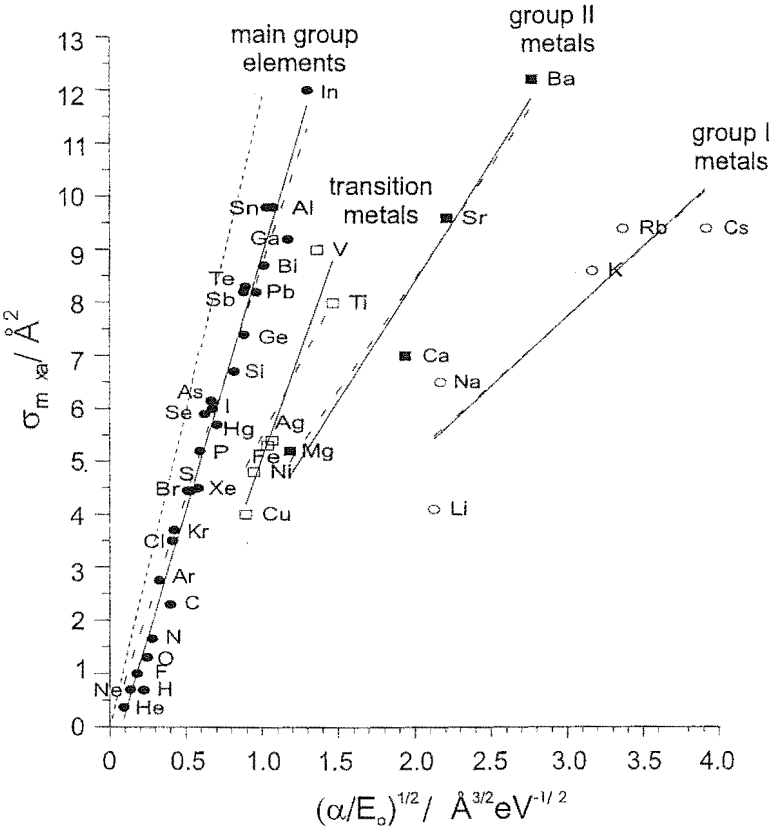

Figure 2.2: Correlation of atomic maximum electron impact ionization cross sections ([75] and references therein) with $\left(\frac{\alpha}{E_0}\right)^{1/2}$. The short dashed line is the prediction of the electrostatic model described in the text. r^2 values for linear fits and linear fits through the origin (solid and dashed lines respectively) are as follows: Main group elements: 0.9791 and 0.9916, Transition metals: 0.9035 and 0.9849, Group I Metals: 0.8123 and 0.9873, Group II Metals: 0.9406 and 0.9944

The maximum cross section is then

$$\begin{aligned} \sigma_{\max} &= \pi b_{\max}^2 \\ &= \frac{e}{4\epsilon_0}\left(\frac{\alpha}{E_0}\right)^{1/2} \end{aligned} \tag{2.44}$$

For α in Å^3 and E_0 in eV, the maximum cross section may be written

$$\sigma_{\max} = 11.92\left(\frac{\alpha}{E_0}\right)^{1/2} \tag{2.45}$$

This equation rationalises the observed $\left(\frac{\alpha}{E_0}\right)^{1/2}$ dependence of the atomic maximum electron impact ionization cross section. Though there is a slight zero offset, the slope predicted from (2.45) matches the data for the main group elements fairly closely, as shown in Figure

2.2, suggesting that this simple electrostatic model may offer a useful representation of the ionization process.

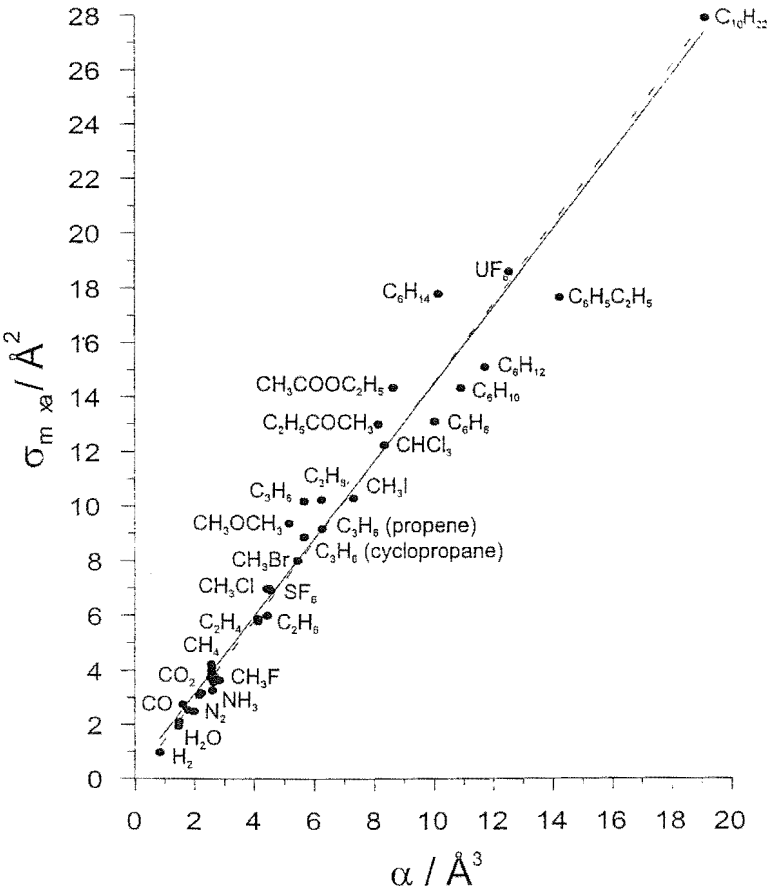

Figure 2.3: Correlation between molecular maximum electron impact ionization cross section[16, 70, 89, 92, 95, 96] and polarizability volume. r^2 is 0.9687 for the linear fit (solid line) and 0.9801 for the linear fit through the origin (dashed line).

The same correlations between $\sigma_{\max}$, α and $\left(\frac{\alpha}{E_0}\right)^{1/2}$ are found for molecular targets, as shown in Figures 2.3 and 2.4. The effect occurs even when the molecule has a permanent dipole moment. This may indicate that any effect of the permanent dipole on the maximum cross section averages to zero in a randomly oriented sample, while the average polarizability, and therefore average induced dipole, is always non-zero.

Least squares fits to the data shown in Figures 2.1 to 2.4 provide a series of empirical expressions, summarized in Table 2.1, for predicting maximum electron impact ionization cross sections. With the exception of the Group I and II metals and transition elements, for which only a few data points are available, the correlation coefficients r for the linear least

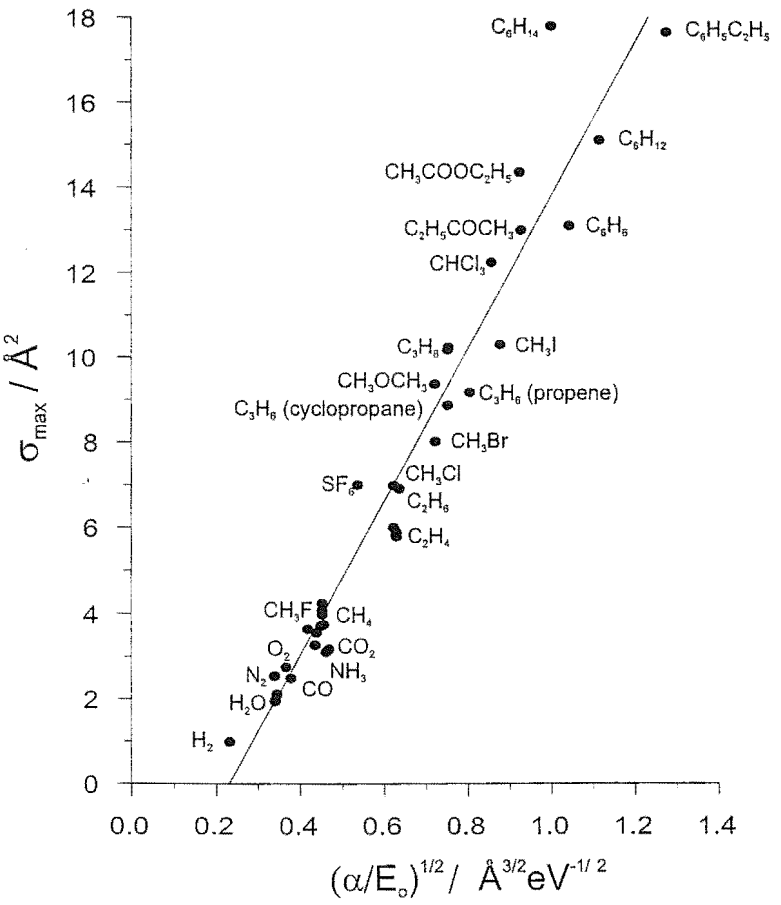

Figure 2.4: Correlation between molecular maximum electron impact ionization cross section[16,70,89,92,95,96] and $\left(\frac{\alpha}{E_0}\right)^{1/2}$. r^2 is 0.9451.

square fits are around 0.99†. In most cases, a linear least squares fit and a linear fit forced through the origin give very similar results, the notable exception being the plot of maximum cross sections as a function of $\left(\frac{\alpha}{E_0}\right)^{1/2}$ for molecules.

The calculation of molecular ionization efficiency curves

Further investigation into the correlation between the electron impact ionization cross section and the molecular polarizability can give some insights into the energy dependence of the cross section.

The polarizability volume may be envisaged in terms of a sphere of charge which is distorted 'isotropically'—in the sense that the same distortion arises regardless of the incident direction of the ionizing electron—as an electron approaches, giving rise to an induced dipole

† The quantities reported in the figure captions are r^2 values

Table 2.1: Relationships for the calculation of maximum total electron impact ionization cross sections from polarizabilities α and ionization potentials E_0 based on fits to literature experimental data.

σ_{max} as a function of α	Linear fit	Linear fit through origin
Main group elements	$\sigma = 1.190\alpha + 0.490$	$\sigma = 1.275\alpha$
Group I metals	$\sigma = 0.131\alpha + 2.394$	$\sigma = 0.185\alpha$
Group II metals	$\sigma = 1.162\alpha + 3.391$	$\sigma = 1.774\alpha$
Transition metals	$\sigma = 3.362\alpha + 1.681$	$\sigma = 4.481\alpha$
Molecules	$\sigma = 1.418\alpha + 0.310$	$\sigma = 1.455\alpha$
σ_{max} as a function of $\left(\frac{\alpha}{E_0}\right)^{1/2}$		
Main group elements	$\sigma = 9.635\left(\frac{\alpha}{E_0}\right)^{1/2} - 0.718$	$\sigma = 8.734\left(\frac{\alpha}{E_0}\right)^{1/2}$
Group I metals	$\sigma = 2.637\left(\frac{\alpha}{E_0}\right)^{1/2} - 0.166$	$\sigma = 2.583\left(\frac{\alpha}{E_0}\right)^{1/2}$
Group II metals	$\sigma = 4.505\left(\frac{\alpha}{E_0}\right)^{1/2} - 0.591$	$\sigma = 4.234\left(\frac{\alpha}{E_0}\right)^{1/2}$
Transition metals	$\sigma = 8.041\left(\frac{\alpha}{E_0}\right)^{1/2} - 2.960$	$\sigma = 5.499\left(\frac{\alpha}{E_0}\right)^{1/2}$
Molecules	$\sigma = 17.973\left(\frac{\alpha}{E_0}\right)^{1/2} - 4.135$	NA

$\mu^* = \alpha E$. The radius of the 'polarizability sphere' is given by

$$r_\alpha = \left(\frac{3\alpha}{4\pi}\right)^{1/3} \tag{2.46}$$

If the molecular electronic charge is considered to be equally distributed throughout the polarizability volume, it is possible to determine a root-mean-square (rms) radius for the electron distribution

$$r_{\text{rms}} = \sqrt{\frac{3}{5}} r_\alpha \tag{2.47}$$

and a corresponding 'effective diameter' d_{rms} for the molecule.

$$d_{\text{rms}} = 2\sqrt{\frac{3}{5}}\left(\frac{3\alpha}{4\pi}\right)^{1/3} \tag{2.48}$$

Ionization efficiency curves rise sharply from a threshold energy, the ionization potential, to a peak cross section at around 50–120 eV, declining again at higher energies. Assuming that the ionization cross section is dependent on the interaction of an electron wave with the molecule, the peak in the ionization efficiency curve might be expected to correspond to a 'resonance condition' in which the de Broglie wavelength of the incident electron matches the

molecular diameter defined above. The electron wavelength is given by

$$\lambda = \frac{h}{p} = \left(\frac{h^2}{2meE}\right)^{1/2} \tag{2.49}$$

in which p, m and E are the momentum, mass and energy (in eV) of the electron and h is Planck's constant. Setting λ equal to d_{rms} gives an expression for the electron energy at which the ionization cross section is a maximum.

$$E_{\mathrm{max}} = \frac{5h^2}{24me}\left(\frac{4\pi}{3}\right)^{2/3}\alpha^{-2/3} \tag{2.50}$$

This expression predicts the position of the maximum accurately for a wide range of molecules and depends only on the molecular polarizability volume. The rms molecular diameter was calculated for a series of molecules and is plotted against the electron wavelength at the peak in the measured ionization efficiency curve in Figure 2.5. The correlation is essentially exact within the expected experimental errors.

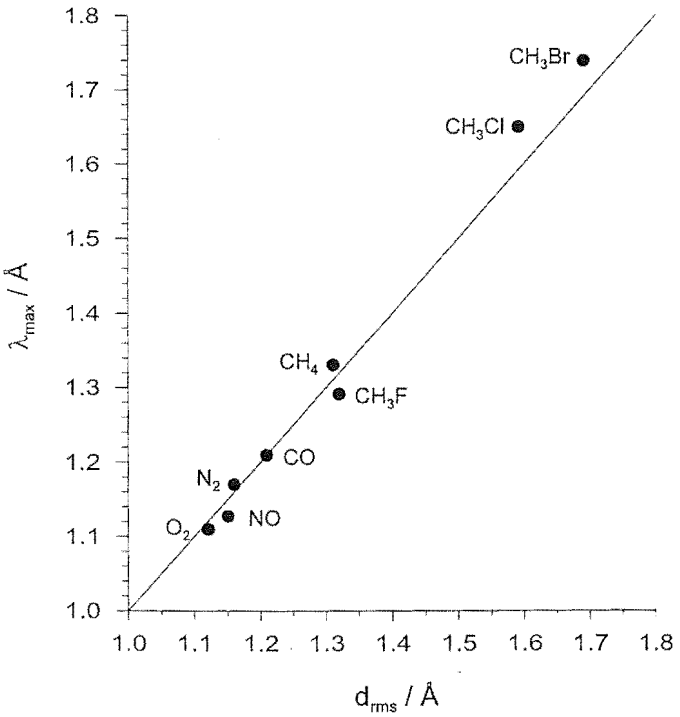

Figure 2.5: The dependence of the position of the peak in the ionization efficiency curve on the rms molecular diameter.

The ionization cross section will fall off as the electron wavelength becomes longer or shorter than the molecular diameter, since the interaction of the molecule with the de Broglie wave will become weaker. The functional dependence of the cross section on the de Broglie

wavelength was modelled with the expression below, which essentially assumes the percentage deviation from the maximum cross section is proportional to the percentage deviation of the de Broglie wavelength of the electron from d_{rms}.

$$\sigma \propto 1 - \frac{|\lambda - \lambda_{\max}|}{\lambda_{\max}} \tag{2.51}$$

The above expression may be scaled by the maximum cross section to give

$$\sigma = \sigma_{\max}\left(1 - \frac{|\lambda - \lambda_{\max}|}{\lambda_{\max}}\right) \tag{2.52}$$

Substituting for λ and $\lambda_{\max}$ from Equations (2.49) and (2.50) gives

$$\sigma = \sigma_{\max}\left[1 - \frac{1}{2}\sqrt{\frac{5}{3}}\left(\frac{4\pi}{3\alpha}\right)^{1/3}\left|\left(\frac{h^2}{2meE}\right)^{1/2} - 2\sqrt{\frac{3}{5}}\left(\frac{3\alpha}{4\pi}\right)^{1/3}\right|\right] \tag{2.53}$$

The maximum cross section used may be an experimental value, a value calculated using the BEB, DM or electrostatic models described earlier, or may be obtained from the empirical relationships between maximum cross section and polarizability listed in Table 2.1.

The above function generally falls off too rapidly after the peak for small molecules, when compared with the experimental results of Rapp and Englander-Golden[16] and Djuric *et al*,[95] though the ionization efficiency curves of the methyl halides[97] are fairly closely matched. Another problem is that the threshold, while reasonably accurate for the methyl halides, is often overestimated by up to 10 or 20 eV for smaller molecules.

In order to improve the threshold behaviour, the function $\frac{E-E_0}{E}$, which appears in the classical binary encounter treatment of electron impact ionization,[17] was incorporated. This function was normalised to a peak value of unity through multiplication by the factor $\frac{E_{\max}}{E_{\max}-E_0}$ and added to the right hand side of Equation (2.53). The resulting expression is normalised to the maximum cross section by the factor $\frac{\sigma_{\max}}{2}$, leading to the following relation between the ionization cross section and the electron energy.

$$\sigma = \frac{\sigma_{\max}}{2}\left[\left(\frac{E_{\max}}{E_{\max}-E_0}\right)\left(\frac{E-E_0}{E}\right) + 1 - \frac{1}{2}\sqrt{\frac{5}{3}}\left(\frac{4\pi}{3\alpha}\right)^{1/3}\left|\left(\frac{h^2}{2meE}\right)^{1/2} - 2\sqrt{\frac{3}{5}}\left(\frac{3\alpha}{4\pi}\right)^{1/3}\right|\right]$$

or alternatively

$$\sigma = \frac{\sigma_{\max}}{2}\left[\left(\frac{E_{\max}}{E_{\max}-E_0}\right)\left(\frac{E-E_0}{E}\right) + 1 - \frac{|\lambda - \lambda_{\max}|}{\lambda_{\max}}\right] \tag{2.54}$$

in which $\lambda_{\max}$ is found from Equations (2.50) and (2.49). This modification improves the predicted threshold to within 1 or 2 eV in most cases. Clearly, the derivation of Equations

2.2.1 is far from rigorous. However, the expression is found to reproduce experimentally measured ionization efficiency curves surprisingly well considering the simplicity and ease of application of the model on which it is based. Since the model does not have the $\frac{\ln E}{E}$ dependence at high energies which is a well documented prediction of the Bethe theory,[64] there will be an increasing discrepancy with experiment as the collision energy is increased. Even so, the model performs well within the energy range investigated in this work. The functional form of Equation 2.54 means that there is a discontinuity in the derivative of the function at the maximum, when $\lambda = \lambda_{max}$, but this affects only a small region of the ionization efficiency curve, and satisfactory values of the cross section are still obtained over this region. The only parameters required in order to apply the model are the ionization potential and polarizability volume of the target molecule, and Equation 2.2.1 provides a useful expression for gaining a rough idea of the form of the ionization efficiency curve in situations where theoretical rigour is not critical. The results of the model will be compared with those of the DM and BEB theories in Section 2.3.

2.3 *Results*

2.3.1 Ab Initio *Calculations based on the electrostatic model*

The maximum electron impact ionization cross sections predicted by the electrostatic model (Section 2.2) have been determined for the inert gases and a range of small molecules[89,98] and compared with ionization cross sections reported in the literature. The effect of the basis set and level of theory used in the molecular orbital calculations on the final cross section obtained has been investigated and found to follow systematic trends.

Inert Gases

The inert gases provided ideal candidates for exploring the effect of changing the basis set and level of theory in these calculations, since their spherical symmetry makes the cross section independent of the relative orientation of the electron and target. Calculations were carried out[88] first at Hartree–Fock (HF) level, and later using fourth order Möller–Plesset perturbation theory (MP4) as well as coupled cluster (CCSD(T)) and quadratic configuration interaction (QCISD(T)) methods. Initially calculated ionization potentials were used in the calculations, but the effect of using experimental values was also investigated. The calculated

maximum electron impact ionization cross sections and ionization potentials are shown in Table 2.2

Table 2.2: Maximum electron impact ionization cross sections for the inert gases calculated using the electrostatic model.

Atom	Method	IP / eV		Cross Section/Å^2		
		calc	expt[a]	calc[b]	calc[c]	expt[d]
He	HF/6-31G*	23.43	24.59	0.38	0.37	0.37,0.38
	HF/6-311G**	23.44		0.44	0.44	
	MP4/6-311G**	24.28		0.43	0.43	
	CCSD(T)/6-311G**	24.28		0.43	0.43	
	QCISD(T)/6-311G**	24.28		0.43	0.43	
Ne	HF/6-31G*	19.65	21.56	1.05	1.00	0.72, 0.74, 0.78
	HF/6-311G**	19.75		1.03	0.99	
	MP4/6-311G**	21.13		1.01	1.00	
	CCSD(T)/6-311G**	21.06		1.09	1.08	
	QCISD(T)/6-311G**	21.06		1.01	0.99	
	QCISD(T)/6-311G**(2df)	21.29		1.05	1.04	
	QCISD(T)/6-311G**(3df)	21.34		1.09	1.08	
Ar	HF/6-31G*	14.66	15.76	2.62	2.53	2.54, 2.70, 2.86
	HF/6-311G**	14.63		2.66	2.56	
	MP4/6-311G**	15.28		2.60	2.56	
	CCSD(T)/6-311G**	15.12		2.61	2.56	
	QCISD(T)/6-311G**	15.22		2.60	2.56	
Kr	HF/6-31G*	13.18	14.00	3.52	3.42	3.70, 3.72, 4.26
	HF/6-311G**	13.16		3.61	3.50	
	MP4/6-311G**	13.82		3.50	3.48	
	CCSD(T)/6-311G**	13.80		3.51	3.48	
	QCISD(T)/6-311G**	13.80		3.50	3.47	
Xe	HF/3-21G*	11.44	12.13	4.24	4.13	4.59, 4.98, 5.46

[a] from references[2–4]

[b] Cross sections obtained using the calculated ionization potential

[c] Cross sections using the experimental ionization potential

[d] from references[16,33–37]

With the exception of neon, for which the cross section is overestimated by around 20%, there is good agreement between calculated and experimental cross sections. In general,

expanding the basis set leads to an increase in the calculated ionization cross section, while moving to a higher level of theory with the same basis set leads to a decrease. Both of these effects are small however, and there is little gain in carrying out expensive calculations when a simple Hartree–Fock treatment is sufficient to reproduce experiment satisfactorily. Similar results are returned when the calculated ionization potential is replaced by the experimental value. As expected, for cases in which the calculated ionization potential is less than the experimental value, the calculated cross section is higher due to the fact that the Coulomb potential reaches the ionization energy at a larger interparticle separation.

For these atomic species it is also possible to develop an alternative approach to that described in Section 2.2.1 for predicting the electron energy at which the maximum cross section is obtained. It is assumed that the electron is ionized from the highest lying occupied atomic orbital. This valence electron is treated as a particle in a classical orbit for which an orbital frequency may be calculated. The inbound electron is treated as a wave, and it is assumed that coupling between the bound and projectile electrons, leading to energy transfer and ionization, is most likely to occur when the frequency of the projectile electron wave matches the orbital frequency of the bound electron.

The energy of the bound electron is the sum of kinetic and potential energy components.

$$E = K + V \tag{2.55}$$

The kinetic energy K is due to the classical orbital motion, while the potential energy V is the Coulomb potential experienced by the bound electron as a result of the effective nuclear charge

$$V = -\frac{Z_{\text{eff}}e}{4\pi\epsilon_0 r} \tag{2.56}$$

where

$$Z_{\text{eff}} = Z - S \tag{2.57}$$

In the above equation Z is the nuclear charge and S is the screening factor,[73] which accounts for shielding of the nuclear charge by atomic electrons in inner shells. The kinetic energy $K = E - V$ may then be determined using the total binding energy for the highest occupied orbital returned from the molecular orbital calculations. For a particle in a classical circular orbit the kinetic energy may also be written

$$K = \frac{1}{2}I\omega^2 = \frac{1}{2}m_e r^2\omega^2 \tag{2.58}$$

Table 2.3: Comparison of experimental and calculated positions of the peak in the ionization efficiency curves for the inert gases.

Atom	Peak position / eV	
	model	experiment (approximate)
He	95	110
Ne	154	160
Ar	71	75
Kr	63	65
Xe	57	55

where I is the moment of inertia, ω the angular velocity, m_e the mass, and r the orbital radius of the bound electron. The orbital frequency is then given by

$$\nu = \frac{\omega}{2\pi} = \frac{1}{\pi}\sqrt{\frac{2K}{m_e r^2}} \tag{2.59}$$

The peak in the ionization efficiency curve appears when this orbital frequency is equal to the frequency of the incoming electron wave, giving the energy at the peak as

$$E_{\max} = h\nu = \hbar\sqrt{\frac{2K}{m_e r^2}} \tag{2.60}$$

When this model is applied to the inert gases the experimentally observed trend in $E_{\max}$ is reproduced. The calculated energies are compared with the experimental results of Stephan *et al*[75] in Table 2.3. The electron energy at the peak in the cross section generally decreases with increasing atomic mass, with the exception of neon, for which the experimentally measured maximum occurs at a much higher energy. The anomaly in the case of neon is thought to be due to the fairly small orbital radius for the highest occupied orbital. The 2p shell of Ne has a radius of 0.35 Å, similar to the 0.30 Å radius of the 1s shell in He. However, the orbital kinetic energy for Ne is much greater, leading to a higher peak energy. The orbital radii for the remaining inert gases are significantly larger than He and Ne, and since the factor r^2 appears in the denominator of Equation (2.60) the energy of the peak decreases again for these heavier atoms.

Molecules

Based on the results for the inert gases, only HF/6-31G* level calculations were carried out for the majority of molecular species. The results of these calculations and available experimental

data are shown in Table 2.4. More detailed results, including threshold distances r_{th} for the various molecular orientations, are included in Appendix A. Except for CO_2, and possibly CO and NH_3, depending on which of the experimental values is correct, there is good agreement between the calculated and experimental maximum electron impact ionization cross sections. The overestimation of the cross section in the case of CO_2 is thought to be an artefact of the averaging procedure described in Section 2.2. Most of the molecules can be considered to be broadly spherical in shape, so that averaging over the six directions of electron approach defined by the positive and negative cartesian axes centred on the molecular centre of mass gives a reasonable approximation to the orientation averaged molecular cross section. For a linear molecule such as CO_2 using this procedure leads to too great a weight being given to approach along the principal axis of the molecule and the cross section is correspondingly too high. As will be explored in Section 2.3.3, it is possible to extend the idea of an ionization cross section into three dimensions to give a 'volume of ionization'. An alternative averaging procedure is then to use the mean radius of the ionization volume to determine the cross section.[99] This approach generally yields a lower cross section than cartesian averaging for polyatomic molecules and a higher cross section for diatomics. For most molecules the values obtained using the 'volume averaging' method are within 10% of those obtained using cartesian averaging, while for CO_2 there is a 25% decrease in the calculated cross section, giving a value of 4.00 $Å^2$, closer to the experimentally determined value of 3.55$Å^2$.

The effects of changing the level of theory and basis set on the cross section were investigated for two representative molecules, CO and H_2O, and the results are illustrated in Tables 2.5 and 2.6. For both molecules there is a significant increase in the ionization potential and decrease in the ionization cross section on moving above Hartree–Fock level. The HF calculations using the 6-31G* and 6-311G** basis sets show the same increase in calculated cross section on expansion of the basis set which was observed for the inert gases. The increase is not simply due to a change in the calculated ionization potential, since for CO the HF/6-311G** ionization potential is larger than the HF/6-31G* value, while for H_2O the reverse is true. The same trend is reproduced in the MP2 calculations on CO.

For H_2O the cross sections calculated using any method above Hartree–Fock level are virtually identical, regardless of the basis set used. This is thought to be coincidental, since significant variation in the critical distances calculated for electron approach along each axial direction was noted, even though the changes cancelled in the averaging procedure. The cross

Table 2.4: 'Cartesian averaged' maximum electron impact ionization cross sections for small molecules calculated using the electrostatic model.

Molecule	IP/eV		Cross section/Å^2		
	calc	expt[a]	calc[b]	calc[c]	expt[d]
H_2	15.30	15.43	0.95	0.94	0.97
N_2	18.06	15.58	2.40	2.61	2.53
O_2	12.88	12.07	2.87	2.97	2.62–2.98
CO	12.86	14.01	2.91	2.84	2.05–2.66
NO	9.75	9.26	3.42	3.52	3.15
H_2O	10.25	12.61	2.42	2.11	2.05
CO_2	12.16	13.77	5.62	5.35	2.05, 3.55
NH_3	8.25	10.16	3.58	3.17	2.4–3.01
CH_4	12.11	12.51	3.90	3.83	3.7

[a] From references[2–4]

[b] Cross sections obtained using calculated ionization potentials.

[c] Cross sections obtained using experimental ionization potentials.

[d] From references[15,96,100–107]

section for CO is much more sensitive to a change in the level of theory used, an increase in the level of theory generally leading to a decrease in the calculated cross section as observed for the inert gases. In contrast to H_2O, calculations at MP4 and QCISD(T) levels gave significantly different results, with the latter returning a cross section almost equal to the Hartree–Fock value.

Again, these effects are small and in general Hartree–Fock level calculations give reasonable agreement with experiment.

2.3.2 *Comparison of theories*

The maximum electron impact ionization cross sections predicted by the electrostatic model for a range of small molecules are compared with the results of BEB and DM calculations and with experiment in Figure 2.6. Results obtained using both types of averaging procedure described in Section 2.3.1 are shown, though volume averaging was not carried out for every molecule studied. DM calculations were not carried out for $CHCl_3$ since the population analysis would have been prohibitively time consuming. The maxima predicted by the

Table 2.5: Effect of level of theory and basis set on electron impact ionization cross section of CO calculated using the electrostatic model.

Method	IP / eV	Cross section / Å^2
Experiment	14.01	2.05–2.66
HF/6-31G*	12.86	2.91
HF/6-311G**	12.88	2.93
MP2/6-31G*	14.02	2.79
MP2/6-311G**//MP2/6-31G*	14.16	2.82
MP4/6-311G**//MP2-6-31G*	14.16	2.81
QCISD(T)/6-311G**//MP2/6-31G*	13.69	2.88

Table 2.6: Effect of level of theory and basis set on electron impact ionization cross section of H_2O calculated using the electrostatic model.

Method	IP / eV	Cross section / Å^2
Experiment	12.61	2.05
HF/6-31G*	10.25	2.42
HF/6-311G**	10.29	2.48
MP4/6-311G**//MP2/6-31G*	11.60	2.34
CCSD(T)/6-311G**//MP2-6-31G*	11.57	2.34
QCISD(T)/6-311G**//MP2/6-31G*	11.57	2.34
QCISD(T)/6-311G**(2df)//MP2/6-31G*	11.77	2.35
QCISD(T)/6-311G**(3df)//MP2/6-31G*	11.77	2.34

electrostatic model agree with the DM and BEB results in most cases.

Obviously, when compared with the DM and BEB theories, which return the full ionization efficiency curve, the electrostatic model is limited since it can only give the peak value. However, as shown in Section 2.3.3, this is compensated for in part by the orientation information which the model can supply. The conceptual simplicity of the model is also appealing.

In Figure 2.7, the ionization efficiency curves predicted by the polarization model are shown along with the experimental results of Rapp and Englander-Golden,[16] Djuric *et al*[95] and Harris *et al*[97] for a range of molecules. The BEB and DM curves are also shown for comparison. In all cases the BEB model reproduces the experimental results very closely,

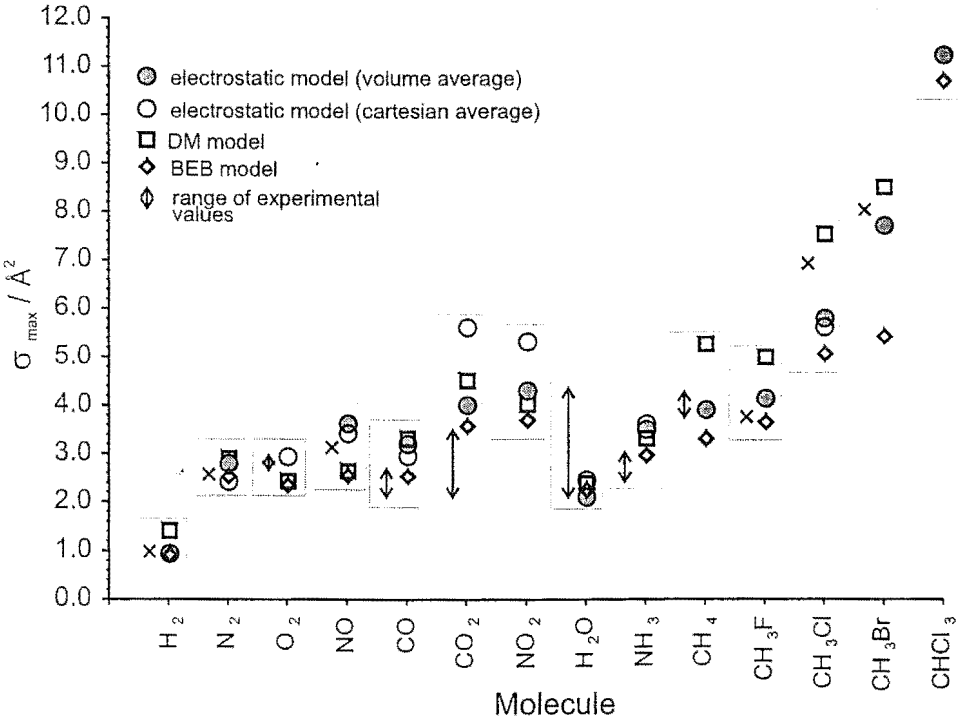

Figure 2.6: Comparison of electrostatic, BEB and DM models for calculation of the maximum in the ionization efficiency curve with experiment for a range of small molecules.

with the polarizability model also showing good agreement in most cases. The DM cross sections are generally too large, with the peak appearing at too low an electron energy, and also tend to fall off too fast at high energies. The poor performance of this model may be due in part to the low level of theory used in carrying out the population analyses for the molecules studied, since the atomic orbital populations greatly affect the final cross section returned by the theory.

One of the principal disadvantages of the polarizability model is the discontinuity at the peak, though with some refinement of the model it is probable that the discontinuity could be eliminated. It should also be remembered that the polarizability model can only give the shape of the ionization efficiency curve, and the results must be scaled by the maximum cross section to give the actual cross section as a function of energy. The method does have the significant advantage that no knowledge of the molecular orbitals involved is needed; the only quantities required are the ionization potential and the polarizability volume, both of which are widely available in the literature for most species.

Of the three theories used in the calculation of electron impact ionization efficiency curves, the BEB model of Kim and Rudd shows the closest agreement with experiment for the systems

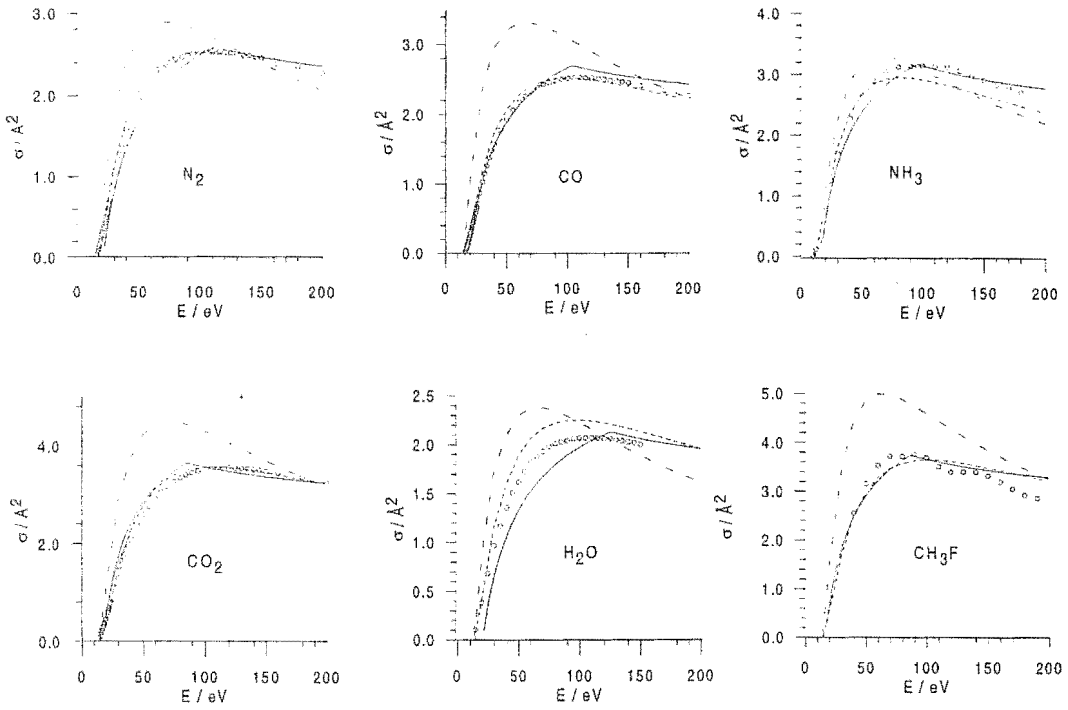

Figure 2.7: Comparison of the polarization model (solid line) with DM (long dashed line) and BEB (short dashed line) calculations and experimental results (open circles)[16,95,97] for N_2, CO, CO_2, H_2O and NH_3.

studied, a significant achievement since this is the only theory which has no dependence on experimentally determined quantities or empirical parameters. The polarizability model gives reasonable agreement for the molecular systems investigated over the energy range studied, though at high energies it will break down since it lacks the $\frac{\ln E}{E}$ dependence in the limit as $E \rightarrow \infty$ predicted by Bethe.[64]

2.3.3 *The effect of orientation on the electron impact ionization cross section*

In carrying out calculations using the electrostatic model, the positions of all the atoms in the target molecule relative to the ionizing electron must be specified as part of the input to the molecular orbital code used to calculate the threshold separation. This has the result that the cross section obtained is a function of the relative orientation of the electron and the target molecule, and that the model should provide a method for investigating the orientation dependence of the electron impact ionization cross section. The recent crossed particle

beam experminents of Aitken and coworkers[6] have shown that the electron impact ionization cross sections for several symmetric top molecules are dependent on the electron–molecule orientation. It was found that ionization is more likely if the electron impacts on the positive end of the molecular dipole, suggesting that molecules exhibit a shape with respect to electron impact ionization. These shapes are amenable to calculation using the electrostatic model; if calculations are carried out for a range of impact angles it is possible to map an 'electron impact ionization surface', an extension of the concept of an ionization cross section into three dimensions. The surface essentially represents an equipotential surrounding the molecule; according to the model ionization occurs when an electron penetrates the surface. The ionization cross section for a particular orientation is equivalent to the cross sectional area of a slice through the surface.

Ionization surfaces have been calculated for several of the molecules considered in Section 2.3.1 and are shown in Figures 2.8 and 2.9. Because the available graphics package[108] could only be used to plot single valued functions it was necessary to construct the complete enclosed surface from two separate plots. This was not possible for molecules such as ammonia and the methyl halides, which do not possess a suitable plane of symmetry, so that only the relative cross sections presented to an electron approaching from the two ends of the molecular dipole are shown for CH_3Cl and NH_3.

The surfaces shown in Figures 2.8 and 2.9 support the experimental conclusion that electron impact ionization cross sections are strongly orientation dependent. In all cases the cross section is greater for impact on the positive end of a dipolar molecule, in qualitative agreement with the experimental results of Aitken *et al.*[6] This is intuitively correct since the incoming electron, carrying a negative charge, is more strongly attracted to regions of positive charge.

Many of the models which are currently used for the calculation of ionization efficiency curves rely on some form of the additivity rule,[69] in which a molecular ionization cross section is treated as a sum of the cross sections of the constituent atoms, to extend their field of validity from atomic to molecular species. Theories incorporating this rule are generally fairly successful at reproducing the energy dependence of molecular electron impact ionization cross sections. The ionization surfaces presented here clearly show distinct 'spheres of ionization' centred on each atom, giving an indication that the representation of a molecular cross section as a sum of atomic cross sections may be very close to the true case and providing validation

for one of the fundamental assumptions implicit in many of the current theories of electron impact ionization.

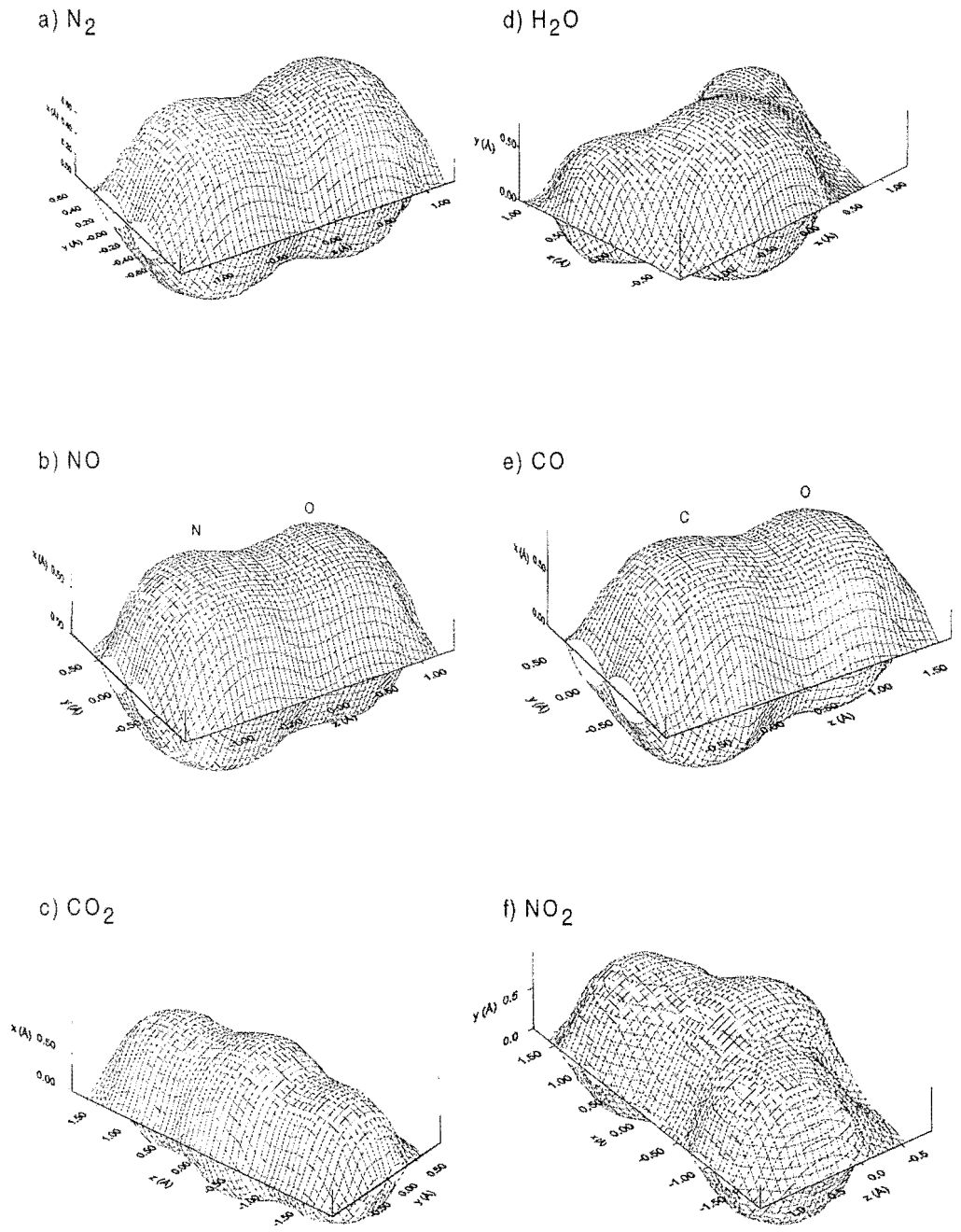

Figure 2.8: Electron impact ionization surfaces for a series of small molecules

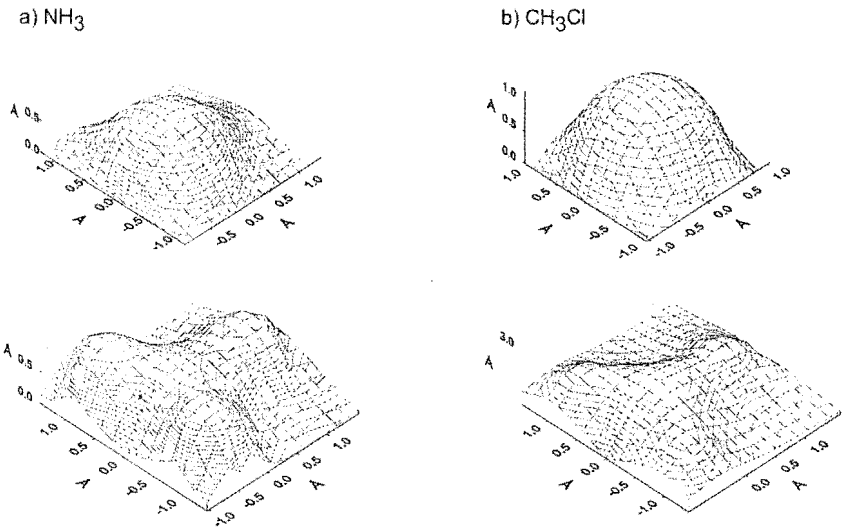

Figure 2.9: View from either end of the molecular dipole of the electron impact ionization surfaces for NH_3 and CH_3Cl.

It should be noted that the form of the molecular electron impact ionization surface will be energy dependent. The steric ratio R for electron impact ionization is defined as the ratio of the ionization cross section at the positive end of the molecular dipole to that at the negative end.

$$R = \frac{\sigma_+}{\sigma_-} \tag{2.61}$$

Experiments have shown that for CH_3Cl the steric ratio decreases by approximately 14% as the electron energy is decreased from 240 to 100 eV.[7,8] As the electron energy decreases towards the threshold for ionization and the electron wavelength increases to molecular dimensions, it is expected that the ionization surfaces would smoothly lose their shape, transforming to spherical symmetry and shrinking as the threshold energy is approached. As the electron energy is increased above the maximum in the ionization efficiency curve—the energy corresponding to the plots shown in Figures 2.8 and 2.9—the shapes would be expected to sharpen up slightly as the electron wavelength decreases below atomic orbital dimensions.

The orientation dependence of the electron impact process for the methyl halides was also investigated using the DM method and compared with experimental results for CH_3Cl. It is assumed that an electron incident on the negative end of the molecular dipoles results in elec-

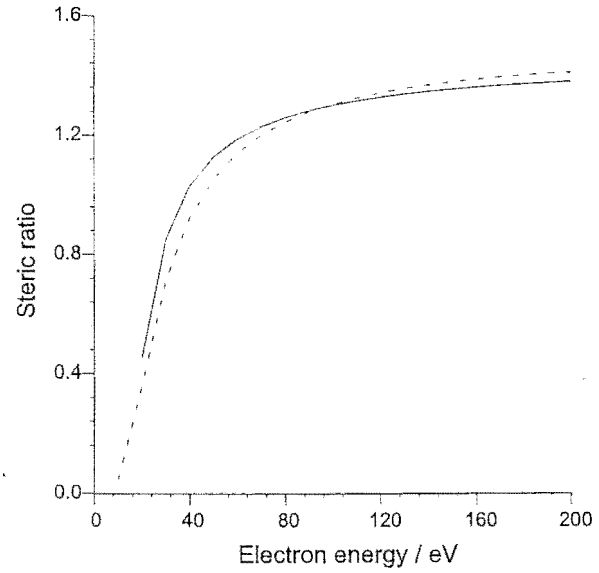

Figure 2.10: Steric ratio as a function of electron energy for CH_3Cl (solid line) and CH_3Br (dashed line) calculated using the DM theory.

tron loss from an atomic orbital centred on the halogen atom, while an electron approaching the positive end leads to electron loss from a carbon or hydrogen orbital. A cross section for the halogen end may then be calculated by summing only over chlorine atomic orbitals, and similarly for the methyl end by summing over carbon and hydrogen orbitals. The steric ratio R is then given by the ratio of these two cross sections. Since the DM theory gives the cross section as a function of electron energy the energy dependence of the steric ratio may be calculated, and it is found that the decrease in R with decreasing electron energy observed experimentally is correctly reproduced. This energy dependence is shown for the molecules CH_3Cl and CH_3Br in Figure 2.10.

The influence of fragmentation processes occuring during electron impact ionization on the steric ratio are indirectly accounted for in the method described above. The major fragmentation product in the electron impact ionization of CH_3Cl is CH_3^+. It is thought that this is formed through broadside collisions between the electron and the molecule, which result in electron loss from the C-Cl bond, while end on collisions yield the molecular ion through electron loss from an orbital centred on the chlorine atom or the methyl group. The simple scheme described above of dividing the molecule into a chlorine atom and a methyl group incorporates broadside collisions, and therefore fragmentation channels of the ionization process.

The measured value[6] of the steric ratio for the total ionization cross section of CH_3Cl at an electron energy of 200 eV is 1.6. At this energy the DM model gives 1.3. The electrostatic model yields a value of 1.4 for the steric ratio at the maximum in the ionization efficiency curve. The two theories are seen to be in good agreement with each other and in reasonable agreement with experiment. The DM results for CH_3Br are very similar to those for CH_3Cl, as shown in Figure 2.10. The electrostatic model predicts a steric ratio of 1.5, again in good agreement with the DM theory, though no experimental measurements were available for comparison in this case.

Part II

DESIGN AND CHARACTERISATION OF AN ELECTRON/ION–MOLECULE CROSSED BEAM MACHINE FOR FUTURE STUDIES

INTRODUCTION

The following chapters will detail the design and characterisation of a crossed beam ion imaging experiment for the study of collisions between electrons or ions and oriented molecules.

The first major consideration for these experiments was the need for an ion source capable of producing a pulsed high intensity, low energy ion beam suitable for collision studies. Design and characterisation of the source is described in Chapter 7. The beam crossing region is based around an ion optics assembly which provides the electric fields necessary for orienting the molecular beam and directing ionic collision products towards the ion imaging detector. Dedicated pulsed electronics units were built in the Electronics Workshop to provide the required electrostatic potentials. A new lid was required for the scattering chamber in order to allow the ion imaging detection system to be mounted directly above the beam crossing region. These components are detailed in Chapter 10. Further modifications to the molecular beam machine included the addition of two new vacuum chambers, one to house a resonance cell used in characterisation of the molecular beam, the other to accommodate the ion source or electron gun. The molecular beam machine as it now stands is described in Chapter 3

A discussion of the preparation of rotationally state selected and spatially oriented molecular beams of symmetric top molecules is presented in Chapter 4. A range of experiments, described in Chapters 5 and 6, were carried out to characterise the molecular beam. Beam velocity distributions and intensity profiles were measured using standard methods. Radiofrequency resonance spectroscopy was employed to investigate the rotational quantum state distribution within a beam of CH_3F and to determine the effect of factors such as hexapole voltage and beam temperature on the distribution. CH_3F was chosen for the study since its rotational spectrum is not complicated by nuclear quadrupole coupling.

Upper Stark state selected molecular beams are known to be attenuated by M_J changing collisions with background molecules when the pressure within the hexapole is high. Cross sections for these collision processes have been determined previously[109] from measurements of hexapole focusing as a function of background gas pressure within a single hexapole collision

cell. However, these experiments were limited by poor resolution and also by the fact that complete single state selection was not possible due to several rotational states focusing at the same hexapole voltage. The RF resonance technique allows truly state selective measurement of cross sections and was employed to carry out a thorough study into M_J changing collisions of CH_3F with a range of scattering gases. The cross sections measured were found to be in good agreement with the earlier results.

Attention was turned next to an investigation into the various factors affecting spatial orientation of the molecular beam. The minimum field strengths required to orient beams of methyl halide molecules between a pair of homogeneous field plates were measured and compared with various results presented in the literature. The presence of charged reagents and products in the planned crossed beam experiments requires that any orienting fields are switched to ground potential before the collision event. If orientation effects are to be observed the delay between switching the field plates and release of the ion or electron beam must be less than the time it takes for the molecular beam to spatially deorient. Little or no consideration has been given to these 'scrambling lifetimes' in the literature and there have been no published measurements of this parameter. The likely timescale of the deorientation process has been considered in terms of the hyperfine interaction between the rotational motion and nuclear spin of a symmetric top molecule. Various attempts were made to experimentally verify these predictions but were complicated by the velocity distribution within the molecular beam. Suggestions are made for future experiments which should eliminate the problem.

Software has been developed for the determination of product ion differential cross sections and translational energy distributions from the raw ion images obtained in the crossed beam experiments. Experience in use of the data analysis techniques used in this part of the project, and in the analysis of results from several of the crossed beam characterisation experiments, was gained during six months spent working with the reaction dynamics groups of Dr Mark Brouard and Professor John Simons (Physical and Theoretical Chemistry Laboratory, University of Oxford). An overview of these techniques is given in Chapter 8. The work carried out at Oxford, a study into the stereodynamics of the $H+H_2O \rightarrow OH+H_2$ reaction, is presented in Chapter 9. The data analysis software developed for the ion imaging experiments is described in Chapter 10.

The various components for the crossed beam experiments have now been assembled and

installed inside the molecular beam machine. Preliminary experiments to check the complete system are discussed in Chapter 10, together with a discussion of problems encountered which will need to be overcome before the crossed beam experiments are carried out.

3. MOLECULAR BEAM MACHINE

3.1 Introduction

The molecular beam machine used in the present work is a highly versatile instrument capable of producing focused beams of rotationally state selected and spatially oriented symmetric top molecules for use in a variety of single beam and scattering experiments. The apparatus has been developed over a period of several years, with frequent modifications and extensions being made to accomodate changes in research interests. Initially it consisted of two vacuum chambers; the first housed a supersonic nozzle source and the second a quadrupole mass spectrometer detector. The two chambers were separated by a skimmer assembly and a flight tube. In this configuration it was used in the measurement of beam velocity distributions, cluster size distributions and appearance potentials of cluster ions.[7,110,111]

A change in research area from investigations of clusters to oriented molecule work[7] prompted the first major modifications to the machine, involving the addition of two chambers between the nozzle source and detector chambers to hold the 833 mm long hexapole used for state selection and orientation of the molecular beam. During this stage the hexapole field was characterised and its focusing effect on a wide range of symmetric top molecules determined from the relative intensities of arrival time distributions for pulsed beams as a function of hexapole voltage.

The next stage in the development of the machine extended its capabilities into crossed beam work. The size of the nozzle source chamber was increased as part of an effort to improve the pumping capacity and a differentially pumped buffer chamber was installed between the nozzle source chamber and the first hexapole chamber. These modifications allowed higher nozzle source stagnation pressures and/or nozzle open times than were previously attainable, while still maintaining a high quality vacuum in the hexapole chambers during beam operation. The most important aspect of the modifications was the addition of a custom made scattering chamber, described in more detail in Section 3.6. Research carried out during this phase of the machine's development includes the electron impact ionization asymmetry

experiments mentioned in Chapters 1 and 2,[6–8] and the upper Stark state collisional relaxation cross section measurements[109,112] discussed in Chapter 6.

Several modifications were required in order to carry out the experiments described in this thesis. Two new vacuum chambers were added to accommodate a resonance cell for molecular beam spectroscopy and an ion or electron source for crossed beam experiments. The resonance cell chamber was installed between the first and second hexapole chambers, while the second new chamber was added as a side arm to the scattering chamber, perpendicular to the molecular beam axis. In addition to solving the problem of limited space in the scattering chamber, housing the ion source in a separate chamber allows differential pumping and maintains a clean, oil–free vacuum in the scattering chamber. The final major change was a new lid for the scattering chamber, designed to accomodate the ion imaging detection system used in the crossed beam experiments.

The components of the molecular beam machine in its current configuration will be described in more detail in the following sections. The machine is illustrated in Figure 3.1. A schematic of the internal components is presented in Figure 3.2.

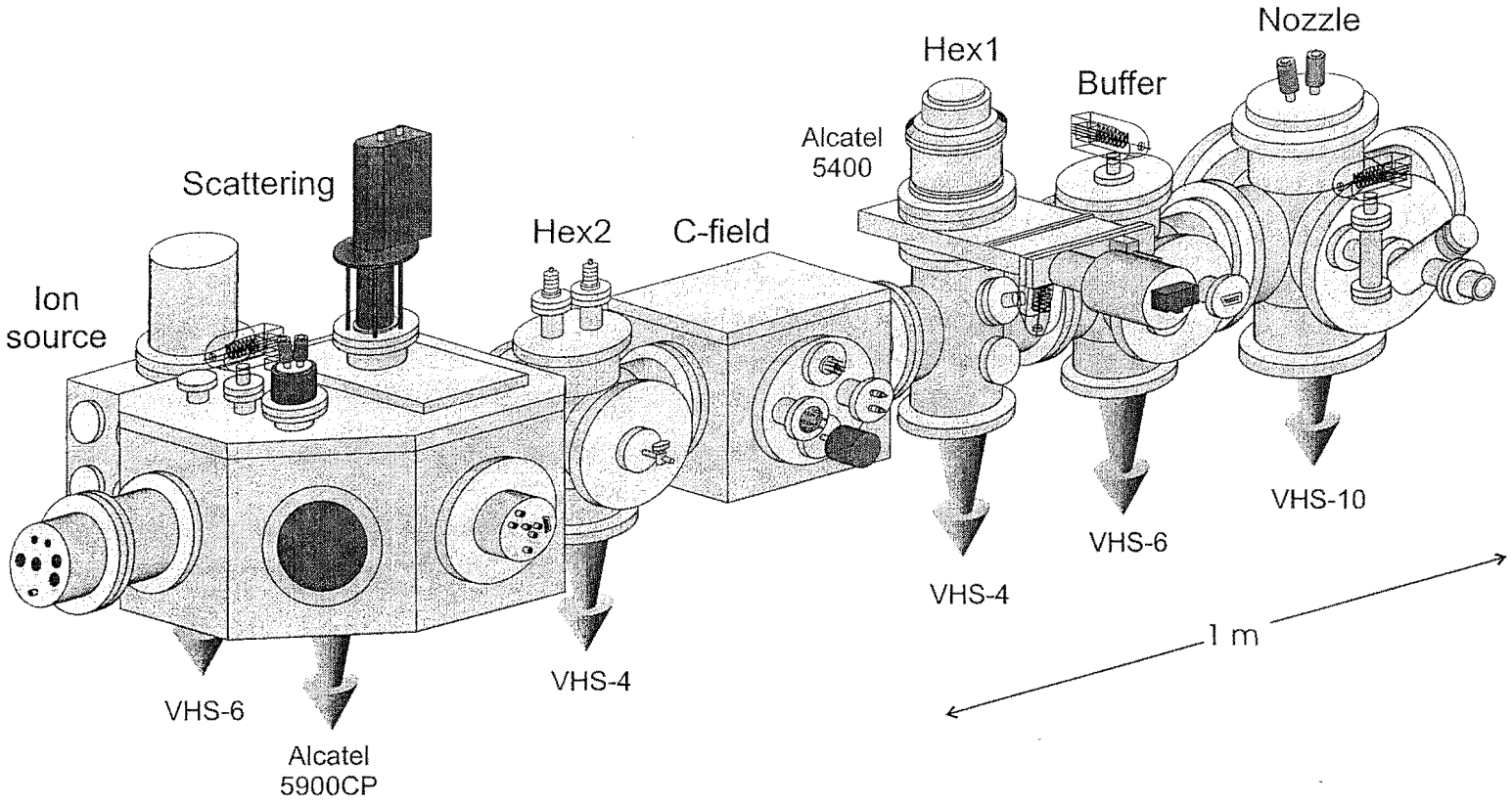

Figure 3.1: Schematic of the molecular beam machine. Chambers discussed in Sections 3.2 to 3.6 are labelled.

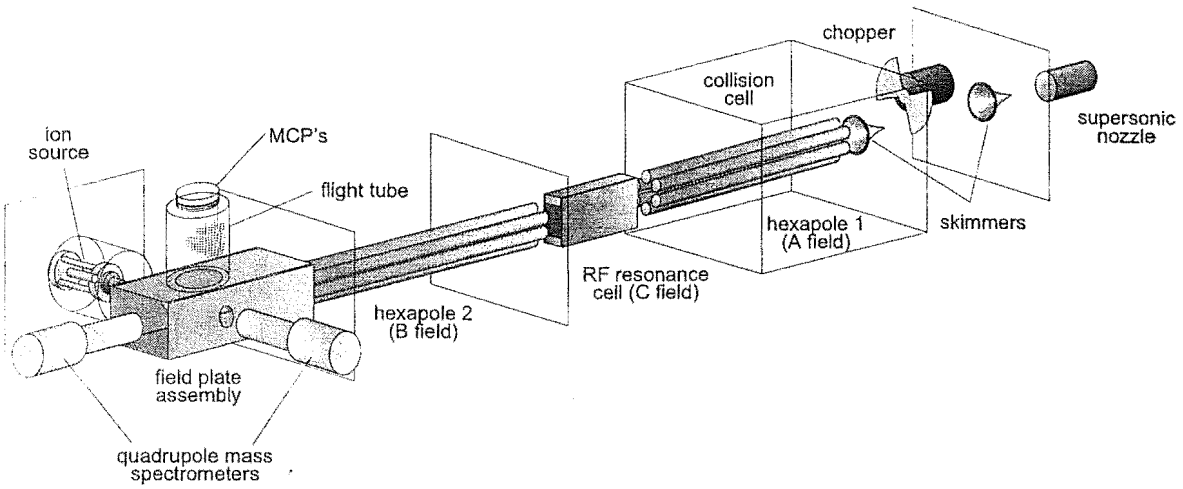

Figure 3.2: Schematic of the internal components of the molecular beam machine.

3.2 Nozzle source chamber

The nozzle source chamber is designed around an 8″ Huntington Laboratories six way cross with 10″ OD stainless steel ConFlat flanges on each face. This chamber has the highest pumping requirements due to the large gas load introduced when the supersonic nozzle source is operating. The chamber is pumped by a 5300 ℓs^{-1} (for air) Varian VHS-10 oil diffusion pump backed by a 1080 ℓmin^{-1} Alcatel 2063C mechanical pump. The mechanical pump is connected to the outlet of the diffusion pump with a length of flexible stainless steel bellows and can be isolated by an Airco Temescal 3″ Fig 5121 gate valve. A 10″ gate valve separates the diffusion pump assembly from the chamber via a spacing spool attached to the bottom face of the six way cross. In order to allow rough pumping of the machine the diffusion pump can be bypassed; the chamber is then pumped directly by the mechanical pump through a separate length of stainless steel bellows which is normally isolated from the chamber by a Huntington Laboratories ES–150 high vacuum bellows valve attached to a side flange of the six way cross.

The top face of the cross carries a liquid nitrogen trap which provides cryogenic pumping for the chamber. A copper baffle, suspended from the trap by copper plates on either side of the nozzle source, is positioned in the spool above the diffusion pump to reduce backstreaming of diffusion pump oil vapour into the vacuum chamber. One side arm of the chamber is taken up with a glass window, the other with an ion gauge and the high vacuum valve to the mechanical pump. The nozzle source chamber is attached to the buffer chamber through a

10″ to 8″ OD ConFlat adapter flange.

3.2.1 Alignment rods

The various internal components of the molecular beam machine are mounted on a pair of 10 mm alignment rods which extend from the nozzle source chamber to the end of the second hexapole chamber. The rods are fixed in place parallel to the beam axis and each consist of two sections. The pair of rods making up the first section are cold pressed into flanges situated at either end of the buffer chamber and extend only from the nozzle source chamber to the first hexapole chamber. These are used to align the supersonic nozzle source, skimmers and a rotating chopper to the beam axis. A communicating set of rods, on which the hexapole and resonance cell are mounted, are held in position by ball joints at the buffer chamber end and an anchor plate (shown in Figure 3.3) bolted to the chamber wall at the scattering chamber end.

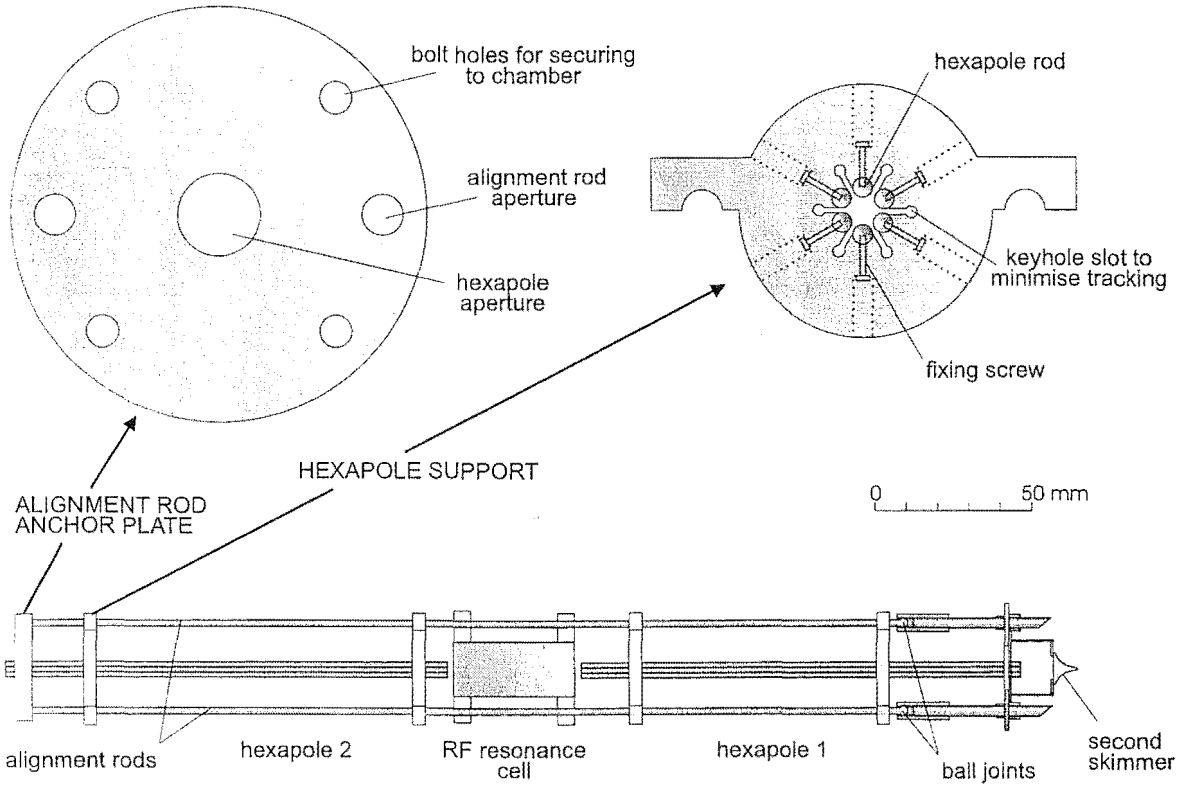

Figure 3.3: The aligment rod and hexapole assemblies.

The nozzle source, skimmers, hexapoles and detector must be in near perfect aligment in order to maintain the integrity of the molecular beam as it travels from the nozzle source

chamber to the scattering chamber. During the alignment procedure a He–Ne laser (Applied Laser Systems, 670 nm 5 mW) is substituted for the supersonic nozzle, allowing the beam path to be visualised. A pair of centre-drilled perspex blocks are placed on the alignment rods between the laser and the first skimmer, the three apertures provided by the two blocks and the skimmer defining the beam axis. Once the laser beam is aligned to this axis the hexapoles, hexapole exit aperture and beam detector can be centred to the laser beam. The rod arrangement described above means that the front end of the hexapole is automatically aligned to the beam axis, and the back end can be adjusted by loosening the bolts which fix the perspex alignment rod mount and pivoting the entire assembly on the ball joints. Small corrections in the position of the quadrupole mass spectrometer used to detect the molecular beam are possible by adjusting a stand which sits on the floor of the scattering chamber and supports the weight of the quadrupole assembly.

3.2.2 *Supersonic nozzle source and carriage assembly*

The supersonic nozzle source assembly is mounted on a linear motion feedthrough attached to an 8″ OD flange, which seals onto the vacuum chamber via a 10″ to 8″ adapter flange. Since the beam source chamber is accessed regularly for alignment of the hexapoles and quadrupole mass spectrometer, a Viton O–ring seal replaces the usual copper ConFlat seal on the 8″ flange. To further aid access to the chamber, the 8″ flange is bolted to a stand attached to a translator plate on the machine support frame, so that the entire assembly simply slides out and is supported during alignment.

The nozzle source itself fits into an aluminium carriage which slides onto the alignment rods, ensuring that the molecular beam is directed along the axis of the machine. Three different types of supersonic supersonic nozzle sources have been used, depending on whether a continuous or pulsed molecular beam is required. The nozzle source assembly and the three supersonic nozzle sources are shown in Figure 3.4

The continuous nozzle source consists of a small cavity with a 75μm orifice, to which the beam gas is supplied through a gas inlet feedthrough in the 8″ OD flange via a length of $\frac{1}{4}$″ diameter stainless steel bellows. For pulsed beam applications this nozzle is replaced with either a piezoelectric nozzle source (Physikalisch–Chemisches Institut, der Universität Zürich) or an electromagnetically operated nozzle (General Valve Corporation model 9–181). The 70 μm orifice of the electromagnetic nozzle is sealed with a small teflon poppet which

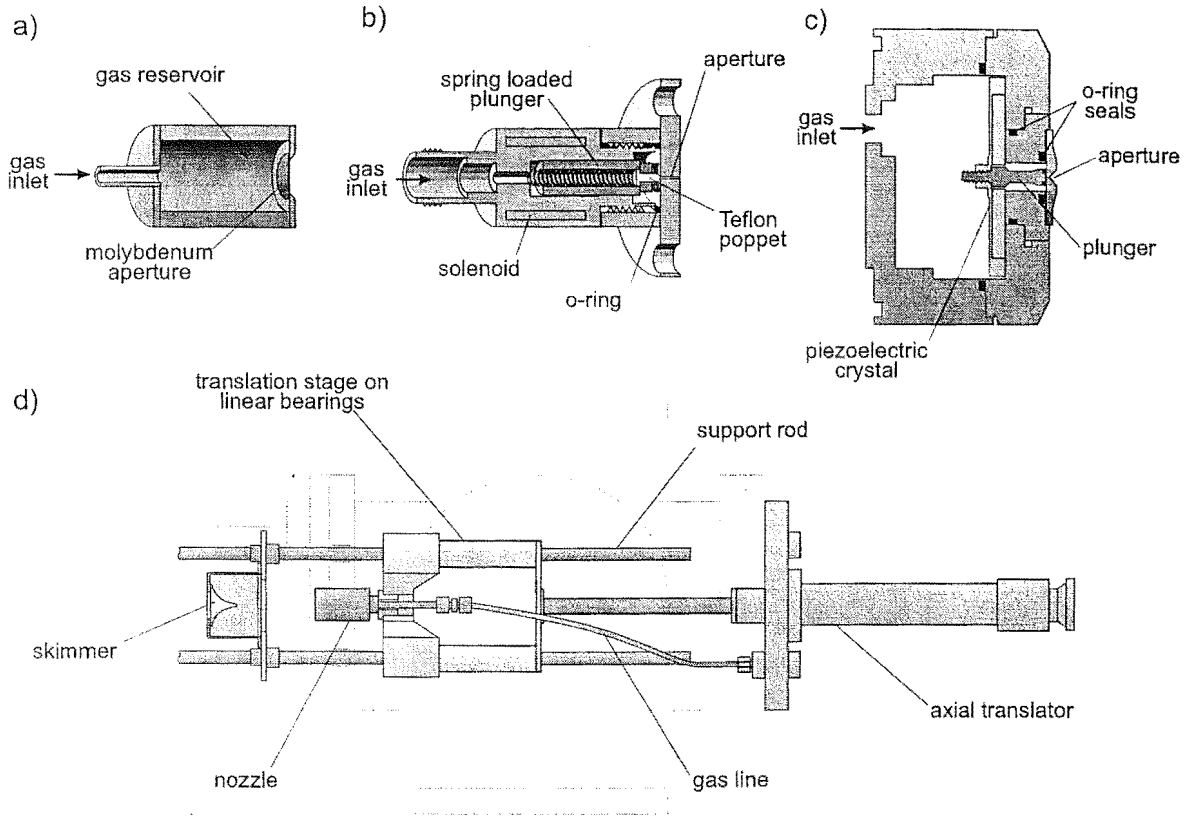

Figure 3.4: Cutaway views of: a) the continuous nozzle source; b) the electromagnetic pulsed nozzle source; and c) the piezoelectric pulsed nozzle source; d) top view of nozzle source assembly

fits inside a spring loaded plunger. When a solenoid inside the nozzle source is energised the plunger is drawn back against a spring, allowing gas through the orifice. On de-energisation the nozzle reseals under the action of the spring. One of the major problems with this type of nozzle source is that as the teflon poppet wears flakes of teflon to block the orifice. The spring loading mechanism can also cause bounce in the sealing mechanism, leading to double pulses of gas escaping from the source. For these reasons the piezoelectric nozzle source is generally used when a pulsed beam is required. The piezoelectric nozzle source has a 70 μm orifice in a small gas reservoir which is sealed with a plunger mounted onto the front of a piezoelectric crystal (Physik Instrumente P–286.20). When a voltage is applied the crystal deforms and pulls the plunger back, allowing the beam gas to escape into the vacuum chamber. The frequency at which the nozzle operates can be varied from 0 to 500 Hz with open times continuously variable from 0.1 to 3 ms. Recently the control unit for the piezoelectric nozzle has been modified to allow a voltage to be applied to the crystal continuously. The nozzle

source can now be used to generate either a pulsed or continuous molecular beam, eliminating the need for frequent interchanging of the supersonic nozzles for different types of experiments.

3.3 Buffer chamber

A Huntington Laboratories 6″ six way cross with 8″ OD ConFlat flanges forms the buffer chamber. The chamber is pumped by a 2400 ℓs^{-1} Varian VHS–6 diffusion pump backed by a 700 ℓmin^{-1} Edwards E2M40 mechanical pump.

3.3.1 Skimmers

The buffer chamber is separated from the nozzle source and first hexapole chambers by a pair of metal plates which slide onto the alignment rods and fit tightly into the arms of the chamber. Each plate has a conical electroformed nickel skimmer (Beam Dynamics) mounted in the centre through which the molecular beam passes. The first and second skimmers have apertures of 1.0 mm and 1.5 mm respectively and the position of the nozzle source is adjusted on the linear translator in order to optimise the nozzle–skimmer distance (see Section 4.1.2.

3.3.2 Rotating chopper

A rotating chopper is installed in the buffer chamber to allow beam modulation when the continuous supersonic nozzle source is in use. The chopper consists of a rotating blade driven by a vacuum rated synchronous motor which mechanically gates the molecular beam. The blade was cut to give beam modulation with a mark space ratio of one, suitable for applications using the lock–in technique described in Section 5.4. An optical switch straddling the chopper blade produces a TTL signal corresponding to the open phase of the chopper, providing a clean frequency reference. The frequency at which the beam is chopped can be varied over the range 0–800 Hz.

3.4 Hexapole and C field chambers

The first hexapole chamber is a designed around a Varian 6″ four way cross with 8″ OD flanges. A partition is installed between the first hexapole chamber and the C field chamber to provide a well defined collision path length for molcular beam attenuation experiments in which the first hexapole is pressurised and used as a collision cell (Chapter 6). The

partition is made from two pieces of thin stainless steel sheet, which clamp together over the alignment rods and bolt to the inside wall of the C field chamber. A 10 mm central aperture allows for passage of the molecular beam and additional clearance holes accomodate electrical connections to the first hexapole.

The C field chamber was fabricated in the department's Mechanical Workshop and takes the form of a square box with 8″ ConFlats machined on three side faces. On the remaining side and the base of the chamber are two 8″ OD ConFlat flanges mounted on short spigots. The lid is removable and seals on a Viton O–ring. The second hexapole chamber is a Huntington Laboratories 6″ six way cross with 8″ OD ConFlat flanges and forms a continuous volume with the C field chamber. The three chambers are pumped by two 1200 ℓs^{-1} Varian VHS-4 diffusion pumps attached to the first and second hexapole chambers. The pumps are isolated from the chambers by Airco Temescal 5010 gate valves and backed by a 345 ℓmin^{-1} Alcatel 2021 mechanical pump and a 75 ℓmin^{-1} Alcatel 2004A mechanical pump respectively. The diffusion pump on the first hexapole chamber can be bypassed through a Veeco high vaccum bellows valve attached to the side port of the gate valve to allow rough pumping of the chamber with the 2021 mechanical pump. In addition to the two diffusion pumps, there is a 400 ℓs^{-1} (for N_2) Alcatel 5400 turbomolecular pump attached to the top of the first hexapole chamber and backed by a second Alcatel 2021 mechanical pump. The 5400 and a larger turbomolecular pump attached to the underside of the scattering chamber are used for pumping overnight, when the diffusion pumps are valved off from the machine. The two turbo pumps maintain an overnight pressure of between 10^{-6} and 10^{-5} Torr. During the day, the smaller turbomolecular pump is isolated from the chamber by a VAT ultrahigh vacuum CF 150 pneumatic gate valve. A doughnut shaped liquid nitrogen trap mounted on an interface flange between the C field and second hexapole chambers provides additional cryogenic pumping.

The positive and negative high voltages required for the two sets of hexapole rods are supplied through two pairs of high voltage feedthroughs. For the first hexapole these are located on one of four $2\frac{3}{4}''$ flanges attached to the 8″ flange on one side of the C field chamber, while the feedthroughs for the second hexapole are mounted on two separate $2\frac{3}{4}''$ flanges on the top of the second hexapole chamber. At present the hexapoles are operated at the same voltage and the two sets of feedthroughs are linked externally, though experiments planned for the future will require that the voltages can be varied independently.

The remaining three $2\frac{3}{4}''$ flanges on the side of the C field chamber are used to mount an ion gauge, an MKS 1000 Torr Baratron used for monitoring the pressure during venting or rough pumping of the machine, and a multipin electrical feedthrough carrying the RF and DC potentials for the radiofrequency resonance cell.

A scattering gas can be admitted to the first hexapole chamber for molecular beam attenuation experiments using a Leybold Heraeus 283-41 DN 10 KF variable leak valve mounted on a $2\frac{3}{4}''$ flange on the side of the chamber. The leak valve has been modified for computer controlled operation using a Howard Industries 1-19-4307 stepping motor connected to a Crytallap STD-206 driver unit and interfaced to a PC. The pressure in the first hexapole chamber is monitored by an ion gauge and an MKS 690 baratron, both attached to side flanges in the four way cross. During attenuation experiments the baratron is used to calibrate the ion gauge to allow pressure measurements to be taken below the sensitivity range of the baratron.

3.4.1 Hexapoles

The hexapole assembly is shown in Figure 3.3. Each hexapole consists of a set of six $\frac{1}{4}''$ diameter stainless steel centreless ground rods 530 mm long, screwed into a pair of perspex supports mounted on the alignment rods, which fix the hexapole rods on an inscribed radius of 4.74 mm. Keyhole shaped slots machined between in the supports between the rod positions minimise discharging across the perspex surface when high voltages are applied to the rods. A pair of Glassman EH 0–10 kV power supply units provide the positive and negative high voltages required to operate the hexapole. The perspex mounts are designed to slot over the alignment rods, locating the hexapoles on axis inside the machine. An adjustable iris at the end of the second hexapole, usually set to a diamter of around 2 mm, forms the exit aperture from the hexapole region. The iris is mounted on a can which pushes into the interface flange between the scattering chamber and the second hexapole chamber.

3.4.2 Radiofrequency resonance cell

Two resonance cells with different plate geometries, both shown in Figure 3.5, have been used in the work described in this thesis. The cell designs and principle of operation will be discussed in detail in Chapter 5. The cells are interchangeable and either can be positioned on the alignment rods between the first and second hexapole on a pair of perspex mounts (not shown in figure). Electrical feedthroughs lead from each of the four elements of the cell to

a vacuum feedthrough on the side of the C field chamber and supply the required operating voltages to the cell. The cell is enclosed in a Faraday cage to prevent any appreciable field penetration into the cell from the hexapole rods. 10 mm holes in each end of the cage allow passage of the molecular beam.

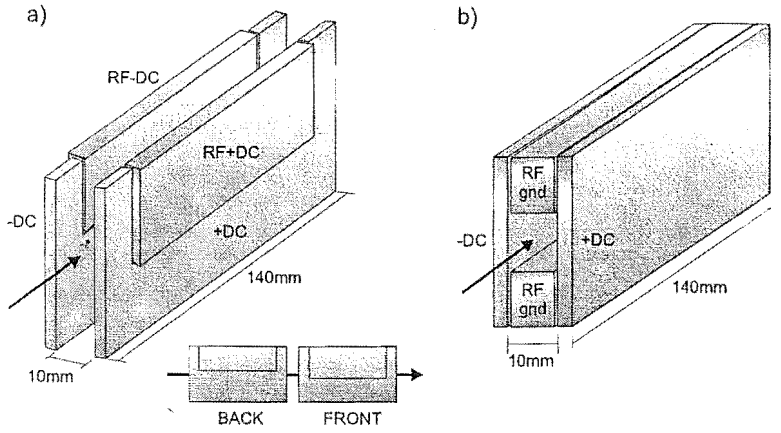

Figure 3.5: a) Split parallel plate and b) double parallel plate RF resonance cells used in the measurement of relative populations of rotational quantum states in beams of symmetric top molecules. The DC field orients the symmetric top molecules while the RF field stimulates ΔM transitions between the rotational states present in the molecular beam. Arrows indicate the beam direction.

3.5 Ion source chamber

The ion source chamber was fabricated in the Departmental Mechanical Workshop and at present is used to accomodate either the ion source described in Chapter 7 or the Pierce electron gun described in Chapter 10. The cubic design is similar to that used for the C field chamber, the main difference being that the lid is not removable. The front face of the chamber is fitted with a short spigot terminating in an 8″ ConFlat flange which forms the seal to the scattering chamber. A 6″ ConFlat machined into the back face of the chamber serves as the attachment point for the ion source / electron gun assembly. One side face has four $2\frac{3}{4}''$ ConFlats used for an ion gauge and electrical feedthroughs, and 8″ ConFlats are machined into the remaining three faces. The chamber is pumped by a Varian VHS-6 diffusion pump backed by a 726 ℓmin^{-1} Varian SD700 mechanical pump, which also backs the turbomolecular pump on the scattering chamber. A 6″ gate valve is used to isolate the diffusion pump from the chamber when required.

The ion and electron sources, detailed in Chapters 7 and 10, can be interchangeably mounted onto the front end of a Huntington Laboratories PM-600 xyz translator which attaches to the ion source chamber on the side opposing the scattering chamber. The front end of the assembly extends through the ion source chamber into the scattering chamber. The high operating temperatures and porous components of the ion source mean that degassing can be a problem on the first few heating cycles after initial pumpdown. For this reason, when the ion source is in place a cylindrical partition is fitted into the interface flange between the ion source and scattering chamber to allow the source to be differentially pumped. The partition also provides electrical shielding, preventing stray electric fields from the ion source lenses from penetrating into the scattering chamber. The partition is usually removed when the electron gun is installed. A small grounded can attached to the gun itself terminates field lines from the lens elements, and differential pumping is not necessary.

3.6 Scattering chamber

The scattering chamber was designed to provide a beam crossing region which can be customised for a wide variety of experiments. The chamber consists of a base, mid–section and lid which seal together on BS–470 Viton O–rings. An assortment of $2\frac{3}{4}''$ and $8''$ flanges around the sides of the chamber provide spaces to mount detectors, feedthroughs and other apparatus, while drilled and tapped holes on a $1''$ grid on the inside of the mid–section facilitate installation of vacuum components within the chamber. Several more flanges are set on spigots into the base of the chamber. The original lid was not suitable for the requirements of the crossed beam experiment described in Chapter 10, and a second lid, described in Section 10.2.4, was fabricated for this work. The new lid accomodates the ion imaging detection system, electrical feedthroughs and an ion gauge.

The microchannel plate detectors of the ion imaging system should be kept in an oil free vacuum environment, and for this reason the scattering chamber is pumped by an 880 ℓs^{-1} (for N_2) Alcatel 5900CP turbomolecular pump. The turbo pump shares a foreline and backing pump with the $6''$ diffusion pump on the ion source chamber. A liquid nitrogen trap located on the base of the chamber provides cryogenic pumping.

In addition to the field plate assembly and flight tube required for crossed beam experiments, which will be described in detail in Chapter 10, the scattering chamber also houses detectors for both the charged and neutral beams and the ion imaging system for product

ion detection. The molecular beam is monitored using an Extranuclear Laboratories 4–270–9 quadrupole mass spectrometer fitted with the electron impact ion source from a Vacuum Generators SXP-300 quadrupole. The electron beam can be monitored using either a Faraday cup detector or the purpose designed phosphor screen described in Section 10.2.2. The electron detector is replaced with the Vacuum Generators quadrupole for ion beam detection. Collision products are detected using a custom designed Photonic Science Ltd. ion imaging system mounted to a 6 $''$ flange on the scattering chamber lid. The imaging system and associated electronics will be described in more detail in Chapter 10.

3.7 Gas handling and liquid nitrogen system

All gases are supplied to the machine through $\frac{1}{4}''$ diameter copper pipe and/or stainless steel bellows. Valves are generally of the Swagelock JN type. A vacuum line pumped by an Edwards mechanical pump to which cylinders can be attached is used to prepare gas mixtures. The pressure in the line is monitored by an MKS 221AA 10,000 Torr baratron. The line is used to admit gas to the supersonic nozzle source and also for admitting a quencher gas to the hexapole region during beam attenuation experiments. The vacuum line can be divided into two halves for these experiments, allowing the two supplies to be controlled independently. When the continuous nozzle source is used the line to the nozzle is fitted with an MKS Type 250B flow controller coupled to a Type 2218D 1000 Torr baratron, allowing the nozzle source stagnation pressure to be accurately controlled.

As mentioned in previous sections, each diffusion pump is fitted with a baffled liquid nitrogen trap to prevent backstreaming, and several other traps in various locations around the machine provide extra cryogenic pumping of condensable gases. The traps are filled through a series of insulated 3/8 $''$ copper pipes which form a continuous network. A timer regulates filling of the traps from a 75 L dewar pressurised from a cylinder of oxygen–free nitrogen (BOC gases). The same line that serves the liquid nitrogen system is also used for venting the machine through a feedthrough valve in the front flange of the nozzle source chamber. A second cylinder of nitrogen is used to pressurise the pneumatically operated gate valves which isolate the two turbo pumps on the C field and scattering chambers to the machine.

3.8 Computer interfacing

Several of the electronics units used with the molecular beam machine are computer interfaced, allowing automated data collection in a wide range of experiments. The PC through which these components are interfaced is a 486 fitted with both PCL-7388 D/A and PCL-8255 D/D I/O cards in addition to the usual serial and parallel interface ports. The two Glassman high voltage power supplies used for the hexapoles are set to the required voltage by a 0–10 V signal from a 12 bit digital to analog converter interfaced through the PCL-8255 digital card. The DC voltage applied to the RF cell is also controlled by a 0–10 V signal from the 7388 card. An RS-232 serial interface is used to retrieve information on current settings and frequency reference from the lock–in amplifier used in the RF spectroscopy experiments. Analog signals from the lock–in amplifier, the quadrupole mass spectrometers, and several other units, are sent to the PC through the 7388 card. Pressure measurements can be taken from either the baratron or the ion gauge on the hexapole collision cell chamber through an RS-232 serial interface, and the pressure in this chamber is set by using a stepping motor, controlled through an IEEE parallel interface, to regulate the Leybold–Heraeus leak valve on the side of the chamber.

4. THEORY OF ROTATIONALLY STATE SELECTED AND SPATIALLY ORIENTED MOLECULAR BEAMS

Molecular beams have revolutionised the fields of spectroscopy and chemical dynamics, providing a directed source of internally cold molecules with a well defined velocity distribution. Quantum state selection provides a further degree of refinement, and can be achieved using either laser techniques or, in the case of certain types of molecules, electric fields. The experiments described in Chapters 5, 6 and 10 involve the use of a beam of spatially oriented, rotationally state selected symmetric top molecules. The following sections detail the various factors involved in beam production in the molecular beam machine described in Chapter 3.

4.1 Molecular beam sources

A molecular beam is formed when gas from a containment reservoir flows through an orifice into a vacuum. The flow characteristics of the beam depend on the value of the Knudsen number, defined as

$$K_n = \frac{\lambda}{\phi} \tag{4.1}$$

in which ϕ is the diameter of the orifice and λ is the mean free path of the molecules inside the source. Molecular beam sources fall into two categories, depending on whether K_n is greater than or less than unity. If $K_n > 1$ the source is effusive. If $K_n < 1$ it is supersonic.

4.1.1 Effusive sources

In an effusive source the diameter of the orifice is less than the mean free path of the molecules in the source, so that most molecules arriving at the aperture pass through it without undergoing a collision. The velocity distribution of the gas inside the source is Maxwellian.[113]

$$N_s(v)dv = \frac{4n_0}{\sqrt{\pi}} \frac{v^2}{v_{\mathrm{mp}}^3} e^{-v^2/v_{\mathrm{mp}}^2} dv \tag{4.2}$$

where $v_{\mathrm{mp}} = \sqrt{2kT/m}$ is the most probable velocity and n_0 is the number density inside the source.

Since the molecules leave the source without undergoing a collision it might be expected that this distribution is maintained in the effusive beam. However, because molecules travelling at a high velocity inside the source encounter the aperture more frequently than slower moving molecules and therefore have a higher probability of exiting the source, the velocity distribution in the beam is skewed relative to the source veloctity distribution. The beam velocity distribution is therefore:

$$N_b(v)dv = \frac{v}{v_{\mathrm{mp}}} N_s(v)dv = \frac{4n_0}{\sqrt{\pi}} \left(\frac{v}{v_{\mathrm{mp}}}\right)^3 e^{-v^2/v_{\mathrm{mp}}^2} \frac{dv}{v_{\mathrm{mp}}} \tag{4.3}$$

The spatial distribution of molecules leaving the source has a cosine dependence on the angle θ between the molecular velocity vector and the beam axis. The emitted intensity in molecules per steradian ω is

$$I(\omega)d\omega = \frac{1}{4\pi} n_0 \bar{v} A \cos\theta d\omega \tag{4.4}$$

In the above equation A is the area of the orifice and $\bar{v} = (8kT/\pi m)^{1/2}$ is the average velocity of the molecules in the source. The total rate of effusion is found by integrating Equation 4.4 over the two polar angles θ and ϕ to give

$$I = \frac{1}{4} n_0 \bar{v} A \tag{4.5}$$

Effusive sources produce very low intensity beams compared to the supersonic sources to be discussed in the next section. This problem can be largely overcome by using laser drilled multichannel arrays in place of a single aperture,[114] giving huge increases in intensity while retaining the angular distribution of the beam.[115] Interference between gas flow from individual channels can be neglected in most cases, so that the equations used for a single channel or orifice also apply for a source with multiple channels.

One of the main advantages of the effusive source is that the rate of effusion, and also the velocity and angular distributions in the beam, can be calculated from kinetic gas theory. Because essentially no collisions occur as molecules leave the source the beam gas is in thermal equilibrium and contains a well defined equilibrium distribution of vibrational and rotational states. This distribution of internal states can be altered by heating or cooling the source, and the resulting distributions are still well characterised. However, the fact that the beam is

thermal, with a wide thermal velocity and angular distribution, also has several disadvantages. The wide angular distribution of molecules leaving the source means that collimation is essential in order to obtain a directed beam. Since most molecular beam experiments require a fairly monoenergetic beam a velocity selector is required in order to obtain a beam of the desired energy from an effusive source. In addition to making velocity selection necessary, the thermal velocity distribution also means that the energy range available using an effusive beam is limited. The beam energy can be increased by heating the source. though only to energies up to around 0.1 eV. Effusive sources are useful when beams of low vapour pressure materials are required[114] and are most often used in the preparation of beams of alkali metal atoms such as potassium and sodium.

4.1.2 Supersonic sources

Supersonic or nozzle sources have a distinct advantage over effusive sources in most applications, producing a high intensity beam with a narrow velocity distribution. During the supersonic expansion, internal energy of the gas inside the source is converted into translational kinetic energy of the beam. Because the nozzle diameter is greater than the mean free path of the molecules inside the source, multiple collisions occur as the gas passes through the throat of the nozzle. These collisions transfer momentum to the axial direction giving a high velocity along the axis and a small random velocity perpendicular to the axis. Since the translational kinetic energy of the beam is provided by the internal energy of the molecules in the nozzle rather than from an external source, the beam molecules are internally cold.

Structure of the supersonic expansion

The structure of a supersonic expansion is very different to the $\cos\theta$ flux distribution produced from an effusive source. Inside the nozzle source the gas is in the 'stagnation state' at pressure P_0 and temperature T_0. The gradient $P_0 - P_b$ between the pressure inside the source and the background pressure in the vacuum system causes the gas to accelerate through the converging nozzle as the area decreases towards the source exit. In order to obtain a supersonic expansion the pressure ratio P_0/P_b must exceed the critical value[114]

$$G = \left(\frac{\gamma+1}{2}\right)^{\frac{\gamma}{\gamma-1}} \tag{4.6}$$

where γ is the ratio of heat capacities C_p/C_v. If $P_0/P_b < G$ then the flow exits subsonically, the exit pressure at the nozzle is nearly equal to the background pressure P_b and there is no further expansion. When $P_0/P_b > G$ then the Mach number M at the nozzle is equal to one. The Mach number is defined as the ratio of the mean velocity u of the gas molecules to the local speed of sound.

$$M = \frac{u}{(\gamma k T_0/m)^{1/2}} \tag{4.7}$$

Under these conditions the exit pressure is equal to P_0/G, approximately one half of the stagnation pressure (since $G \approx 2$), and is independent of the background pressure. Because the pressure at the nozzle exit is now greater than the background pressure the gas expands under the boundary conditions imposed by the background pressure. As a supersonic flow expands, M increases as the flow increases so that the gas is travelling faster than the local speed of sound beyond the nozzle exit. This has some interesting consequences.

Information is transferred at the speed of sound. Once the gas begins to expand from the source exit, M increases so that the flow is moving faster than the rate of information transfer. The gas flow has no 'knowledge' of the boundary conditions downstream (i.e. the background pressure P_b) and overexpands. This leads to the formation of a series of shock waves; very thin nonisentropic regions characterised by large density, temperature, pressure and velocity gradients. The formation of shock waves provides a mechanism for slowing the supersonic flow and reducing the Mach number to subsonic values so that the flow can adjust to downstream boundary conditions. The structure of a supersonic expansion is shown in Figure 4.1. There are two sections to the shock wave system; the Mach disk shock normal to the beam axis, and the barrel shock which is cylindrically symmetrical about the beam axis. The isentropic region in the centre is known as the 'zone of silence'. As the gas continues to expand the collision frequency in this region drops to zero, freezing the internal energy and velocity distributions of the beam gas at much lower characteristic temperatures than the stagnation temperature T_0

Skimmers

In order to extract a molecular beam from the expansion a skimmer is placed on axis with its tip sampling the zone of silence. The position of the skimmer is important. If it is placed too far from the nozzle the turbulence of the Mach disk and barrel shock waves will disrupt

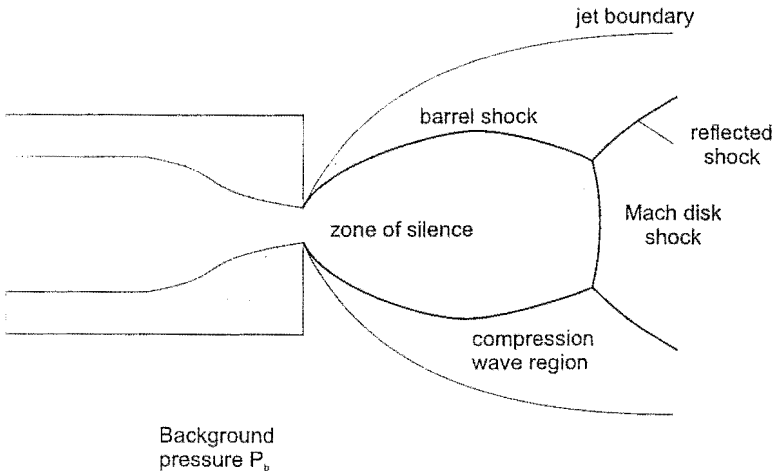

Figure 4.1: Structure of a supersonic expansion.

the flow of the beam. The position x_M of the Mach disk, measured in nozzle diameters d, has been found empirically[116] to be given by

$$\frac{x_M}{d} = 0.67 \left(\frac{P_0}{P_b} \right)^{1/2} \tag{4.8}$$

The tip of the skimmer must therefore be closer to the nozzle than this distance. However, if skimmer is too close to the nozzle it will act as a virtual source and produce an effusive beam. In order to obtain an ideal beam, which has high intensity, a high velocity along the axis, and a small velocity spread, the skimmer must be designed so that it disturbs the beam as little as possible. In practice, this means that the following requirements must be met[117]

1. The edges of the skimmer orifice should be as sharp as possible.

2. There should be a small exterior angle at the orifice to ensure the shock wave is 'attached'.

3. The interior angle should be large to prevent scattering of beam molecules by molecules reflected from the skimmer surface.

The region of the expansion sampled by the skimmer is essentially collision free* and the beam which is formed exhibits the characteristics of free molecular flow.

* There is still a small probability of collisions due to the width of the (narrow) velocity distribution of the molecules in the beam

Beam characteristics

While it is not possible to derive the complete velocity distribution for a supersonic beam from first principles, several important properties can be determined from simple thermodynamic considerations if the expanding gas is assumed to be ideal.

During the supersonic expansion process the total enthalpy of the gas inside the source is converted into translational kinetic energy of the beam, so that the maximum possible kinetic energy, corresponding to the case in which all the enthalpy of the gas inside the nozzle is converted to translational energy, is given by

$$\frac{1}{2}mu_{\max}^2 = H_0 = \int_{T_f}^{T_0} C_p dT \tag{4.9}$$

where H_0 and T_0 are the total enthalpy and temperature of the gas inside the source, and T_f is the final temperature of the beam. Assuming that the heat capacity C_p is independent of temperature over this range, so that $C_p = \frac{\gamma k}{\gamma - 1}$, and that the final beam temperature is very low, so that $T_0 - T_f \approx T_0$, then the maximum or terminal velocity of the beam is

$$u_{\max} = \left(\frac{2kT_0}{m}\frac{\gamma}{\gamma - 1}\right)^{1/2} \tag{4.10}$$

This expression has been found to accurately agree with experiment in most cases. Exceptions occur when the approximations made in the derivation are not valid, such as in the case of NO, for which the heat capacity varies markedly with temperature over the range of interest. In these cases the integration in Equation 4.9 must be carried out in full.

A molecular beam is often characterised in terms of the parameters α, S and M.[113]

$$\begin{aligned} \alpha &= \left(\frac{2kT}{m}\right)^{1/2} \\ S &= \frac{u}{\alpha} > 1 \\ M &= \frac{u}{(\gamma kT/m)^{1/2}} = \left(\frac{2}{\gamma}\right)^{1/2} S \end{aligned} \tag{4.11}$$

in which u is the mean flow velocity of the beam. The quantity α is the most probable random velocity in the beam, and gives a measure of the width of the speed distribution in the beam. The speed ratio S is an indication of the degree of monochromaticity in the beam, and the Mach number M, mentioned previously, is the ratio of the beam velocity to the local speed of sound. Once the Mach number is known, several thermodynamic variables of the free jet may be calculated.[114] Using the definition of M and Equation 4.9 leads to an expression for

the ratio of the beam temperature to the source temperature.

$$\frac{T}{T_0} = \left(1 + \frac{\gamma - 1}{2} M^2\right)^{-1} \tag{4.12}$$

The beam velocity can then be written in terms of M as

$$u = M \left(\frac{\gamma k T_0}{m}\right)^{1/2} \left(1 + \frac{\gamma - 1}{2} M^2\right)^{-1/2} \tag{4.13}$$

The ratio of the pressure in the beam to that inside the source is given by

$$\frac{P}{P_0} = \left(\frac{T}{T_0}\right)^{\gamma/(\gamma-1)} = \left(1 + \frac{\gamma - 1}{2} M^2\right)^{-\gamma/(\gamma-1)} \tag{4.14}$$

The velocity distribution of particles within a supersonic molecular beam cannot be directly calculated as it can for an effusive beam. However, it has been found that the distribution can be fitted well by a three dimensional Maxwell–Boltzmann type distribution centred on the mean flow velocity u

$$f(v) = N \left(\frac{v}{\alpha}\right)^2 \exp\left(\frac{-(v-u)^2}{\alpha^2}\right) \tag{4.15}$$

where N is a normalisation coefficient. The mean flow velocity u and mean random velocity α may be determined by fitting Equation 4.15 to time of flight data from pulsed molecular beam experiments.[110]

Seeded beams

From Equation 4.10 it is seen that the velocity of a molecular beam depends on the mass and heat capacity of the beam gas, so that for a given species there is a characteristic beam velocity. In many scattering experiments it is important to be able to control the energy of the reagents in order to set the collision energy for the scattering process under study. This requires a method for controlling the velocity of the beam. In an effusive beam, the velocity can be altered to a certain extent by heating or cooling the gas in the source, though in practice a rotating drum or toothed wheel is used. In a supersonic beam velocity control is generally achieved by seeding. If a mixture of gases is expanded through a supersonic nozzle the final velocity of the beam is determined by the *average* mass and heat capacity of the gases in the mixture. Equations 4.12 to 4.14 can still be used with the appropriate mean values $\bar{m}$ and $\bar{\gamma}$. Seeding a molecule of molecular mass m into a carrier gas with a molecular mass greater than m results in a lower flow velocity than that for a pure beam, while seeding

into a lighter gas gives a higher velocity. The ratio of seed to carrier gas can be altered to give beam velocities which span the range between the terminal velocities of the seed and carrier gas.

4.2 Rotation of symmetric top molecules

A symmetric top molecule has equal moments of inertia about two of its three principle axes. The moments of inertia about the two equal axes, I_x and I_y, are usually both designated I_B, while I_z is labelled either I_A or I_C depending on whether it is smaller or larger than I_B. If I_z is smaller than I_B, as in the case of CH_3Cl, the molecule is a prolate symmetric top. If it is larger, as for $CHCl_3$, the molecule is an oblate symmetric top.

A symmetric top molecule possesses a permanent electric dipole moment. This can be utilised for state selection and orientation of these molecules in the presence of an electric field through the first order Stark effect.

The Stark energy of a dipolar molecule is defined as the interaction energy between the molecular electric dipole μ and an applied electric field $\mathbf{E}$, and is given by the projection of the dipole onto the electric field.

$$W = -\mu \cdot \mathbf{E} = -\mu E \cos\theta \tag{4.16}$$

in which θ is the angle between the electric field vector and the molecular dipole. The negative sign reflects the fact that an electric dipole vector is defined to point towards the positive end of the dipole, while an electric field vector points towards decreasing field.

For convenience, two reference frames are defined. The first is a laboratory (lab) frame comprising a set of 'space fixed' axes XYZ, in which the Z axis is parallel to the electric field direction. The second is a 'moving' frame defined by a set of 'molecule fixed' axes xyz, in which the z axis lies parallel to the molecular symmetry axis.

4.2.1 The rotational Hamiltonian

The kinetic energy of a symmetric top molecule rotating about a fixed point in space is,

$$\begin{aligned} E_{\text{rot}} &= \frac{J_x^2}{2I_A} + \frac{J_y^2}{2I_B} + \frac{J_z^2}{2I_C} \\ &= \frac{1}{2I_B}(J_x^2 + J_y^2) + \frac{J_z^2}{2I_C} \end{aligned} \tag{4.17}$$

where $I_B = I_x = I_y$ and $I_C = I_z$ are the moments of inertia perpendicular and parallel to the molecular axis, and J_x, J_y and J_z are the angular momenta about the molecular axes.

In order to reference these angular momenta back to the lab frame, Euler's angles θ, ϕ and χ are introduced. θ and ϕ are the usual polar angles describing the orientation of the molecular z axis in the lab frame coordinate system, while χ is the angle of rotation about the molecular axis. The rotations required to map XYZ onto xyz, as shown in Figure 4.2, are:

1. $\phi\mathbf{Z}^\dagger$ maps (X, Y, Z) onto (X', Y', Z)
2. $\theta\mathbf{Y}'$ maps (X', Y', Z) onto (X'', Y', z)
3. $\chi\mathbf{z}$ maps (X'', Y', z) onto (x, y, z)

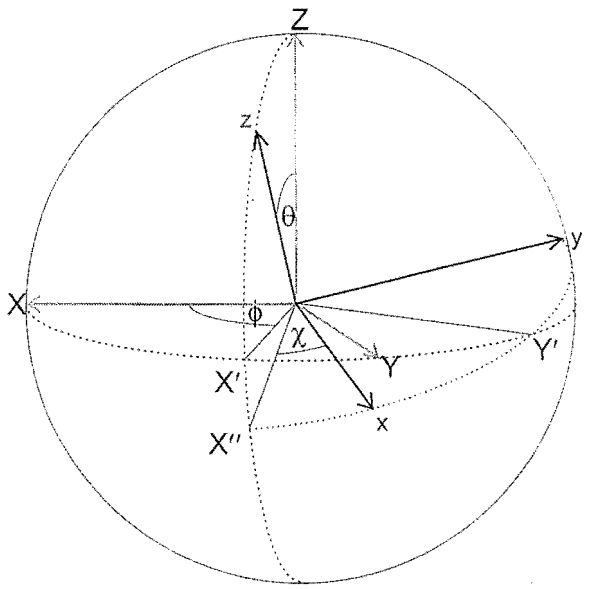

Figure 4.2: Euler's angles relating the set of molecule fixed axes xyz to a set of space fixed axes XYZ for a symmetric top molecule

In order to obtain the rotational Hamiltonian for the system, the angular momentum operators $\hat{J}_x$, $\hat{J}_y$ and $\hat{J}_z$ must be determined. The operator corresponding to the component of the total angular momentum along a given axis[118] is $-i\hbar\frac{\partial}{\partial\phi}$, where ϕ is the angle of rotation about the axis. Euler's angles involve rotations by angles ϕ, θ and χ about the Z, Y' and z axes respectively. The operators for the components of the total angular momentum

† $\phi\mathbf{Z}$ indicates a rotation by angle ϕ about the Z axis.

lying along these three axes are therefore

$$\hat{J}_Z = -i\hbar\frac{\partial}{\partial\phi} \qquad \hat{J}_{Y'} = -i\hbar\frac{\partial}{\partial\theta} \qquad \hat{J}_z = -i\hbar\frac{\partial}{\partial\chi} \tag{4.18}$$

Expressions must now be found which relate the molecule fixed angular momentum operators $\hat{J}_x$, $\hat{J}_y$ and $\hat{J}_z$ to the operators defined in Equation 4.18. $\hat{J}_z$ is given directly by the above equation, while the remaining two operators may be obtained as follows:

By definition, $J_{Y'}$ is the scalar product of the total angular momentum $\mathbf{J}$ and a unit vector $\mathbf{e_{Y'}}$ lying along the Y' axis.

$$J_{Y'} = \mathbf{e_{Y'}} \cdot \mathbf{J} \tag{4.19}$$

If we write $\mathbf{J}$ as

$$\mathbf{J} = \mathbf{e_x}J_x + \mathbf{e_y}J_y + \mathbf{e_z}J_z \tag{4.20}$$

in which $\mathbf{e_x}$, $\mathbf{e_y}$ and $\mathbf{e_z}$ are unit vectors along the x, y and z axes, $J_{Y'}$ becomes

$$J_{Y'} = (\mathbf{e_{Y'}} \cdot \mathbf{e_x})J_x + (\mathbf{e_{Y'}} \cdot \mathbf{e_y})J_y + (\mathbf{e_{Y'}} \cdot \mathbf{e_z})J_z \tag{4.21}$$

Each of the scalar products in the above equation is simply the cosine of the angle between the two unit vectors involved. These angles are easily determined from Figure 4.2, and the resulting scalar products are:

$$\begin{aligned} \mathbf{e_{Y'}} \cdot \mathbf{e_x} &= \cos(\frac{\pi}{2} - \chi) = \sin\chi \\ \mathbf{e_{Y'}} \cdot \mathbf{e_y} &= \cos\chi \\ \mathbf{e_{Y'}} \cdot \mathbf{e_z} &= 0 \end{aligned}$$

Substituting these values into Equation 4.21 gives

$$J_{Y'} = (\sin\chi)J_x + (\cos\chi)J_y \tag{4.22}$$

The component of angular momentum along the Z axis, J_Z, may be determined as a sum of scalar products in the same way. The analagous expression to Equation 4.21 is

$$J_Z = (\mathbf{e_Z} \cdot \mathbf{e_x})J_x + (\mathbf{e_Z} \cdot \mathbf{e_y})J_y + (\mathbf{e_Z} \cdot \mathbf{e_z})J_z \tag{4.23}$$

From Figure 4.2 it can be seen that[‡]

$$\begin{aligned} \mathbf{e_Z} \cdot \mathbf{e_x} &= (\mathbf{e_Z} \cdot \mathbf{e_{X''}}) \cos\chi = -\sin\theta\cos\phi \\ \mathbf{e_Z} \cdot \mathbf{e_y} &= -(\mathbf{e_Z} \cdot \mathbf{e_{X''}}) \sin\chi = \sin\theta\sin\phi \\ \mathbf{e_Z} \cdot \mathbf{e_z} &= \cos\theta \end{aligned} \tag{4.24}$$

Substitution of Equations 4.24 into Equation 4.23 leads to

$$J_Z = -(\sin\theta\cos\chi)J_z + (\sin\theta\sin\chi)J_y + (\cos\theta)J_z \tag{4.25}$$

Equations 4.22 and 4.25 can now be solved simultaneously to obtain J_x and J_y as functions of J_Z, $J_{Y'}$ and J_z, yielding

$$\begin{aligned} J_x &= -\cos\chi\csc\theta J_Z + \sin\chi J_{Y'} + \cos\chi\cot\theta J_z \\ J_y &= \sin\chi\csc\theta J_Z + \cos\chi J_{Y'} - \sin\chi\cot\theta J_z \end{aligned} \tag{4.26}$$

Substituting the operator forms of J_Z, $J_{Y'}$ and J_z from Equation 4.18 into the above expressions for J_x and J_y leads to expressions for the angular momentum operators $\hat{J}_x$, $\hat{J}_y$ and $\hat{J}_z$ in terms of the Euler angles θ, ϕ and χ.

$$\begin{aligned} \hat{J}_x &= -i\hbar\left(-\cos\chi\csc\theta\frac{\partial}{\partial\phi} + \sin\chi\frac{\partial}{\partial\theta} + \cos\chi\cot\theta\frac{\partial}{\partial\chi}\right) \\ \hat{J}_y &= -i\hbar\left(\sin\chi\csc\theta\frac{\partial}{\partial\phi} + \cos\chi\frac{\partial}{\partial\theta} - \sin\chi\cot\theta\frac{\partial}{\partial\chi}\right) \\ \hat{J}_z &= -i\hbar\frac{\partial}{\partial\chi} \end{aligned} \tag{4.27}$$

Equation 4.17, describing the classical rotational kinetic energy of a symmetric top molecule, can now be used with the above operators to determine the Hamiltonian for the system. The rotational Hamiltonian will involve the squares of the angular momentum operators defined

[‡] In Equations 4.23 $\mathbf{e_Z} \cdot \mathbf{e_{X''}}$ was found by projecting $\mathbf{e_Z}$ onto the negative X'' axis:

$$\mathbf{e_Z} \cdot \mathbf{e_{X''}} = -\cos\left(\frac{\pi}{2} - \theta\right) = -\sin\theta$$

in Equation 4.27, namely:

$$\begin{aligned}
\hat{J}_x^2 &= -\hbar^2 \Big[\sin^2\chi\frac{\partial^2}{\partial\theta^2} + \cos^2\chi\csc^2\theta\frac{\partial^2}{\partial\phi^2} + \cos^2\chi\cot^2\theta\frac{\partial^2}{\partial\chi^2} \\
&\quad -2\sin\chi\cos\chi\csc\theta\frac{\partial^2}{\partial\theta\partial\phi} + 2\sin\chi\cos\chi\cot\theta\frac{\partial^2}{\partial\theta\partial\chi} - 2\cos^2\chi\csc\theta\cot\theta\frac{\partial^2}{\partial\phi\partial\chi} \\
&\quad +\cos^2\chi\cot\theta\frac{\partial}{\partial\theta} + 2\sin\chi\cos\chi\cot\theta\csc\theta\frac{\partial}{\partial\phi} - \sin\chi\cos\chi(1+2\cot^2\theta)\frac{\partial}{\partial\chi} \Big] \\
\hat{J}_y^2 &= -\hbar^2 \Big[\cos^2\chi\frac{\partial^2}{\partial\theta^2} + \sin^2\chi\csc^2\theta\frac{\partial^2}{\partial\phi^2} + \sin^2\chi\cot^2\theta\frac{\partial^2}{\partial\chi^2} \\
&\quad +2\sin\chi\cos\chi\csc\theta\frac{\partial^2}{\partial\theta\partial\phi} - 2\sin\chi\cos\chi\cot\theta\frac{\partial^2}{\partial\theta\partial\chi} - 2\sin^2\chi\csc\theta\cot\theta\frac{\partial^2}{\partial\phi\partial\chi} \\
&\quad +\sin^2\chi\cot\theta\frac{\partial}{\partial\theta} - 2\sin\chi\cos\chi\cot\theta\csc\theta\frac{\partial}{\partial\phi} + \sin\chi\cos\chi(1+2\cot^2\theta)\frac{\partial}{\partial\chi} \Big] \\
\hat{J}_z^2 &= -\hbar^2\frac{\partial^2}{\partial\chi^2}
\end{aligned} \tag{4.28}$$

The Hamiltonian is then given by:

$$\begin{aligned}
\hat{H} &= \frac{1}{2I_B}(\hat{J}_x^2 + \hat{J}_y^2) + \frac{1}{2I_C}\hat{J}_z^2 \qquad (4.29)\\
&= -\frac{\hbar^2}{2I_B}\left[\frac{\partial^2}{\partial\theta^2} + \csc^2\theta\frac{\partial^2}{\partial\phi^2} + \cot^2\theta\frac{\partial^2}{\partial\chi^2} - 2\cot\theta\csc\theta\frac{\partial^2}{\partial\phi\partial\chi} + \cot\theta\frac{\partial}{\partial\theta}\right] - \frac{\hbar^2}{2I_C}\frac{\partial^2}{\partial\chi^2} \\
&= -\frac{\hbar^2}{2I_B}\left[\frac{\partial^2}{\partial\theta^2} + \cot\theta\frac{\partial}{\partial\theta} + \csc^2\theta\frac{\partial^2}{\partial\phi^2} + (\frac{I_B}{I_C} + \cot^2\theta)\frac{\partial^2}{\partial\chi^2} - 2\cot\theta\csc\theta\frac{\partial^2}{\partial\phi\partial\chi}\right] \\
&= -\frac{\hbar^2}{2I_B}\left[\frac{1}{\sin\theta}\frac{\partial}{\partial\theta}\left(\sin\theta\frac{\partial}{\partial\theta}\right) + \csc^2\theta\frac{\partial^2}{\partial\phi^2} + (\frac{I_B}{I_C} + \cot^2\theta)\frac{\partial^2}{\partial\chi^2} - 2\cot\theta\csc\theta\frac{\partial^2}{\partial\phi\partial\chi}\right]
\end{aligned}$$

The solution of the Schrodinger equation for a freely rotating symmetric top is outlined in Appendix B. In the absence of an electric field the energy levels are given by

$$\frac{E_0}{h} = BJ(J+1) + (C-B)K^2 \tag{4.30}$$

in which

$$J = k_{\max} + \frac{1}{2}|K + M_J| + \frac{1}{2}|K - M_J| \tag{4.31}$$

It can be shown that $J(J+1)\hbar$ is the square of the total angular momentum, $\hbar K$ is its projection on the molecular axis z, and $\hbar M_J$ its projection on the space fixed axis Z. The parameter $k_{\max}$ is defined in Appendix B. As illustrated in Figure 4.3, the motion of a quantum mechanical symmetric top is precessional, in analogy to its classical counterpart. The molecule fixed axis precesses about the total angular momentum vector **J** at an angle defined by the quantum number K. The precessional motion of **J** around the space fixed Z axis is described by the quantum number M_J.

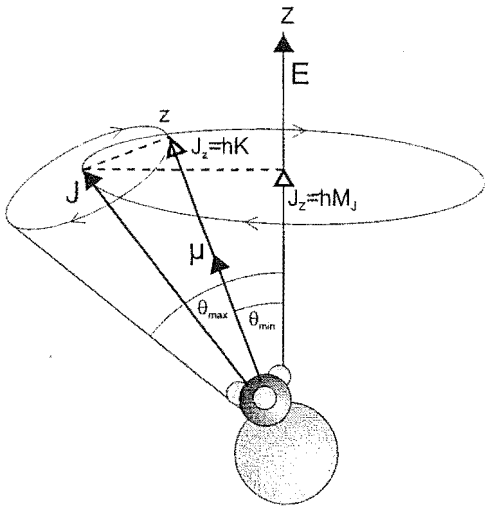

Figure 4.3: Precessional motion of a symmetric top molecule.

When a symmetric top molecule is subjected to an electric field, the Hamiltonian $\hat{H}_0$, given by Equation 4.30, is modified by the interaction of the molecular dipole with the electric field by an amount corresponding to the first order Stark energy W_1.

$$\hat{H} = \hat{H}_0 - \mu E cos\theta \tag{4.32}$$

The coordinate system is chosen such that the electric field lies along the space fixed axis Z. The Stark energy represents a fairly small alteration to the zero field rotational energy and consequently first order perturbation theory can be used to obtain the correction to the zero order energy. This correction is given by[119]

$$\begin{aligned} W_1 &= \langle\psi_0|\mu E\cos\theta|\psi_0\rangle \\ &= -\mu E\frac{KM_J}{J(J+1)} \\ &= -\mu E\langle\cos\theta\rangle \end{aligned} \tag{4.33}$$

where ψ_0 are the zeroth order wavefunctions described in Appendix B and $\langle\cos\theta\rangle$ is the average of $\cos\theta$ over the precessional motion about **J**.

If the product KM_J is greater than zero the energy of the state is decreased relative to the field free case. These states are termed lower Stark states and are attracted to regions of high electric field. Conversely, if KM_J is less than zero the energy is increased relative to the field free case, the molecule is in an upper Stark state and is repelled by an electric field. If KM_J is equal to zero the Stark energy is zero and an electric field has no effect on the

symmetric top molecule. The fact that upper and lower Stark states undergo very different trajectories in an electric field due to their differing Stark energies forms the basis for the technique of hexapole state selection of symmetric top molecules.

4.3 Trajectories of symmetric top molecules through a hexapole electrostatic field - upper Stark state selection

A hexapole consists of a set of six rods arranged at the points of a regular hexagon. The hexapole field is generated by application of positive and negative voltages to alternate rods. As is the case for quadrupoles, octapoles, and any generalised 2n-pole, an ideal hexapole field is generated when the rods are of hyperbolic cross section. However, the difficulties implicit in machining hyperbolic rods means that they are rarely used in practice, and a hexapole is usually composed of 6 circular rods evenly spaced on an inscribed radius r_0 as shown in Figure 4.4. If the inscribed radius is chosen so that the curvature of the circular rods is a close approximation to that of hyperbolic rods at r_0 then the electric field produced inside the hexapole will be very close to that of the ideal case.

In order to determine the trajectory followed by a symmetric top molecule as it traverses the hexapole field, it is necessary to set up and solve the relevant equations of motion for the system. The first step is to determine the Stark energy of a symmetric top in the hexapole field.

The electric potential of the (ideal) hexapole field in cylindrical coordinates[§] (r, ϕ, d) is

$$V(r,\phi) = V_0 \left(\frac{r}{r_0}\right)^3 \cos 3\phi \tag{4.34}$$

where V_0 is the magnitude of the voltage applied to the rods. The electric field is therefore

$$\begin{aligned} \mathbf{E} &= -\nabla V \\ &= -\left(\frac{\partial}{\partial r}\,\mathbf{e_r} + \frac{\partial}{\partial \phi}\,\mathbf{e}_\phi + \frac{\partial}{\partial z}\,\mathbf{e_z}\right) V(r,\phi) \\ &= 3V_0 \frac{r^2}{r^3} \cos 3\phi\ \mathbf{e_r} - 3V_0 \left(\frac{r}{r_0}\right)^3 \sin 3\phi\ \mathbf{e}_\phi \end{aligned} \tag{4.35}$$

where $(\mathbf{e_r}, \mathbf{e}_\phi, \mathbf{e_z})$ are the unit vectors associated with the cylindrical coordinates r,ϕ and z. The magnitude of the electric field is simply

$$E = \sqrt{\mathbf{E}\cdot\mathbf{E}} = 3V_0 \frac{r^2}{r_0^3} \tag{4.36}$$

[§] (r, ϕ) are the usual polar coordinates as shown in Figure 4.4. d is the distance along the hexapole

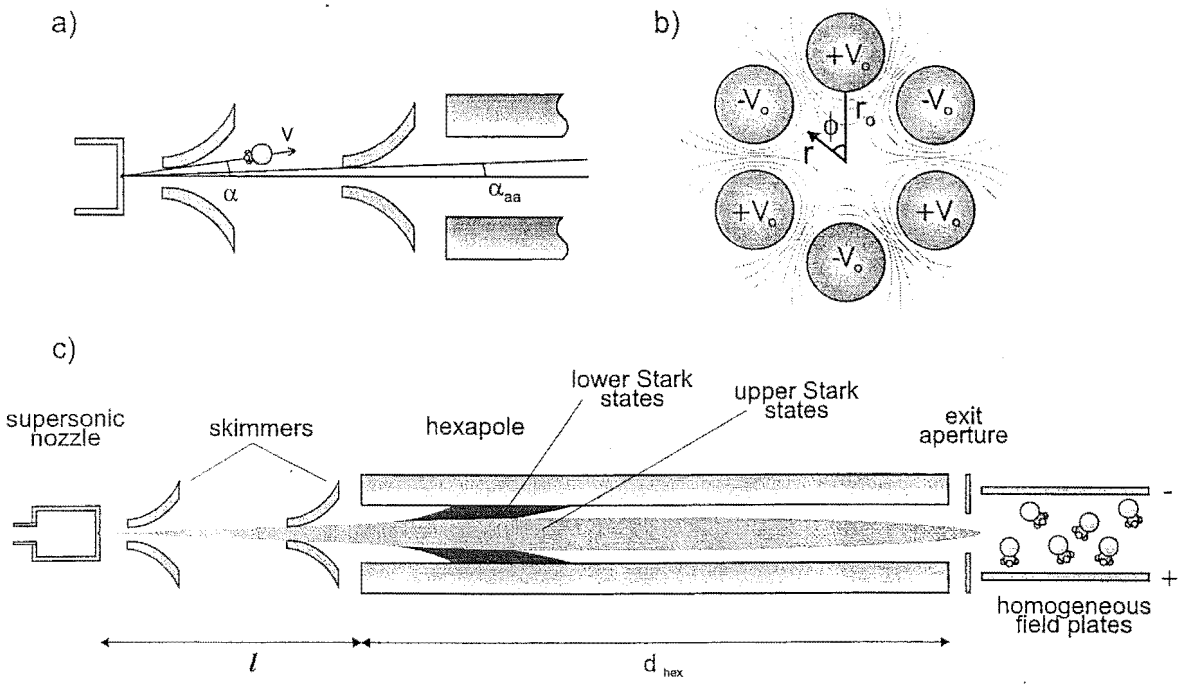

Figure 4.4: a) The hexapole entrance: nozzle exit angle and velocity and hexapole acceptance angle defined by second skimmer are shown; b) Cross section through the hexapole showing electric field lines, inscribed radius r_0 and polar coordinates (r, ϕ); c) Experimental setup required for the preparation of state selected spatially oriented molecular beams.

and the first order Stark energy is therefore

$$\begin{aligned} W_1 &= -\mu E \langle \cos\theta \rangle \\ &= -3\mu V_0 \frac{r^2}{r_0^3} \frac{KM_J}{J(J+1)} \end{aligned} \tag{4.37}$$

It is now straightforward to set up the radial equation of motion for the system. The radial force exerted on the dipole by the hexapole field is

$$\begin{aligned} F_r = m\ddot{r} &= -\frac{\partial W_1}{\partial r} \\ &= -6\frac{\mu V_0}{r_0^3} \frac{KM_J}{J(J+1)} r \end{aligned} \tag{4.38}$$

where $\ddot{r}$ represents the second derivative of r with respect to time. The equation of motion is then

$$\ddot{r} + 6\frac{\mu V_0}{m r_0^3} \frac{KM_J}{J(J+1)} r = 0 \tag{4.39}$$

This falls into a well known class of second order differential equation. There are three classes of solution, depending on whether KM_J is positive, negative or zero. For the case

where KM_J is positive (lower Stark states) the general solution is

$$r(t) = Ae^{\omega t} + Be^{-\omega t} \tag{4.40}$$

where A and B are constants, and

$$\omega = \left(\frac{6V_0\mu}{mr_0^3} \frac{|KM_J|}{J(J+1)} \right)^{1/2} \tag{4.41}$$

is the angular velocity of the trajectory. These trajectories are divergent and will be lost from the beam via collisions with the hexapole rods. When KM_J is zero the hexapole field has no effect on the molecular dipoles since they are perpendicular to the field, and the molecules follow straight line trajectories through the hexapole:

$$r(t) = At + B \tag{4.42}$$

For the case where KM_J is negative (upper Stark states) the general solution is

$$r(t) = A\sin(\omega t) + B\cos(\omega t) \tag{4.43}$$

In this case ω is the angular frequency of the sinusoidal trajectory followed by the molecule as it passes through the hexapole. Upper Stark state molecules undergo simple harmonic motion in the hexapole field and are focused onto the hexapole axis at some point in the trajectory. This forms the basis of rotational state selection using a hexapole field and will be discussed in more detail in section 4.5

The hexapole therefore acts to filter out lower Stark states from the beam, allowing only states for which $KM_J \leq 0$ to pass through the rods. It is fairly straightforward to determine the value of the constants A and B in terms of the nozzle exit angle α, the nozzle exit velocity v, and the distance l from the nozzle to the second skimmer, which defines the entrance to the hexapole. These parameters are shown in Figure 4.4

Time $t = 0$ is defined as the instant at which the molecule enters the hexapole. At this instant the radial displacement from the centre of the hexapole is

$$r(0) = l\tan\alpha \approx l\alpha \tag{4.44}$$

The approximation $\tan\alpha = \alpha$ is valid since the nozzle exit angle α is very small (of the order of 0.25 degrees). The radial velocity at $t = 0$ is

$$\dot{r}(0) = v\sin\alpha \approx v\alpha \tag{4.45}$$

In order to find the constants A and B for each of the three cases (KM_J positive, negative and zero) these values are substituted into the general solutions and their derivatives. For upper Stark state molecules Equation 4.43 gives:

$$\begin{aligned} r(0) &= B = l\alpha \\ \dot{r}(0) &= A\omega = v\alpha \end{aligned} \tag{4.46}$$

The full solution for the convergent trajectory of an upper Stark state molecule through the hexapole is therefore:

$$r(t) = l\alpha \cos(\omega t) + \frac{v\alpha}{\omega} \sin(\omega t) \tag{4.47}$$

For an $KM_J = 0$ state the solution is

$$r(t) = (vt + l)\alpha \tag{4.48}$$

and for a lower Stark state or divergent trajectory

$$r(t) = \frac{\alpha}{2}\left[(l + \frac{v}{\omega})\ e^{\omega t} + (l - \frac{v}{\omega})\ e^{-\omega t}\right] \tag{4.49}$$

The fraction of lower Stark state molecules which are successfully transmitted through the hexapole is small and these states will not be included in the following discussion. The $KM_J = 0$ states are not affected by the hexapole field and simply add a constant background to any observed upper Stark state focusing effect. The fraction of $KM_J = 0$ states which survive the entire trajectory through the hexapole will be fairly small, since unless the nozzle exit angle α is very close to zero the trajectories of these molecules will diverge to a radial displacement exceeding the hexapole exit aperture and they will not be transmitted. Effectively only those molecules travelling along the hexapole axis will exit, and it is fairly simple to remove these remaining molecules from the beam by placing a beam stop at some point along the hexapole axis[¶]. Any molecules travelling along the axis will then collide with the beam stop and be lost from the beam. The diameter of the beam stop is critical, since it must be able to quench the $KM_J = 0$ states, while having little effect on the transmission probability of the focusing upper Stark state molecules. With a beam stop in place, a beam containing essentially only upper Stark states is transmitted by the hexapole.

[¶] In addition to removing $M = 0$ states from the beam, beam stops are also commonly used to remove harmonics from the beam. To remove the first harmonic a beam stop is required at the halfway point along the hexapole field. To remove the second harmonic requires a beamstop a third of the way along etc.

4.4 Conditions for successful transmission through the hexapole

It has already been shown that for the most part only upper Stark states can successfully traverse a hexapole field. However, within this category there are several geometrical conditions which must be satisfied:

1. The molecule must enter the hexapole. This requires that the nozzle exit angle α is less than the acceptance angle $\alpha_{\rm aa}$ defined by the size of the aperture in the second skimmer. In addition to this constraint on the maximum value for α, there will also be a constraint on the minimum allowed angle if a beam stop is present at the beginning of the hexapole . In this case the entrance condition is $\alpha_{\rm bs} < \alpha < \alpha_{\rm aa}$.

2. The radial displacement of the molecule must not exceed the inscribed radius of the hexapole at any point along its trajectory. This condition also places a constraint on α. At the point of maximum displacement along the trajectory the radial velocity is zero. From Equation 4.47,

$$\begin{aligned} \dot{r}(t) &= -l\alpha\omega\sin(\omega t) + v\alpha\cos(\omega t) = 0 \\ &\Rightarrow \quad \omega t = \tan^{-1}(\frac{v}{\omega l}) \end{aligned} \tag{4.50}$$

   In order to find the range of α for which the trajectories stay within the inscribed radius of the hexapole, the above expression is substituted back into Equation 4.47 with $r(t)$ set to r_0, and the resulting equation is solved for α

$$\begin{aligned} r_0 &= l\alpha\cos(\tan^{-1}(v/\omega l)) + \frac{v\alpha}{\omega}\sin(\tan^{-1}(\frac{v}{\omega l})) \\ &= l\alpha\frac{1}{(1+(v/\omega l)^2)^{1/2}} + \frac{v\alpha}{\omega}\frac{v/\omega l}{(1+(v/\omega l)^2)^{1/2}} \\ &= \frac{v\alpha}{\omega}\left(\frac{\omega^2 l^2}{v^2}+1\right)^{1/2} \\ &\Rightarrow \quad \alpha_{\rm trans} = \frac{\omega r_0}{v}\left(\frac{v^2}{\omega^2 l^2 + v^2}\right)^{1/2} \end{aligned} \tag{4.51}$$

   The angle $\alpha_{\rm trans}$ represents the maximum nozzle exit angle for which an upper Stark state molecule can be successfully transmitted through the hexapole rods.

3. The molecule must exit the hexapole i.e. the radial displacement at the end of the hexapole must be less than the radius of the exit aperture $r_{\rm ea}$. This can also be rephrased in terms of a limit on the nozzle exit angle α. The molecule will exit the hexapole at a

time $t_{\text{exit}} = l_{\text{hex}}/v$, where l_{hex} is the length of the hexapole. The maximum angle α_{ea} satisfying the above condition is found from

$$\begin{aligned} r_{\text{ea}} &= l\alpha\cos\left(\frac{\omega l_{\text{hex}}}{v}\right) + \frac{v}{\omega}\sin\left(\frac{\omega l_{\text{hex}}}{v}\right) \\ \Rightarrow \quad \alpha_{\text{ea}} &= \frac{r_{\text{ea}}}{l\cos\left(\omega l_{\text{hex}}/v\right) + \frac{v}{\omega}\sin\left(\omega l_{\text{hex}}/v\right)} \end{aligned} \tag{4.52}$$

From these three conditions it is seen that the maximum angle α_{max} at which a molecule can leave the nozzle and still survive a trajectory through the hexapole is the smaller of the three angles α_{aa}, α_{traj} and α_{ea}.

Molecules leaving the nozzle at a given angle α and velocity v can be projected onto a circle of radius $l\tan\alpha \approx l\alpha$ at the hexapole entrance. Assuming the angular distribution of beam molecules near the hexapole axis is uniform, the number of molecules reaching the entrance to the hexapole at any given angle α is proportional to the circumference of this circle.

$$P(\alpha) \propto \pi l^2\alpha^2 \tag{4.53}$$

The fraction of molecules entering the hexapole which are successfully transmitted is therefore

$$A(V_0, v, \rho) = \frac{\pi l^2\alpha_{\text{max}}^2}{\pi l^2\alpha_{\text{aa}}^2} = \frac{\alpha_{\text{max}}^2}{\alpha_{\text{aa}}^2} \tag{4.54}$$

where $\rho = \cos\theta$. The probability of transmitting a given $|JKM_J>$ state is found by integrating $A(V_0, v, \rho)$ over the velocity distribution $f(v)$ of the molecules in the beam (given in Equation 4.15)

$$P_{JKM_J}(V_0) = \int_0^\infty A(V_0, v, \rho) f(v) dv \tag{4.55}$$

The total transmission at a given hexapole voltage is then

$$T(V_0) = \sum_{JKM_J} P_{JKM_J}(V_0) f_{JK} \tag{4.56}$$

where f_{JK} is the fraction of molecules in state $|JK>$.

$$f_{JK} = \frac{S(I,K)(2J+1)e^{-W_0/kT_{\text{rot}}}}{\sum_{J=0}^{\infty}\sum_{K=-J}^{J} S(I,K)(2J+1)e^{-W_0/kT_{\text{rot}}}} \tag{4.57}$$

In the above equation W_0 is the rotational energy in the absence of an applied electric field and the $S(I,K)$ are the statistical weighting factors or degeneracies for the states due to nuclear spin.[120] These weighting factors are given in Table 4.1.

Table 4.1: Statistical weighting factors for symmetric top molecules. n is an integer.

$K = 0$	$S(I,K) = 4I^2 + 4I + 3$
$K = 3n$	$S(I,K) = 2(4I^2 + 4I + 3)$
$K \neq 3n$	$S(I,K) = 2(4I^2 + 4I)$

4.5 Selection of $|JKM_J>$ states

The frequency of the sinusoidal oscillation of an upper Stark state molecule passing through a hexapole depends on both its rotational state and the hexapole voltage. Consequently, in addition to filtering out lower Stark state molecules, the hexapole can also be used to preferentially focus specific rotational states. The period of a complete oscillation is $2\pi/\omega$. Since a molecule will focus back to the axis in half a complete oscillation the distance d along the hexapole axis at which it focuses is given by

$$d = vt_{\text{foc}} = \frac{v\pi}{\omega} \tag{4.58}$$

Substituting Equation 4.41 for ω and rearranging gives the voltage at which a particular $|JKM_J>$ state will focus at a given distance along the hexapole field.

$$V_{\text{foc}}(\rho, d) = \frac{\pi^2 r_0^3 m v^2}{6\mu d^2 \rho} \tag{4.59}$$

If d in the above equation is set to the length of the hexapole the desired state will be focused onto the exit aperture at the voltage V_{foc}, and in the ideal case of the aperture being small enough to prevent non-focused states from passing through, the beam which leaves the hexapole will consist of molecules in a single $|JKM_J>$ state. In practice, since a decrease in the size of the exit aperture is accompanied by a considerable reduction in beam signal, the resolving power of the hexapole for individual states must be compromised in order to retain acceptable signal levels. Usually this means that other states with a similar focal length will also be transmitted by the hexapole, though the selected state will dominate the transmitted beam. It is also possible to select various harmonics of the fundamental frequency of the sinusoidal trajectories by setting d to the appropriate fraction of the hexapole length ($d_{\text{hex}}/2$ for the first harmonic, $d_{\text{hex}}/3$ for the second harmonic and so on) when calculating the focusing voltage.

4.6 Orientation

As described above, the molecules in the molecular beam transmitted by the hexapole are all in upper Stark states. They are aligned with their dipoles opposing the applied electric field, but they are not yet oriented in space since the hexapole field is inhomogeneous. In order to spatially orient the beam it is allowed to pass adiabatically into a region of weak homogeneous electric field maintained between a pair of parallel plates positioned directly after the hexapole. As the beam leaves the hexapole the molecular dipoles rotate in space to line up against the new homogeneous field and orientation is achieved. Experiments described in Chapter 5 indicate that a field of around 2 V cm^{-1} or more is required in order to achieve orientation.

The degree of orientation is determined by the rotational states of the molecules in the beam. The average angle between the electric field vector and the molecular dipole for a given $|JKM_J>$ state is given by

$$<\cos\theta>=\frac{KM_J}{J(J+1)} \tag{4.60}$$

For illustration, the average values of θ for the first few rotational states are given in Table 4.2.

Table 4.2: Average orientation angles θ for some rotational states of symmetric top molecules

$\|JKM_J>$	$\|111>$	$\|211>$	$\|221>$	$\|222>$	$\|311>$	$\|321>$	$\|322>$	$\|331>$	$\|332>$	$\|333>$
$\frac{MK}{J(J+1)}$	1/2	1/6	1/3	2/3	1/12	1/6	1/3	1/4	1/2	3/4
θ	60.0	80.4	70.5	48.2	85.2	80.4	70.5	75.5	60.0	41.4

In practice, there will be a distribution of states, and therefore orientations, entering the homogeneous orienting field. The distribution of orientations in the beam as it leaves the hexapole can be found from Equation 4.56 by inclusion of the orientation probability density function $F_{JKM_J}(V_0)$ in the summation over $|JKM_J>$ states.

$$P(V_0,\rho)=\sum_{JKM_J} P_{JKM_J}(\rho)F_{JKM_J}(V_0)f_{JK} \tag{4.61}$$

5. MOLECULAR BEAM CHARACTERISATION

This chapter describes experiments carried out to investigate the properties of the state selected molecular beams produced in the molecular beam machine described in Chapter 3. Beam intensity profiles and parallel velocity distributions have been measured using variations on standard techniques, an RF electric resonance spectroscopy cell has been used to interrogate the rotational quantum state distribution within the beam, and the effects of spatial orientation and deorientation on the beam signal have been examined.

5.1 Nozzle source

As described in Section 3.2.2, several types of supersonic nozzle source have been used in the molecular beam machine for various different applications. Most of the experiments described here were initially developed using the continuous nozzle source. The principal disadvantage of this source is that the available pumping speed limits the maximum nozzle stagnation pressure to around 150–200 Torr and introduces the requirement of a flow controller to step down the much higher pressure in the gas line to this range. Replacement of the continuous nozzle with a piezoelectric nozzle, which can be used in either pulsed or continuous mode, has largely removed the limitation on the stagnation pressure since the effective size of the nozzle aperture, and therefore the gas flow rate from the stagnation chamber into the vacuum system, can be controlled by varying the high voltage applied to the piezoelectric crystal. The planned addition of a second 10″ diffusion pump to the nozzle chamber in the near future will lead to a further increase in the attainable stagnation pressure. A high stagnation pressure is desirable since it leads to an improved supersonic expansion and a colder molecular beam.

5.2 Beam profile

For measurements of the beam intensity profile the beam signal is monitored as a razor blade is stepped through the beam. The blade is mounted at 45° to the beam axis on a linear

translator positioned in front of the quadrupole mass spectrometer. The beam signal falls off as the beam is progressively blocked from reaching the detector by the razor blade, and eventually reaches a constant value. A plot of signal against razor blade position represents the integral of the beam intensity profile. The profile itself is easily recovered by numerically differentiating the beam signal with respect to the position of the blade.

The focusing effect of the hexapole electric field is clearly seen when beam profiles are measured in the presence and absence of a voltage on the hexapole rods. Figure 5.1 shows profiles for a beam of CH_3F at hexapole voltages of 0 and ± 5000 V, in which the hexapole enhancement is clearly evident. The FWHM for the focused beam is approximately 2 mm, and for the unfocused beam approximately 3 mm, though this is largely determined by the diameter of the hexapole exit aperture.

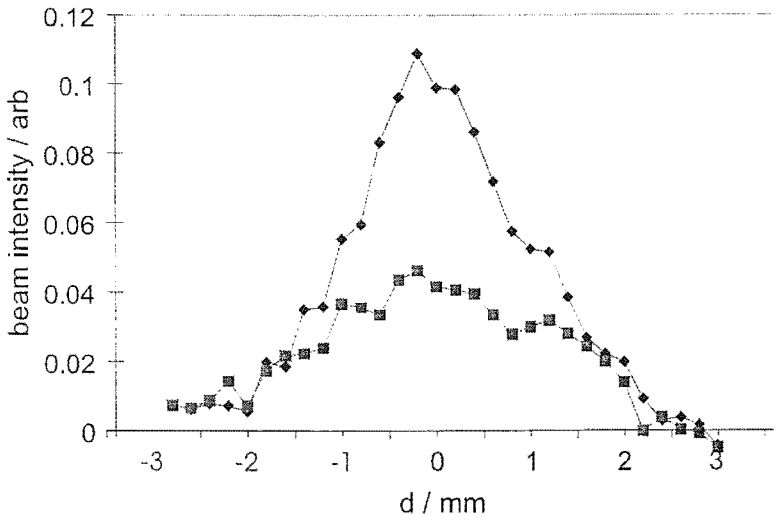

Figure 5.1: Intensity profiles for focused (diamonds) and unfocused (squares) beams of CH_3F.

5.3 Parallel velocity distribution

Traditionally, beam velocity distributions for continuous molecular beams have been measured by chopping the beam with a rotating slotted blade. The slot is generally very narrow so that only a short pulse of gas is allowed past the chopper. The distribution $f(t)$ of flight times is then measured and converted to a velocity distribution $f(v) = f(l/t)$, where l is the distance from the chopper to the detector and t is the flight time. In order for the experimentally determined velocity distribution to accurately reflect the true distribution within the beam factors such as the shape of the slot in the chopper blade and the electronic response

function of the detector, both of which tend to broaden the time of flight profile, must be carefully corrected for.

In the present experiments a variation on the standard chopped beam method was used. The existing chopper blade had previously been cut so that the beam was chopped with a mark space ratio of one for use in experiments involving a lock–in amplifier. This meant that the method described above could not be used without carrying out modifications to the chopper. Instead, a digital storage oscilloscope was used to capture the falling edge of the quadrupole mass spectrometer signal from the chopped beam, which contains all of the required velocity information. Fitting of the signal to Monte Carlo simulations of the decay allows the velocity distribution within the beam to be determined. The simulations are based around the trial distribution Equation 4.15:

$$f(v)dv = Av^2 \exp \frac{-m(v-u)^2}{2kT_{\|}} dv \tag{5.1}$$

in which m is the molecular mass of the beam gas, u is the mean flow velocity of the beam, k is Boltzmann's constant, $T_{\|}$ is the parallel translational temperature of the beam and A is a normalization constant. This expression has been shown previously[110] to provide a good description of the parallel velocity distribution in a supersonic molecular beam. Simulations of the effect of parallel translational temperature on the velocity distribution and signal decay of the chopped beam are shown in Figure 5.2 for a beam with a mean flow velocity of 600 ms^{-1}.

The steps involved in the Monte Carlo simulation program `beamvel`, included in Appendix F, are as follows:

1. For each trajectory a molecular velocity v_i is selected using a random number generator, accorded a weight w_i from Equation 5.1 and converted to a flight time tof_i beween the chopper and the detector.

2. A time t_i is then randomly selected over the interval of interest (usually 0–5 ms from the time at which the beam is chopped) and the contribution s_i to the time of flight signal at time t_i from a molecule travelling at velocity v_i is determined. For any time less than the flight time of the molecule from the chopper to the detector ($t_i \leq tof_i$) the signal from the molecule is set to w_i, while at times greater than tof_i, when this velocity component has been chopped from the beam, it is set to 0.

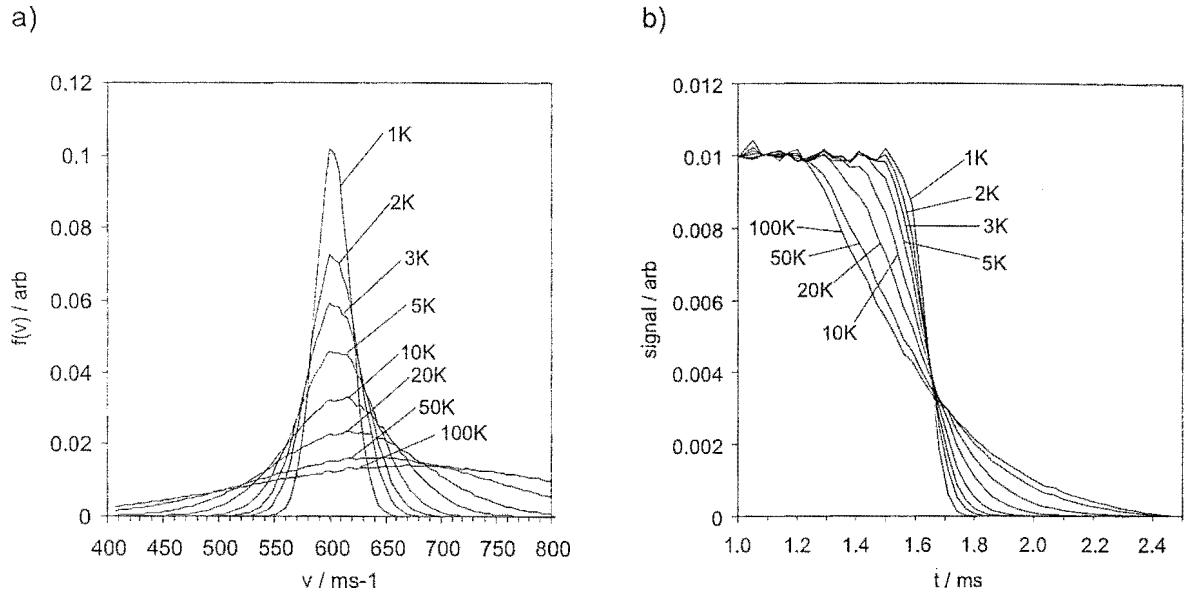

Figure 5.2: Effect of $T_{\|}$ on a) the parallel velocity distribution and b) the detected decay signal of a chopped supersonic molecular beam with a mean flow velocity of 600 ms^{-1}.

Table 5.1: Optimised values of mean flow velocity u and parallel translational temperature $T_{\|}$ for continuous molecular beams.

Beam gas	CH_3F	CH_3Cl	CH_3Br	CF_3H	CCl_3H
u / ms^{-1}	690	553	423	482	410
$T_{\|}$ K	35	40	35	35	35

3. The times t_i are binned into discrete units for output and the corresponding signals s_i summed within each bin to give the final time of flight distribution, which is then normalised to the experimental data set. The parameters u and $T_{\|}$ of Equation 5.1 are varied in the input in order to optimise the fit between the calculated and experimental data.

Measurements were made on neat beams of CH_3F, CH_3Cl, CH_3Br, CF_3H and CCl_3H at stagnation pressures of 100–150 Torr. Fitted profiles together with the corresponding velocity distribution are shown in Figure 5.3. The optimised values of u and $T_{\|}$ for each profile are given in Table 5.1.

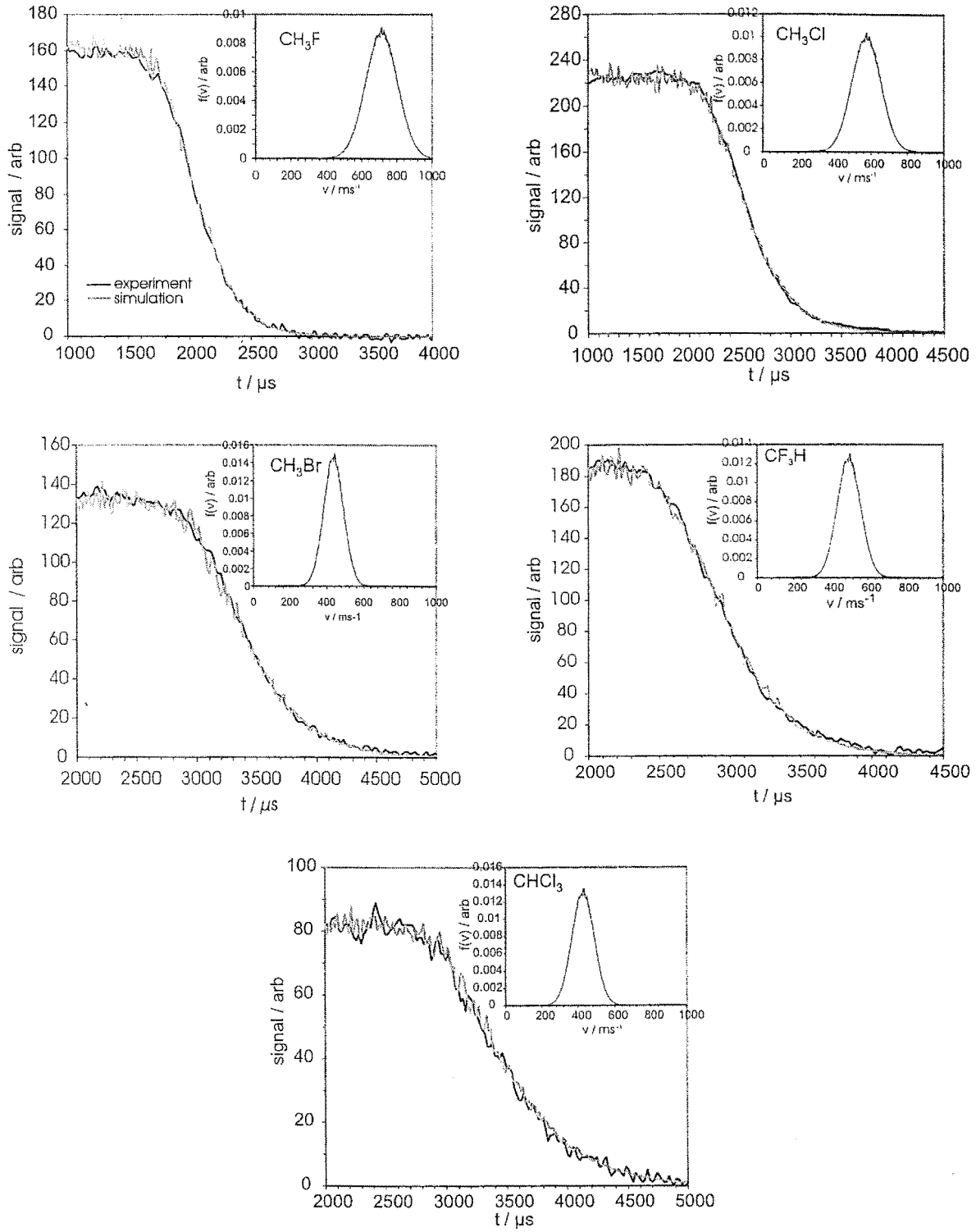

Figure 5.3: Experimental (black line) and simulated (grey line) time of flight profiles and extracted velocity distributions for supersonic molecular beams of symmetric top molecules.

5.4 Rotational quantum state populations

Relative populations of the rotational states present in the molecular beam were measured using radiofrequency electric resonance spectroscopy. The experimental arrangement of a pair of hexapoles separated by a resonance cell was described in Chapter 3. According to convention, the two sections of hexapole are referred to as the A and B fields, while the resonance field constitutes the C field. The resonance field consists of perpendicular components of DC and RF fields and can be tuned to excite specific transitions amongst rotational states of symmetric top molecules entering the RF cell.[121]

A symmetric top molecule in an electric field has a first order Stark energy given by

$$W = -\mu E \frac{KM_J}{J(J+1)}. \tag{5.2}$$

The spectroscopic selection rules for rotational transitions of symmetric top molecules in an inhomogeneous electric field are*

$$\begin{aligned} \Delta J &= 0, \pm 1 \\ \Delta K &= 0 \\ \Delta M_J &= 0, \pm 1 \end{aligned} \tag{5.3}$$

In the current experiments the beam is irradiated with RF tuned to specific $\Delta M_J = \pm 1$ transitions, so that $\Delta J = 0$ and the energy of a transition is given by

$$\begin{aligned} \Delta W &= -\mu E \frac{KM_J}{J(J+1)}[M_J - (M_J \pm 1)] \\ &= \pm \mu E \frac{K}{J(J+1)} \end{aligned} \tag{5.4}$$

In order to excite a ΔM_J transition the frequency of the microwave radiation must satisfy $h\nu = \Delta W$, so that

$$\frac{\mu E}{h\nu} = \frac{J(J+1)}{K} \tag{5.5}$$

This shows that in order to record a spectrum of the $|JK>$ states in the molecular beam either the DC field strength E or the RF frequency ν must be swept while the other is held constant. In order for a transition to occur there must be some component of the exciting

* Oka[122,123] suggests that $\Delta M_J > \pm 1$ transitions are possible under some circumstances.

radiation along the transition dipole of the molecule. Because the transition dipole moment of a symmetric top is orthogonal to the molecular axis, the RF radiation which excites the ΔM_J transitions must have a component at right angles to the DC field, with which the molecular axes align. Two RF cell geometries satisfying these requirements were designed and tested and are shown in Figure 3.5 of Chapter 3. The first, design a) in the figure, is based on the cell geometry used by Wiediger *et al*[121] and consists of a pair of split polished copper parallel plates across which a DC field is applied. Each plate is sectioned into two pieces in such a way that when an additional RF potential is applied to half of each plate a component of the oscillating field is present perpendicular to the DC field. The second design, b) in Figure 3.5, consists of two pairs of polished copper parallel plates mounted at right angles to each other to form a narrow, open ended box. A DC field is established between one pair of plates and RF is applied across the other. Four different electrical supply configurations were considered for the second cell. The performance of the two cells, and the four possible configurations for cell b), was evaluated by comparing scans of a single spectral line collected under identical conditions for the five cases. These scans are shown in Figure 5.4. The split plate cell is seen to give superior resolution and is preferred for carrying out spectral scans of the rotational states in the beam. However, the second cell gives significantly higher signal amplitudes, probably due to the more favourable relative orientations of the RF and DC electric vectors, and was chosen for the attenuation experiments described in Chapter 6. The broader resonances obtained using the second cell are also an advantage for these experiments, which involve tuning the resonance field to an individual quantum state. As shown in Figure 5.4, arrangements (iv) and (v) give comparable signal intensity and peak shape. Arrangement (v) is preferred due to the relative simplicity of the electronic configuration required.

In the present experiments the DC field is swept at constant RF. Because the number of molecules which undergo transitions is only a very small fraction of the total beam intensity the lock–in technique is used to record a spectrum. A lock–in amplifier measures very small AC signals and is essentially a filter tuned to the frequency of the signal. In addition to the signal input, a lock–in amplifier requires a reference input (i.e. the signal modulation frequency) with which to set the bandpass filter, and also the phase difference between the reference frequency and the oscillation of the signal.

The RF applied to the cell is fixed at between 1 and 3 MHz with an amplitude of around 1.5 V and is supplied by a Hewlett Packard 33120A waveform generator. The RF amplitude

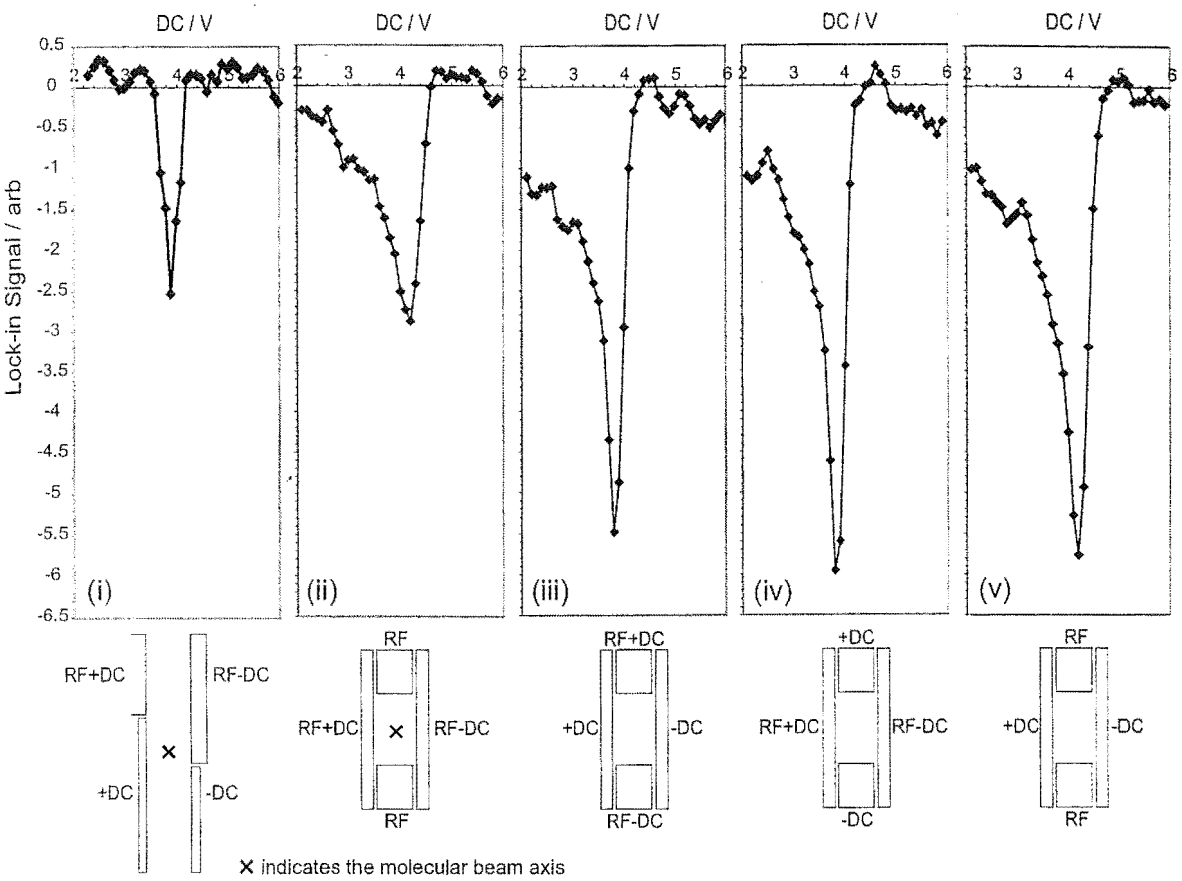

Figure 5.4: Scans of the $|111>$ peak using (i) the split parallel plate resonance cell and (ii)-(v) four different electrical supply configurations for the double parallel plate resonance cell. Scans were run at a hexapole voltage of 2000 V with an RF frequency of 2 MHz and RF amplitude of 1 V

is modulated by a square wave with a duty cycle of 0.5 and a frequency of usually between 100 and 500 Hz provided by the frequency generator of a Goldstar OS-9020G oscilloscope. The square wave also provides the reference to a Stanford Research Systems SR510 lock–in amplifier. The phase on the lock–in is set to compensate for the delay between the modulation applied to the RF cell and the modulation in the detected signal introduced by the flight time of the beam from the cell to the detector. The DC field is provided by Spellman MSO.3N12/C and MSO.3P12/C computer controllable power supplies and is typically swept in steps of 0.1V or less. During the half cycle when the RF is applied to the cell, $\Delta M_J = 1$ transitions occur, converting upper Stark state molecules with $M_J = -1$ to $M_J = 0$ states which no longer focus in the B field and are consequently lost from the beam. This results in the molecular beam signal measured at the quadrupole mass spectrometer dropping by typically around 1%

relative to the half cycle when the RF field is off and no transitions are occuring. The resulting AC signal from the mass spectrometer is supplied to the input of the lock–in amplifier, and the difference signal ($S_{(\text{RF on})} - S_{(\text{RF off})}$) yields a spectrum of the rotational states present in the beam when plotted against the DC potential applied to the RF cell. Figure 5.5 shows three such spectra for CH_3F measured under different experimental conditions†. Spectra a) and b) were recorded at hexapole voltages of 3000 V and 5000 V respectively for a neat beam of CH_3F. The effect of the hexapole voltage on the focusing of different states is clearly seen in the differing peak intensities for the two spectra. For example, in moving from 3000 V to 5000 V, the peaks corresponding to the $|11>$, $|33>$ and $|44>$ states decrease in intensity, while those for the $|43>$, $|31>$, $|52>$ and $|73>$ states increase. Higher $|JK>$ states appearing at DC potentials greater than 40 V are focused only at the higher hexapole voltage and do not appear at all in the 3000 V spectrum.

A comparison of spectra b) and c) shows the effect of seeding on the rotational state distribution. Spectrum c) was recorded under identical conditions to b) but using a beam of 10% CH_3F seeded in an argon carrier gas instead of a neat CH_3F beam. Seeding should lower the rotational temperature of the beam, and this is seen to be the case. While the neat beam spectrum displays a large number of peaks corresponding to quantum states up to $J = 8$, the seeded beam is dominated by three peaks, corresponding to the $|21>$, $|31>$ and $|41>$ states, in decreasing order of intensity, with virtually no contribution from higher J states, indicating a much colder beam.

In principle, if the rotational state distribution is known it should be possible to determine the rotational temperature of the molecular beam. However, the signal measured at the mass spectrometer for each rotational state is not only a function of its thermal population, but also of its hexapole transmission characteristics. Because the transmission characteristics of each state depend on the potential applied to the hexapole rods, this factor would have to be eliminated by averaging spectra measured over a wide range of hexapole voltages. In practice it is almost impossible to keep the experimental conditions constant for long enough to make this approach feasible.

† The spurious background signals observed at DC voltages below around 5 V were found to be due to the inability of the Spellman 300 V power supplies to deliver these low voltages incrementally. The problem has since been rectified by replacing these supplies with a pair of 0-30 V supplies manufactured in the department's Electronics Workshop. An example of a spectrum run with the new power supplies can be found in Figure 6.3.

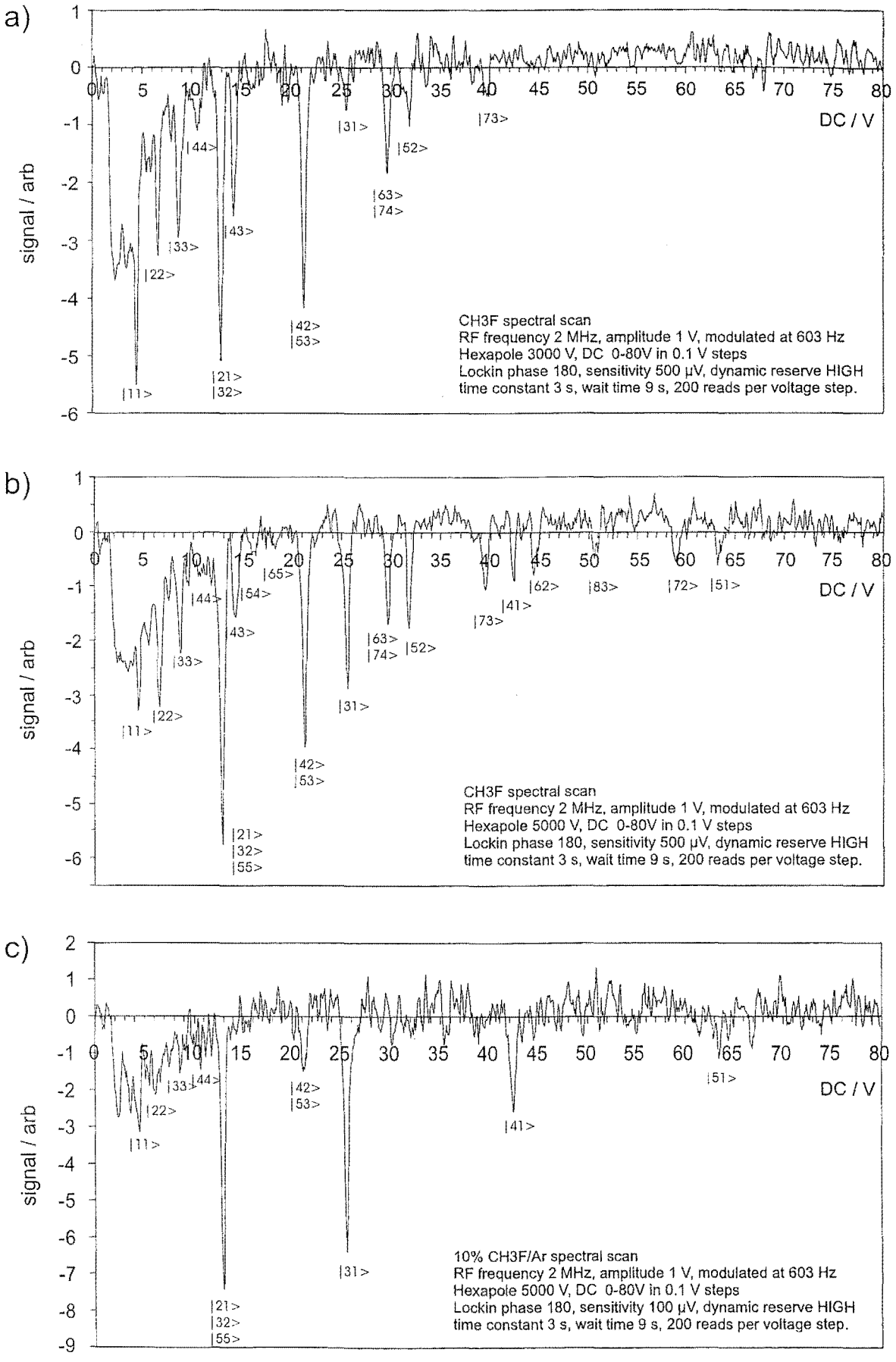

Figure 5.5: Effect of hexapole voltage and seeding on RF resonance spectra of CH_3F: a) neat beam, 3000 V; b) neat beam, 5000 V; c) seeded beam, 5000 V.

The RF resonance technique shows great promise as a method of state selection for investigations into the effect of reagent quantum state on collision processes. If the resonance cell is tuned to modulate the population of a particular rotational state, products of collisions with that state should show the same modulation. In a series of experiments to be described in Chapter 6, this technique has been applied to the measurement of collisional relaxation cross sections for selected rotational states of CH_3F with a range of scattering gases.[124]

In experiments for which resonance tagging of states is not appropriate, the ability to easily record a spectrum of the rotational states present in a molecular beam will allow significant state selection to be achieved simply by optimisation of the system for transmission of the state of interest. This can largely be accomplished through control of the supersonic expansion, use of seeded beams, and careful choice of the hexapole voltage.

5.5 *Orientation properties of symmetric top molecules*

In addition to being used for the resonance spectroscopy experiments described in Section 5.4 and Chapter 6, the RF cell can be used simply to provide a region of homogeneous field for orienting the molecular beam as it exits the first section of hexapole. The experimental arrangement of two sections of hexapole separated by a region of uniform electric field allows the orientation characteristics of the beam to be investigated through a study into the effect of the homogeneous field strength on the beam signal detected at the quadrupole mass spectrometer.

After passing through the A field the beam consists predominantly of upper Stark states. If the C field is non–zero the molecules make adiabatic transitions from the A field into the C field, and from the C field into the B field. They remain in the same rotational state throughout their trajectories through the system and will virtually all be transmitted through the B field to the detector. If the C field is zero the Stark energy levels become degenerate and the M_J quantum number is undefined. The molecular dipoles are no longer 'tied' to a direction defined by the local electric field vector and hyperfine coupling between the rotational motion and nuclear spin of the beam molecules, discussed in more detail in Section 5.5.2, results in spatial deorientation as the beam passes through the field free region. If complete spatial scrambling occurs in this region the molecules will have random orientations as they enter the B field, and the orientation of any given molecule with respect to the field direction in the hexapole will determine whether it becomes an upper Stark state, lower Stark

state, or $KM_J = 0$ state in the B field. The upper Stark state component of the beam will be transmitted to the detector, but a significant fraction of the beam will be lost as non–focusing states in the B field. This leads to a considerable drop in the beam signal relative to the case when the C field is non–zero, a phenomenon which can be used to probe the various factors affecting orientation of the beam, such as the minimum field strength required and the timescale over which scrambling occurs.

Brooks *et al*[125] were the first to use a split hexapole—parallel plate C field arrangement to investigate the effect of the uniform electric C field strength on the dipole scrambling of quantum state selected beams of symmetric top molecules. They concluded that a minimum uniform field of 10 Vcm^{-1} is required to preclude deorientation in the C field with subsequent degradation of focusing in the B field. Kaesdorf *et al*[126] used a hexapole field to state select CH_3I molecules for a study of the angular resolved photoelectron spectroscopy of oriented molecules. In order to minimise the effects of electric field on the photoejected electrons, the molecular beam was directed through a slowly decreasing uniform orienting electric field. The molecules experienced a field strength which reduced from 10 to 0.3 Vcm^{-1} over a distance of 360 mm. Since an orientation effect was observed in these experiments, some degree of spatial orientation was preserved during passage through the weak field.

Ghandi and Bernstein[127,128] investigated the effect of the uniform orienting field strength on spatial orientation over the range from 0 to 1.0 $kVcm^{-1}$ by measuring the spatial distribution of product ions produced from polarised laser photofragmentation of CH_3I. The angular distribution of product ions allowed the ratio of upper to lower Stark states in the original beam to be determined as a function of the uniform orienting field strength for the $|111>$ and $|222>$ rotational states. Molecules in the $|111>$ state spent 350 μs in transit through the uniform field before encountering the laser beam, while the flight time for the $|222>$ state was 640 μs. The original degree of orientation for a molecular beam of CH_3I could be recovered providing the uniform field strength exceeded 0.3 Vcm^{-1} for the $|222>$ state and 0.6 Vcm^{-1} for the $|111>$ state. In addition, it was shown that even though the rotational angular momentum **J** couples with the nuclear spin **I** through the hyperfine interaction in the weak orienting field to yield an ensemble of $|FJKIM_F>$ states, they are decoupled as the beam passes from the weak field region into a strong field. The ensemble is restored to its original $|JKM_J>$ distribution for electric field strengths of around 300 Vcm^{-1} or more.

5.5.1 Beam attenuation due to dipole scrambling

The effect of spatial scrambling in the C field region on the total beam signal was investigated by measuring hexapole transmission curves (beam signal as a function of hexapole voltage), first with a field of 20 Vcm^{-1} between the parallel plates of the RF cell, then with zero field. The results of these measurements for the four symmetric top molecules studied are shown in Figure 5.6.

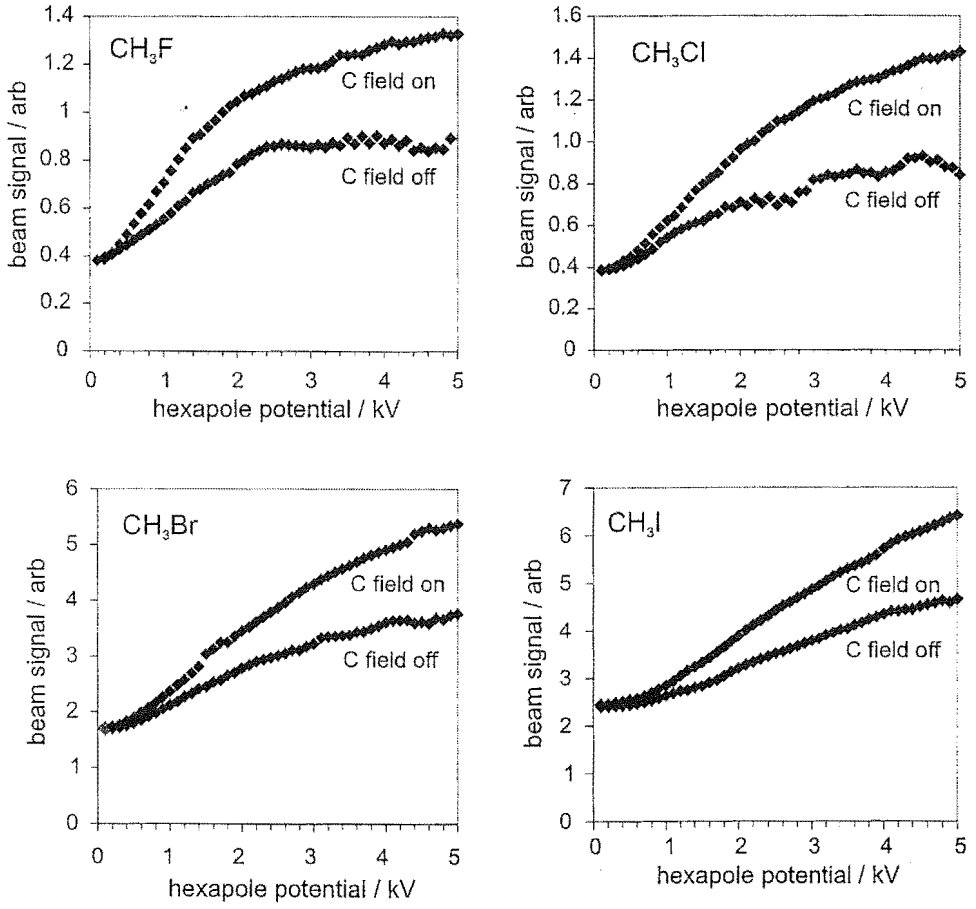

Figure 5.6: Hexapole transmission curves for beams of CH_3F, CH_3Cl, CH_3Br and CH_3I for C fields of 20 and 0 Vcm^{-1}.

As described in Chapter 4, focusing of upper Stark states to the beam axis when potentials are applied to the hexapole rods leads to an increase in signal, usually referred to as the hexapole enhancement. For the purpose of this study the enhancement is defined as the ratio of the beam signal with the hexapole field on to that with the field off. At a hexapole potential of ± 5000 V the enhancement is found to decrease by around 40% when the homogeneous field in the C region is switched off. The overall signal attenuation has contributions from

each of the $|JK>$ rotational states present in the beam according to the differing numbers of possible M_J states. If it is assumed that after spatial scrambling has occured in the C field region, a given $|JK>$ state entering the B field reprojects in the strong inhomogeneous field to give equal populations of the possible M_J states, it may be expected that the fractional drop in signal for the state should be roughly equal to $K/(2K+1)$, the fraction of beam molecules entering non–focusing lower Stark states. This was tested by carrying out Monte Carlo simulations of molecular trajectories through the system[‡]. If the C field is on, a molecule remains in the same state for its entire trajectory; if the field is zero the molecule is randomly assigned to a new M_J state as it enters the B field. Each trajectory is weighted according to the rotational state distribution calculated using statistical thermodynamics. The number of successful trajectories (i.e. trajectories that reach the detector) for zero and non-zero C fields are used to determine hexapole enhancments for the two cases averaged over the rotational state distribution within the beam. Simulated and measured ratios of the hexapole enhancement with the C field off to that with the C field on at a hexapole voltage of 5000 V and beam rotational and translational temperatures of 30 K are shown in Table 5.2, and are seen to be in fairly close agreement. Each simulated value is determined from the fate of 10,000 trajectories flown through the system.

Table 5.2: Measured and calculated ratios of hexapole enhancements with zero C field to those with non-zero C field.

	Enhancement ratio	
Beam	Expt	Calc
CH_3F	0.67	0.74
CH_3Cl	0.62	0.74
CH_3Br	0.69	0.69
CH_3I	0.73	0.68

5.5.2 *Hyperfine coupling*

Spatial deorientation of oriented symmetric top molecules under field free conditions occurs through the hyperfine interaction, in which the rotational angular momentum **J** of the molecule couples with the total nuclear spin **I**. Coupling between the two angular momentum

[‡] The program used to carry out these calculations, enhance, is included in Appendix F.

vectors splits the $|JKM_J>$ rotational state distribution into an ensemble of $|FJKIM_J>$ states, in which the new total angular momentum quantum number F is given by the vector sum of **J** and **I** and can take the values $|J+I|, |J+I-1|, \ldots, |J-I|$. The effect of hyperfine coupling on spatial orientation, which depends on the first order Stark effect for its success, depends on the relative magnitudes of the Stark and hyperfine splittings. Hyperfine coupling can be divided into weak field and strong field cases.[120] Intermediate field cases are more complicated to treat, and will not be discussed here.

Weak field case

In the weak field case the Stark energy is much smaller than the hyperfine energy, and the hyperfine levels are only slightly perturbed by the electric field. In this case μ precesses about the total rotational angular momentum **J**, **J** precesses around the total angular momentum **F**, and **F** precesses around the electric field vector **E**. The precessional motion around the electric field is slow compared to the interaction between **J** and **I** and does little to affect the hyperfine coupling. The molecular state is well described by the quantum numbers I, J, F and M_F: M_J is no longer a good quantum number since it is not a constant of the molecular motion. Averaged over time the angle between the molecular dipole and the electric field vector is given by

$$\cos\theta = \cos\theta_{KJ}\cos\theta_{JF}\cos\theta_{FE} \tag{5.6}$$

where

$$\begin{aligned} \cos\theta_{KJ} &= \frac{K}{J} \\ \cos\theta_{JF} &= \frac{J^2+F^2-I^2}{2JF} \\ \cos\theta_{FE} &= \frac{M_F}{F} \end{aligned} \tag{5.7}$$

The Stark energy is therefore

$$\begin{aligned} W &= -\mu E\cos\theta \\ &= -\frac{\mu K M_F(J^2+F^2-I^2)E}{2J^2F^2} \\ &= -\frac{\mu K[J(J+1)+F(F+1)-I(I+1)]M_F E}{2J(J+1)F(F+1)} \end{aligned} \tag{5.8}$$

Strong field case

In the strong field case the Stark energy is much greater than the hyperfine energy. The precession of **J** around **E** is so fast that the nuclear orientation cannot respond on the same timescale, and **I** and **J** are said to be decoupled. Because the vector sum of **I** and **J** is not constant under these conditions, F is no longer a good quantum number, and the state is described by the quantum numbers I, M_I, J and M_J, where M_I is the projection of I onto the field direction. The Stark energy levels are the same as for the case in which there is no hyperfine coupling.

The rotational spectra discussed in Section 5.4, in which the observed peaks correspond to ΔM_J rather than ΔM_F transitions, indicate that the strong field regime provides an appropriate description of the hyperfine coupling in the current experimental arrangement when C fields of greater than a few volts per centimetre are established. The upper limit for the 'strong field' description is set by the position of the peak corresponding to the $|11>$ rotational state, appearing at a field strength of 4.2 Vcm^{-1}.

The spin–rotation energy is given to first order by[129]

$$E_{SR} = \mathbf{I} \cdot C \cdot \mathbf{J} \tag{5.9}$$

where C is the spin–rotation matrix. For a symmetric top molecule $C_{xx} = C_{yy} \neq C_{zz}$. The average of these components over molecular orientation, $C = \frac{1}{3}(2C_{xx} + C_{zz})$, should give a rough idea of the magnitude of the expected hyperfine interaction energies E_{SR}. These values[130] are given for CH_3F, CH_3Cl, CH_3Br and CH_3I in Table 5.3. The estimated hyperfine energies are of the order of 4×10^{-30} J. For the $|111>$ state at an electric field strength of 4.2 Vcm^{-1} the Stark energy is 1.29×10^{-27} J, nearly three orders of magnitude larger than the hyperfine energy, indicating that the assumption of strong field conditions is valid.

5.5.3 *Orienting field requirements*

The minimum required orienting field can be measured directly by monitoring the beam signal as a function of the electric field established between the two parallel plates at constant hexapole voltage. The voltages applied to both sets of hexapole rods were kept fixed at ± 5000 V for these experiments. As shown in Figure 5.7, as the C field strength is increased the beam signal rises. This is due to the fact that as a field is established it becomes possible for the beam molecules to undergo adiabatic transitions into the C field and remain in upper

Table 5.3: Estimate of the hyperfine interaction energy for the methyl halides based on the spin–rotation matrix elements.

Molecule	C_{xx} / kHz	C_{yy} / kHz	$C = \frac{1}{3}(2C_{xx} + C_{yy})$ / kHz	$E_{SR} = hC$ / J
CH_3F	0.8	14.66	5.42	3.59×10^{-30}
$CH_3^{35}Cl$	1.5	15.0	6.0	3.98×10^{-30}
$CH_3^{37}Cl$	1.5	15.0	6.0	3.98×10^{-30}
$CH_3^{79}Br$	1.301	16.271	6.291	4.17×10^{-30}
$CH_3^{81}Br$	1.849	15.819	6.506	4.31×10^{-30}
CH_3I	1.744	15.494	6.327	4.19×10^{-30}

Stark states which focus in the B field. The rise in signal is steep at first, but starts to level off above field strengths of 1 Vcm^{-1}. Orientation is essentially complete at field strengths greater than 3 or 4 Vcm^{-1}. These results are consistent with the data obtained by Kaesdorf *et al.* who reported orientation effects in the photoionization of CH_3I with orienting fields as low as 0.3 Vcm^{-1}. While this is lower than the field strength required to fully orient a beam of symmetric top molecules, the present experiments show that a significant fraction of the beam is oriented at this potential, and small orientation effects should be observable. The field strength required for complete orientation appears to vary slightly amongst the four molecules studied, with CH_3Cl and CH_3Br orienting at lower fields than CH_3F and CH_3I, though the differences are quite small. The reason for the observed variation is not immediately apparent, since there are several factors affecting orientation which should be considered. The magnitude of the molecular dipole moment and total nuclear spin, as well as the beam velocity, which determines the length of time for which molecules experience the C field, and beam rotational temperature, which determines the distribution of rotational states within the beam, all differ for the four methyl halides studied and are all likely to affect orientation to some degree.

These measurements of the minimum orienting field required were carried out for a beam containing a distribution of rotational states determined by the rotational temperature. It is interesting to compare these results with the experiments carried out by Ghandi and Bernstein,[128] in which the field dependence of orientation for single rotational states of CH_3I was determined. The measured field strengths of 0.3 Vcm^{-1} and 0.6 Vcm^{-1} required for complete orientation of the $|111>$ and $|222>$ states are significantly lower than the values

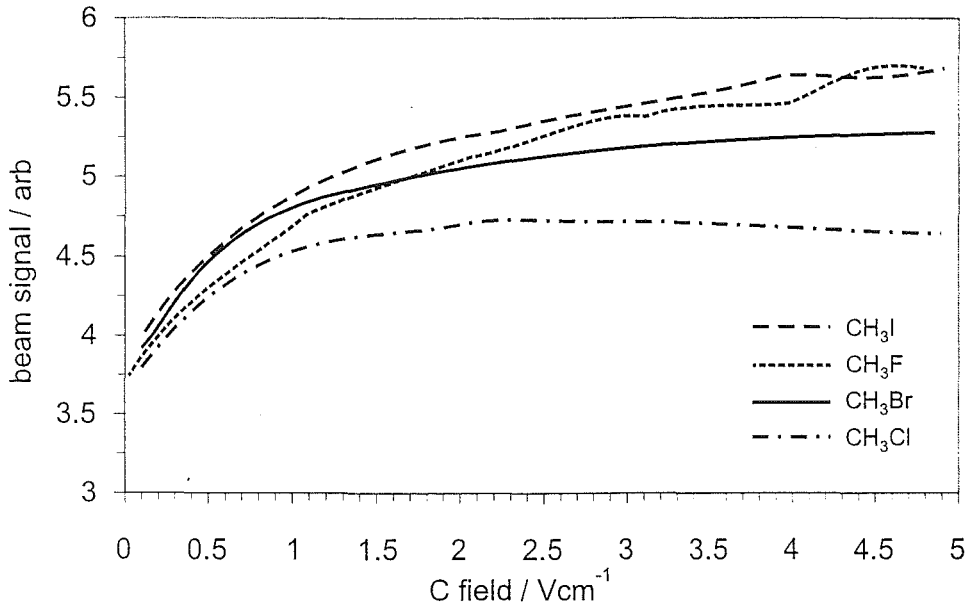

Figure 5.7: Rise in beam signal with increasing C field as adiabatic transitions into and out of the uniform field become possible.

measured for the distribution of states present in the beams used in this work. A likely explanation for the dependence of the required orienting field on rotational state is as follows. The molecules orient through an interaction between the molecular dipole μ and the electric field $\mathbf{E}$. The energy of interaction is simply the Stark energy $\mu E < \cos\theta >$, where θ is the angle between the two vectors and $< \cos\theta >= \frac{KM_J}{J(J+1)}$. It seems a reasonable assumption that orientation becomes possible when the interaction energy reaches some threshold value W_{thresh}, so that the required minimum orienting field for a given state is

$$E_{JKM_J} = \frac{W_{\text{thresh}}}{\mu} \frac{J(J+1)}{KM_J} \tag{5.10}$$

If this assumption is valid, then plotting the beam orientation data from single state experiments against $\mu E < \cos\theta >$ rather than against E should give similar curves for each rotational state, which reach a constant value at a similar value of the ordinate. Though Ghandi and Bernstein made measurements for only two rotational states of CH_3I, use of their data to test the ideas described above seems to support the hypothesis (Figure 5.8).

Radiofrequency resonance spectroscopy of CH_3F and CH_3Cl beams[121,131] indicates that rotational states up to $J = 7$ are present in appreciable amounts in the beams used in the present work. Higher J states will tend to increase the required orienting field measured in experiments which average over all rotational states present, explaining the higher measured

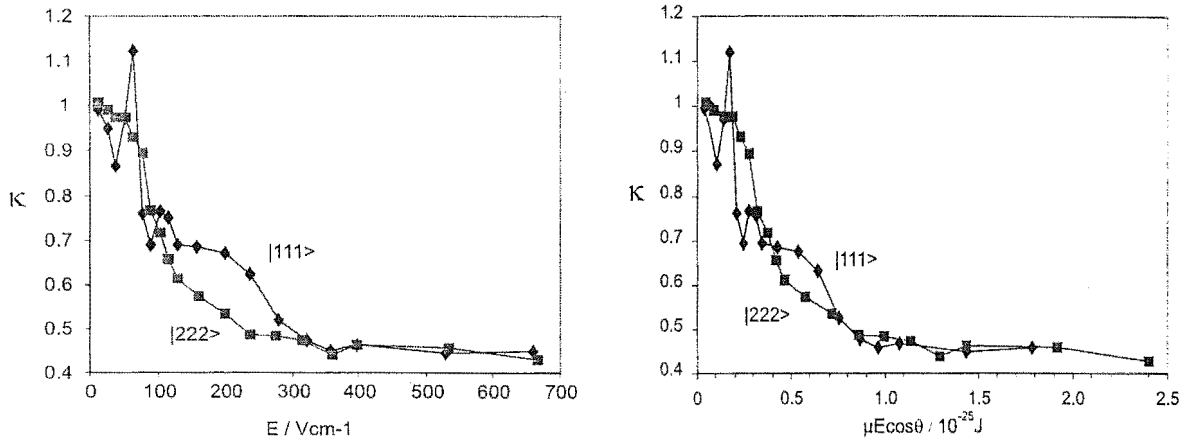

Figure 5.8: Ratio of upper to lower Stark states as a function of a) homogeneous field strength E and b) $\mu E < \cos\theta >$ for CH_3I. Data from Reference.[128]

values when compared with the single state data of Ghandi and Bernstein. If the value of W_{thresh} determined from Bernstein's data is used to average E_{JKM_J} for CH_3I over the states up to $J = 7$, complete orientation is predicted at a field strength of 3.9 Vcm^{-1}, in accord with the field strength at which the beam signal levels off for CH_3I in Figure 5.7.

5.5.4 *Mean deorientation lifetimes*

The time required for complete spatial scrambling is an important factor in the design of any experiment which seeks to investigate orientation effects on physical and chemical processes involving oriented beams. Knowledge of the lifetime is of heightened importance when reagents or products of a process carry an electrical charge, since under these conditions a field free region is almost always required at some point in the experiment in order to prevent the orienting field from perturbing charged particle trajectories. Harland *et al*[6] set a lower limit for the orientation lifetime during an investigation of orientation effects on electron impact ionization cross sections for a range of symmetric top molecules. In their experiments ionizing collisions between crossed beams of electrons and oriented molecules occured between a pair of field plates which provided the homogeneous field for orienting the molecular beam. In order to eliminate any effects of the orienting field on the electron beam, the field was switched to ground a short time before each pulse of electrons entered the crossing region. An orientation effect was observed with a delay of 0.1 μs, indicating that spatial scrambling was not occuring on this time scale.

Since spatial scrambling takes place through the hyperfine interaction, it might be ex-

pected that the lifetime for scrambling should be of the order of the hyperfine precessional period. In Section 5.5.2 it was noted that the hyperfine frequencies for the methyl halides studied here are of the order of 6 kHz. This corresponds to a precessional period of around 150 μs. If scrambling occurs on this timescale it should be accessible to experimental measurement.

The most straightforward way to measure a deorientation lifetime would be to use a fast oscilloscope to record the beam signal as a function of time after switching the C field to ground. Unfortunately, the signal decay due to spatial scrambling is massively broadened by the beam velocity distribution, making extraction of a decay constant impracticable.

The time for which the beam experiences field free conditions may be controlled by pulsing the potential applied to the parallel plates of the RF cell to ground potential for set intervals. If the pulse is longer than the time it takes for the molecular dipoles to spatially scramble, a dip in the beam signal is observed, as shown in Figure 5.9 for a pulse width of 250 μs. The observed dip is delayed relative to the voltage pulse by the flight time of the beam from the parallel plates to the detector and broadened by the beam velocity distribution.

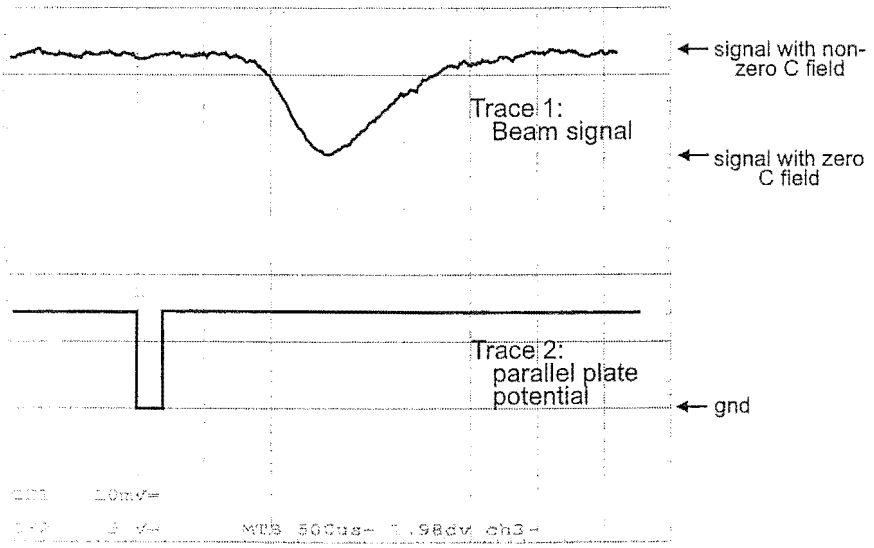

Figure 5.9: Dip in the CH_3F beam signal observed on pulsing the C field to ground. The upper trace shows the beam signal while the lower trace shows the potential difference applied across the parallel field plates.

The 'height' of the dip should be directly proportional to the amount of spatial scrambling occuring within the zero field interval, and it was hoped that this could be used in the measurement of deorientation lifetimes. Experiments were conducted in which the signal dip

was measured as a function of the zero field time. If it is assumed that spatial scrambling follows first order kinetics, the dip in beam signal, $S(\Delta t)$, where Δt is the zero field interval, is given by,

$$S(\Delta t) = S_{\max}(1 - e^{-k\Delta t}) = S_{\max}(1 - e^{-\Delta t/\tau}) \tag{5.11}$$

where $S_{\max}$ is the maximum dip in the signal, k is the first order rate constant and τ is its reciprocal, the time constant or mean lifetime for scrambling.

A plot of the signal dip against the zero field time should therefore be an inverted exponential function which can be fitted to obtain the time constant for deorientation. In practice, however, it was not possible to fit the data in this way to obtain reasonable, reproducible values for the decay constant. It is thought that there are two major problems with this approach. The first is the short length of the C field region. This limits the maximum zero field time to the flight time of the beam through the RF cell. For CH_3F this flight time is around 200 μs, roughly the same as the expected value for the time constant, severely limiting the range over which meaningful data can be collected. A second, related consideration is that many of the beam molecules will exit the C field region before experiencing the entire width of the zero field pulse. Because the distribution of velocities within the beam leads to a broad time of flight distribution of molecules arriving at the detector, the signal detected at any one instant will have contributions from molecules which have experienced zero field conditions for the entire range of times from 0 up to Δt. This means that the signal is not strictly described by Equation 5.11, but is in fact some kind of integral over this function.

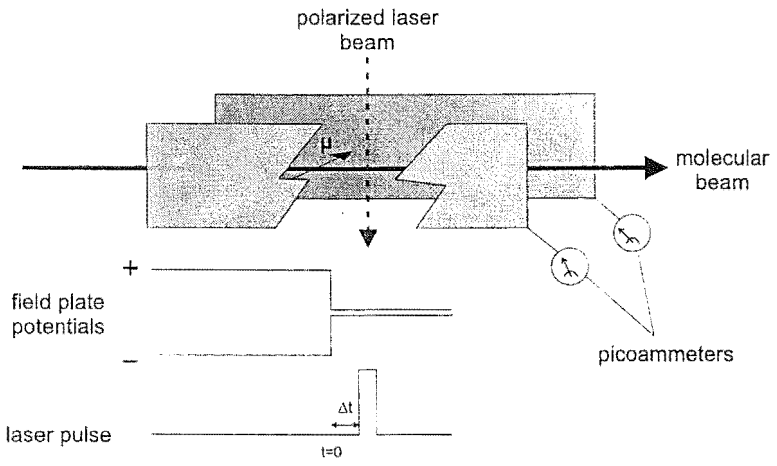

Figure 5.10: Experimental arrangement required for the measurement of deorientation lifetimes for a beam of oriented symmetric top molecules in field free space.

It would appear that the distribution of velocities within the molecular beam precludes using the split hexapole / C field arrangement to measure time dependent orientation properties. However, the technique used by Bernstein and coworkers[127,128] to measure the required orienting field could easily be adapted for measurement of deorientation lifetimes. The required experimental arrangement is shown in Figure 5.10. The upper Stark state selected molecular beam is oriented by a uniform electric field maintained between a pair of homogeneous field plates. At $t = 0$ the field plates are switched to ground potential and after a set delay Δt a polarised laser beam is used to photoionize the beam. Product ions striking the two field plates are detected by a pair of sensitive picoammeters, and a plot of the ratio of the two signals against Δt should give the deorientation decay curve, from which the scrambling lifetime can be extracted. In fact, it is possible to extract an approximate value of the lifetime for CH_3I from the published results of Ghandi and Bernstein.[128] Based on the degree of orientation measured under zero field conditions after the 640 μs flight time to the ionization region for the $|222>$ state, the orientation lifetime can be estimated to be approximately 220 μs. This is roughly the value which would be expected from the analysis carried out in Section 5.5.2. It should be possible to carry out these experiments in the near future.

6. UPPER STARK STATE COLLISIONAL RELAXATION CROSS SECTIONS FOR SINGLE ROTATIONAL STATES OF CH_3F

6.1 Introduction

It has been noted[8,112] that in experiments involving hexapole state selected and oriented molecular beams, orientation effects may disappear when the background pressure within the hexapole is high. This has been attributed to collisions between upper Stark state molecules and background gas atoms or molecules. These rotationally inelastic collisions convert an upper Stark state, following a focusing trajectory through the hexpole, to a non focusing state via ΔJ and/or ΔM_J transitions. The experiments discussed in this chapter use the resonance technique described in Chapter 5 to characterise the attenuation process. The results can be directly compared with a previous study carried out by Blunt *et al.*[109]

Measurements of state resolved rotationally inelastic collision cross sections were first carried out by Toennies and coworkers[132–135] in the early 1960's on diatomic molecules. In these experiments an electrostatic quadrupole filter was used to prepare a rotationally state selected beam of TlF, which was then focused into a gas filled collision chamber. A second quadrupole filter placed slightly off axis was used to analyse the state distribution of the scattered beam molecules. Cross sections for ΔJ transitions were measured for a variety of scattering gases and were found to be highly dependent on the scattering species. Total collisional attenuation cross sections for the $J = 2$ rotational state of TlF ranged from 152 $Å^2$ using He as the scattering gas, to 2140 $Å^2$ using NH_3. In a later study[136,137] crossed molecular beams were used to investigate the inelastic collision cross sections of CsF seeded in Xe with a range of scatterers, including the inert gases, N_2, CO_2, CH_4, SF_6 and symmetric top alkyl halides. The use of crossed beams greatly improved the resolution by narrowing the velocity distribution of the scattering gas relative to the 'bulb' type experiment. Cross sections reported for $(\Delta J = 1, 2; \Delta M_J = 0, 1)$ transitions ranged from 0.5 to 620 $Å^2$ depending on the particular transition and also on the scattering gas.

Blunt *et al*[109] have recently published collisional attenuation cross sections for neat and seeded beams of CH_3Cl with a range of scatterers. A hexapole electrostatic filter was used for state selection and the hexapole chamber itself was pressurized for the attenuation experiments. Cross sections were found to lie in the range from 200 $Å^2$ for neat CH_3Cl on Ne to 670 $Å^2$ for a beam of 5% CH_3Cl in Xe on N_2. Collision cross sections of CH_3F with various scattering gases were also measured.[138]

It was shown in Chapter 5 that molecular beam radiofrequency electric resonance spectroscopy is a highly useful technique for interrogating the rotational states present in a molecular beam of oriented symmetric top molecules, and might also prove useful for tagging individual rotational states in studies of collision processes. This chapter presents an application of the resonance technique to the determination of collisional attenuation cross sections for rotationally state selected molecular beams. Cross sections with a range of scattering gases have been measured for the $|11>$, $|21>$ and $|31>$ $|JK>$ states of CH_3F.

6.2 Experimental

The molecular beam machine used to perform these experiments was described in Chapter 3. The continuous nozzle source was used, with stagnation pressures of typically 100-200 Torr. The hexapole exit aperture was set to 2.5 mm. As mentioned in Chapter 3, the first hexapole chamber is separated from the adjoining chambers by a skimmer with a 1.5 mm aperture at one end, and a stainless steel partition with a 9 mm aperture at the other end. The chamber thus forms a collision cell which can be pressurised with a scattering gas during attenuation experiments, providing a known path length over which collisional attenuation of the beam can occur. There is a small amount of scattering gas leakage from the first hexapole chamber into the adjacent chamber, which houses the RF cell. However, the pressure in the second chamber never rises high enough during the course of an experiment to cause significant attenuation of the beam in this chamber, remaining always at least an order of magnitude lower than the pressure in the collision cell.

The double parallel plate resonance cell (design b) of Figure 3.5) was chosen for use in the experiments described here. The larger signal amplitude compared with the split parallel plate cell is an advantage and the broader resonances facilitate in tuning of the cell to a particular rotational state. Operation of the resonance cell was described in detail in Section 5.4. The effect of RF amplitude on the beam signal for this cell is shown in Figure 6.1. The

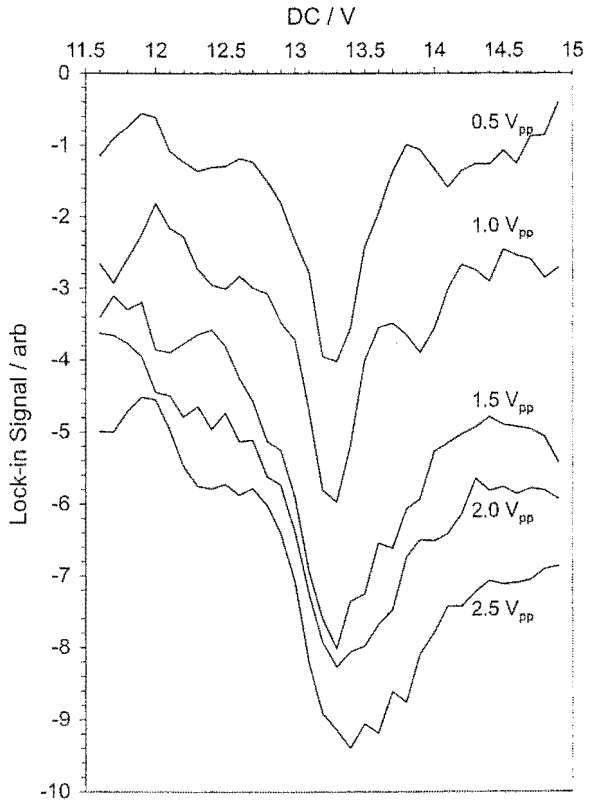

Figure 6.1: Effect of RF amplitude on the resonance signal measured for the $|21>$ peak of a 10% CH_3F/Ar beam at a hexapole voltage of 3000 V and RF frequency of 2 MHz.

signal increases with increasing RF amplitude as increasing numbers of molecules undergo transitions. However, signal saturation becomes a problem at very high amplitudes. An amplitude of 1.0 V_{pp} was chosen for the current experiments.

In order to measure a collision cross section the DC potential is tuned to the energy of the desired rotational state and the hexapole high voltage is set for transmission of the state. Gas is admitted to the first hexapole chamber through a Leybold Hearaeus leak valve which is computer controlled using a Crystalap STD206 stepping motor. The pressure is usually incremented from around 4×10^{-6} Torr to 3×10^{-5} Torr in steps of 1×10^{-6} Torr. The modulated signal detected by the lock–in amplifier is measured as a function of the scattering gas pressure and converted to a cross section.

The cross section obtained in a beam attenuation experiment is determined from measured quantities using Beer's law

$$\ln \frac{I_0}{I} = n\sigma\ell = \frac{\sigma\ell P}{k_B T} \tag{6.1}$$

in which I and I_0 are the transmitted and incident beam intensities, n is the particle number

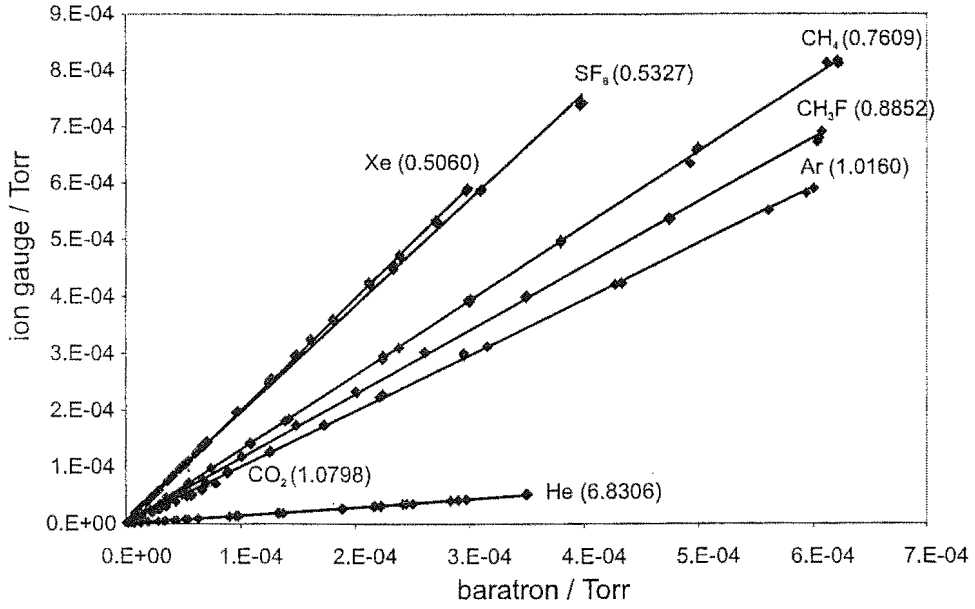

Figure 6.2: Ion gauge calibration curves for He, Ne, Ar, Xe, CO_2, CH_4, CH_3F and SF_6. HPS919 ion gauge readings are plotted against MKS670 baratron readings for each gas. Ion gauge correction factors for each species are given in parentheses.

density in the collision region, ℓ is the path length through the collision region, σ is the cross section, P is the pressure in the collision region, k_B is Boltzmann's constant, and T is the temperature of the collision gas.

In the current experiments the A field region is pressurized, defining the path length as the distance from the second skimmer to the exit aperture of the first hexapole, 0.548 m.

The pressure in the collision cell can be accurately measured using a Model 690A high accuracy (0.15% of reading) 0.1 Torr MKS Baratron with Model 670 signal conditioner down to pressures of 1×10^{-5} Torr. For the current experiments an MKS Instruments Model 919 hot cathode controller coupled to a Duniway T-100-K ion gauge is calibrated against the Baratron over the range from ~0.5 mTorr to 1×10^{-5} Torr. The ion gauge can then be used to make absolute pressure measurements over the range of interest. Ion gauge calibration curves are shown in Figure 6.2. Pressure measurements using the 919 controller are reproducible to within ±5%. The absolute accuracy of the cross section is dominated by the pressure measurements; 0.15% above 1×10^{-5} Torr and up to 5% for pressures below 1×10^{-5} Torr, according to instrument specifications. In practice, the attenuation curves show no obvious difference where measurements overlap these ranges and the absolute accuracy of the cross sections reported in this work is thought to be better than 5%.

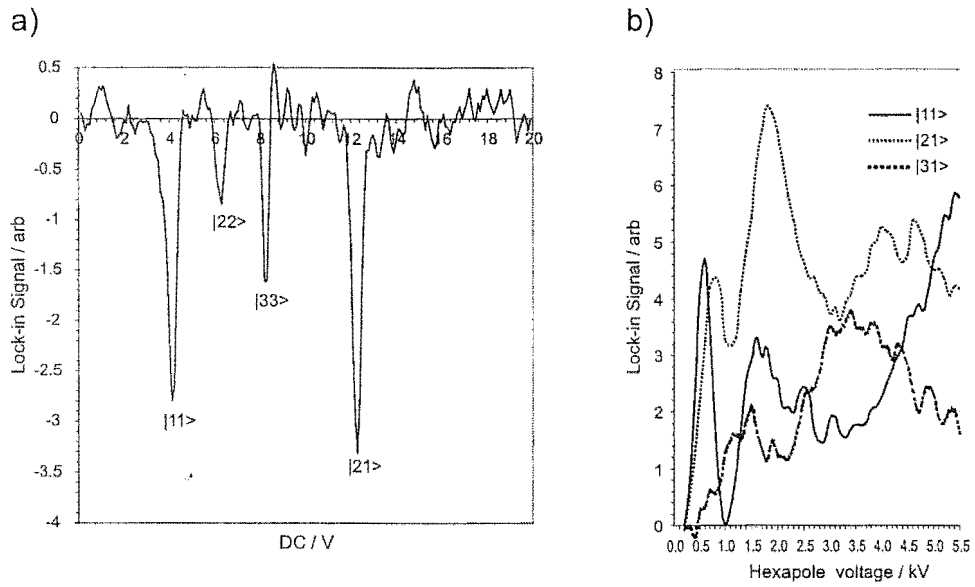

Figure 6.3: a) Resonance spectrum of the rotational states present in a seeded beam of 10% CH_3F/Ar at a hexapole voltage of 4000 V, RF frequency 2 MHz and amplitude 1 V; b) hexapole transmission curves for the $|111>$, $|211>$ and $|311>$ rotational states.

6.3 Results and discussion

All of the experiments described here were carried out using a seeded beam of 10% CH_3F in argon. Initially, a resonance spectrum was measured in order to identify the rotational states present in the beam. This spectrum is shown in Figure 6.3 along with hexapole transmission curves (resonance signal as a function of hexapole rod voltage) for each major component of the beam.

Reasonable signal levels could be obtained for three rotational $|JK>$ states; $|11>$, $|21>$ and $|31>$. Cross section measurements made at each of the maxima in the hexapole transmission curves show an unexpected dependence of the measured cross section on the hexapole voltage, with cross sections measured at low hexapole voltages (< 2000 V) tending to be significantly higher than those at higher voltages, often by around 15%. This effect appears to be associated with the differing amplitudes of the fundamental, first harmonic and second harmonic trajectories of the symmetric top molecules through the hexapole at successively higher hexapole voltages. The presence of the resonance cell should have the smallest effect on the second harmonic type trajectories, due to their lower maximum radial displacement and the fact that the molecules are travelling almost parallel to the axis when they enter the resonance cell. For this reason, all cross sections were measured at a hexapole

voltage of 5200 V. This choice had the additional advantage that unlike the first or second harmonics, which appear at significantly different hexapole voltages for the various states, reasonable signal levels could be obtained for all three states at a single hexapole voltage. Five to ten repeated measurements were averaged to give the reported cross sections, shown in Table 6.1. A typical data set is shown in Figure 6.4.

Table 6.1: Collisional attenuation cross sections for individual rotational states of a seeded beam of 10% CH_3F with a range of scatterers at a hexapole voltage of 5200 V.

State	Scatterer	σ / Å^2 (resonance method)	σ / Å^2 · (hexapole collision cell[138])
$\|111>$	He	246 ± 6	247
$\|111>$	Ar	284 ± 10	270
$\|111>$	Xe	317 ± 25	319
$\|111>$	N_2	390 ± 21	390
$\|111>$	CO_2	287 ± 16	–
$\|111>$	CH_4	376 ± 44	–
$\|111>$	CH_3F	654 ± 40	–
$\|111>$	SF_6	316 ± 19	–
$\|211>$	Ar	350 ± 24	–
$\|311>$	Ar	366 ± 17	–

The cross sections presented in Table 6.1 correspond to internuclear separations over the range from 8.8 to 14.5 Å. It has been shown previously[109] that the velocity dependence of these cross sections is consistent with a long range interaction based on dispersion and dipole–induced dipole contributions and that cross sections calculated assuming ΔM_J only transitions, which involve energies of < 1 Jmol^{-1} give values close to those measured.

The cross sections for collisional attenuation of the $|111>$, $|211>$ and $|311>$ states by argon are seen to increase with increasing J, from 284 Å^2 for the $|111>$ state to 366 Å^2 for the $|311>$ state. As J increases, the spacing of the Stark energy levels, and therefore the energy which must be transferred during a collision in order for a change in M_J state to take place, decreases. High impact parameter collisions should therefore become more efficient as J increases, leading to the observed increase in the attenuation cross section.

Attenuation cross sections for the $|111>$ state were measured for a wide range of scattering

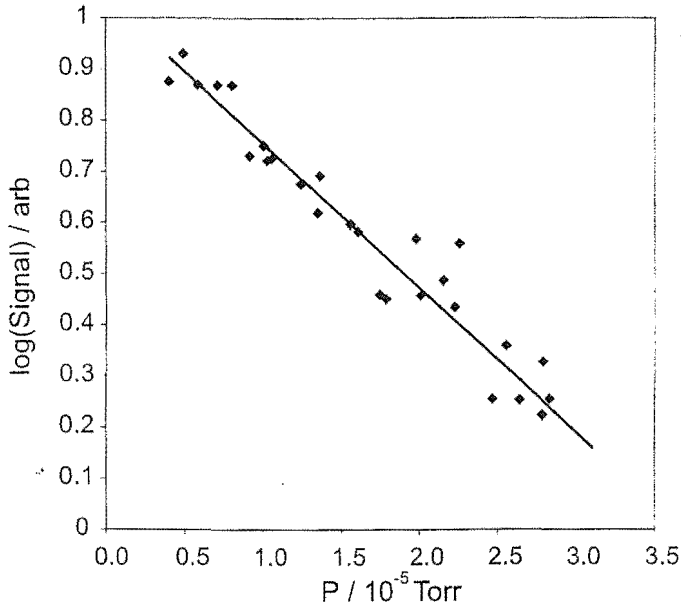

Figure 6.4: A typical data set used to determine the cross section for collisional attenuation of the $|111>$ state of CH_3F by Ar at a hexapole voltage of 5200 V.

gases. Data from earlier experiments of Blunt *et al*[109,138] were available for comparison in the case of the inert gases and nitrogen. In the previous experiments a single long hexapole collision cell replaced the double hexapole – resonance cell arrangement used in the work reported here. Hexapole transmission curves were measured as a function of scattering gas pressure in the hexapole and the collisional attenuation cross section for a given hexapole voltage was determined from the Beer-Lambert law as described in Section 6.2. Cross sections for individual rotational states can in theory be obtained once the hexapole voltage at which they focus is known. However, in practice the resolution of the experiment is fairly low, and the signal at a given hexapole voltage will have contributions from several states other than the one of interest. It was only possible to extract cross sections for the $|11>$ state with any degree of certainty. Despite these limitations, the cross sections measured using this technique are found to be in good agreement with those measured using the current method, in which the only contribution to the signal is from the rotational state to which the resonance cell is tuned. The excellent correspondence between the two sets of data inspires confidence in the reliability of the resonance method for the measurement of collisional attenuation cross sections.

In addition to the measurement of cross sections for comparison with previous data, a series of measurements was made using SF_6, CH_4, CH_3F and CO_2 as scattering gases. As

expected, there is a general increase in the cross section with increasing molecular size, and a large cross section for resonant scattering from CH_3F. The uncertainty associated with this cross section is a little higher than for other scattering gases due to lower signal to noise for these measurements. This is thought to be due to low levels of CH_3F leaking from the collision cell chamber into the chamber housing the quadrupole mass spectrometer, increasing the background level of CH_3F which is superimposed on the weak beam signal.

These measurements of M_J changing collision cross sections for state selected molecular beams of CH_3F seeded in Ar have shown that radiofrequency resonance methods provide a powerful technique for determining the properties of individual rotational states in a beam of symmetric top molecules. In the future the technique could be very useful for tagging individual states in crossed beam experiments.

7. DESIGN AND CHARACTERISATION OF A LOW ENERGY ION SOURCE FOR CROSSED BEAM EXPERIMENTS

The ion source described here was developed for use in the ion imaging experiments detailed in Chapter 10. It is based around a design used by Vietzke *et al*[139–141] in the early 1970's for production of low energy halide ion beams suitable for use in the measurement of excitation functions for the gas phase reactions of Cl^-, Br^- and I^- with CH_4 and CH_3F. Alkali metal and halide ions are formed through surface ionization of alkali metal halide vapour incident on a hot film of lanthanum hexaboride. A multistage electrostatic lens system positioned directly ahead of the ionizer has been designed to focus the low energy ion beam into the beam crossing region.

7.1 Ion production on a heated LaB_6 surface

The thermionic emission properties of the alkaline earth and rare earth borides have been well studied.[142] These materials emit copious quantities of electrons from their surface at temperatures above approximately 1000°C. Lanthanum hexaboride, with its low work function of 2.66 eV, gives the highest emission, a property which has led to its widespread use as a filament material for applications in gas chromatography, mass spectrometry, and electron microscopy.[142–147] The structure of LaB_6 is based around a three dimensional boron lattice, into which La atoms are embedded in the interlattice spacings. The valence electrons of La are not involved in bonding to the boron lattice and are free to move within the solid, giving a metallic character to the material. In combination with the strong bonds between lattice boron atoms this provides not only good electrical conductivity, but also high thermal and chemical stability. On heating, La atoms at the surface evaporate away from the stable boron framework and are immediately replaced by diffusion of metal atoms from within the solid. This means that an active cathode surface is always maintained and makes LaB_6 an ideal filament material.

In addition to thermionic emission of electrons, positive and negative ions may also be

produced from the LaB_6 surface when suitable precursor atoms or molecules are present. As an example, Fujii *et al*[144] observed emission of negative ions such as CN^-, PO^-, PO_2^- and PO_3^- from an electrically heated filament coated with a mixture of LaB_6 and SiO_2 when nitrogen or phosphorus containing compounds were present. The ion source described here was designed to produce ions from alkali metal halide vapour incident on an LaB_6 surface at high temperature. Emission of both Cs^+ and Cl^- has been observed from CsCl vapour, with several additional ionic species detectable under certain conditions (Section 7.3.1).

The concentration of neutrals and ions on a heated surface at thermal equilibrium is described by the Saha-Langmuir equation.[148] For a given atomic or molecular system the ratio of ionic to neutral species at thermal equilibrium at temperature T is given by.[149,150]

$$\frac{n_i}{n_0} = \frac{g_i}{g_0} \exp\left(\frac{\Delta}{kT}\right) \tag{7.1}$$

where n_i and n_0 are the densities of the ionic and neutral species desorbed from the surface, and g_i and g_0 are the statistical weights of the ground states of the ionic and neutral species. Δ is a function of the ionization potential (IP) or electron affinity (EA) of the neutral and the work function (ϕ) of the surface, and is given by $\phi - IP$ for positive ion formation and $EA - \phi$ for negative ion formation. It can be seen from Equation 7.1 that ionization will be most efficient when there is a large difference between the work function of the surface and the electron affinity or ionization potential of the precursor neutral. Vietzke *et al*[140] assumed that halide ions were formed through ionization of the neutral halogen atom on the LaB_6 surface. The electron affinities of the halogens are from 0.5 to 1 eV higher than that of LaB_6, ranging from 3.063 eV for iodine to 3.613 eV for chlorine, with fluorine and bromine lying between the two extremes at 3.448 and 3.363 eV respectively;[94] all four can therefore be ionized by LaB_6. While this explains halide ion production, it does not give insight into the mechanism of Cs^+ production. The ionization potential of Cs is 3.893 eV, too high for it to be ionized by LaB_6, with its work function of just 2.66 eV.

A literature search revealed several postulated mechanisms for negative surface ionization processes, mostly related to alkali metal thermionic ionization detectors. All involve ionization of a neutral atomic or covalently bonded molecular species on the surface.

Kolb *et al* suggested a gas phase chemiionization reaction occuring on emission of excited metal atoms from a rubidium surface as a mechanism of operation for their alkali–silicate

bead thermionic ionization detector for nitrogen and phosphorous containing compounds.

$$M^* + R \rightarrow M^+ + R^- \tag{7.2}$$

In the above equation M is the metal atom emitted from the surface and R is a radical. The above mechanism is feasible whenever the electron affinity of the radical exceeds the ionization potential of the excited metal atom. This obviously requires that the alkali metal is evaporated from the glass bead. However, it has been shown by Brazhnikov and coworkers[151] that good detection sensitivity is obtained using this type of thermionic ionization detector even when evaporation is prevented by using non volatile alkali salts in the filament, a property which is clearly inconsistent with the suggested mechanism.

An alternative mechanism, which does not require the metal atoms to leave the surface, was proposed by Oláh and coworkers.[149] In this mechanism radicals are adsorbed onto the surface and the metal atoms then catalyse electron transfer to the radical, resulting in the formation of a negative ion. When a negative bias is applied to the surface the ions are released.

$$\begin{aligned} R_{\text{vap}} &\rightarrow R_{\text{ads}} \\ M + R_{\text{ads}} &\rightarrow M^+ + R^-_{\text{ads}} \\ R^-_{\text{ads}} &\rightarrow R^-_{\text{gas}} \\ M^+ + e^- &\rightarrow M \end{aligned} \tag{7.3}$$

These two mechanisms are possibilities for production of Cl^- ions from CsCl incident on a hot LaB_6 surface, but it seems unlikely that chlorine is initially present as a neutral atom. There are several mechanisms for ion production which seem reasonable based on the thermodynamic data[152] shown in Table 7.1 for the species expected to be present on the surface.

1. Electron transfer from CsCl to a La^+ ion on the LaB_6 surface leads to production of Cs^+ ions and neutral La and Cl.

$$CsCl + La^+ \rightarrow Cs^+ + Cl + La \qquad \Delta H = 3.08 \text{ eV} \tag{7.4}$$

The difference between the electron affinity of Cl and the work function of LaB_6 means that the chlorine atoms produced in the above reaction can undergo negative surface

Table 7.1: Thermodynamic data for the species involved in ionization of CsCl on a lanthanum hexaboride surface.

Species	ΔH_f / eV	IP / eV	EA / eV	ϕ / eV
Cl^0	1.26	-	3.607	-
Cl^-	-2.549	-	-	-
Cs^0	0.816	3.893	-	-
Cs^+	4.709	-	-	-
CsCl	-2.705	-	-	-
La^0	4.463	-	-	-
La^+	10.057	-	-	-
LaB_6	-	-	-	2.66

ionization to give Cl^-.

$$Cl \xrightarrow{LaB_6} Cl^- \qquad EA - \phi = 1.233 \text{ eV} \tag{7.5}$$

The first step in this mechanism is 3 eV endothermic in the gas phase due to the high bond strength of the Cs—Cl bond. However adsorption to the LaB_6 surface may well weaken this bond and make this process more energetically favourable. La^+ ions have a fairly high electron affinity of 5.61 eV and it is possible that a fairly strong physical or chemical bonds to the electronegative chlorine atom may be formed before the electron transfer takes place. There are several alternatives to the second step. In addition to undergoing surface ionization the neutral Cl radicals may also undergo recombination on the surface to form Cl_2. Alternatively Cl may be desorbed from the surface before either of these processes can occur.

$$\begin{aligned} 2\ Cl &\rightarrow Cl_2 \\ Cl_{(ads)} &\rightarrow Cl_{(g)} \end{aligned} \tag{7.6}$$

These competing processes may help to explain the fact that the detected positive ion emission current from the ion source is always considerably larger than that for negative ion emission.

2. The second mechanism is initiated by electron attachment and subsequent fragmentation of the CsCl, either in the gas phase or on the surface, followed by charge transfer

between the neutral Cs produced and a La^+ ion.

$$CsCl + e^- \rightarrow Cs + Cl^- \qquad \Delta H = 1.4 \text{ eV} \tag{7.7}$$

$$Cs + La^+ \rightarrow Cs^+ + La \qquad \Delta H = -1.72 \text{ eV} \tag{7.8}$$

The charge transfer step should be highly efficient since it is a fairly exoergic process. While this mechanism cannot explain the difference in the signal sizes for positive and negative ions, it does have the advantage of a lower energy barrier, at least in the gas phase, for the first step.

3. A third possiblity is that the CsCl dissociates into neutral Cl and Cs on the LaB_6 surface. Negative surface ionization of Cl would then lead to Cl^- ion formation (second step of mechanism 1), while charge exchange between Cs and La^+ ions as in the second step of mechanism 2 would result in the production of Cs^+ ions.

7.2 *Ion source design*

The basic components of the ion source are a silica oven, which acts as the alkali metal salt reservoir, a resistively heated porous graphite disk coated with LaB_6 on which ionization occurs and a series of plane element electrostatic lenses for extraction and focusing of the ion beam. In addition, some mechanism is required for removal of electrons from the beam when the source is being used for negative ion production. This problem is discussed in Section 7.3.1*.

The ion source assembly is shown in Figure 7.1. Two flanges joined together by three circular rods form the basic support structure. The base flange is mounted onto the 6″ flange of a Huntington Laboratories PM–600 *xyz* translator. This allows the ion source position to be adjusted to facilitate alignment of the ion beam with the molecular beam axis when the source is installed in the molecular beam machine. The small oven, in which alkali halide vapour is formed prior to ionization, consists of a length of silica tubing wrapped in fibreglass insulation material. For the measurements described in this chapter the oven was packed with CsCl.

A major problem associated with using LaB_6 as an ionizing material is its high reactivity with refractory metals at the temperatures required for ion formation. At high temperatures

* If the oven is not filled the ion source could be used as a highly efficient electron gun with a few modifications to the lens system.

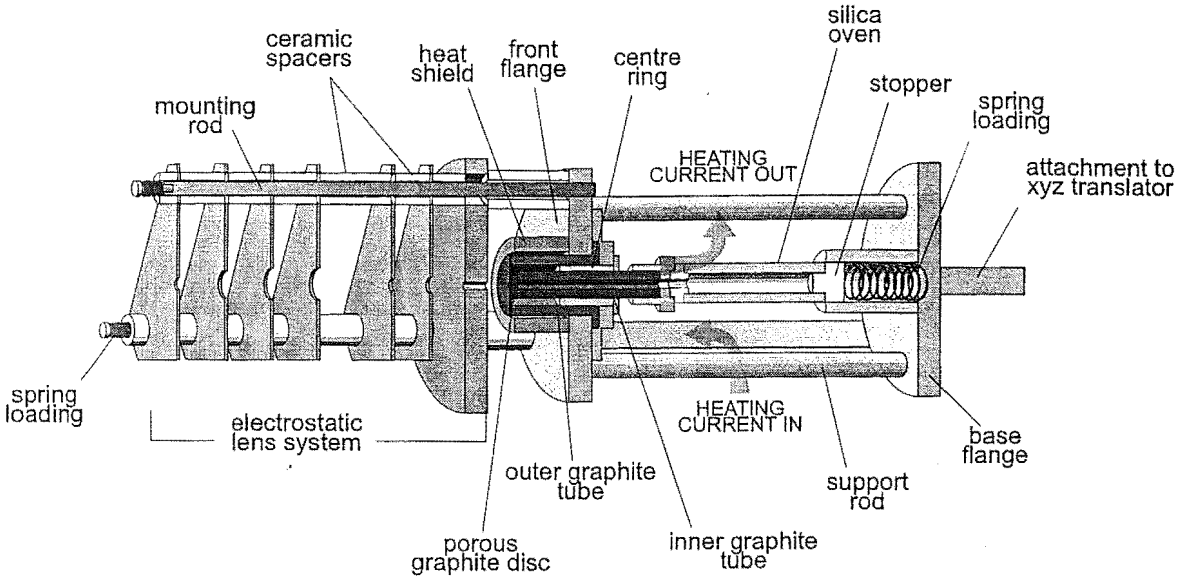

Figure 7.1: Cutaway view of the halide ion source.

boron atoms diffuse into the metal substrate and lanthanum atoms evaporate from the surface as the LaB_6 structure disintegrates. In applications where filaments directly coated with LaB_6 powder have been used, the emission of electrons falls off rapidly after just a few hours of operation due to this degradation process.[139] These problems are overcome in the ion source described here by using graphite as the substrate onto which LaB_6 is coated.

The electrical heating circuit is made up of three graphite parts. A 1 mm thick disk of porous graphite is sandwiched between two concentric graphite tubes as shown in Figure 7.2. A ceramic centre ring separates the two tubes and aligns the components of the ionizer tip. Because LaB_6 powder does not bind well to graphite, it is formed into a slurry with ethanol and deposited onto the top face of the porous disk using an eye-dropper. As the alcohol evaporates the LaB_6 remains behind as a stable layer and is baked[153] onto the graphite surface as the tip is heated to operating temperature. It was found that if the LaB_6 is coated too heavily onto the graphite disk the negative ion signal becomes unmeasurably small. This is possibly due to space-charge effects caused by electrons emitted from the hot LaB_6 surface which scatter the negative ions before they can be focused by the lens system.

A spring loading system ensures a good electrical contact between the graphite parts and helps to keep the various components centred along the length of the source. The spring itself is housed inside a short length of stainless steel tube centred on the base flange of the source and presses against the ceramic stopper at the base of the oven. A second stopper,

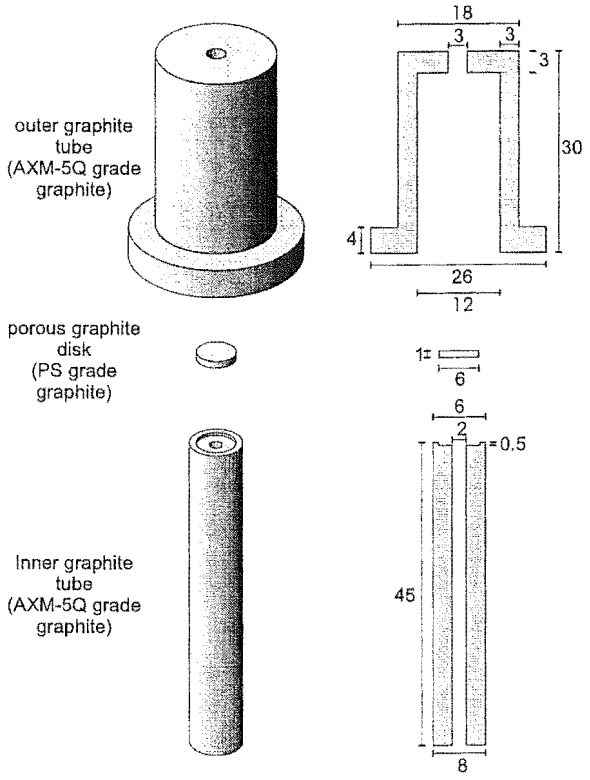

Figure 7.2: Components of the graphite tip for the halide ion source. All dimensions in mm.

with a small aperture to allow alkali halide vapour from the oven through to the ion source tip, fits between the front end of the oven and the holder for the inner graphite tube. The small graphite disk is pressed into the front end of the inner graphite tube and is held firmly between the two concentric tubes, the outer of which is fixed in place on the front support flange of the source, by pressure from the spring at the base of the source. A pair of copper bars mounted to the support flanges of the source form the electrical connection from the outer graphite tube to the vacuum feedthrough via a length of copper braid, while four lengths of copper braid attached to the stainless steel holder for the inner graphite tube form the connection to the negative terminal of the feedthrough. A ceramic heat shield encasing the graphite section of the source reflects heat back towards the tip. The high current required to heat the tip, typically around 60 A at 3-4 V, is supplied by an Oxford Instruments MK3 DC power supply.

Initially the oven was wrapped in nichrome wire and separately heated to produce alkali halide vapour. However, it was found that enough heat was transferred from the tip of the source to make this unnecessary, and the wire wrapped oven was replaced with the thermally

insulated silica tube described earlier. A thermocouple located beneath the fibreglass insulation and in thermal contact with the outer oven wall indicates that the oven typically reaches temperatures of around 300–500°C. Alkali halide vapour produced in the oven passes along the inner graphite tube and diffuses through the heated porous graphite disk, with ionization occuring as it strikes the LaB_6 surface. Typical operating temperatures for the resistively heated tip are in the range 1300–1500°C. The tip is biased positive or negative depending on the polarity of the ion beam required.

The temperature of the tip and also of the alkali halide oven are monitored using C type (tungsten vs tungsten/26% rhenium) thermocouples. The C type thermocouple is calibrated up to 2800°C and provides the highest calibrated temperature of any wire thermocouple. A standard calibration curve for this thermocouple[154] is shown in Figure 7.3. As discussed in Section 7.3.1, the positioning of the thermocouple relative to the tip meant that further temperature measurements with an optical pyrometer were necessary in order to accurately calibrate the thermocouple reading to the ion source tip temperature.

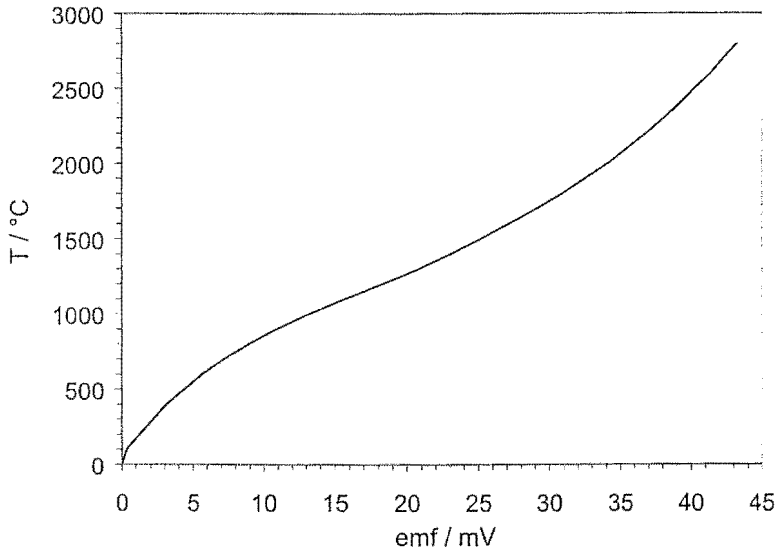

Figure 7.3: Standard calibration curve for a C type (tungsten vs tungsten/26% rhenium) thermocouple.[154]

7.2.1 *Electrostatic lens system*

For crossed beam experiments an ion beam is required with a well defined translational energy of typically less than 10 eV. This provides an energy range of up to four or five electron volts above the reaction threshold of the endoergic reactive collisions to be studied. It is well

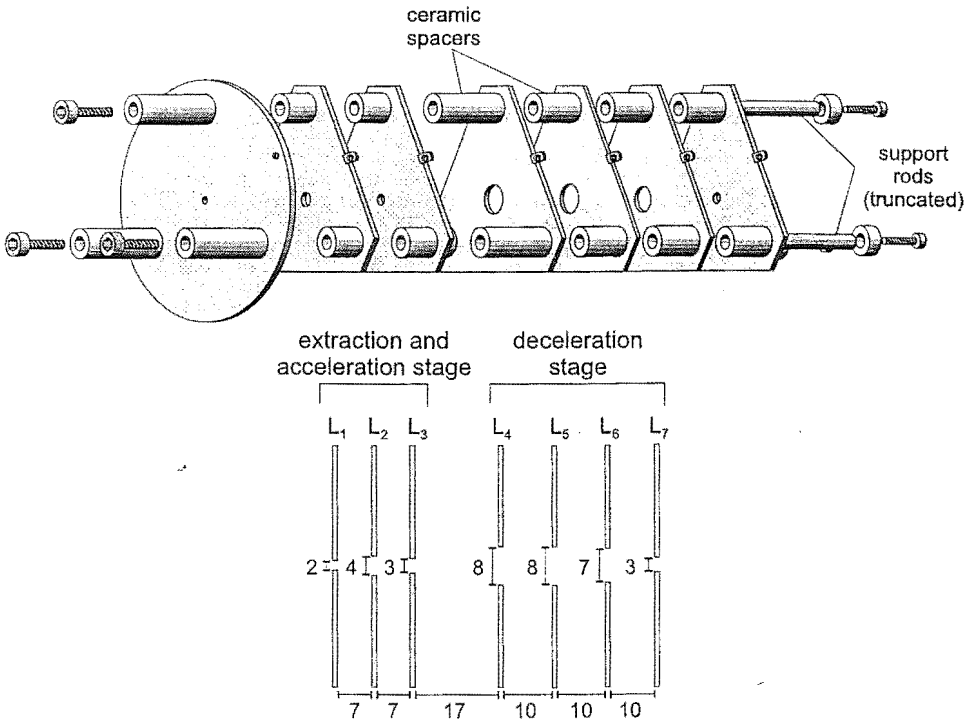

Figure 7.4: Electrostatic lens system used for extraction and focusing of a low energy ion beam.

known that in the energy region below 100 eV space charge effects can have a major impact, not only on the intensity, but also the beam shape and energy of an ion beam. Simpson and Kuyatt[155] showed that a further limit is imposed on the beam current at low energies, in addition to the space–charge limit, due to thermal effects at the emitter surface. These limitations can be overcome if the thermal energy of the ions and the space–charge effects are decoupled by first accelerating the ions to a fairly high energy, and then decelerating to the required energy; the so called 'multistaging principle'. This technique was first applied to the production of low energy ion beams by Haskell and coworkers in 1966.[156]

The halide ion source incorporates a multistage lens system consisting of seven electrostatic plane lens elements, as shown in Figure 7.4. The first four elements comprise the extraction and acceleration stage, while the final three lenses form the deceleration section. The lenses are mounted on a set of three stainless steel rods bolted to the front flange of the ion source. Ceramic spacers isolate each lens from the rods and from adjacent elements. Small springs located at the front end of the lens system prevent damage to the ceramic components during the heating and cooling cycle by allowing for thermal expansion. Initially the lenses were all constructed from 0.9 mm thick stainless steel. However, preliminary tests

showed that stainless steel could not withstand the high temperatures to which the first lens element is exposed, and to solve this problem a water cooled copper lens was constructed (for full details see Appendix E). Eventually this was replaced with a molybdenum element, the high melting point of which eliminated the need for water cooling.

SIMION6.0[32] calculations were carried out to simulate ion trajectories through the system, and indicated that a well collimated beam should be obtainable down to energies as low as 0.5 eV. During experimental testing of the ion source it was found that a fairly intense ion signal could be measured for energies as low as 0.1 eV, particularly for positive ions.

7.3 Characterisation

7.3.1 Temperature profile of the tip

Before coating the porous graphite tip with LaB_6 and packing the oven with the alkali halide salt, an optical pyrometer was used to measure the dependence of the tip temperature on the heating power. The lens system was removed and the ion source mounted in a test chamber with a window directly in front of the tip. A modified Varian AA3 AC high current/low voltage power supply was used to supply the heating current for these measurements, though this was replaced at a later stage by a DC supply to enable the ion source tip to be floated at a constant potential so that the ion energy could be controlled. The optical pyrometer could be used to measure temperatures above 800°C by viewing the ion source tip through the window in the vacuum chamber. It was found that once the temperature reached approximately 1100°C the temperature was linearly proportional to the heating power. This dependence is shown in Figure 7.5.

The thermocouple which records the temperature of the tip is located as close to the tip as possible, in contact with the inner graphite tube. Comparing the thermocouple temperature readings, using the calibration curve shown in Figure 7.3, with the temperatures measured using the optical pyrometer indicates that there is a significant temperature differential between the graphite disk and the position of the thermocouple. It was therefore necessary to recalibrate the thermocouple to the optical pyrometer reading so that the thermocouple could be used independently to measure the temperature of the tip. The temperature differential was found to have a linear dependence on temperature and is plotted in Figure 7.6 in terms of the measured emf at the thermocouple and a 'corrected' emf. The corrected emf is the ther-

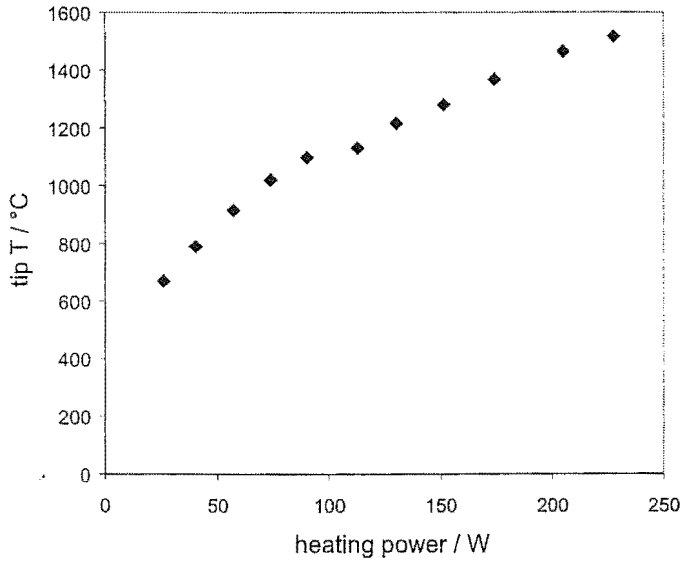

Figure 7.5: Dependence of ionizer temperature on heating power.

mocouple emf which corresponds to the optical pyrometer reading and was calculated using the standard C–type thermocouple calibration curve in Figure 7.3. This linear relationship can be used to correct the standard calibration curve to give the true tip temperature as a function of the emf induced across the thermocouple. The calibration curve is shown in Figure 7.6. A polynomial fit to the curve provides an analytic expression for the temperature corresponding to a given thermocouple reading.

$$\begin{aligned} T &= -778.453 + 442.997V - 48.0841V^2 \\ &\quad +3.01098V^3 - 0.0919914V^4 + 0.00116595V^5 \end{aligned} \tag{7.9}$$

The thermocouple which monitors the alkali halide oven temperature is used with the standard calibration curve. Since the oven temperatures are at the lower end of the thermocouple range and the position of the thermocouple means the reading may not accurately represent the temperature inside the oven near the front end, where most of the vapourisation occurs, the thermocouple reading is only used as an indication of the oven temperature. This temperature is not critical so long as it is high enough to ensure a significant vapour pressure of the alkali halide salt.

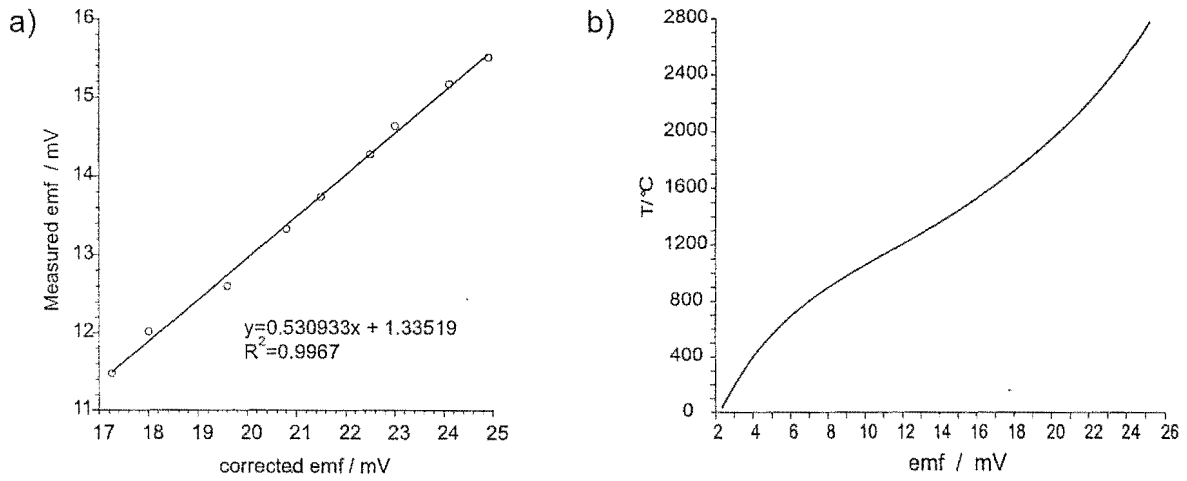

Figure 7.6: a) Temperature differential between inner graphite tube and porous graphite tip; b) Calibration curve for C type thermocouple used to measure temperature of ion source tip

Element	Voltage bias / V	Electron current / nA
L_2	50	-0.5385
L_3	80	- 3.7567
L_4	120	-10.4525
L_5	80	-0.6864
L_6	10	-2.6421
L_7	0	-7.5876

Table 7.2: Measured electron currents reaching each electrostatic lens element.

Electron emission

Before the oven was packed with CsCl, the porous disk at the ionizer tip was coated with LaB_6 and the source heated to operating temperature in order to determine whether electrons traversing the ion lens system would be a problem when the tip and lenses were biased for negative ion transmission. The lenses were set to the approximate values which would be used to focus a 5 eV negative ion beam and electron currents to each lens were measured using a Keithley Model 486 picoammeter. The first lens is not included in the results shown in Table 7.3.1 since any electrons not entering the lens system strike this element giving rise to a large current signal, often up to several microamps.

Sizeable electron currents to all of the lens elements were detected, with several nanoAmps

collected on the final lens. This is comparable to the expected ion currents, indicating that electrons would form a significant component of any 'negative ion' beam and should be removed. Removal of the electron component can be achieved by either mass or velocity/momentum selection of the beam. Mass selection involves setting up a fairly weak magnetic field to trap the electrons. SIMION6.0 simulations indicated that a magnetic field of 200-500 Gauss between the tip and the first ion lens should be sufficient to remove electrons from the beam, while the ions, with their much higher mass, would be unaffected by the field. This is consistent with measurements made by Vietzke *et al*[139] for their halide ion gun. Several attempts were made to establish such a field, but none were successful. Initially a pair of ceramic magnets (Magnetic Supplies N.Z. Ltd.) were mounted on the first electrostatic lens element. The field strength between the pole faces was measured with a Hall probe to be 280 Gauss. These magnets have a Curie temperature of around 400°C, though magnetisation begins to fall off irreversibly at around 150°C, and despite the fact that the lens was water cooled at that time demagnetisation was a problem. The same problem occurs if the magnets are mounted on the final lens element due to heat conduction along the mounting rods for the lens system, which are only insulated from the lenses themselves by a thin lip on the ceramic spacers which separate the lenses. At a later stage, when the ion source was installed in the molecular beam machine, magnets were mounted on the scattering chamber side of the partition between the two chambers, eliminating the problem of overheating. However, no ions were observed with this configuration and the ion imaging detector showed that the magnetically trapped electrons were forming a space-charge cloud around one magnet pole, preventing ions from entering the scattering chamber.

Attempts to construct an electromagnet for the purpose were equally unsuccessful. Such an electromagnet must not only fit the physical size restrictions which are imposed by the location of the ion source chamber dimensions, it must also produce a strong enough magnetic field to remove electrons from the beam despite the rather large pole separation imposed by the space limitations. In addition, it must be capable of running continuously in a vacuum without overheating. This requires a cooling system to remove not only the heat generated by the current flow through the electromagnet windings, but also the heat radiated from the tip of the ion source. These difficulties could not be readily overcome without major workshop involvement.

There are several possible alternatives to magnetic field separation of electrons from ions

based on velocity or momentum separation rather than mass selection. One possiblility would be to install a hemispherical velocity analyser tuned to the ion beam velocity between the ion source and the crossing region, though this would require significant modifications to the current layout of the ion source and scattering chambers. A second approach would be to separate the components of the beam via time of flight. A short flight tube with an electrostatic lens at each end should be sufficient to achieve this separation. The first lens element is used to gate the beam and send a pulse of ions down the flight tube. A second gating pulse on the element at the far end of the flight tube is delayed by a time equal to the flight time of the selected ionic component of the beam. Provided the flight tube is long enough the electron and ion components of the pulse entering the flight tube will arrive at the far end at significantly different times, and only the component for which the delay is tuned will be transmitted. Again, fairly major modifications to the chamber layout would be required to acommodate the flight tube. Neither of the methods suggested above have been tested at the present time, but both may need to be examined in the future.

Ion emission

After the preliminary measurements described above, the silica oven was packed with CsCl (AnalaR Biochemical BDH Chemicals Ltd) and the ion source installed on axis with a Vacuum generators SXP300 quadrupole mass spectrometer.

As noted in Section 7.1 the observed positive ion signal is considerably larger than the negative ion signal; this may well be due at least in part to a lower detection efficiency of the mass spectrometer for negative ions. Reasonable signals for both Cs^+ and Cl^- can be detected down to energies well below 1 eV. Total ion emission curves were measured as a function of ion source temperature by connecting a Keithley 486 picoammeter to the first electrostatic lens element and monitoring the ion signal to this lens as a function of the ion source tip temperature as the source was heated or cooled. It was found that the data measured as the ion source cooled was more reliable since the signal is not affected by instabilities in the high current supply which can cause fluctuations in the tip temperature during the heating cycle. The 0-2 V analogue output from the Keithley and the signal from the thermocouple used to monitor the tip temperature were taken through separate channels of a three channel isolation amplifier to a PC for data collection. Ion emission as a function of tip temperature is shown in Figures 7.7 for positive and negative ions. It should be noted that the emission

curve for negative ions also includes a considerable contribution from electrons emitted from the hot LaB_6 surface of the ion source tip.

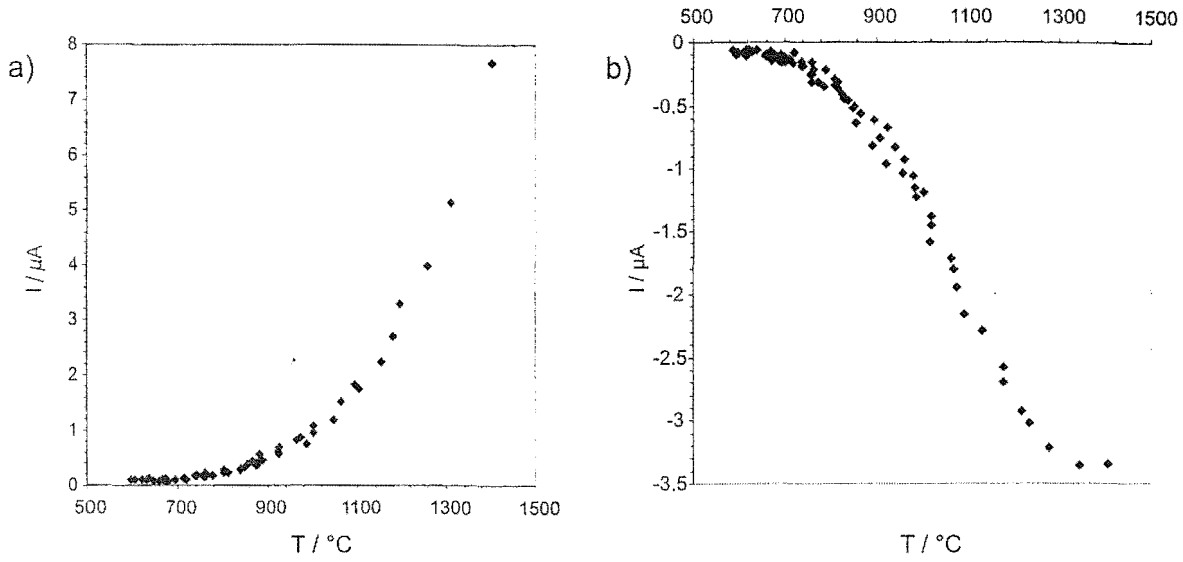

Figure 7.7: a) Positive and b) negative ion current reaching L_1 as a function of ionizer tip temperature for a CsCl packed oven. Tip potential 5 V, L_1 -50 V, L_2-L_6 grounded.

Positive ion emission begins at approximately 700°C, with the signal rising exponentially as the temperature is increased. The cutoff temperature of the curves corresponds to the maximum current which can be supplied to the source by the high current DC supply. This is initially around 60 A, but drops to below 50 A at high temperatures due to the increase in resistance of the graphite on heating. Negative signals also start to increase at around 700°C. However, a Cl^- ion signal cannot be detected at the quadrupole mass spectrometer until significantly higher temperatures are reached, indicating that electrons are the primary component of the beam at lower temperatures. The negative signal appears to level off at a temperature of around 1300°C. A possible explanation for the larger observed positive ion signal is given in Section 7.1.

When the ion source lenses and tip are biased for transmission of Cl^- ions several other negative ions, including O^-, CN^-, and OH^- are observed at higher tip voltages. These ions are formed by electron impact ionization of background gas within the lens system by electrons emitted from the hot LaB_6 surface. By adjusting the lens potentials these signals can be reduced, though ideally electrons should be removed from the beam before entering the lens system.

Initially Cs^+ was the only positive ion observed. However, over a period of several months

of testing a significant K^+ impurity in the beam signal became detectable. The origin of the K^+ is unknown, though a high temperature process involving the ceramic components or the fibreglass electrical insulation used in the source seems the most likely explanation, particularly since the problem was first noticed after replacement of the water cooled first lens element. Thorough cleaning of the source reduced the K^+ signal somewhat. No significant impurities have been observed in the negative ion beam.

8. ION IMAGING AND DATA ANALYSIS TECHNIQUES

The crossed beam experiment described in this thesis utilizes the fairly new technique of ion imaging for product ion detection. The first part of this chapter details the principle of operation of an ion imaging system and provides a brief history of chemical dynamics experiments in which the technique has been employed. This is followed by a discussion of the Monte Carlo simulation and data fitting techniques used in the data analysis software developed for the crossed beam experiments, described in Chapter 10, and also in analysing data from the molecular beam characterisation experiments described in Chapter 5. Initial experience was gained in the use of both simulation and data fitting methods while involved in a study into the stereodynamics of the $H+H_2O$ reaction at Oxford University, where such techniques are extensively used in the extraction of dynamical information from Döppler resolved laser induced fluorescence profiles. The work carried out at Oxford will be included separately in Chapter 9.

8.1 Literature review: the ion imaging technique

Several experimental techniques are available for the measurement of velocity distributions and differential cross sections for bimolecular reactions and photo–ionization processes. In the classic crossed beam experiment a moveable time–of–flight mass spectrometer is employed for mass selective detection of the products of a bimolecular reaction. While the complete differential cross section, product velocity distribution and sometimes even product internal state information can be determined in this way, the method is time consuming since data must be collected one angle at a time, and inaccuracies in the measurements can arise due to drift in experimental conditions over the long signal collection times involved.

The increasing availability of lasers in recent years has introduced a range of spectroscopic detection techniques to the field of chemical dynamics. Schemes such as resonance–enhanced multiphoton ionization (REMPI), laser induced fluorescence (LIF) and coherent anti–Stokes Raman scattering (CARS) provide quantum state selective product detection,[157–163] allow-

ing the determination of product quantum state distributions and integral cross sections. REMPI is often combined with time–of–flight measurements, which give the one dimensional projection of the product velocity distribution, to allow simultaneous extraction of product state information and product speed distributions.[164–170] A specialised application of this is hydrogen Rydberg time–of–flight detection,[171–173] which provides high translational energy resolution for reactions in which hydrogen or deuterium are formed. As explained in detail in Chapter 9, measurement of Döppler resolved LIF or REMPI spectra provides a means for obtaining information on vector correlations between reagent and product relative velocities and angular momenta under certain conditions.

The first experiments in which product spatial distributions were directly imaged were carried out by Solomon.[174] In their 'photolysis mapping' experiments a glass hemisphere coated on the inside with a thin film of tellurium was used as the photolysis cell. Polarised light from a mercury lamp was used to photolyse bromine and iodine samples within the cell, and after some hours of exposure to the light an anisotropic lightening of the tellurium coating was observed due to etching by the halogen atom photofragments. The photolysis mapping technique has since been applied to several other molecules[175,176] and provided the inspiration for the development of the much more sophisticated ion imaging technique to be discussed here.

Ion imaging detection was originally developed for use in the study of photodissociation processes and is fast becoming the detection method of choice for a wide range of chemical dynamics experiments. The ion imaging technique allows the spatial distribution of a product species to be directly visualised, and offers the previously unparalleled opportunity of recovering the entire three dimensional angular and velocity distribution of a photolysis or reaction product in essentially a single measurement. A schematic of an ion imaging detector is shown in Figure 8.1

The first stage in the system is a pair of microchannel plates (MCP's) arranged in a chevron configuration. Each channel plate consists of an array of tiny laser drilled holes or 'channels' in a thin silica disk coated with a special resistive material. The principle of operation is identical to that of more conventional particle multipliers. When a charged particle strikes a channel wall at the front face of the plate secondary electrons are released from the surface. The secondary electrons propagate through the channel, producing further secondary electrons each time they collide with the coated surface. Each ion striking the

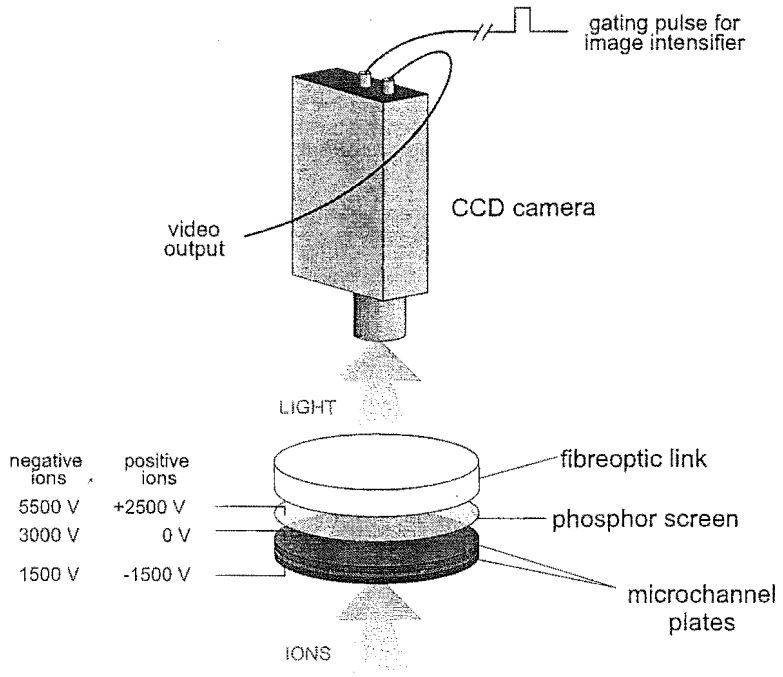

Figure 8.1: Schematic of an ion imaging detector.

front face of the MCP therefore gives rise to a small current pulse at the rear face. The gain under typical operating conditions can be up to 7×10^7 secondary electrons per ion strike.[177] The burst of electrons strikes a fast phosphor screen and excites the phosphor, producing a flash of light. The resulting image on the phosphor screen is transferred through either a lens or a fibreoptic bundle, which usually forms the vacuum interface, to a CCD (charge–coupled device) or CID (charge–injection device) camera. Images can then be viewed on a monitor and/or captured on a PC equipped with a frame grabber card for further processing.

In a typical photofragment imaging apparatus the ion imaging detector forms part of a modified Wiley–McLaren time of flight mass spectrometer, with repeller and extractor field plates followed by a flight tube positioned directly below the imaging detector.[177] A pulsed molecular beam enters the vacuum chamber containing the ion imaging optics and is intersected by two laser pulses as it passes below the detector. The first pulse dissociates the parent molecule, while the second ionises a selected rovibrational state of one of the fragments. After a short time delay of around 100 ns a voltage is applied across the extraction plates to accelerate the ion cloud towards the detector. With careful adjustment of the voltages applied to the two field plates the ion cloud will be flattened into a pancake as it strikes the detector.

This type of apparatus has been widely used to investigate the photodissociation dynamics of a large range of molecules.[177,178] More recently the techniques have been extended to probe the products of reactive encounters. Walter *et al*[179,180] studied translational energy release in dissociative electron attachment to small halocarbons such as C_2Cl_4, $CFCl_3$ and CH_3I. In these experiments a thermal energy potassium atom beam is passed through a collision chamber containing the halocarbon gas. A laser intersecting the beam at right angles is used to excite the atoms to high lying Rydberg states, in which the Rydberg electron behaves essentially as a free electron. On colliding with the target gas dissociative recombination reactions of the type $e^-+AB \rightarrow AB^{*-} \rightarrow A^-+B$ occur. Any negative ions formed in the process are extracted through a flight tube to a position sensitive detector situated above the plane of the atom and laser beams. The random orientation of the scattering gas means that angular information cannot be obtained, but translation energy distributions for the product ions can be extracted from the experimental data. For some of the molecules studied, such as CCl_4, $CFCl_3$, these distributions agree well with statistical theories of unimolecular decay, indicating that the excess energy of the bound complex is well distributed among internal modes before dissociation occurs. However, in other cases dissociative attachment results in a considerable fraction of the excess energy appearing as translation in the product, indicating rapid dissociation on a repulsive potential energy surface and implying that the electron is captured directly into an antibonding orbital localised on the ejected halide atom.

Bontuyan *et al*[181] were able to measure state to state differential cross sections for rotationally inelastic collisions of NO with Ar, in the first application of ion imaging to product detection in a crossed beam experiment. Pulsed molecular beams of the two reagents are intersected at right angles and scattered NO molecules are ionized state selectively via (1+1) REMPI using a tunable UV laser pulse propagated counter to the Ar beam. The resulting ions are extracted upwards through a flight tube to an ion imaging detector. The Ar beam is toggled on and off during the experiments and the difference images accumulated as the laser is scanned through the different product rotational states. The collision energy can be controlled by seeding the NO in different carrier gases and experiments were carried out at collision energies of 0.1, 0.21 and 0.35 eV. It is possible to determine the collision energy from the Newton diagram for the crossed beams, which can be directly visualised by counterpropogating the ionizing laser beam, tuned to the major rotational component of NO in the beam, along each of the two beams in turn. For these measurements the Ar beam is

seeded with a small quantity of NO to allow visualisation. Ions formed along the beam tracks appear as a line on the image, while ions formed at the point where the two beams cross are displaced in the image due to the forward momentum of NO in the beam, and appear as a distinct spot on each beam axis. The resulting image allows both beam velocities, and therefore the center of mass collision energy, to be determined. The crossed beam experiments show rotational rainbow peaks in the angular distributions of the scattered NO which move to backward scattering angles with increasing final rotational state.

The first experiments for which ion imaging was used to detect the products of reactive scattering were those of Buntine *et al*,[182] who investigated the H+HI→H_2+I reaction. In this study a supersonic expansion of HI is intersected by a tunable laser, producing translationally hot H atoms with a bimodal speed distribution* through HI photolysis. The nascent H_2 products are ionized through (2+1) REMPI and directed towards the ion imaging detector. The resulting images can be analysed to extract the product translational energy distribution, giving interesting insights into the possible reaction channels accessible, though as in the case of the dissociative recombination study of Walter and coworkers described above, the random orientation of the reagents means that angular information cannot be recovered. The same group have also carried out experiments on the H+D_2 reaction.[183,184] The reagents are prepared in separate beams; a beam of HI is crossed with a D_2 beam and photolysed to produce the H atom reactant. In this case the well defined initial velocity vectors allow angular information to be extracted from the ion images. A beam of HI is crossed with a D_2 beam and photolysed to produce the H atom reactant. This arrangement has the advantage that because the two velocity components of the photolytically produced H atoms have orthogonal angular distributions, a single reagent velocity channel can be selected to collide with the D_2 beam by choosing the appropriate photolysis laser polarisation. The D atom product was ionized by two colour (1+1) REMPI and imaged. The images show strong forward scattering of the atomic fragment, with a small amount of sideways scattering thought to be due to products associated with internally excited HD coproduct.

8.2 Image reconstruction and data analysis

As explained in Section 8.1, an ion image is a two dimensional projection of the three dimensional product ion velocity distribution. The raw images alone contain a great deal of

* The two H atom channels correspond to the I($^2P_{3/2}$) and I($^2P_{1/2}$) coproducts.

qualitative information on the process under study.[178] The outer edge of the image and any visible rings within the image can be directly converted into the maximum velocity of the product ions and can also yield information about the internal energy of the unobserved coproduct, though contributions from different channels are likely to overlap. In experiments with angular resolution the general form of the differential cross section for the collision process is usually evident in the unprocessed images. However, in order to obtain quantitative information from an ion image it is usually necessary to use image transformation or simulation techniques to reconstruct the three dimensional velocity and angular distribution for the observed products. In polarized laser photolysis studies the angular distribution reflects the symmetry of the electronic transition involved in the dissociation, while in studies of reactive collisions the three dimensional distribution can be used to determine the differential cross section and product velocity distribution for a collision process. It may also be possible to determine branching ratios for the various product quantum states by comparing the relative areas of visible rings in the reconstructed image which correspond to different product internal states.

8.2.1 The Abel inversion method

If the three dimensional product distribution has an axis of symmetry, an inverse Abel transform can be carried out on the raw image to recover the initial distribution. For an experiment in which the y axis defines the symmetry axis and the products are extracted along the direction of the z axis, the ion image $i(x, y)$ is obtained from the product ion distribution $P(x, y, z)$ by integrating over z

$$i(x, y) = \int_{-\infty}^{\infty} P(x, y, z) dz \tag{8.1}$$

A single row of the image is obtained from the projection of a slice $s(\sqrt{x^2 + z^2}) = s(r) = P(x, y_0, z)$ taken perpendicular to the symmetry axis at some fixed value y_0 of y, onto the xy plane.

$$f(x) = i(x, y_0) = \int_{-\infty}^{\infty} s(\sqrt{x^2 + z^2}) dz = 2 \int_{0}^{\infty} s(\sqrt{x^2 + z^2}) dz \tag{8.2}$$

Converting to polar coordinates gives the Abel transform.

$$f(x) = 2 \int_{x}^{\infty} \frac{s(r) r}{\sqrt{r^2 - x^2}} dr \tag{8.3}$$

where $r^2 = x^2 + z^2$. The inverse transform,

$$s(r) = \frac{1}{\pi} \int_r^\infty \frac{df(x)/dx}{\sqrt{x^2 - r^2}} dx \tag{8.4}$$

allows $s(r; y_0)$ to be obtained for each row $f(x; y_0)$ of the projected image. There are several computer algorithms available for performing the inverse Abel transform.[185]

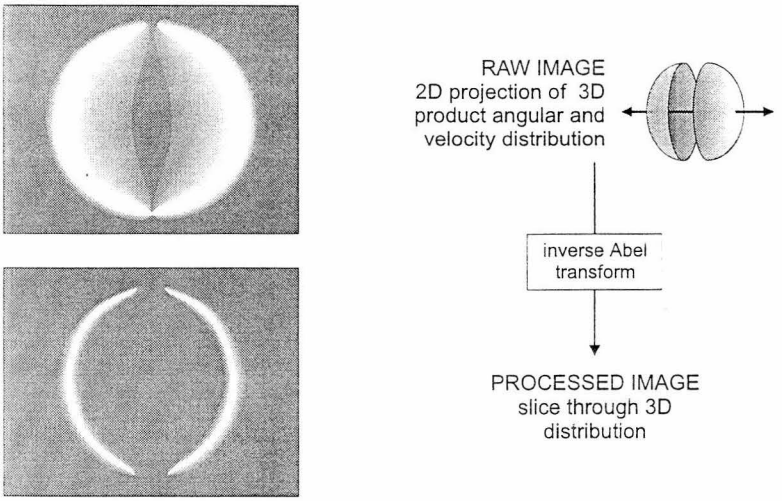

Figure 8.2: Illustration of the Abel transform image reconstruction technique.

Carrying out the inverse Abel transform on an ion image results in an image of a slice through the center of the three dimensional distribution, as shown in Figure 8.2. The Abel transform method has been widely used in many ion imaging studies of photodissociation processes and gives a unique solution for the three dimensional velocity distribution.

8.2.2 Forward simulation method

While the Abel inversion method has the advantage that the transform is unique, it is also extremely sensitive to noise and it is difficult to deconvolute the effects of machine functions such as molecular beam or laser beam width[181] from the image. The method can only be used for systems with an axis of cylindrical symmetry, and the difficulties mentioned above mean it is not always the method of choice even for these systems. An alternative strategy for reconstruction of the 3D scattering pattern is forward simulation of the images, in which an image is constructed by performing an iterative convolution over experimental parameters for various different trial functions in order to determine the trial function which best matches the image under study. This type of method allows a much more accurate treatment of machine

parameters, though it does not yield a mathematically unique set of product distributions and can be computationally expensive. There are two different approaches to a forward simulation analysis. If integrable forms of the various experimental parameters are available the trial distributions can be directly integrated over the experimental parameters to simulate the observed results.[186,187] Alternatively, Monte Carlo simulations may be performed;[188] this is often the only choice when easily integrable forms of experimental parameters are not available. The Monte Carlo method has the advantage that the effect of varying experimental parameters may be easily investigated, making it a useful tool for experimental optimisation, though at a cost of increased computational time.

8.3 Data analysis methods

8.3.1 Monte Carlo simulation methods

Simulation can be defined as a technique of performing sampling experiments on a model of a system under study.[189] Because the sampling process involves the use of random numbers the method is often referred to as Monte Carlo simulation†

Computer simulation was once regarded as almost a final resort method in the field of data analysis, to be tried only when all else had failed. However, advances in software and processing speed have made simulations an increasingly valuable tool which is widely used in a large number of disciplines. In cases where analytic solutions to the equations modelling a system cannot be found, Monte Carlo simulation is often the only option, and consequently it is now one of the most powerful and commonly used techniques for analyzing complex systems. The applications of the Monte Carlo simulation technique described in this thesis are essentially evaluations of multidimensional integrals over the various velocity distributions, laser and particle beam profiles, and machine parameters involved in a range of molecular dynamics experiments.

Simulated data can be used in several ways. When applied to the interpretation of experimentally measured data, the simulation generally tries to replicate the experimental data set. The parameters which were used in the simulation to obtain the best fit result are then assumed to be a good indication of the values of the corresponding parameters in the system being modelled. This is the strategy used in modelling beam velocities in

† The term was first introduced during the second World War as a code word for a project involving Monte Carlo simulations on problems related to the atomic bomb.

Chapter 5 and in the analysis software for the ion imaging experiments described in Chapter 10. An application of Monte Carlo simulation to the generation of a set of basis functions used in fitting data from reaction dynamics experiments is described in Chapter 9. Computer simulation of an experiment can also provide valuable guidance in the design and optimisation of an experimental system, allowing the effects of changes to the system to be investigated at the computer before they are tested in the laboratory. An example of this type of application is given in Chapter 10.

In order to carry out a Monte Carlo simulation of a system, a well defined model is required, parameterised in terms of a finite set of variables. Initialization consists of selection of a large number of parameter sets using a random number generator. Trajectories are then run through the model system for each of the parameter sets. The required data is extracted from each trajectory and averaged to give the final result. The functional dependence of the system on a particular variable can be investigated by carrying out simulations for a range of fixed values of the parameter.

Convergence and variance reduction methods

For a number of sample points N, the basic theorem of Monte Carlo integration estimates the integral of a function f over a multidimensional volume V to be[190]

$$\int f dV \approx < f > V \pm V\sqrt{\frac{< f^2 > - < f >^2}{N}} \tag{8.5}$$

in which the second term is a one standard deviation error estimate which gives a rough indication of the probable error in the integral. The angled brackets indicate the mean over the N sample points. i.e.

$$\begin{aligned} < f > &\equiv \frac{1}{N}\sum_{n=1}^{N} f(x_n) \\ < f^2 > &\equiv \frac{1}{N}\sum_{n=1}^{N} f^2(x_n) \end{aligned} \tag{8.6}$$

Essentially, Equation 8.5 states that the error in a Monte Carlo integral decreases as $N^{-1/2}$. A check should be made that enough points are included in a Monte Carlo calculation to ensure that the multidimensional integral over the various distributions included in the simulation has converged to the true value[‡]. In the application of the Monte Carlo procedure

[‡] In practice, if a Monte Carlo simulation is not sufficiently converged then rerunning the simulation program with a higher value of N will change the result obtained.

to the extraction of differential cross sections and product translational energy distributions from composite Döppler profiles and ion images described in Sections 9.1.2 and 10.2.7, poor convergence will lead to erroneous results. There are methods which can be used to improve the rate of convergence, such as importance sampling and stratified sampling,[189,190] but these were not easily adapted to the simulation problems described here and will not be discussed further. An alterative approach to improving the convergence is to use a quasi–random number generator for sampling from the various distributions involved in the Monte Carlo integral. This will be discussed in more detail in the next section.

Random number generators

One of the most basic requirements for carrying out a Monte Carlo simulation is a reliable random number generator. A standard random number generator generally produces numbers which are uniformly distributed between 0 and 1, commonly called 'uniform deviates'. These uniform deviates can be used to generate random numbers from any other distribution, such as a Gaussian velocity distribution, which might be required in the simulation.

Random numbers generated by a computer program are not really random in the true sense of the word and are often called pseudo–random numbers. Each digit occurs with approximately equal probability, but by the very nature of a computer program, the next number in the sequence is precisely defined by the preceding value through the computer code, and the series of random numbers obtained from such a program is reproducible. There are several statistical tests for randomness which a pseudo–random number generator should pass before it is used in a Monte Carlo application. However, the main requirement is that the program that produces a random sequence should be different from and statistically uncorrelated with the program that uses it.[190] Any two random number generators should give the same results when coupled to the simulation program. The random number generators used in this work will now be discussed in more detail. The majority of these algorithms were obtained from the book *Numerical Recipes in Fortran*.[190]

Uniform deviates: The most commonly used uniform deviate generators use a recurrence relation to return a series of integers between 0 and $m-1$, where m is some large number, given an initial arbitrary number as a starting point. This type of generator is known as a

linear congruential generator and the recurrence relation takes the form,

$$x_{i+1} = ax_i + c \pmod{m} \tag{8.7}$$

The uniform deviate returned is usually x_{i+1}/m and lies between 0 and 1. The series will eventually repeat itself. In the above equation m, a and c are positive integers called the modulus, multiplier and increment. The 'randomness' of the numbers returned depends heavily on the values taken by these three parameters, and they must be chosen carefully to ensure that the period of the sequence is of maximum length i.e. m random numbers will be returned before it repeats. If this requirement is satisfied then the repeat length is independent of the initial seed value. This type of random number generator has the advantage that it is very fast, but the disadvantage that there is a degree of sequential correlation on successive calls. Park and Miller[191] have shown that with careful choice of m and a, the increment c can be set to zero. The resulting algorithm

$$x_{i+1} = ax_i \qquad a = 7^5, \quad m = 2^{31} - 1 \tag{8.8}$$

has passed all tests for randomness and has been widely and successfully used. It is currently accepted as a minimal standard against which to judge other random number generators. The main problem with this generator is that there are low order serial correlations present e.g. a very small random number tends to be followed by a smaller than average value, which could lead to problems in some applications. These can easily be removed by including a shuffling algorithm so that a random deviate x_i is not output on the ith call but on some later call. This random number generator (`ran1` from *Numerical Recipes*) passes the statistical tests the unshuffled algorithm fails and was used in the majority of the applications described here.

The period of `ran1` is around 10^8, sufficient for most applications. Occasionally a value of N was required which exceeded this number, and a random number generator with a longer period (`ran2`) was substituted. This long period random number generator simply combines two sequences with different periods additively to give a sequence with a period equal to the least common multiple of the two periods.

All of the above random number generators can be used to return uniform deviates lying between any two limits A and B by carrying out the simple transformation

$$x_i' = A + (B - A)x_i \tag{8.9}$$

Gaussian deviates: Several of the probability distributions which must be sampled in the applications described in this thesis have well defined functional forms. One strategy for dealing with this in the Monte Carlo integration would be to sample uniform deviates and weight each point with the corresponding probability from the appropriate distribution. This is the approach adopted in several cases, such as sampling of the velocity of a molecule travelling in a supersonic molecular beam. However, in some cases, in which the functional form of the distribution is particularly simple, the uniform deviate can be transformed to give random numbers distributed according to the new probability distribution. This is the case for particle beam profiles and thermal velocities, which have a Gaussian probability distribution. The uniform deviates described in Section 8.3.1 have the following probability distribution:

$$P(x)dx = \begin{cases} dx & 0 < x < 1 \\ 0 & \text{otherwise} \end{cases} \tag{8.10}$$

normalised so that $\int_{-\infty}^{\infty} P(x)dx = 1$. If some function of x is taken, $y(x)$, then the probability distribution of y satisfies

$$\begin{aligned} |P(y)dy| &= |P(x)dx| \\ \Rightarrow P(y) &= P(x)\left|\frac{dx}{dy}\right| \end{aligned} \tag{8.11}$$

This can be used to generate an arbitrary distribution of y parameters. For a distribution $P(y) = f(y)$, where f is a positive function whose integral is unity, the equation that must be solved is

$$\frac{dx}{dy} = f(y) \tag{8.12}$$

It is immediately apparent that $x = \int f(y)dy = F(y)$, so that the required transformation to take a uniform deviate x into one distributed as $f(y)$ is

$$y(x) = F^{-1}(x) \tag{8.13}$$

where F^{-1} is the inverse of the indefinite integral of $f(y)$. Obviously, the number of functions for which it is possible to calculate F^{-1} is limited, but the Gaussian is one such function. Gaussian deviates with zero mean and unit variance can be generated with the algorithm `gasdev`[190] and are easily transformed to give the required widths for the various probability distributions required for beam parameters.

Quasi–random numbers: Quasi–random number generators are a special type of random number generator which are 'self–avoiding'. They will never pick the same point twice and tend to fill in the sample space more and more finely as N increases, without the clustering effects that tend to occur when pseudo–random number generators are used. These random number generators generally consist of some multidimensional mathematical sequence and are therefore not actually 'random' at all. The major advantage of quasi–random over pseudo–random number generators as far as Monte Carlo applications are concerned lies in the fact that they sample the space much more evenly. For this reason convergence of the Monte Carlo integral is much faster, with the error term often approaching N^{-1} dependence rather than the $N^{-1/2}$ dependence obtained with a pseudo–random number generator. Several quasi–random number generators were tested for use in the simulations described in Chapter 9, including the Halton sequence,[190] Sobol sequence[192] and eta sequences.[193] While the convergence properties seemed to be better for a given number of points sampled, the main disadvantage of these random number generators was their slow sampling speed. Both the Halton and eta sequences were far too time inefficient to be incorporated into the programs, and eventually it was decided to forfeit the faster convergence properties offered by the quasi–random number generators for the much faster sampling speed of a pseudo–random number generator.

8.3.2 *Fitting algorithms*

Fitting of experimental data involves setting up a model defined by a set of adjustable parameters and determining the set of parameters which give the best agreement with the data. A fitting problem is nearly always formulated in terms of minimisation of a 'figure–of–merit' function (often called a 'merit function' or 'fitting function'), which represents the agreement between the model and the experimental data. By convention, small values of the fitting function represent good agreement; large values represent poor agreement. The adjustable parameters are then varied according to some algorithm until a 'best fit' parameter set, corresponding to the lowest possible value of the fitting function, is obtained. Because experimental data is usually subject to measurement errors and noise it is only very rarely that an exact fit to any model can be achieved.

One of the most commonly used fitting functions, and the one chosen for all of the fitting problems presented in this work, is the χ^2 function, the sum of the squares of the differences

between the experimental data and the model at each experimental point.

$$\chi^2 = \sum_{i=1}^{N} \left(\frac{(y_i^{\text{expt}} - y_i^{\text{fit}})}{\sigma_i} \right)^2 \tag{8.14}$$

where y_i^{expt} are the experimental data points, $y_i^{\text{fit}} = y(x_i; a_1 ... a_k ... a_K)$ are the fitted data point and σ_i is the standard deviation associated with each data point. In many cases σ_i is not known and is simply set to unity.

The two types of fitting procedure used in this work, namely least squares fitting and genetic algorithms, will be described in the following sections.

Least squares fitting

If the derivative of Equation 8.14 is taken with respect to each of the fitting parameters a_k a set of (in general) non-linear equations is obtained which must hold at the χ^2 minimum.

$$\sum_{k=1}^{K} \left(\frac{y_i^{\text{expt}} - y_i^{\text{fit}}}{\sigma_i^2} \right) \left(\frac{\partial y(x_i; a_1 ... a_k ... a_K)}{\partial a_k} \right) = 0 \qquad k = 1, ..., K \tag{8.15}$$

Linear least squares: The simplest type of least squares fitting problem is that for which the model has a linear dependence on the fitting parameters i.e. a problem for which the model is a linear combination of a set of fixed basis functions $f_k(x)$.

$$y(x) = a_1 f_1(x) + a_2 f_2(x) + ... + a_k f_k(x) + ... + a_K f_K(x) = \sum_{k=1}^{K} a_k f_k(x) \tag{8.16}$$

For this case χ^2 becomes

$$\chi^2 = \sum_{i=1}^{N} \left(\frac{y_i - \sum_{k=1}^{K} a_k f_k(x_i)}{\sigma_i} \right)^2 \tag{8.17}$$

and the set of simultaneous equations to be solved is

$$0 = \sum_{i=1}^{N} \frac{1}{\sigma_i^2} \left(y_i - \sum_{j=1}^{K} a_j f_j(x_i) \right) f_k(x_i) \qquad k = 1, ..., K \tag{8.18}$$

Equation 8.18 can be rearranged and formulated as a matrix equation.

$$\sum_{j=1}^{K} A_{kj} a_j = b_k \tag{8.19}$$

where

$$A_{kj} = \sum_{i=1}^{N} \frac{f_j(x_i) f_k(x_i)}{\sigma_i^2} \tag{8.20}$$

and

$$b_k = \sum_{i=1}^{N} \frac{y_i f_k(x_i)}{\sigma_i^2} \tag{8.21}$$

The resulting simultaneous equations are known as the normal equations of the least squares fit, and can in many cases be solved by standard matrix methods such as Gauss–Jordan elimination to give a unique solution for the set of fitting parameters. However, there are a large number of cases where these methods will fail. This commonly occurs when a data set does not make a clear distinction between two or more of the basis functions and the matrix A_{kj} becomes singular. In these cases, alternative solution methods such as singular value decomposition[190] may be employed.

Non-linear least squares: When the model has a non-linear dependence on the set of adjustable parameters a_k the data fitting problem becomes more complicated and an iterative procedure is required to find the optimum parameters. In the case where the model function is linear in the fitting parameters, contours of constant χ^2 on the χ^2 surface are ellipsoids.[194] In the non-linear case the contours are distorted, but become almost elliptical in the vicinity of the minimum on the surface. There are two common approaches for solving the optimisation problem. In one method, sometimes referred to as the Gauss[195] or Gauss–Newton method,[196] the model function $f(\mathbf{x}, \mathbf{a})$ is expanded in a Taylor series up to first order.

$$f(x_i, \mathbf{a} + \boldsymbol{\delta}) \approx f(x_i, \mathbf{a}) + \sum_{k=1}^{K} \left(\frac{\partial f_i}{\partial a_k} \right) \delta_k \tag{8.22}$$

or in vector notation

$$\mathbf{f} = \mathbf{f}_0 + \mathbf{F}\boldsymbol{\delta} \tag{8.23}$$

where the vectors $\mathbf{a}$ and $\boldsymbol{\delta}$ the current best fit parameters and a correction vector. For an experimental data set represented by the vector $\mathbf{y}$, the value of χ^2 predicted by the linearised equations above is

$$\chi^2 = \sum_{i=1}^{N} (y_i - f_i)^2 \tag{8.24}$$

Equations 8.22 and 8.23 are linear in the correction vector $\boldsymbol{\delta}$ and the correction can therefore be found by the standard least squares method of solving the system of equations

$$\frac{\partial \chi^2}{\partial \delta_k} = 0, \qquad k = 1, ..., K \tag{8.25}$$

in a manner similar to that for linear least squares fitting.

Because the Taylor expansion is only an approximation to the true fitting function the new best fit parameters $a_k + \delta_k$ are only the next approximation to the true least squares best fit parameters. The steps outlined above are repeated iteratively until there is little or no further improvement, at which point it is assumed the optimum parameter set has been determined. It is fairly common for this method to suffer from failure to converge.

An alternative strategy is the gradient or 'steepest descent' methods, which simply take a step down the χ^2 surface in the direction of the negative gradient of χ^2 to determine the new best fit parameters at each iteration. These methods have the disadvantage that they tend to be slow to converge.

The most widely used algorithm in non-linear least squares fitting was proposed by Marquardt,[194] based on an earlier suggestion by Levenberg and uses a combination of the two methods described above. The Levenberg–Marquardt method uses the steepest descent approach at points far from the minimum on the χ^2 surface, and switches continuously to the Taylor series method as the minimum is approached.

While gradient descent methods have many advantages, there are also a number of disadvantages. They generally perform very well for simple surfaces with a single minimum. However. on more complicated surfaces, which may have several minima. there is no guarantee that the parameter set to which the algorithm converges will be the global minimum, since the program will terminate at the first local minimum it reaches from its starting point on the surface. When fitting complex surfaces it is a good idea to try several different starting points on the χ^2 surface to ensure the fit converges to the same point in each case. Steepest descent methods are also very sensitive to noisy data and attempts to fit a large number of parameters are often unsuccessful. A very real problem with calculus based fitting methods is the requirement that both χ^2 and its derivatives with respect to each fitting parameter are able to calculated, a condition which makes them unsuitable for a number of fitting problems. Many of the problems associated with steepest descent methods are overcome by genetic algorithms.

Genetic algorithms

A genetic algorithm (GA) is an iterative procedure based on the concept of Darwinian evolution and 'survival of the fittest'. In this context, the 'fittest' is the set of parameters which

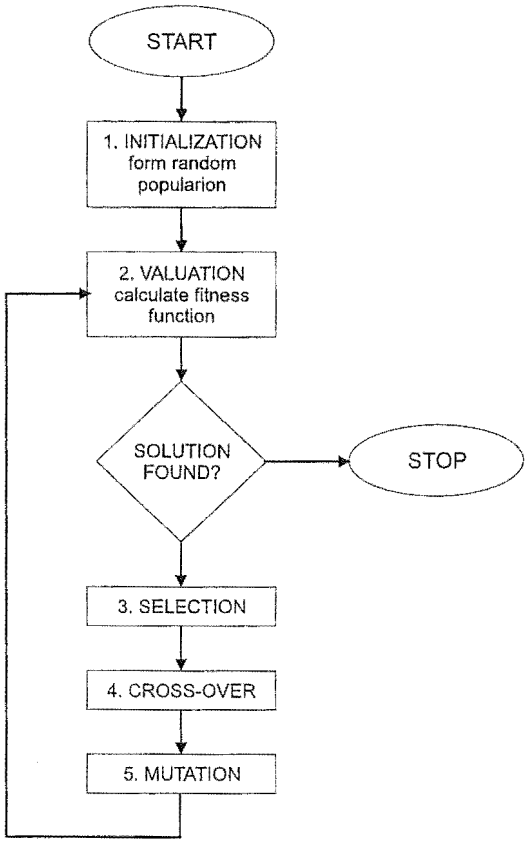

Figure 8.3: Flow diagram representation of a generalised genetic algorithm.

minimize χ^2 or some other fitness function and best reproduce the experimental data. Other than the set of best fit parameters that a genetic algorithm fitting procedure aims to identify, it has little in common with the calculus based methods described in Section 8.3.2. A flow diagram of the basic steps comprising a generalised GA is shown in Figure 8.3.

The various steps in the process are described in more detail below.[197,198]

1. The first step involves selection of sets of trial fitting coefficients. In genetic algorithm terminology each set of coefficients is known as a *chromosome* or *string*, each position within a string is called a *gene* and its value is an *allele*. The set of chromosomes make up the *population*. The minimum and maximum values for each adjustable parameter are specified at the beginning of the program, and each string contains coefficients selected randomly from within these limits. The initial population or 'first generation' of strings therefore spans the entire χ^2 surface.

2. χ^2 is calculated for each string. The criterion for stopping the optimization is usually either completion of a user specified number of generations, or a χ^2 below some

threshold value. If either of these conditions have been met then the string with the lowest χ^2 at this point in the program is selected as the 'best fit' set of parameters. Otherwise the χ^2 value for each string is converted to a 'fitness', used later to determine which chromosomes will be selected for breeding to produce the population of the next generation. The relationship chosen between the quality of the string (embodied in χ^2) and its fitness is essentially arbitrary, but it must give good solutions a high fitness and poor solutions a low fitness. A good choice of this fitness relationship can increase the convergence rate of the algorithm significantly.

3. A subset of strings must now be selected for breeding, based on the fitnesses determined in step 2. By analogy with their biological counterpart, it would be unreasonable to simply choose every string with high fitness to reproduce. In nature poorly adapted individuals sometimes produce offspring where fitter individuals fail. The selection method should be biased in favour of fit strings while still allowing poor strings a chance of breeding. A commonly used option is known as the 'roulette wheel'.[197] Each string is allocated a section of an imaginary roulette wheel whose width is proportional to its fitness. When the roulette wheel is 'spun' using a random number generator, the number of times a string is picked is proportional to its fitness. Very fit strings are likely to be picked several times, while poorer strings may not be picked at all. A second technique is known as 'stochastic remaindering'. The strings are all scaled to an average fitness of unity. The integer part of the fitness determines the initial number of copies made for each string (note that at this point no strings of below average fitness are selected). The number of copies made is subtracted from the fitness so that all strings now have a fitness less than unity. The strings that will be used to make up the remainder of the required population are now selected probabilistically by selecting strings at random, generating a random number, and reproducing the string if the random number is less than the fitness value. Fitnesses are set to zero after a string is selected to prevent a string being selected twice and the procedure is repeated until the required population size is obtained. Unlike the roulette wheel method, for which there is some probability that the fittest strings will not be selected, the method of stochastic remaindering ensures the fittest strings will always be copied. Often a small modification is made to the selection procedure to ensure the fittest string in a population always continues into the next generation, preventing crossover or mutation

from destroying the best string. This is usually achieved by flagging the best string in each population. If the best of the new generation is of lower fitness than the best of the previous generation then the least fit string of the new generation is replaced with the best string of the previous generation.

4. The next stage is breeding between the selected parent strings to produce a new generation of offspring. The GA analogue to mating in nature is the 'cross–over' operator. Pairs of strings are picked at random, cut into two at a randomly selected point and the two halves crossed over between the strings[§]. As an example, the two strings (1,3,5,7,9) and (2,4,6,8,10) may be crossed over at the third gene to give two child strings (1,3,5,8,10) and (2,4,6,7,9). The crossover operator ensures that on average each child string receives half of its genes from each parent, and inherits characteristics from both parent strings. If both parents were fit strings, there is a reasonable probability that one or both of the offspring will be better than the parents.

5. In analogy with nature, mutations are introduced into a small number of the new chromosomes. A mutation consists of replacing a small number of randomly selected genes within the population with new, arbitrarily selected values. Without mutation, the available genes are limited to those in the initial population. Mutations introduce variety and prevent the population from stagnating. While a small number of mutations, of the order of 0.1% of the genes, is helpful, increasing the probability of mutation too much can cause problems. Convergence will be slowed if mutation occurs too often, since fit genes will be constantly replaced by poorer mutated versions.

   After mutation the new population is saved as the next generation and reentered into the loop at step 2.

Genetic algorithms have several advantages over the more conventional calculus based fitting methods. While standard least squares fitting methods perform a single point search and are susceptible to convergence to a false minimum, genetic algorithms search many regions of the χ^2 surface at once and are consequently more likely to find the true global minimum. This is a particular advantage when dealing with complicated surfaces or noisy data, for which traditional 'hill climbing' methods often fail. The χ^2 surface often becomes much more complicated as the number of adjustable parameters increases, and the genetic

[§] Two point crossovers, in which each parent string is cut in two places, are also commonly used.

algorithm approach becomes more and more valuable as the scale of the problem grows. However, simply because the GA does not perform a calculus based minimization there is no guarantee that the absolute minimum of the surface will be found, though the best fit solution encountered will be very close to this value. For this reason GA's are sometimes used in conjunction with a steepest descent method. The genetic algorithm is used to approach the minimum in the χ^2 surface as closely as possible, and a gradient descent method starting from the GA's best fit set of coefficients is used to 'fine tune' the solution.

A second important advantage of genetic algorithms is that they only require knowledge of χ^2; no derivative information is needed. This makes a GA accessible for a much broader range of problems than gradient descent methods, for which the gradient must be calculated at each step in order to determine the direction in which the optimisation should move on the χ^2 surface. An important consequence of this insensitivity to the gradient of the surface at this point is that genetic algorithms are fairly insensitive to even quite high levels of noise on the data to be fitted.

The primary disadvantage of a GA program over a conventional fitting method is that run times are generally significantly longer, mostly due to the fact that each operation must be carried out on all the strings in the population rather than on only the current best–fit solution as is the case in the calculus based methods. While this can be a major consideration for large problems with many fitting parameters, there are many smaller applications where the cost is offset by the ease with which a GA can be set up and applied to a wide range of different problems with only small changes in computer code.

Both types of fitting procedure considered above have different merits, and one will often outperform the other for a particular problem. This is illustrated in the various data fitting problems encountered over the course of the work presented in this thesis. The extraction of cross sections for collisionally induced ΔM_J transitions from molecular beam attenuation data, as described in Chapter 6, is well suited to conventional least squares fitting techniques. Chapter 10 includes a discussion of a method of fitting a set of basis functions to data from ion imaging experiments, in which the Levenberg–Marquardt algorithm was used with great success. Data from the reaction dynamics experiments carried out at Oxford (Chapter 9) could be equally well analysed using the standard Levenberg–Marquardt non-linear least squares approach or a genetic algorithm.

9. DYNAMICS OF THE $H+H_2O \rightarrow OH+H_2$ REACTION

This chapter details work carried out during six months spent in the research group of Dr Mark Brouard at the University of Oxford. During this time software was developed to analyse data from laser pump–probe experiments into the stereodynamics of photoinitiated bimolecular reactions*, specifically the reaction between translationally hot H atoms and H_2O. The experiments involved will be described, though the measurements themselves did not form part of the work carried out during the visit. The theory of photoinitiated bimolecular reactions is fairly involved and is presented separately in Appendix C.

9.1 Experimental: Laser pump–probe experiments and Döppler resolved laser induced fluorescence spectroscopy

The intensity, well defined frequency and high degree of collimation of a laser beam make it ideal for applications in the study of reaction dynamics. A generalised laser pump-probe experiment requires two laser beams and consists of two main steps.

1. A laser pulse from the first ('pump') laser is used to excite a reagent to a specific quantum state.

2. After a short time delay, during which the excited atom or molecule undergoes reaction with another species present, one of the products is detected using the second ('probe') laser, most commonly by measuring its laser induced fluorescence (LIF) or resonance enhanced multiphoton ionization (REMPI) spectrum.

In the present application of this technique to the photoinitiated reaction of 'hot' H atoms with H_2O, the photolysis precursor H_2S and target molecule H_2O are present at approximately equal partial pressures inside the reaction cell, with a total pressure of around 200 mTorr. The pump (photolysis) and probe lasers are two frequency doubled tunable dye lasers, pumped by the same XeCl excimer laser. An optical delay of around 23 ns separates the times at

* The software is not included in Appendix F but may be obtained on request.

which the pump and probe laser pulses enter the cell. The linearly polarized pump laser is used to photodissociate the H_2S precursor at 225 nm (this is equivalent to the first stage of the generalised experiment described above, except that the reagent is excited into the continuum rather than into a specific quantum state), producing atomic hydrogen with a high translational kinetic energy. Only H_2S molecules with some component of their dipole lying along the laser polarization axis are dissociated, leading to the velocity of the H atom fragment being preferentially aligned along the polarization axis of the laser. The CM angular distribution of the photolysis products is generally fairly broad and is usually expressed in terms of an angular differential cross section as follows.

$$\frac{d\sigma}{d\omega_t} = \frac{\sigma}{4\pi}[1 + \beta P_2(\cos\theta_t)] \tag{9.1}$$

in which σ is the total cross section, ω_t is the solid angle (θ_t, ϕ_t) into which products are scattered, β is the translational anisotropy parameter (described in more detail in Appendix C), and $P_2(\cos\theta_t)$ is a second order Legendre polynomial in the cosine of the angle θ_t between the fragment recoil direction and the photolysis polarization vector.

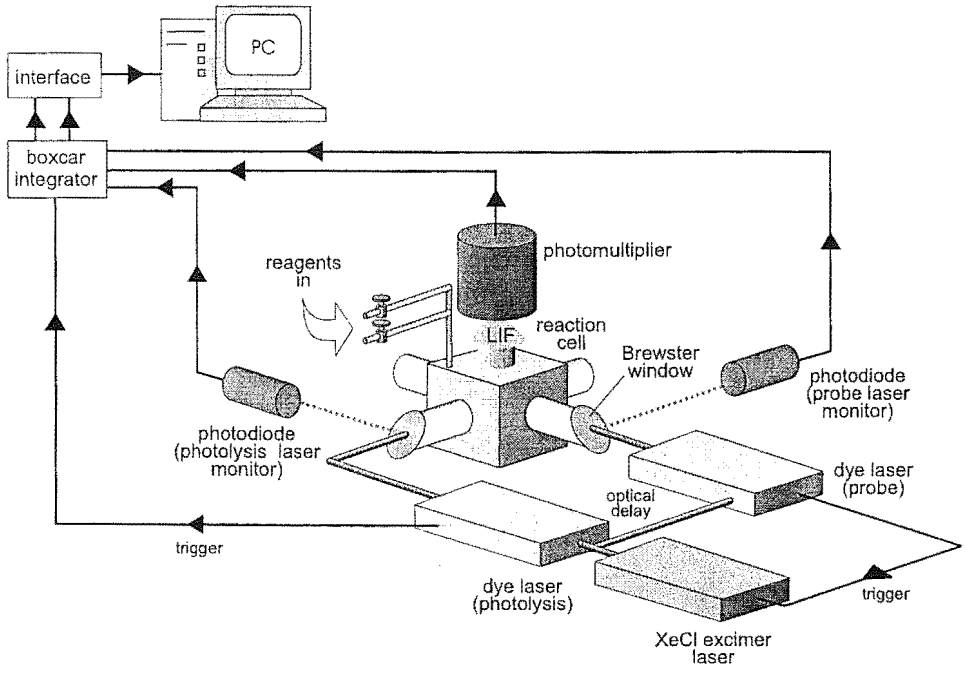

Figure 9.1: Schematic of the experimental apparatus

Velocity aligned H atoms undergo reaction with H_2O molecules to produce OH and H_2 in a range of internal states. Detection of the OH product follows through measurement of its Döppler resolved laser induced fluorescence spectrum. OH is formed in the $X\,^2\Pi$ electronic

ground state. The probe laser is used to excite the nascent OH to the $A\,^2\Sigma^+$ state via one photon absorption, after which it relaxes back to the ground electronic state with a fluorescence lifetime of approximately 700 ns, emitting a single photon. The single photon involved in both the absorption and emission stages of the process earns this technique the name (1+1) LIF. A photomultiplier tube mounted above the reaction cell is used to detect the fluorescence, and the probe and photolysis laser intensities can be monitored using photodiodes which measure the intensity of scattered light from the Brewster windows through which the beams enter the cell. Two boxcar integrators collect the signals from the photomultiplier and probe photodiode and transfer the data to a PC. A schematic of the experimental apparatus is shown in Figure 9.1.

In preliminary studies a coarse scan of the v=0 band of the OH produced in the reaction is carried out at a laser bandwidth of 0.25cm^{-1} and the lines assigned[199] in order to select a suitable rotational level for further investigation. In the current study the J=1 and J=5 levels were selected. The J=5 level is split by an interaction between the electronic orbital angular momentum and nuclear angular momentum into two Λ–doublet components. In the classical high J limit, the A' component of the Λ–doublet corresponds to the unpaired electron density lying in the plane of the molecular rotation, while the A'' component has the unpaired electron density lying perpendicular to the plane of rotation, along the $\mathbf{j}'$ vector. The determination of separate vector correlations for each component of the Λ–doublet requires that both a main line and a satellite line corresponding to each component are able to be resolved, a condition which is satisfied for the J=5 line.

Once a rotational state has been selected, an intra-cavity etalon is placed inside the laser cavity, narrowing the laser bandwidth to 0.08 cm^{-1}. Döppler profiles can then be recorded by scanning the probe laser frequency over the line of interest.

The ultimate aim of an experiment in reaction dynamics is to determine the full three dimensional centre of mass frame velocity and angular distribution. This cannot be directly measured in the experiments described here, but information on the lab frame product velocity can be extracted from the Döppler resolved LIF profiles of the state selected product since the Döppler shift is a measure of the projection of the product velocity vector along the propagation axis of the probe laser. The component of the product velocity along this axis, v_p is given by the scalar product of the product velocity vector $\mathbf{v}$ and the unit vector along

the laser propagation axis $\mathbf{k_a}$.

$$v_p = \mathbf{k_a} \cdot \mathbf{v} \tag{9.2}$$

By measuring these projections for several different relative orientations of the photolysis and probe lasers, information on several moments of the full distribution can be obtained using the theory described in Appendix C. Profiles must be recorded for three different orientations of the two laser beams and their polarization vectors. According to the convention of Dixon,[200] these geometries are known as 'Case A', 'Case B' and 'Case D' and are shown in Figure 9.2

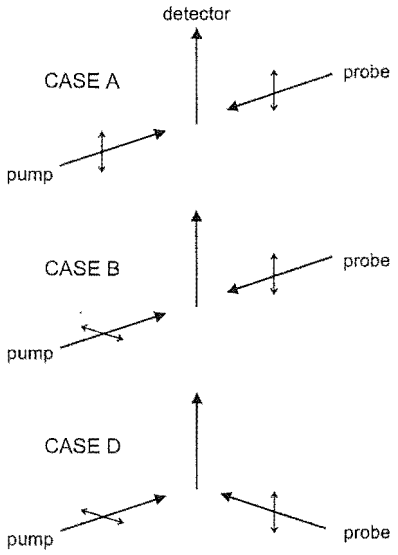

Figure 9.2: Alignment of the polarization vectors and propagation directions of the pump and probe lasers for each of the three experimental cases used in the determination of polarization dependent differential cross sections (PDDCS's) and the translational kinetic energy distribution ($P(f_T)$).

In order to use the established theory to extract information from the experiments, the raw data must be manipulated to form 'composite Döppler profiles'. Details of this procedure are given in Appendix D. Each composite profile contains information on an individual moment of the three dimensional scattering probability distribution and reflects the velocity distribution of the OH product through the Döppler shift. These profiles can be directly fitted using the techniques described in Sections 8.3.1 and 9.1.2 in order to extract dynamical information on the reaction process. For ease of notation the following definitions are introduced for the five

commonly used composite Döppler profiles described in Appendix D.

$$\begin{aligned} \beta_{00}(0,0) &\equiv \beta_{\mathrm{sp}} \\ \beta_{20}(2,0) &\equiv \beta_{kv} \\ \beta_{20}(0,2) &\equiv \beta_{kj'} \\ \beta_{00}(2,2) &\equiv \beta_{vj'} \\ \beta_{20}(2,2) &\equiv \beta_{kvj'} \end{aligned} \tag{9.3}$$

The first profile, β_{sp} contains information on the product speed distribution. This can be used in conjunction with β_{kv} to determine the product differential cross section and translational energy distribution $P(f_T)$. The remaining profiles, $\beta_{kj'}$, $\beta_{vj'}$ and $\beta_{kvj'}$ yield information on rotational vector correlations.

9.1.1 *Background collision theory*

In the simplest type of bimolecular reaction for which these experiments can be carried out, namely the reaction between an atom and a diatomic molecule, determination of the differential cross section is straightforward. The velocities of both the photolysis precursor and the molecular reagent can be neglected to a good first approximation[201] so that the relative velocity vector $\mathbf{k}$ lies along the hot atom velocity vector and is parallel to the velocity of the centre of mass $\mathbf{v}_{\mathrm{CM}}$. Since there is no internal excitation in the atomic co-product, each lab frame product speed corresponds to a single CM frame scattering angle, as shown in Figure 9.3

The lab frame product velocity $\mathbf{v}'$ is the vector sum of the CM product velocity $\mathbf{w}'$ and the velocity of the centre of mass $\mathbf{v}_{\mathrm{CM}}$.

$$\mathbf{v}' = \mathbf{v}_{\mathrm{CM}} + \mathbf{w}' \tag{9.4}$$

Squaring both sides and rearranging leads to an expression for the CM scattering angle.

$$\cos\theta_t = \frac{v'^2 - v_{\mathrm{CM}}^2 - w'^2}{2w'v_{\mathrm{CM}}} \tag{9.5}$$

The one–to–one relationship between the lab frame product speed v' and the CM scattering angle θ_t leads to an expression relating the two probability distributions. When combined with Equation 9.5, this gives an expression for the probability of scattering into a given angle,

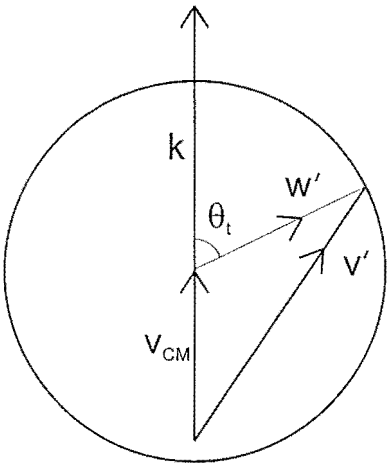

Figure 9.3: Newton diagram for A+BC reaction. k is the relative velocity vector, v_{CM} is the CM velocity, v′ and w′ are the lab and CM frame product velocities and θ_t is the CM frame scattering angle.

i.e. the normalised differential cross section, in terms of the lab frame velocity distribution.

$$\begin{aligned} P(\cos\theta_t)d(\cos\theta_t) &= P(v')dv' \\ \Rightarrow P(cos\theta_t) &= \frac{2\pi}{\sigma}\frac{d\sigma_{00}}{d\omega_t} = \frac{v_{CM}w'}{v'}P(v') \end{aligned} \tag{9.6}$$

where σ is the total integrated cross section. In this case only the speed dependent profile β_{sp} is required to extract the differential cross section. It can be seen that the factor $\frac{v_{CM}w'}{v'}$ is simply the Jacobian for the change of variables from lab frame product velocity to CM frame scattering angle.

For the more general case of a molecular coproduct, which can be formed in a range of internal states, the relationship between lab frame product speed and CM scattering angle is no longer one–to–one. The 'energy budget' for the reaction is not uniquely determined by state selective probing of just one of the products and a new parameter, f_T, the fraction of available energy channeled into product translation, is introduced.

$$f_T = \frac{E'_T}{E_{\text{avail}}} \tag{9.7}$$

When all of the available energy appears in translation of the products, corresponding to the situation in which the coproduct is formed in its ground vibrational and rotational state, f_T will be equal to unity. Conversely, if the coproduct is highly rotationally or vibrationally excited, f_T will be very small, with a limiting value of zero when all the available energy is channeled into internal excitation of the coproduct.

The possibility of internal excitation in the coproduct means that the product speed distribution can no longer be used alone to determine the differential cross section. However, the second moment, $\beta_{20}(2,0)$, also contains information on the differential cross section, and when analysed together, the two profiles yield both the differential cross section and distribution of product translational energies $P(f_T)$. Similarly, the remaining three moments $\beta_{20}(0,2)$, $\beta_{00}(2,2)$ and $\beta_{22}(2,2)$ may be analysed simultaneously to give the three polarization dependent differential cross sections (PDDCS's) $\frac{1}{\sigma}\frac{d\sigma_{20}}{d\omega_t}$, $\frac{1}{\sigma}\frac{d\sigma_{21-}}{d\omega_t}$, and $\frac{1}{\sigma}\frac{d\sigma_{22+}}{d\omega_t}$ described in Appendix C, which give insight into product rotational angular momentum polarization.

9.1.2 Analysis

The extraction of information from composite Döppler profiles is achieved by generating a basis set of composite profiles and fitting a linear combination of these functions to the experimental data, using either a non-linear least squares procedure or a genetic algorithm to perform a χ^2 minimization.

To determine the differential cross section and distribution of product translational energies $P(f_T)$ a basis set consisting of simulated speed and β_{kv} profiles must be constructed. Consider a basis set which consists of an array of composite Döppler profiles, each of which correspond to a specific single value of the CM scattering angle $\cos\theta_t$ and fraction of energy appearing as product translation f_T. If speed and β_{kv} profiles are formed at each of i scattering angles and j values of f_T the result is a basis set of dimension $i \times j$. Each individual basis function can be written $G_{K0}(x, \cos\theta_t^i, f_T^j)$, in which x is the Döppler shift and $\cos\theta_t^i$ and f_T^j are the values of scattering angle and f_T respectively for the particular basis function. A linear combination of these functions can be fitted to experimental profiles according to the following expression,

$$D_{K0}(x) = \sum_i \sum_j c_{ij} G_{K0}(x_p, \cos\theta_t^i, f_T^j) \tag{9.8}$$

in which each coefficient c_{ij} corresponds to a discrete scattering angle and value of f_T.

In practice it is usually assumed that the probability distribution $P(f_T, \cos\theta_t)$ is separable and can be written as the product of a pair of distributions, one in scattering angle and the other in f_T.

$$P(f_T, \cos\theta_t) = P(f_T)P(\cos\theta_t) \tag{9.9}$$

This assumes that the differential cross section does not depend on f_T and vice versa. While this has not been rigorously tested, very good fits to the data are obtained by separating the angular and kinetic parts of the distribution in this way, both for the H+H_2O system to be described here, and also for several other reaction systems,[202] indicating that the assumption is valid, or at least that the degree of inseparability is well within the limits of experimental noise inherent in the data. The coefficients of Equation 9.8 can now be written as the product of a smaller set of parameters, one for each value of f_T and $\cos\theta_t$.

$$c_{ij} = a_i b_j \tag{9.10}$$

The coefficient c_{ij} corresponds to the probability of a product being scattered into angle $\cos\theta_t^i$ with a fraction f_T^j of the available energy appearing in product translation. Once the data has been fitted, the optimised array of expansion coefficients provides the distribution $P(\cos\theta_t, f_T)$. i.e.

$$P(\cos\theta_t) = \sum_i a_i \delta(\cos\theta_t{}^i - \cos\theta_t) \tag{9.11}$$

$$P(f_T) = \sum_j b_j \delta(f_T^j - f_T) \tag{9.12}$$

so that the values of the a_i and b_i coefficients represent the differential cross section and $P(f_T)$ distribution respectively.

A major problem with this procedure is the large number of basis functions, and therefore fitting parameters, required to analyse the experimental data. A minimum requirement for a standard data set is typically twenty values each of $\cos\theta_t$ and f_T, resulting in a basis set consisting of 400 β_{sp} and β_{kv} profiles. This presents a two–fold problem. A basis set of these dimensions represents a sizeable data file for which storage can be a very real problem. Also, the several hundred fitting coefficients required mean that any fitting algorithm will struggle to find a minimum in the χ^2 surface due to the high number of degrees of freedom the problem presents. In order to reduce the number of fitting coefficients required the basis set can be contracted into a set of Legendre moments by numerically integrating the basis functions, weighted by the appropriate Legendre polynomials in f_T and $\cos\theta_t$, over the values of $\cos\theta_t$ and f_T. Contracted basis functions $G_{K0}^{nm}(x)$ are then,

$$G_{K0}^{nm}(x) = \sum_i \sum_j P_n(\cos_{\theta_t}) P_m(f_T') G_{K0}(x, cos\theta_t^i, f_T^i) \tag{9.13}$$

in which $f'_T = 2f_T - 1$, i.e. the parameter f_T transformed to lie within the range from -1 to 1 for which the Legendre polynomials form an orthogonal basis set.

The basis set is now of dimension $n \times m$, with n and m usually less than four, a much more tractable size for a fitting algorithm to handle. Originally the basis set contraction was carried out after the large basis set had been generated, but the software was later modified so that the basis functions are contracted as they are generated; this solves the data storage problem since the large uncontracted basis set is not printed to file. The functions in a typical basis set containing three Legendre moments each in $\cos\theta_t$ and f_T are shown in Figure 9.4

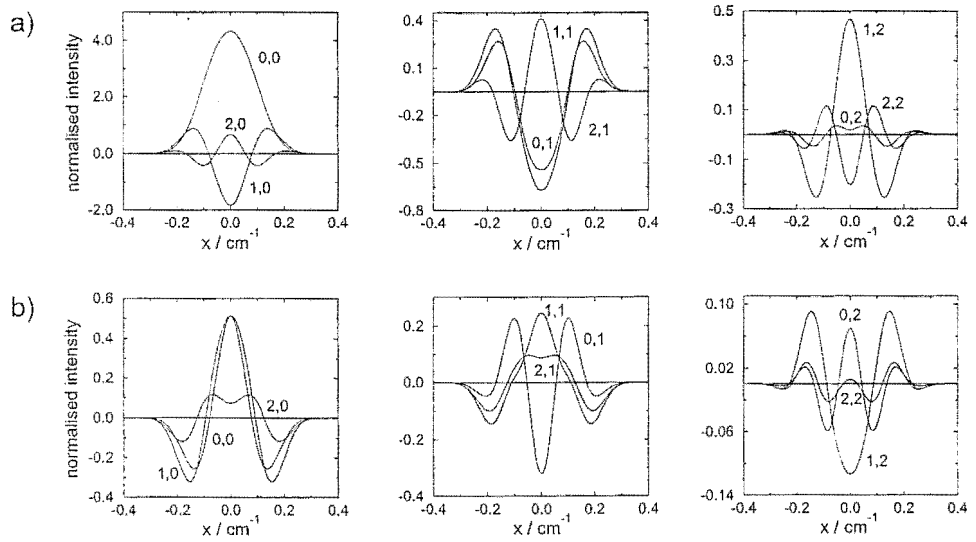

Figure 9.4: Basis set for speed and β_{kv} composite Döppler profiles in the H+H_2O → OH(v=0,J=1)+H_2 reaction, with three moments each in $\cos\theta_t$ and f_T. The indices n,m labelling the plots denote the contracted basis function corresponding to a Legendre polynomial of order n in $\cos\theta_t$ and order m in f_T.

The expression used to fit a linear combination of contracted basis functions to an experimental composite Döppler profile is now

$$D_{K0}(x) = \sum_n \sum_m a_n b_m G^{nm}_{K0}(x) \tag{9.14}$$

Substituting (9.13) into (9.14) gives

$$D_{K0}(x) = \sum_i \sum_j \sum_n \sum_m a_n P_n(\cos\theta^i_t) b_m P_m(f'^j_T) G_{K0}(x, \cos\theta^i_t, f^j_T) \tag{9.15}$$

If this is compared with Equation (9.8) it is seen that carrying out the contraction is

equivalent to setting

$$\begin{aligned} a_i &= \sum_n a_n P_n(\cos\theta_t^i) \\ b_j &= \sum_m b_m P_m(f'^j_T) \end{aligned} \tag{9.16}$$

The Legendre contraction therefore has the effect of reexpressing the differential cross section and $P(f_T)$ distributions as a linear combination of Legendre polynomials, for which the expansion coefficients are the a_n and b_n parameters obtained in fitting the experimental data with the contracted basis set. If these expressions are compared with Equation C.17 of Appendix C it is seen that the normalised differential cross section is given by

$$\frac{2\pi}{\sigma}\frac{d\sigma_{00}}{d\omega_t} = \frac{1}{2}\sum_n a_n P_n(\cos\theta_t) \tag{9.17}$$

where $a_n = (2n+1)S^n_{00}$, while the $P(f_T)$ distribution is

$$P(f_T) = \sum_m b_m P_m(f'_T) \tag{9.18}$$

Each contracted basis function $G^{nm}_{K0}(x)$ is therefore the composite Döppler profile which would be obtained in the case where the differential cross section was equal to $P_n(\cos\theta_t)$ and the $P(f_T)$ distribution to $P_m(f'_T)$.

The amount of detail obtained on the two distributions depends on the number of moments included in the expansion. Ideally, a large number of moments would be used in order to resolve any fine structure present in the two distributions. However, this must be balanced with the joint problems of ensuring that the basis functions are converged properly, discussed in Section 8.3.1, and the reduced sensitivity of the fitting procedure for higher order terms.

Information on the remaining measurable PDDCS's is obtained from the experimental composite Döppler profiles in a similar manner to that described above for the differential cross section and $P(f_T)$ distribution, except that in this case the profiles which are simultaneously fitted are those for the $\beta_{kj'}$, $\beta_{vj'}$ and $\beta_{kvj'}$ moments of the distribution. From equation (C.17) of Appendix C, the PDDCS's may be expressed as a linear combination of modified spherical harmonics.

$$\frac{2\pi}{\sigma}\frac{d\sigma_{kq\pm}}{d\omega_t} = \frac{1}{2}\sum_{k_1} m^{k_1}_{kq\pm} C_{k_1,-q}(\theta_t, 0) \tag{9.19}$$

where

$$m^{k_1}_{kq\pm} = (2k_1+1)S^{k_1}_{kq\pm} \tag{9.20}$$

The relationships between these PDDCS's and the bipolar moments which can be measured experimentally are given in Table D.1.

Again, separability of the kinetic energy and angular dependence of the probability distribution $P(\omega_t, \omega_r, f_T)$ is assumed; this simply infers that the three remaining PDDCS's have the same functional dependence on the product energy. Basis functions are constructed for fitting the $\beta_{kj'}$, $\beta_{vj'}$ and $\beta_{kvj'}$ composite Döppler profiles, each basis function being weighted as it is formed by integrating over the differential cross section and $P(f_T)$ distributions which have previously been determined using the analysis described above. A basis function generated for a specific scattering angle $\cos\theta_t^i$ and a specific PDDCS $\frac{1}{\sigma}\frac{d\sigma_{kq\pm}}{d\omega_t}$ is denoted $G_{K0}(x, \cos\theta_t^i, kq\pm)$.

Since the PDDCS's are expressed as a linear combination of modified spherical harmonics, it is convenient to contract the basis functions in a series of spherical harmonics in order to reduce the number of degrees of freedom for the fitting procedure[†].

$$G_{K0}^{k'}(x, k', s) = \int C_{k'|q|}(\theta_t, 0) G_{K0}(x, \cos\theta_t, kq\pm) d\cos\theta_t \tag{9.21}$$

This is analagous to the Legendre contraction of the basis set carried out in the determination of the differential cross section and $P(f_T)$ distributions. A typical set of contracted basis functions is shown in Figure 9.5.

Each of the bipolar moments $\beta_{kj'}$, $\beta_{vj'}$ and $\beta_{kvj'}$ is dependent on all three PDDCS's, just as the β_{sp} and β_{kv} dependent profiles are dependent on both the differential cross section and $P(f_T)$ distribution. In the same way as these two profiles can be fitted simultaneously with contracted basis functions in $\cos\theta_t$ and f_T to return the differential cross section and $P(f_T)$ distribution, the remaining composite Döppler profiles can be fitted simultaneously to return the three polarization dependent differential cross sections. The contracted basis functions are fitted to the experimental composite Döppler profiles using the following expression,

$$D_{K0}(x) = \sum_{k'} \sum_{|q|} m_{kq\pm}^{k'} G_{K0}^{k'}(x, k', kq\pm) \tag{9.22}$$

to return the coefficients for the expansion of the renormalised PDDCS's given in Equation 9.19. Once the PDDCS's are known the alignment parameters discussed in Appendix C may

[†] Because the spherical harmonics have two indices, care is required to ensure the correct moments are included in the contraction. For example, if three moments were required for each PDDCS, the terms to be included for $\frac{1}{\sigma}\frac{d\sigma_{20}}{d\omega_t}$ would be $C_{00}(\theta_t, 0), C_{10}(\theta_t, 0)$ and $C_{20}(\theta_t, 0)$, the $\frac{1}{\sigma}\frac{d\sigma_{21}}{d\omega_t}$ PDDCS would have moments in $C_{11}(\theta_t, 0)$, $C_{21}(\theta_t, 0)$, and $C_{31}(\theta_t, 0)$, and for $\frac{1}{\sigma}\frac{d\sigma_{22}}{d\omega_t}$ the moments would be $C_{22}(\theta_t, 0)$, $C_{32}(\theta_t, 0)$ and $C_{42}(\theta_t, 0)$.

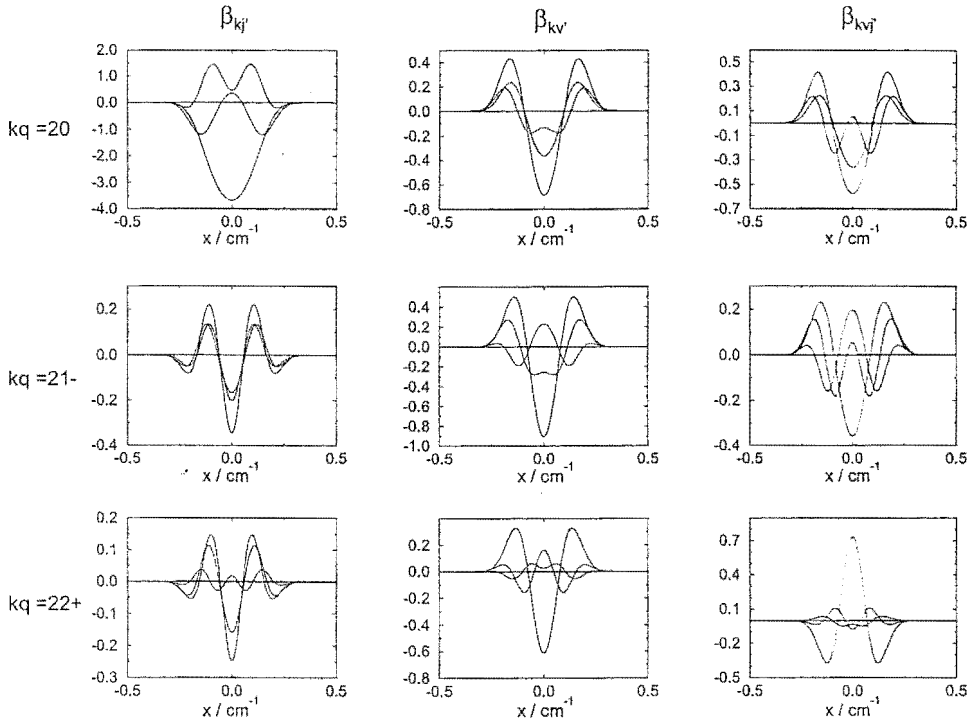

Figure 9.5: Basis set for $\beta_{kj'}$, $\beta_{vj'}$ and $\beta_{kvj'}$ composite Döppler profiles in the H+H$_2$O → OH(v=0,J=5,A')+H$_2$ reaction with three moments in each PDDCS. The columns correspond to the three bipolar moments while the rows separate the PDDCS's.

be determined by integrating over the scattering angle $\cos\theta_t$, and information can then be recovered on the various angular distributions described in Section C.1.

Data fitting

The basis functions are fitted to the experimental composite profiles using either a non–linear least squares or genetic algorithm fitting procedure. The principles behind these two methods are outlined in Chapter 8. Both methods aim to minimise χ^2, the sum of squares of the differences between the experimental data and the fitting function.

For a given function $f(x)$, expressed as a Legendre expansion of the form,

$$f(x) = \frac{1}{2}\sum_n a_n P_n(x) \tag{9.23}$$

the analytic expression for the coefficient of the nth Legendre polynomial is

$$a_n = (2n+1)\langle P_n(x)\rangle \tag{9.24}$$

$$= (2n+1)\int_{-1}^{1} P_n(x) f(x) dx \tag{9.25}$$

For fitting to the speed and β_{kv} profiles the first coefficient in the expansion of the differential cross section and $P(f_T)$ distribution is fixed at unity to ensure that the returned distributions are normalised.

Because the fitting coefficients correspond to the expectation values of the Legendre polynomials over the differential cross section and $P(f_T)$ functions (Equation 9.25). the maximum and minimum values that the fitting coefficients can take are well defined. In the most extreme case, corresponding to single angle scattering in the differential cross section or a single product translational energy in $P(f_T)$, $f(x)$ could be a δ function at the minimum or maximum value of the Legendre polynomial, in which case the coefficient would be equal to this maximum or minimum value over the range $x = -1$ to $x = 1$ multiplied by the scaling factor $2n + 1$. It is often desirable to constrain the fitting coefficients so that they do not exceed their physical limits, as discussed below.

For the $H+H_2O$ system, the fitting procedure is reasonably sensitive to the form of the differential cross section, but it is much more difficult to extract information on the $P(f_T)$ distribution, and the coefficients of this distribution have a tendency to blow up to unacceptable values, particularly for the higher Legendre moments used in the fit. This low sensitivity is largely due to the fact that the kinematics and small energy release for the reaction mean that the OH product is formed with fairly small lab frame velocities. As a result, the Döppler profiles are narrow when compared to reactions in which the energy release is larger, making it more difficult to detect changes in the width of the profile which reflect the distribution of f_T values.

The first attempts to fit the experimental data used the gradient descent method with no constraints imposed on the coefficients other than that the coefficients of the zeroth order moments were unity. When tested on simulated data, so that the differential cross section and $P(f_T)$ distribution were known exactly, the fitting procedure returned reasonable values of χ^2, and successfully fitted the differential cross section, but several of the f_T coefficients returned values far outside their physical limits, giving large oscillations in the fitted distribution and indicating that the fitting program had found a local minimum outside the range for which the coefficients were meaningful. This is a common trap for gradient descent methods, and is especially problematic when attempting to fit noisy data. Imposing constraints on a calculus based fitting algorithm tends to interfere with the fitting procedure, since once a parameter has reached its maximum value the program will effectively stall if the 'downhill' direction

for the current set of coefficients involves exceeding this value. Solution of the non linear fitting equations indicates that the magnitude of the coefficient should be increased to obtain a better fit, yet this is not allowed by the constraint. It is unlikely that the coefficient will ever be reduced from its limiting value, which prevents the algorithm from locating other minima. In practice, constraints could be introduced with some success provided the number of coefficients in the fit was kept low.

Genetic algorithms, described in Section 8.3.2, have the advantage that the minimum and maximum allowed values for each fitting parameter are required as input for the initialization procedure, so that constraining the coefficients to lie within their physical boundaries is a natural part of the code. Because there are a large number of complete sets of coefficients involved at each stage of the algorithm, it is more likely that a global minimum will be found, and therefore less likely that the coefficients will become fixed at their maximum values. For this reason, even though the genetic algorithm has a longer run time than the Levenberg-Marquardt method, it is likely to become the method of choice for application to the fitting of composite Döppler profiles in systems which present a problem to the traditional gradient descent methods.

Though they were not included in the final fits to the data presented here, it is also possible to impose other constraints on the fit by adding 'penalty' or 'smoothing' functions to χ^2. A simple way to stop the higher order coefficients blowing up is to add the sum of the moduli of the coefficients, weighted by some empirically determined parameter, to χ^2. If the penalty function is too high for a particular set of coefficients, this will be interpreted as a poor fitness, and the set will be discarded to make way for sets with a lower penalty function. Another possibility is to introduce a penalty function with the aim of preventing the differential cross section or $P(f_T)$ distribution becoming negative, which clearly represents an unphysical solution since both functions represent probability distributions. The use of penalty functions should be approached with caution, however, to ensure that the penalty function guides the coefficients in the right direction, but without dominating the search for a best fit.

Monte-Carlo Error Analysis

An estimate of the error limits on the differential cross section and $P(f_T)$ distribution returned from the fitting procedure is obtained using a separate error analysis program. As input

the program requires the basis functions used for fitting, the experimental profiles, and the optimized fitting coefficients. Initially, a cutoff value of χ^2 is determined. above which it is deemed that a fit to the data is no longer being obtained. The coefficients are varied by adding randomly generated increments to each one, and χ^2 for the 'fit' is determined by summing the basis functions using the new coefficents and applying Equation 8.14. If the value of χ^2 is less than the cutoff value the differential cross section and $P(f_T)$ distribution corresponding to the particular set of coefficients are calculated at a set number of points. This is repeated for a large number of sets of parameters, allowing the standard deviation associated with each point to be determined. The error limits on the two distributions are then taken as the optimized function plus or minus one standard deviation of the sampled functions whose χ^2 lies below the specified limit.

9.1.3 Results

Simulated Data

Before being used in the analysis of experimental data, the programs were tested on simulated composite profiles, for which the differential cross section and $P(f_T)$ distributions were known. to ensure that the correct functions were returned by the fitting procedure. The polynomial function $f_T^3(1-f_T)$ was used for the trial $P(f_T)$ distribution, and various forms for the differential cross section were generated using a combination of two Gaussians and a baseline. The fits obtained using a genetic algorithm fitting program allowed to run for 10,000 generations and a contracted basis set consisting of four Legendre moments in $\cos\theta_t$ and f_T are shown in Figures 9.6 to 9.10

With the exception of the β_{kv} moment in the case of backward scattering, the fitted composite Döppler profiles are indistinguishable from the original simulated profiles. The much smaller amplitude of the β_{kv} profile for backwards scattering compared with other types of differential cross section accounts for the slightly poorer fit to this data set. Comparison of the differential cross sections and translational energy distributions returned from the fitting procedure with those used in the simulation of the profiles indicates that the methods of analysis employed can be used to extract accurate dynamical information from composite Döppler profiles.

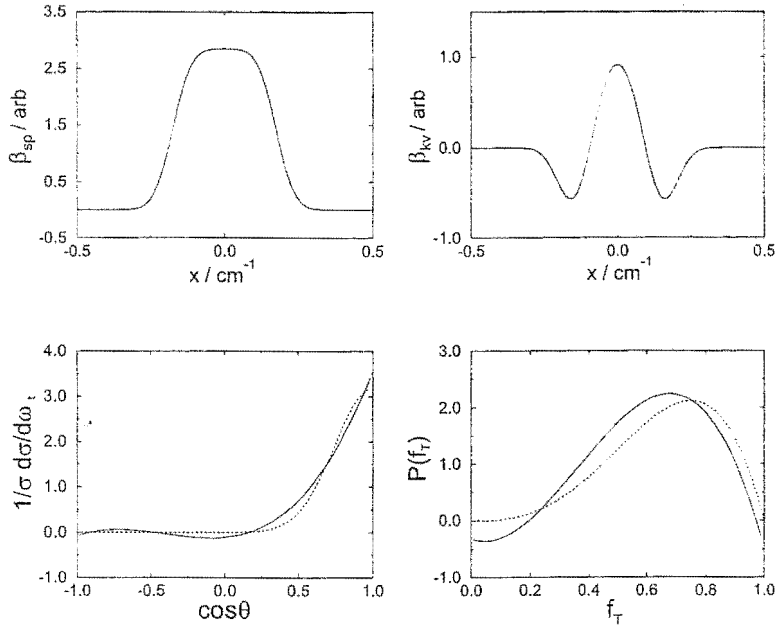

Figure 9.6: Simulated data (dotted lines) and fits (solid lines) for forward scattering, together with input and returned differential cross section and translational energy distribution.

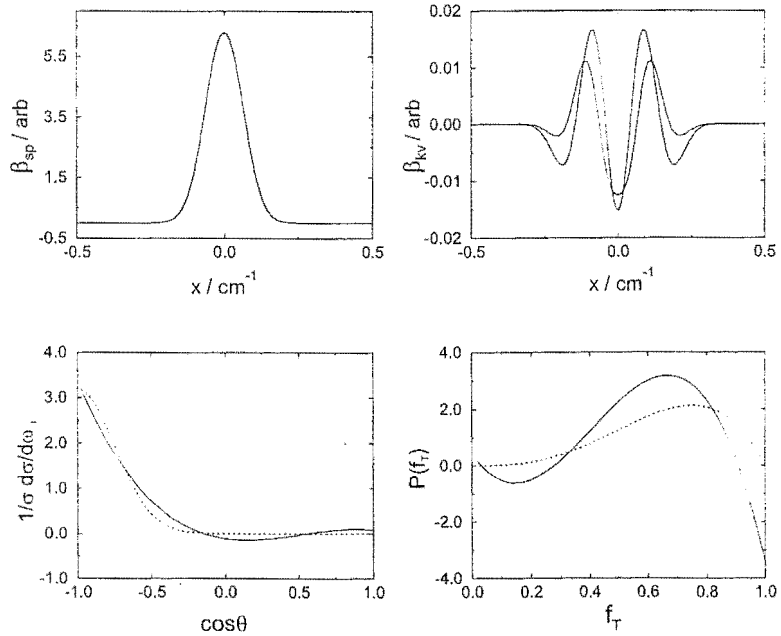

Figure 9.7: Simulated data (dotted lines) and fits (solid lines) for backward scattering, together with input and returned differential cross section and translational energy distribution.

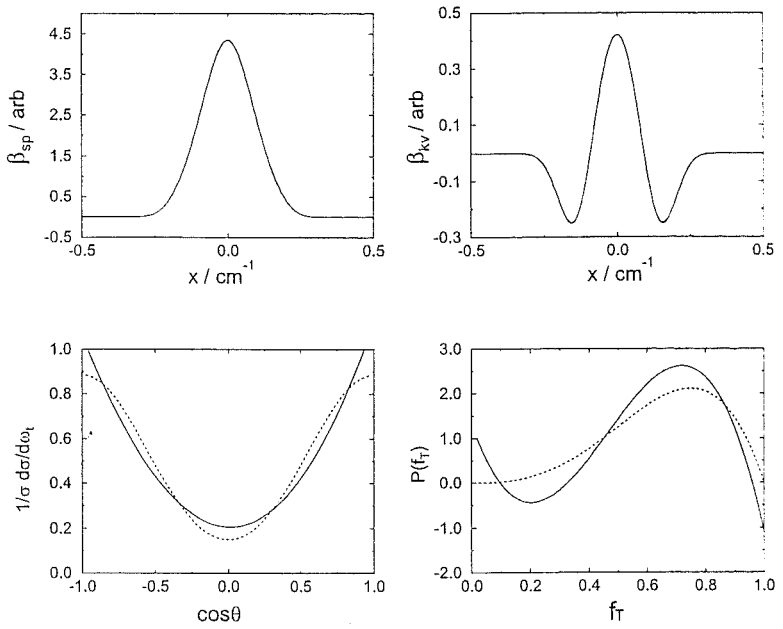

Figure 9.8: Simulated data (dotted lines) and fits (solid lines) for forward–backward scattering, together with input and returned differential cross section and translational energy distribution.

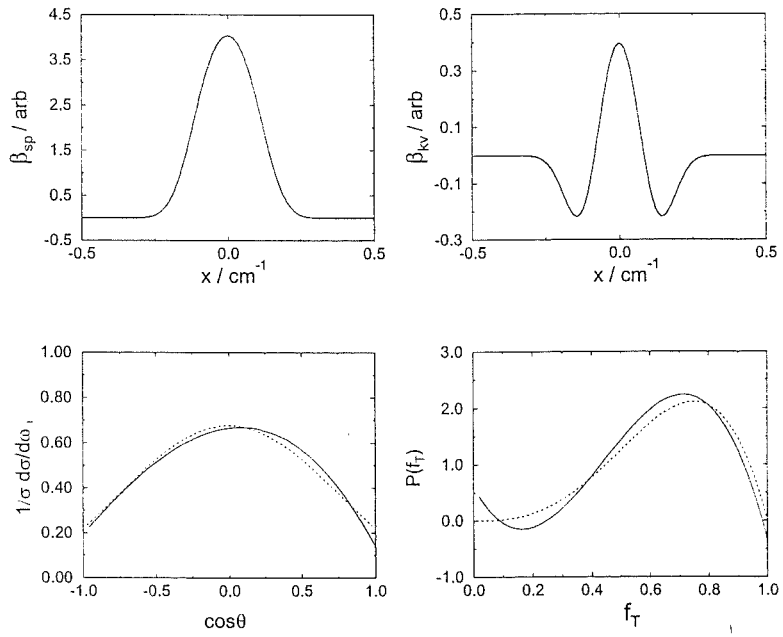

Figure 9.9: Simulated data (dotted lines) and fits (solid lines) for sideways scattering, together with input and returned differential cross section and translational energy distribution.

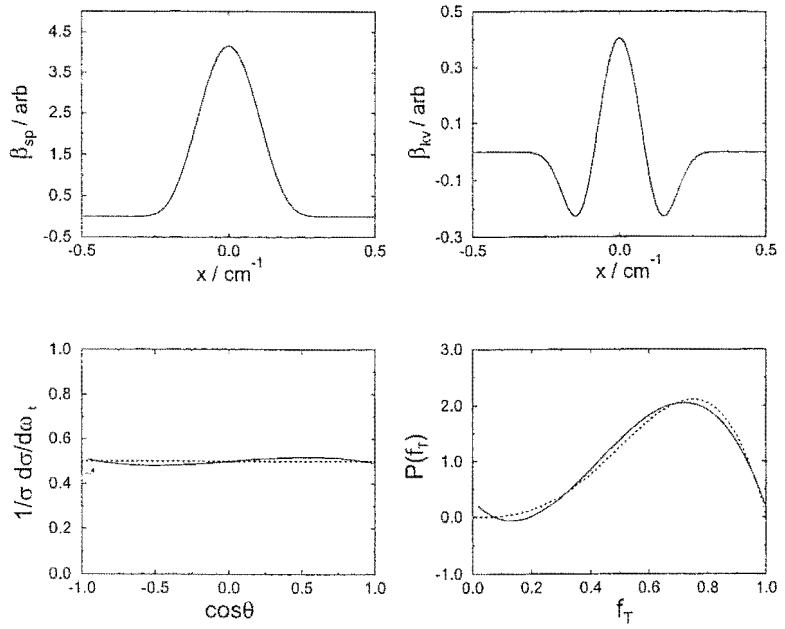

Figure 9.10: Simulated data (dotted lines) and fits (solid lines) for isotropic scattering, together with input and returned differential cross section and translational energy distribution.

Experimental data

Analysis of experimental data from the reaction H+H_2O → OH+H_2 presents some special difficulties. Because the reaction is endoergic by around 26 kJmol^{-1} the kinetic energy release is fairly small. The OH product has a low CM speed and the sensitivity to the scattering angle is reduced. In addition, the low mass of the fast atom means that the velocity of the centre of mass is low, so that not only is the difference between the lab frame velocity vectors for forward and backward scattered OH products small, but the vectors themselves only have small magnitudes. This reducing the sensitivity further since the observed Döppler shifts are small when compared those for reactions with more favourable kinetics.

One advantage of the H+H_2O system is that it presents a special case in which the internal energy levels in the coproduct are widely spaced. This leads to the possibility of using two different two ways to generate basis functions. The first ignores the quantization of the product translational energy and treats f_T as a continuous function, generating random variables and integrating to produce the required number of moments for the contracted basis set. The second method recognises that the values which f_T can take for a given internal state of OH are limited to discrete values by the internal states which may be populated in the H_2 coproduct. At the collision energy of 1.43 eV used in the experiments only ten

rotational levels are accessible, so that only ten values of f_T need to be considered. Basis functions contracted in the $\cos\theta_t$ dimension can then be generated for each of these f_T values and used to fit the experimental profiles. The fitted profiles obtained using both schemes, together with the returned differential cross section and $P(f_T)$ distributions and statistical errors for the fits, are shown in Figures 9.11 to 9.16 for the J=1 and J=5 levels of the OH product. Both Λ-doublet levels of the J=5 level were fitted.

It was found that optimum fits were obtained using three moments each in the $\cos\theta_t$ and f_T dimensions (when applicable) for the Legendre contraction of the basis set‡. This represents a compromise between allowing enough degrees of freedom in the fit to obtain an optimum vaue of χ^2 and at the same time limiting the number of moments which the fitting procedure can handle without the coefficients of the higher moments blowing up to unreasonable values.

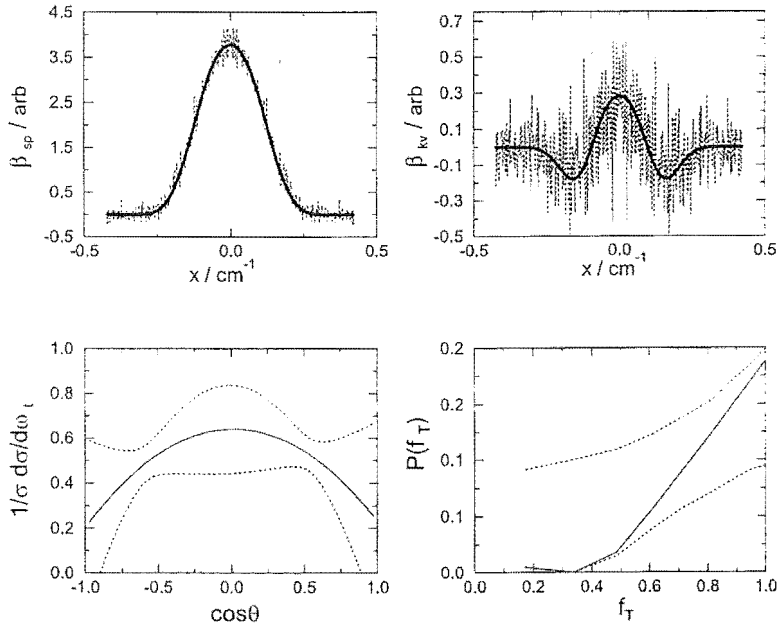

Figure 9.11: Experimental composite Döppler profiles (dotted lines) and best fits (solid lines) for OH($v = 0, J = 1$), together with the returned differential cross section and $P(f_T)$ distribution using basis functions contracted in $\cos\theta_t$ and uncontracted in f_T. χ^2 for the fit was 2.498. Statistical errors are represented by dotted lines.

‡ The number of moments required to obtain a satisfactory fit to a data set is highly dependent on the chemical system under study. For example, in the $H+N_2O$ system at least five moments in f_T are required to obtain a reasonable fit to the composite Döppler profiles, though three moments are sufficient for the differential cross section.

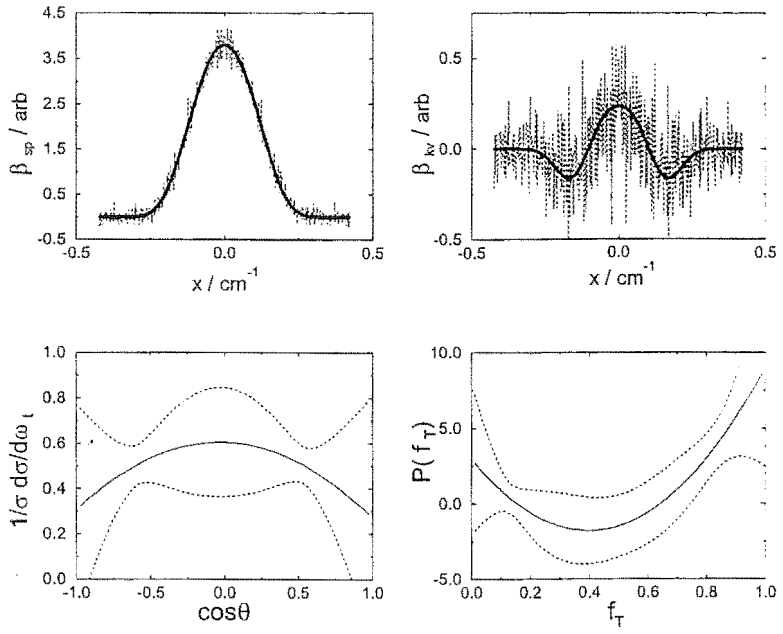

Figure 9.12: Experimental composite Döppler profiles (dotted lines) and best fits (solid lines) for OH($v = 0, J = 1$), together with the returned differential cross section and $P(f_T)$ distribution using contracted basis functions in both $\cos\theta_t$ and f_T. χ^2 for the fit was 2.392. Statistical errors are represented by dotted lines.

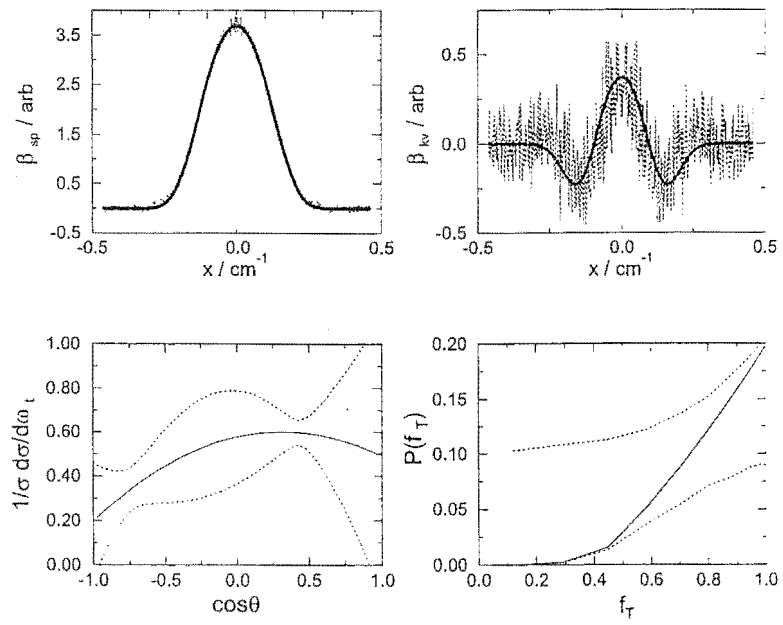

Figure 9.13: As for Figure 9.11 but for the A' Λ-doublet of the ($v = 0, J = 5$) level of the OH product. χ^2 for the fit was 1.834.

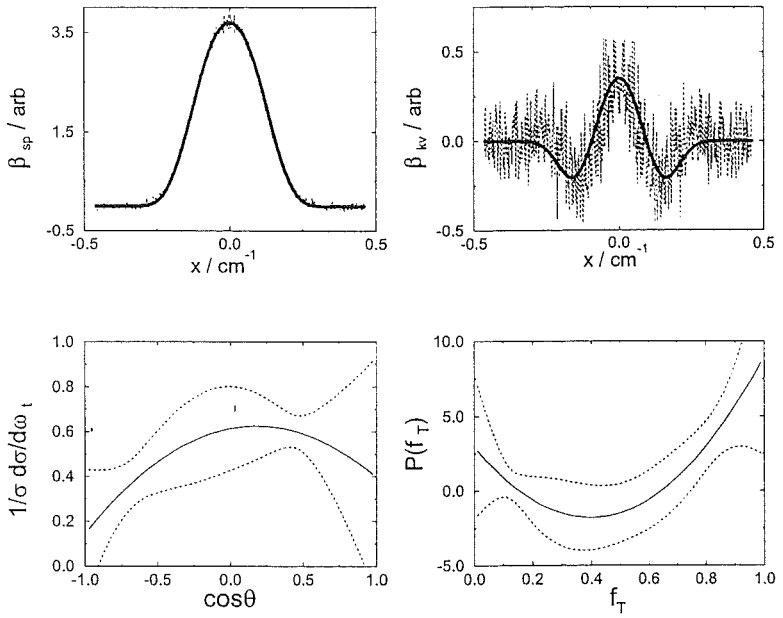

Figure 9.14: As for Figure 9.12 but for the A' Λ–doublet of the $(v = 0, J = 5)$ level of the OH product. χ^2 for the fit was 1.835.

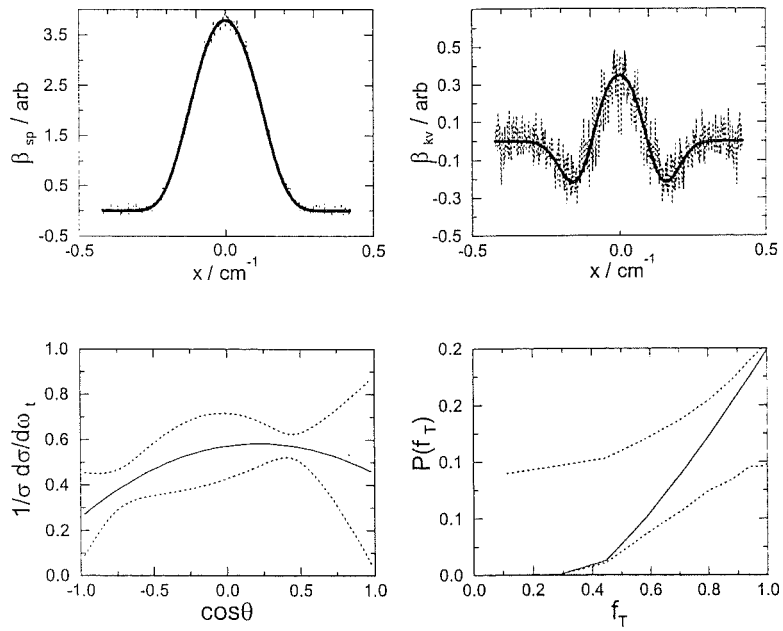

Figure 9.15: As for Figure 9.11 but for the A'' Λ–doublet of the $(v = 0, J = 5)$ level of the OH product. χ^2 for the fit was 1.788.

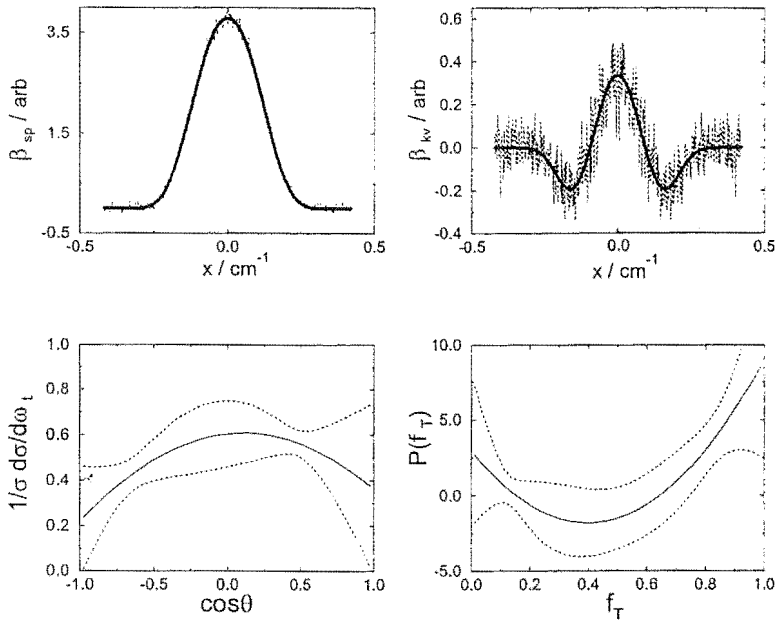

Figure 9.16: As for Figure 9.12 but for the A'' Λ–doublet of the $(v = 0, J = 5)$ level of the OH product. χ^2 for the fit was 1.756.

The differential cross sections and $P(f_T)$ distributions are very similar for all three product rotational states measured, with the distributions returned from the two levels of the $J = 5$ Λ–doublet being virtually indistinguishable. When the differential cross sections for the $J = 1$ and $J = 5$ levels are compared, it is seen that the $J = 5$ product is slightly more forward scattered with respect to the incident H atom direction, though the difference lies well within the error limits of the experimental data and the fitting procedure.

The two different treatments of f_T return very similar distributions. The differential cross section exhibits scattering over all angles in the center of mass frame, with a preference for sideways scattering. The f_T contraction has a negligible effect on the differential cross section and the general form of the $P(f_T)$ distribution is clearly the same for both fitting methods, with most of the available energy appearing as product translation. Fitting with uncontracted basis functions does have the advantage of removing the 'tail' at low f_T which is an artefact of the moment expansion method. Because the f_T coefficients give the $P(f_T)$ distribution directly, rather than just giving the weight for the corresponding Legendre polynomial in the expansion of this quantity, they may be constrained to be greater than zero so that the the returned $P(f_T)$ distribution can only take on positive values. This is not the case when fitting to contracted basis functions. It can be seen that in the moment expansion

the $P(f_T)$ distribution function does pass below zero, which is physically unreasonable, but within the statistical errors of the fit. Despite the obvious advantages of using uncontracted basis functions for the fitting procedure, there are also several disadvantages. Because the fitting procedure must deal with a much larger number of coefficients it is usually necessary to run the fitting program several times to ensure that all the coefficients are converged to their final values. Also, it is only possible to use the method for a very limited number of reactions for which there are only a few accessible internal states for the molecular coproduct. If this is not the case a large number of uncontracted basis functions would be needed, and the fitting procedure would be unlikely to converge to a reasonable solution. With just ten basis functions in f_T it is already seen that the fits to the profiles, as measured by the value of χ^2, are slightly poorer than for the fits using contracted basis functions with only three degrees of freedom in f_T. In the case of the H+H_2O reaction however, for which the analysis is relatively insensitive to the distribution of product translational energies, the method has proved very useful as a check of the validity of the contraction technique.

The product rotational polarization of the OH product was measured for both Λ doublets of the J=5 level. The fitted $\beta_{kj'}$, $\beta_{vj'}$ and $\beta_{kvj'}$ profiles, together with the returned PDDCS's for the two Λ–doublet components are shown in Figures 9.17 and 9.18.

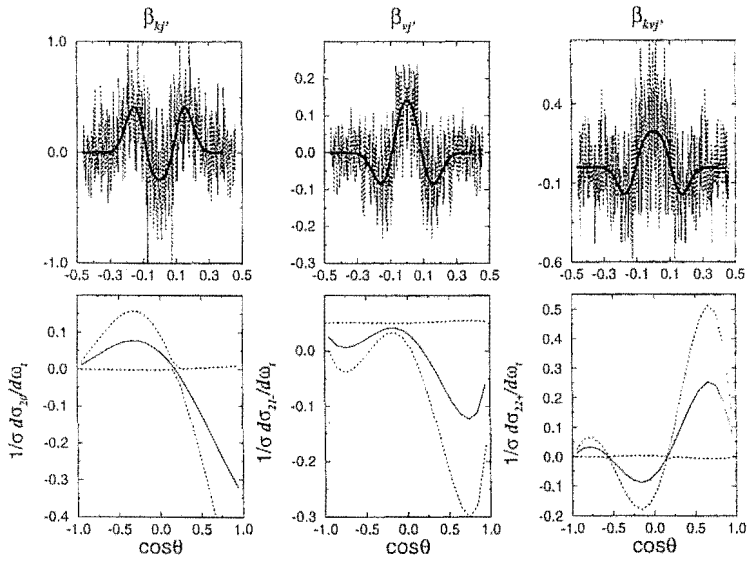

Figure 9.17: The $\beta_{kj'}$, $\beta_{vj'}$ and $\beta_{kvj'}$ experimental composite Döppler profiles (dotted lines) together with best fits (solid lines) and the returned polarization dependent differential cross sections for probing of the A' Λ–doublet level of OH($v = 0, J = 5$).

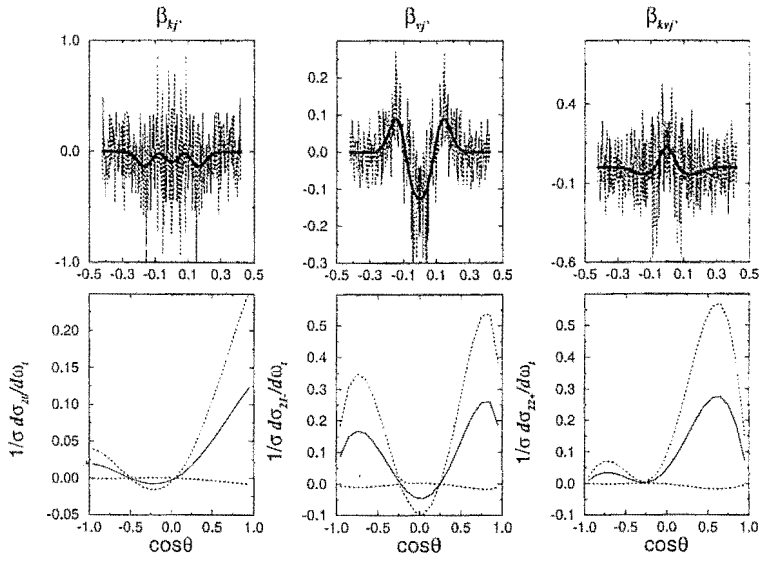

Figure 9.18: As for Figure 9.17 but for the A'' Λ doublet component.

The corresponding distributions $P(\theta_r, \phi_r)$ of j′, calculated from Equation C.23 of Appendix C, are shown in Figures 9.19 to 9.22. In these polar plots the z axis is along the direction of the reagent relative velocity vector **k**, which is essentially the direction of the hot H atom. The product relative velocity **k′** lies in the xz plane, with the x component lying along the positive x axis. Figures 9.19 and 9.20 show that for both components of the Λ doublet j′ lies in the scattering plane. The previous analysis of the speed and β_{kv} dependent profiles suggested that the scattering is fairly isotropic, with a preference for sideways scattering, and a most probable scattering angle, lying slightly in the forward hemisphere, of around 75°. From Figures 9.21 and 9.22, which show the polarization of j′ in the scattering plane, this implies that for the A' component j′ is aligned approximately along the product relative velocity vector, while for the A'' component the two vectors are perpendicular. The rotational motion of the OH in the A' Λ doublet state may be visualised as that of a 'propellor' propagating along the product relative velocity vector. In contrast, the A'' Λ doublet undergoes more of a 'cartwheel' type motion.

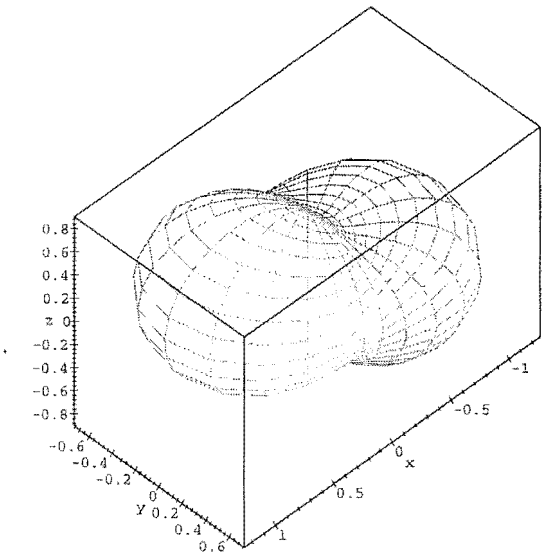

Figure 9.19: Polar plot of the rotational polarization of the OH($v = 0, J = 5, A''$) product of the $H+H_2O$ reaction.

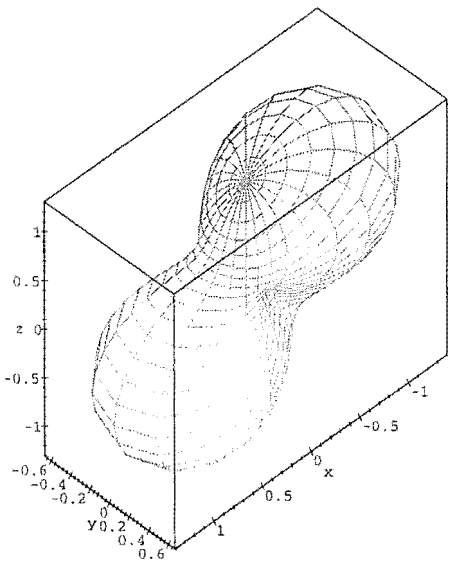

Figure 9.20: As for Figure 9.19 but for the A'' Λ doublet component.

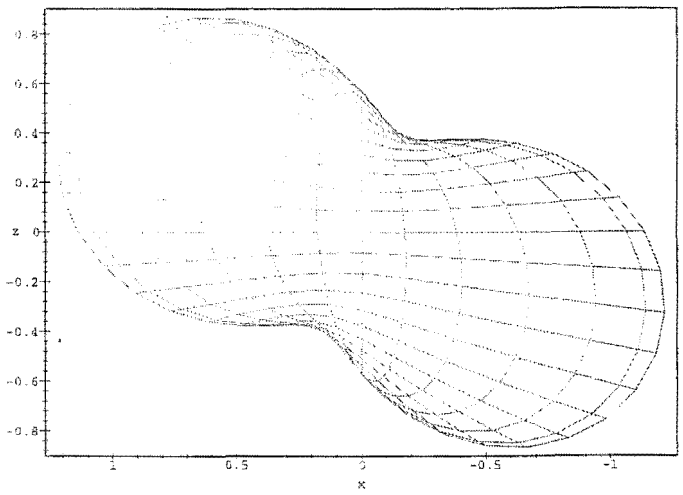

Figure 9.21: Polar plot of the rotational polarization in the scattering plane of the OH($v = 0, J = 5, A'$) product of the H+H_2O reaction.

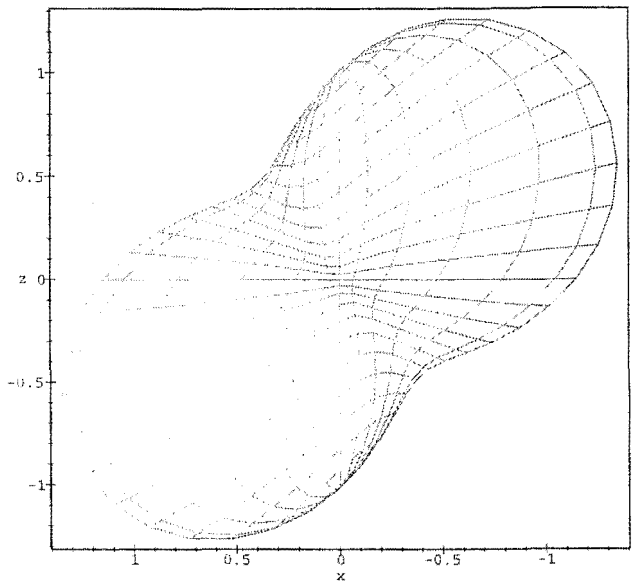

Figure 9.22: As for Figure 9.21 but for the A'' Λ doublet component.

9.2 Discussion

9.2.1 Previous work on the $H+H_2O$ reaction

The $H+H_2O$ reaction has attracted wide interest, both from experimentalists and theoreticians. The reverse reaction is a key process in combustion[203] and also plays a significant role in the chemistry of interstellar space. In addition, the $H+H_2O$ reaction represents one of the simplest four atom systems, and the small number of electrons involved has made it fairly easily accessible to *ab initio* calculations of the potential energy surface, and therefore also to quasi-classical and quantum scattering calculations of the reaction dynamics.

Theoretical studies

The first attempt to calculate a potential energy surface for the reaction was made in 1979 by Walch and Dunning, who used a triple zeta basis set with polarization functions to carry out high quality *ab initio* calculations which included configuration interaction. A saddle point was located in the exit channel with a barrier height of 26 $kJmol^{-1}$, corresponding to a planar H-H-O-H transition state with an H-H-O angle of 165°.

Schatz *et al*[204] used the *ab initio* points calculated by Walch and Dunning to construct an analytic potential energy surface for the purpose of carrying out QCT calculations. They determined excitation functions as a function of reagent vibrational mode as well as overall thermal rate constants. Vibrational excitation in the H_2O reagent was shown to lead to enhanced reaction probability, reflecting the presence of the late barrier in the potential energy surface[§].

Zhang and Light[207] used the Schatz-Elgersma surface to carry out time dependent wave packet calculations to determine quantum state–to–state reaction probabilities for the system. They found that only about 25% of the collision energy appeared as internal excitation of the products, with the fraction going into H_2 vibration being approximately forty times larger than that into vibration of the OH product. The rotational distributions for H_2 in the v=0 state were also strongly dependent on the collision energy, with higher collision energies leading to the population of higher rotational states in the H_2 fragment.

[§] According to the widely used 'Polanyi rules'[205,206] vibrational excitation supplies energy in the correct degree of freedom to overcome a barrier in the exit channel, while translational excitation favours reactions with a barrier in the entrance channel.

The Schatz-Elgersma surface was also used by Clary[208–210] for quantum mechanical scattering calculations, yielding rate constants, integral cross sections and differential cross sections for the reverse reaction of OH with D_2. The product HOD was scattered backwards with respect to the incoming OH molecule, in agreement with the experimental measurements of Alagia *et al.*[211]

Experimental studies

The practical importance of the reverse reaction, $OH+H_2 \rightarrow H+H_2O$ has lead to its kinetics being widely studied,[212,213] with measurements of rate constants and isotope effects having been carried out over the temperature range from 250 to 1050 K. The reaction is very slow at room temperature, with a rate constant of 6.1×10^{-15} $cm^3molecule^{-1}s^{-1}$ at 298 K, corresponding to a cross section of 3.6×10^{-4} Å^2, but the rate increases dramatically at high temperatures. The experimental activation energy depends on the isotopes present, and was found to be 16.9 $kJmol^{-1}$ for $OH+H_2$ and 22.4 $kJmol^{-1}$ for $OH+D_2$. A marked isotope effect at low temperatures indicates that tunnelling of the H/D through the potential barrier becomes important as the temperature is decreased.[214]

As well as kinetic studies, a range of dynamical experiments have been carried out on the system. The endoergic nature of the reaction means that energy must be supplied to overcome the barrier. As in the present work, this is usually achieved using the hot atom technique, in which the H atom reagent is prepared by photolysis of a suitable precursor and is formed with considerable translational kinetic energy. Alternatively, the energy can be provided in the form of vibrational excitation in the H_2O reagent.

Several groups[215–218] have used the hot atom technique to obtain OH product internal state distributions and absolute reactive cross sections over the range of collision energies from 33 to 58 $kJmol^{-1}$ (0.34–0.60 eV). As was demonstrated by the theoretical studies, vibrational excitation of the H_2O reagent strongly favours reaction. Zare and coworkers[219] and Kessler and Kleinermann[218] showed that excitation of the fundamental OH and OD vibrations in HOD increased the reaction cross section by a factor of up to 120 over the increase obtained by channeling a similar amount of energy into reagent translation. In fact, the cross section was found to be approximately constant with H atom energy for energies above threshold. As mentioned earlier, this observation may be explained in terms of the Polanyi rules. An alternative explanation was offered by Zare with his 'cone of acceptance' model, which also

gives insight into the possible dependence of the reactivity on the H atom approach angle.

For ground state H_2O the model assumes that in order to abstract an H atom from the molecule, a fast H atom must impart enough energy along the bond to cause reaction. At a given energy this implies a limited range of impact angles which can lead to reaction, the so called 'cone of acceptance'. Inside this cone the momentum transfer from the H atom is sufficient to cause reaction, while collisions resulting from impacts at angles outside the cone are non–reactive. Since vibration increases the energy along the reaction coordinate (the OH bond), less of the H atom translational energy is required to be directed along the bond. In consequence, the cone of acceptance widens, so that collisions at higher angles can lead to reaction, and the reaction cross section increases.

In addition to the above, Crim and coworkers,[220–223] and later Zare *et al*,[224–226] also showed that specific excitation of either the OH or OD fundamental stretching vibrations leads to selective cleavage of the corresponding bond, even when only a single quantum of energy is supplied. This example of mode selectivity has been supported by both QCT and quantum scattering calculations.[227–230]

Kessler and Kleinermanns[218] measured internal state distributions for the OH product at CM collision energies of 176 and 143 kJmol^{-1} (1.82 and 1.48 eV). No LIF signal from OH in the $v = 1$ state was observed, indicating that OH is formed almost exclusively in the ground vibrational state. The rotational distributions peaked at between $J = 2$ and $J = 3$, so that only around 5% (at 176 kJmol^{-1}) or 8% (at 143 kJmol^{-1}) of the total available energy is channeled into rotational excitation of the OH product. This can be explained by a simple impulsive model in which the light departing H_2 molecule is unable to exert a large repulsive force on the OH fragment. Coupled with the H-H-O bond angle of 104° at the saddle point, the amount of torque exerted along the breaking bond is minimal so that only low rotational states of the product are populated.

Alagia *et al*[211] carried out a crossed beam study of the reverse reaction at an energy of 26.5 kJmol^{-1}, very close to the threshold. These experiments showed that the H_2O product is strongly backward scattered with respect to the initial OH direction. This was explained in terms of the rebound dynamics of a simple H atom transfer reaction, with cleavage of the H-H bond and formation of the new O-H bond occuring simultaneously. As mentioned earlier, the experimental results were convincingly reproduced by Clary's quantum scattering calculations.[229] In contrast to the forward reaction, approximately 65% of the available

energy is channeled into internal excitation of the products, whch may again be explained in terms of the position of the barrier in the potential energy surface. For the reverse reaction the barrier appears in the entrance channel, and translational energy in the reactants, which favours reaction, is transformed into vibrational motion of the products.

Studies by Kleinermanns and Wolfrum[215] and Honda *et al*[217] demonstrated a strong preference for population of the A' Λ-doublet component of the OH reaction product, in which the unpaired electron density lies in the plane of rotation. This is explained in terms of a direct stripping mechanism in which the H atom approaches in the plane of the H_2O molecule. Since any impulse delivered to the OH fragment during bond cleavage must be in this plane the OH product will possess rotation in the plane in which the transition state lies immediately before it dissociates into products. It would be expected that the unpaired electron density will lie along the direction of the breaking bond, i.e. in the plane of rotation. The state averaged A'/A'' ratio was measured to be 3.2.

9.2.2 Present work

The differential cross section and translational energy distribution

Using either method for fitting the β_{sp} and β_{kv} profiles (i.e. contracted or uncontracted basis functions in f_T), the returned f_T distribution shows that most of the available energy is channeled into product translation. This is in agreement with the previously determined product internal state distributions described in Sections 9.2.1 and 9.2.1, and is typical of a reaction with a late barrier in the potential energy surface. When the present results are compared with Zhang and Light's calculations of the product state distributions for the reaction[207] it is found that there is almost quantitative agreement.[231]

To date, there has been little published about the differential cross section for the $H+H_2O$ reaction. The study by Alagia *et al* of the reverse reaction[211] showed that the H_2O product is strongly backscattered with respect to the direction of the reagent OH molecule. Applying the principle of microscopic reversibiblity, it may be expected that the OH from the forward reaction would be forward scattered with respect to the direction of the incident H atom (backward scattered according to Alagia's convention). The present study shows that this is obviously not the case, with significant amounts of scattering over all centre of mass angles and a preference for sideways scattering. The results for the $J = 5$ level show a slight shift towards forward scattering, but this is only a very small effect. One of the major differences

between the experiments of Alagia *et al* and the present study is the collision energy at which the work has been carried out. The study of the reverse reaction was carried out very close to threshold, at an energy lying just 0.03 eV above the barrier, while the present work is at a collision energy which lies around 0.6 eV above the barrier. An explanation for the broad angular scattering observed at this collision energy could lie in the cone of acceptance model described in Section 9.2.1. As the collision energy is increased, a wider range of approach angles of the hot H atom to the H_2O molecule will lead to reaction, since the fraction of the H atom translational energy which must be delivered to the O-H bond in order for reaction to occur is reduced. This widening of the range of attack angles could be expected to manifest itself as a spreading out of the angles at which the product is scattered as the collision energy is increased. This idea is supported by QCT data[232] and also by calculations using the simple modified line of centres model formulated by Smith.[212] It would be interesting to measure the dependence of the differential cross section on the collision energy to see if this is indeed the case, and if the product angular distribution becomes more forward scattered at low collision energies as the results of Alagia and coworkers might suggest. With the current experimental arrangement, it would be difficult to move to lower collision energies, due to the scarcity of suitable photolysis precursors which yield H atoms of a suitable energy, but it should be possible to move to higher energies.

Rotational polarization of the products

Compared to other systems which have been studied[233] the angular momentum polarization effects in the $H+H_2O$ system are fairly small, with the returned PDDCS's lying well within the physical limits defined by Aoiz and coworkers.[234] The results presented in Section 9.1.3 showed that for both Λ–doublet components of the J=5 level of the OH product $\mathbf{j}'$ lies in the scattering plane. The form of the differential cross section for the reaction suggests that for the A' component $\mathbf{j}'$ is aligned approximately along the product relative velocity vector, and the product undergoes a 'propellor' type motion, while for the A'' component the two vectors are perpendicular, resulting in a 'cartwheel' like motion of the OH fragment.

The majority of studies of the $H+H_2O$ reaction system have been carried out at low collision energies, and indicate that the preferred approach direction of the H atom is along the direction of one of the OH bonds of the target H_2O molecule. As the H-H bond forms the O-H bond breaks via a coplanar transition state, so that any impulsive force transferred to the

OH product must act in this plane. The resulting OH rotation must then lie in the scattering plane and the product rotational angular momentum vector $\mathbf{j}'$ will be aligned perpendicular to this plane. The OH product is forward scattered with respect to the direction of the incident hot H atom.

For a collision energy of 1.43 eV, at which the present work was carried out, this does not appear to be the case. Analysis of the speed and β_{kv} dependent profiles showed that the product OH is not strongly forward scattered, but that scattering occurs over all angles, with a preference for sideways scattering. In addition, the polarization of the product rotational angular momentum is found to lie in the xz plane, which is again inconsistent with the mechanism described above. As stated previously, the preferential polarization of the product rotational angular momentum vector is fairly small. The ratio of polarization in the scattering plane to polarization out of the plane, measured by the ratio of the 'waist' to the length of the distributions shown in the polar plots (Figures 9.17 to 9.22), is around 3:1 for the A' Λ–doublet component, and slightly more than 2:1 for the A'' component. The difference in this ratio for the two components is probably due to the different levels of noise on the experimental profiles; the distribution for the A'' component, with the lower polarization, is derived from much noisier data than for the A' Λ–doublet component.

The preferentially in plane polarization of the product rotational angular momentum may be indicating that the target H_2O molecule does not lie in the scattering plane. If only one of the O-H bonds lay in the xz plane then the approach of the hot H atom and subsequent dissociation of the in plane bond would lead to product OH rotational angular momentum of the observed polarization. This would indicate that there is some barrier to the H_2O molecule lying in the scattering plane, the source of which cannot readily be explained.

It is important to bear in mind that the information which may be obtained from these experiments is limited to the preferred alignment of $\mathbf{j}'$ either in or out of the scattering plane, since only even moments of the distribution $P(\theta_r, \phi_r)$ with $k \leq 2$ may be determined using linearly polarized probe radiation. It is always possible that there is an orientation of $\mathbf{j}'$ out of the plane of scattering, which cannot be detected using the currently available techniques. A complete study into the product angular momentum polarisation requires knowledge of the odd moments of the distribution in addition to the even moments already determined. It is possible to calculate all the moments of the distribution using QCT methods, and calculations for the $H+H_2O$ system on the Scatz-Elgersma potential energy surface are

currently underway. Also, if circularly polarized probe light is used it may be possible to measure a limited number of the odd moments, allowing information on the orientation of the angular momentum polarization to be extracted from the experimental data. These experiments are currently being developed. The present results therefore give a small insight into the possible dynamics of the $H+H_2O$ reaction at a higher collision energy than has been used in previous dynamical studies, and it is expected that the understanding of this system will be increased as more information is obtained on the various moments of the product rotational angular momentum distribution.

10. EXPERIMENTAL DESIGN AND DATA ANALYSIS SOFTWARE

This chapter details the design and construction of an experimental system which will be used to study collisions between oriented symmetric top molecules and ions or electrons. In the planned experiments a beam of spatially oriented symmetric top molecules is intersected with a pulsed ion or electron beam and the ionic collision products directed towards an ion imaging detector. The experimental apparatus should allow the dynamics of both electron impact ionization and ion–molecule reactions, as well as their dependence on molecular orientation, to be studied in detail. Schematic diagrams of the crossed molecular beam machine are shown in Figures 3.1 and 3.2.

10.1 Systems to be studied

There are two projects for which the crossed beam apparatus described above will be used. The first is an investigation into the stereodynamics of electron impact ionization, which will extend the work covered in Chapters 1 and 2. The second involves studies of reactive scattering between oriented symmetric top molecules and either alkali metal or halide ions. The first reactions to be explored will be those of potassium and halide ions with the methyl halides CH_3Cl, CH_3Br and CH_3I.

10.1.1 K^++CH_3X reactions

The reactions of potassium ions with symmetric top alkyl halides have been studied previously by the drift tube technique.[112] There appear to be two primary reaction channels.

$$K^+ + CH_3X \rightarrow CH_3^+ + KCl$$

$$K^+ + CH_3X \rightarrow K^+.CH_3Cl$$

The energetics of the halide transfer reaction can be calculated from tabulated heats of formation[152] for the species involved. These reactions are found to be endoergic by around 4.5 eV due to the greater affinity of the halide ion for the methyl group over the K^+ ion.

Thermodynamic data are not available for the association reactions, and molecular orbital calculations were carried out to estimate the reaction energy. Molecular geometries were optimised at HF/LanL2DZ level and energy calculations using the Hartree–Fock geometries were then carried out at B3LYP/LanL2DZ level. These calculations indicated that the association is exoergic by an amount ranging from 0.22 eV for CH_3I to 0.52 eV for CH_3Cl. The geometry optimisations indicated that the product is a loosely bound ion–dipole complex, with the K^+ ion situated at a distance of 3–4 Å from the halide atom along the symmetry axis of the methyl halide molecule. The CX bond is lengthened by a small amount relative to the neutral molecule and the HCX bond angle is reduced slightly. The reaction exoergicities for the two product channels are summarised in Table 10.1. Calculated geometries for the three methyl halides and the association complexes are given in Table 10.2.

Table 10.1: Reaction exoergicities for halide transfer and association reactions of K^+ ions with CH_3Cl, CH_3Br and CH_3I.

Methyl halide	Halide transfer[a]		Association[b]	
	eV	$kJmol^{-1}$	eV	$kJmol^{-1}$
CH_3Cl	4.54	443	-0.519	-50.1
CH_3Br	4.45	430	-0.374	-37.1
CH_3I	4.50	434	-0.228	-22.0

[a] calculated from tabulated data.[152]
[b] B3LYP/LanL2DZ calculations.

Products of the exoergic association reactions should be observable at all ion energies, while the halide transfer products will be observed only at collision energies above the reaction threshold. The dynamics of the halide transfer reaction are expected to be similar to those of the neutral analogue, which is known to occur via a spectator stripping mechanism. If this is the case, the CH_3^+ product should be predominantly backwards scattered, receiving an impulse from fission of the C–X bond as the KCl product continues in the original direction of the K^- ion. In the case of the association reaction pathway, conservation of momentum dictates that the single collision product must be stationary in the centre of mass frame, and should simply travel along with the centre of mass of the reacting system.

Table 10.2: Geometries of CH_3X and $K^+.CH_3X$ association complexes calculated at HF/LanL2DZ level.

Species	Bond lengths / Å	Bond angles / °	Dihedral angles / °
CH_3Cl	CCl 1.8588	HCCl 107.1650	HCClH 120.0000
	CH 1.0746		
$K^+.CH_3Cl$	CCl 1.9039	HCCl 105.0901	HCClH 120.0000
	CH 1.0725	KClC 180.0000	
	KCl 3.0841		
CH_3Br	CBr 2.0133	HCBr 107.1243	HCBrH 120.0000
	CH 1.0745		
$K^+.CH_3Br$	CBr 2.0518	HCBr 105.0515	HCBrH 120.0000
	CH 1.0727	KBrC 180.0000	
	KBr 3.3380		
CH_3Cl	Cl 2.1808	HCl 107.3846	HClH 120.0000
	CH 1.0756		
$K^+.CH_3Cl$	Cl 2.2108	HCl 105.5734	HClH 120.0000
	CH 1.0733	KIC 180.0000	
	KI 3.7010		

10.1.2 X^-+CH_3Y reactions

S_N2 reactions

A considerable amount of theoretical work has been carried out on gas phase S_N2 reactions, together with a number of experimental studies. Theoretical investigations have largely concentrated on determination of the detailed energetics and geometries involved in the reaction process[235–245] with the result that the general form of the potential energy surface is now well established. The potential energy surface along the reaction coordinate consists of two potential wells separated by a central activation barrier. The potential wells correspond to ion–dipole association complexes of C_{3v} symmetry in the entrance and exit channel for the reaction. The height of the central barrier has been shown to decrease with increasing reaction exothermicity.[246]

Quassiclassical trajectory studies[246,247] have been used to probe the dynamics of the

scattering process, and indicate two possible mechanisms for reaction. The trajectory studies were carried out on an analytic potential energy surface[237,248] derived from fits to experimental and *ab initio* data. Provided there is significant vibrational excitation in the C–Y stretch mode of the reagent methyl halide, backside attack of the X^- ion on the methyl halide at an angle of ~180° to the C–Y bond allows the reaction to occur via a direct substitution mechanism.[246] Otherwise, the reaction is thought to occur through an association mechanism involving trapping in the potential energy wells of the entrance and exit channel. Collisional association of the reagents to form the ion–dipole complex occurs through a translation to rotation (T→R) energy transfer process, involving coupling between the orbital angular momentum of the reactants and the rotational angular momentum of the methyl halide molecule. Collisions for which the dynamical stereochemistry does not allow for sufficient energy transfer into rotation do not form complexes,[247] and consequently the calculated association rate constant is less than that of statistical ion–molecule capture theories.[249] Complex formation does not involve energy transfer to CH_3Y vibration and initially energy is only stored in the three low frequency intermolecular modes of the $X^- \cdots CH_3Y$ complex, namely the $X^- \cdots C$ stretch and degenerate bending modes. The dominant fate of the complex is dissociation back into the reactants. However, for the small number of complexes which survive, energy begins to transfer from the $X^- \cdots CH_3Y$ intermolecular modes to the CH_3Y intramolecular modes, and eventually dissociation into the Y^-+CH_3X products becomes possible. The dynamical barrier for energy transfer gives rise to the central barrier observed in the potential energy surfaces for these reactions. The weak coupling between the intermolecular and intramolecular modes of the association complex means that the complex may remain trapped in the central barrier region and undergo multiple crossings of the barrier before forming products or returning to reactants.

The relative importance of the two different mechanisms depends largely on the rotational energy of the CH_3Y reagent. If the methyl halide is rotationless the majority of collisions will have dipole orientation and reaction will occur predominantly through direct substitution if there is enough vibrational excitation in the C–Y bond. If the rotational temperature is raised the association mechanism quickly becomes dominant.

Experimental studies seem to support the *ab initio* and trajectory simulation results. Reaction rates are often slow[250] compared to many other gas phase ion–molecule reactions. This is thought to be a reflection of competition between product formation and dissociation

back into reagents for the ion–dipole association complex due to the considerable activation barrier in the double well potential energy surface. Su and coworkers[251,252] measured rate constants for the highly exothermic S_N2 reactions of F^- with CH_3Cl, CH_3Br and CH_3I, using a variable temperature selected ion flow drift tube. Measurements were made as a function of collision energy at several temperatures. The rate constants obtained were found to be much higher than the corresponding solution phase reactions, but were significantly lower than the capture rate constants for formation of the $F^- \cdots CH_3X$ association complex. This is consistent with the orientation condition on complex formation discussed above. The rate constant was also found to decrease with increasing average relative kinetic energy, reflecting the reduction in the time available for the ion and molecule to move into a favourable orientation for reaction as the relative velocity of the reagents increases.

Li *et al*[253] carried out high pressure mass spectrometric investigations into the reactions of Cl^- and Br^- with several alkyl halides. In these experiments the ion signals from the intermediate association complexes as well as the reaction products were able to be monitored as a function of residence time in the ion source of the mass spectrometer. This allowed equilibrium constants to be measured for the association equilibria, and consequently allowed a determination of the free energy change for formation of the complex and therefore the well depth on the potential energy surface. The overall rate of reaction could be used to determine the intermediate barrier height using a transition state theory analysis of the experimental data. For the cases in which theoretical data was available for comparison agreement was almost quantitative. It was also possible to determine a lifetime for the transient intermediate complex, which was in excellent agreement with the results of the trajectory calculations described earlier. This series of experiments provided the first completely experimental verification of the double well nature of the potential energy surface for the gas phase S_N2 reaction.

DeTuri and coworkers[254] measured excitation functions over the range 0-12 eV for reaction of $^{37}Cl^-$ with $CH_3^{35}Cl$ in a guided ion beam tandem mass spectrometry experiment. The cross section for ^{35}Cl production was found to rise steeply from a threshold of 0.47 eV to a plateau region at collision energies of 3–5 eV, before rising to a peak at 8.5 eV and declining again at higher energies.

Other reaction channels

At suprathermal collision energies several additional reaction channels become accessible for the X^-+CH_3Y system. The formation of Cl_2^- ions in collisions between Cl^- and CH_3Cl at energies above 4.25 eV was observed by DeTuri *et al*,[254] corresponding to the reaction

$$Cl^- + CH_3Cl \rightarrow Cl_2^- + CH_3 \tag{10.1}$$

Zellerman and coworkers[255] observed a products from a number of different reaction channels while carrying out measurements of the total reactive scattering cross sections for collisions of Br^- and I^- ions with CH_3F. S_N2 reaction for these systems is endothermic, with thresholds of 4.6 and 4.7 eV for the Br^- and I^- ions respectively. In addition to the F^- ion product of the nucleophilic substition reaction, the products FX^- and CH_2X^- (X=Br,I) were observed, with H^- also produced in the bromide reaction. The dihalide ion product corresponds to the process analagous to reaction 10.1, while the the CH_2X^- corresponds to a dehydrohalogenation process in which HF is formed as the neutral partner. There are several possibilities for production of the observed H^- ions, and further reaction channels for F^- ion production also become accessible at high collision energies. A summary of the possible product channels for a generalised X+CH_3Y reaction based on the observations of Zellerman *et al* is given below.

$$\begin{aligned}
X^- + CH_3Y &\rightarrow XY^- + CH_3 \\
&\rightarrow CH_2X^- + HY \\
&\rightarrow Y^- + CH_3X \\
&\quad Y^- + CH_3 + X \\
&\quad Y^- + CHX + H_2 \\
&\rightarrow H^- + CH_2YX \\
&\quad H^- + CH_2Y + X \\
&\quad H^- + CHY + HX \\
&\quad H^- + CHX + HY \\
&\quad H^- + CHXY + H \\
&\quad H^- + CXY + H_2
\end{aligned} \tag{10.2}$$

As discussed above, the S_N2 reaction pathway proceeds through a five coordinate tran-

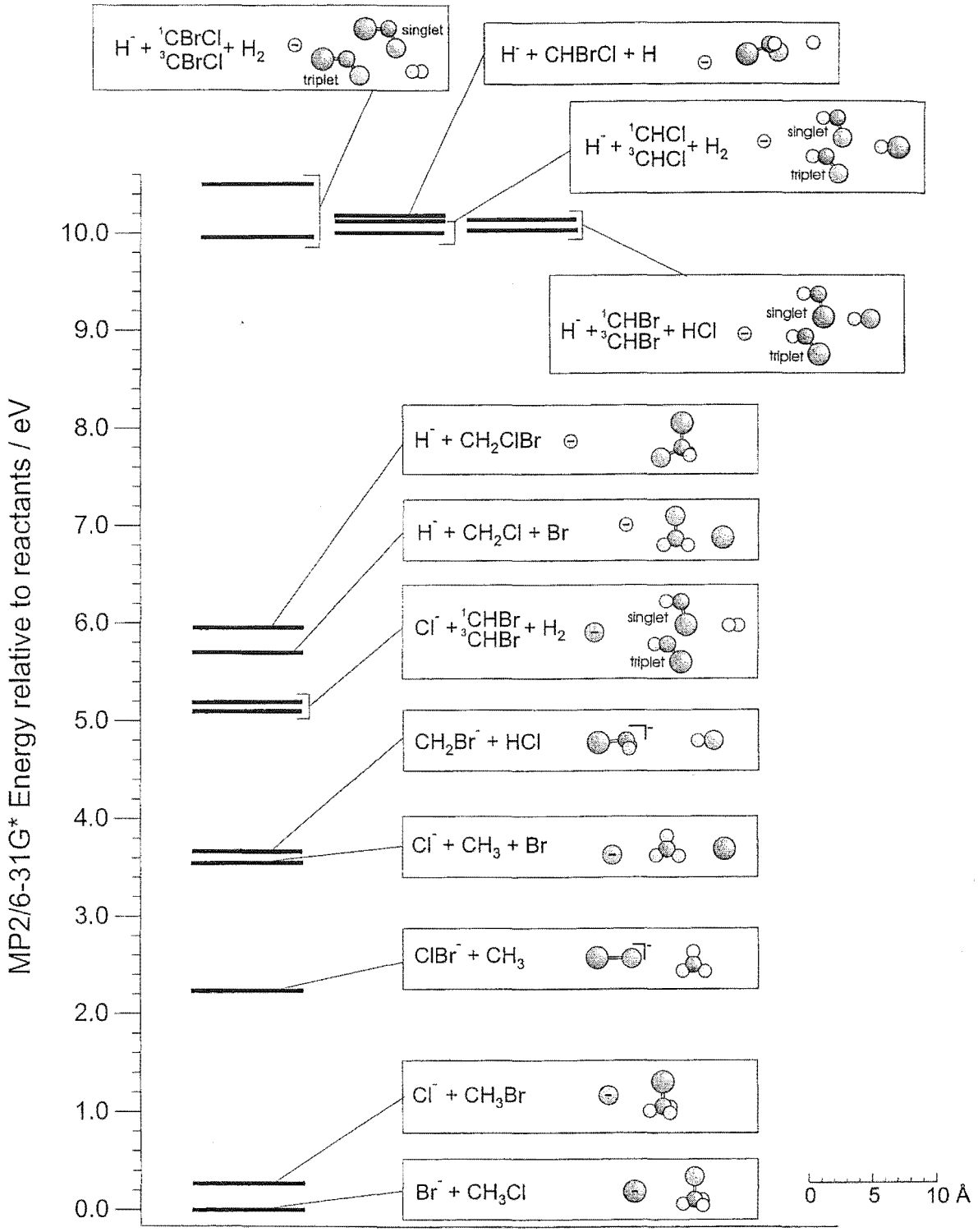

Figure 10.1: Relative energies of accessible product channels for the $Br^- + CH_3Cl$ reaction.

sition state region of C_{3v} symmetry, with the two halogen atoms occupying axial positions. The channels leading to XY^- and CH_2X products are thought to pass through a transition state geometry of C_s symmetry in which the positions of the axial X atom and one of the equatorial protons are interchanged relative to the S_N2 channel.

While a great deal of theoretical work has been carried out on the S_N2 reaction pathway, little or no attention seems to have been paid to the alternative higher energy pathways. *Ab initio* calculations were carried out on the Br^-+CH_3Cl reaction, one of the reactions of interest for the ion imaging studies, in order to further investigate these product channels. Geometry optimizations were carried out at MP2/6-31G* level for each of the eleven product channels listed in Equation 10.2. The relative energies and geometries of the products are shown in Figure 10.1. The S_N2 products are by far the lowest in energy, followed by the pathway leading to the dihalide ion. S_N2 reaction with fragmentation of the CH_3Br product to give atomic bromine and CH_3 is only slightly lower in energy than the channel leading to CH_2Br^- production. Reaction pathways leading to H^- and/or carbene production are significantly higher in energy. These results are not necessarily indicative of the expected appearance energies of the various ionic products since there may well be activation barriers to be overcome for some or all of the possible reaction pathways, as is the case for the nucleophilic substitution reactions, and more detailed calculations are required to establish details of the potential energy surfaces which control these reactions.

The effect of the approach direction of the Br^- ion to the CH_3Cl molecule on the energy of the system was also investigated. Potential energy curves were calculated for four different approaches of the Br^- ion to the molecule as a function of the C–Br^- internuclear separation. At each point for which the energy was calculated the C–Br^- distance was fixed and the remaining geometrical parameters optimised. The calculations were only performed at Hartree–Fock level, but do serve to illustrate significant differences for the four geometries considered. As expected, approach to the CH_3 end of the molecule along the C–Cl bond axis is the lowest energy pathway, and gives rise to the anticipated potential well corresponding to the ion–dipole association complex. A Br^- ion approaching the Cl end of the molecule experiences a strongly repulsive potential at distances less than ~3Å from the Cl atom. This approach geometry is therefore highly unlikely to lead to reaction. Direct approaches to the carbon atom in a direction perpendicular to the C–Cl bond axis, either in the plane of a C–H bond or bisecting the planes between adjacent C–H bonds give rise to similar potential

energy curves. Both exhibit a potential well of around half the depth of that calculated for backside attack, becoming repulsive at a slightly greater Br^-–C internuclear separation. It is possible that these sideways approach geometries could lead to formation of the C_s symmetry transition state mentioned above. The calculations were repeated for approach of Cl^- to CH_3Br, with similar results. Both sets of potential energy curves are presented in Figure 10.2.

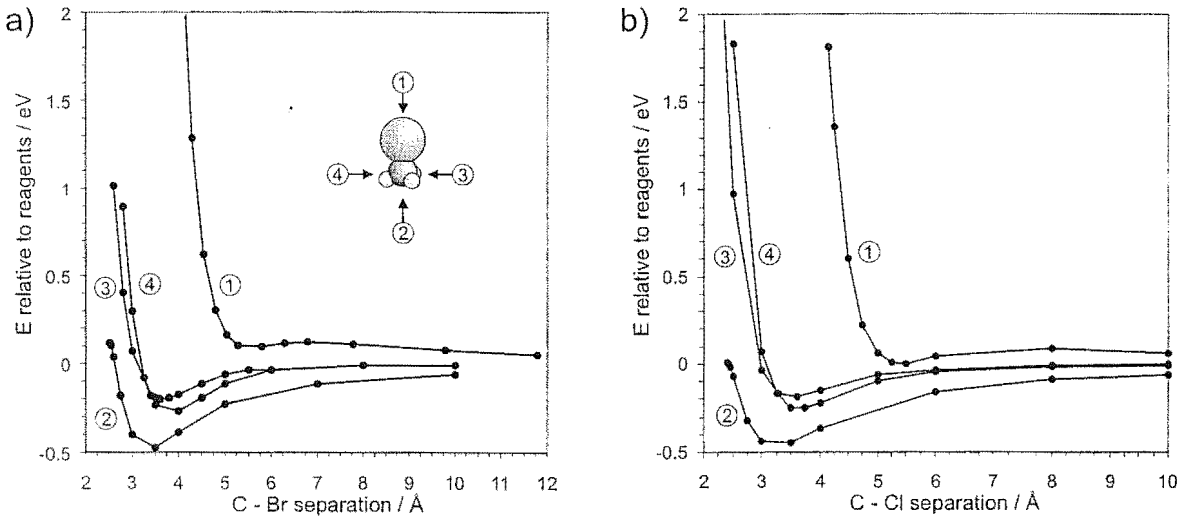

Figure 10.2: Dependence of interaction potential on direction for approach of a) Br^- to CH_3Cl and b) Cl^- to CH_3Br.

Planned experiments

There have been no previous attempts to measure product angular and velocity distributions for any of the reactions discussed in Sections 10.1.1 and 10.1.2 above, and the proposed ion imaging experiments are expected to yield a good deal of information on the stereodynamics of these processes. In particular, a study into the effect of molecular orientation on both the identities of the products observed and their angular distribution should give data which can be directly compared with the predictions of both *ab initio* and quasi-classical trajectory calculations.

10.2 Experiment design

10.2.1 Neutral beam

The production of a beam of oriented symmetric top molecules is discussed in some detail in Chapter 4. The molecular beam apparatus and beam characterisation are detailed in Chapters 3 and 5 and only a brief description will be given here. The molecular beam is produced from a piezoelectric supersonic nozzle source and collimated by a pair of skimmers before entering the first of two hexapoles. The resonance cell positioned between the pair of hexapoles plays no part in the crossed beam experiments at present, though at some time in the future it may be used for reagent state selection using the methods described in Chapter 6. To prevent spatial scrambling of the state selected beam as it passes through the C field a DC potential of a few volts is applied across parallel plates of the cell. The beam is focused through the hexapole field and exits into a region of uniform field maintained between a pair of parallel plates which make up part of the field plate assembly described in Section 10.2.3. Using this arrangement the beam can be oriented with the molecular dipole pointing towards or away from the charged particle beam by applying a potential of the appropriate polarity across the parallel plates.

10.2.2 Ion / electron beam

As mentioned in Chapter 3, the electron gun and ion source can be interchangeably mounted on a Huntington Laboratories PM-600 xyz translator attached to the side of the ion source chamber. Translation in the vertical direction facilitates intersection of the two beams, while translating the source in the horizontal direction may be used to compensate for the centre of mass velocity component of the molecular beam during ion imaging experiments.

Ion source

The ion source to be used in the crossed beam work is capable of producing either alkali metal ions or halide ions. Design and characterisation of the source formed a major part of this project, and was described in detail in Chapter 7.

Pierce electron gun

The electron gun used in this work has been employed previously for crossed beam experiments investigating orientation effects in electron impact ionization.[6–8] It was designed to produce a near monochromatic beam of electrons at energies of >100 eV, though reasonable beams can be obtained at significantly lower energies, and is shown in Figure 10.3. The gun consists of a filament assembly and lens system mounted on a set of four 6BA rods. The lenses are machined from phosphor bronze and are electrically isolated from one another and from the support rods by ceramic spacers. The filament is a piece of 0.7 mm diameter, 0.076 mm thick rhenium ribbon which pokes through the aperture in the Pierce element. The surface of the filament is coated with $BaZrO_3$ in order to reduce its work function. The Pierce element is shaped so that when it is biased negative with respect to the cathode potential the emitted electrons are directed towards the entrance aperture of an Einzel lens system (anode, L1 and L2 in Figure 10.3), which focuses the electrons into a narrow beam. A metal screen surrounds the lens system to shield the scattering chamber from the lens potentials.

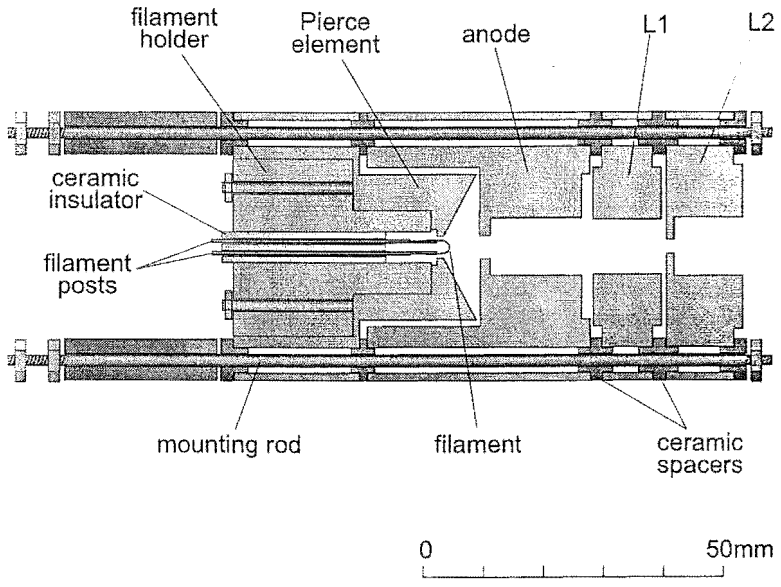

Figure 10.3: Electron gun for use in crossed beam electron impact ionization experiments.

The lens potentials required to focus the electron beam into the crossing region were modelled using SIMION6.0.[32] The potentials required to focus a beam of energy V_0 into the crossing region in the model system are given in Table 10.3.

In practice it is found that the Pierce element potential needs to be significantly higher than predicted to focus the electron beam onto the detector, usually around $1.4V_0$, and the

Table 10.3: Optimum electrostatic lens potentials for Pierce electron gun determined from SIMION6.0 simulations.

Element	Potential / V
Cathode	$-V_0$
Pierce element	$-1.1V_0$
Anode	0
L_1	$2V_0$
L_2	0

Table 10.4: Electrostatic lens potentials used for the Pierce electron gun.

Cathode / V	Pierce / V	Anode / V	L_1 / V	L_2 / V
-30	-41	0	79	0
-40	-57	0	84	0
-50	-72	0	105	0
-60	-106	0	276	0
-70	-105	0	280[a]	0
-80	-117	0	280	0
-90	-127	0	280	0

[a] Maximum potential available from power supply

potential applied to L_1 also needs to be greater than the model potential, particularly as the electron energy is increased. Typical potentials used to obtain maximum signals at a Faraday plate detector for low energy electron beams are given in Table 10.4.

Total emission curves were measured for the electron gun as a function of filament heating current using a 12 V variable current supply from an emission controller unit made in the department's Electronics Workshop. The four electrostatic lens elements were held at ground potential and the filament floated to give the desired electron energy. A Keithley 486 picoammeter was connected to the anode to measure the electron emission current. Emission curves at several electron energies are shown in Figure 10.4. The emission levels out at a filament heating current of around 3.5 A, corresponding to a heating power of 42 W. The total emission current is seen to be a linear function of the potential applied to the cathode.

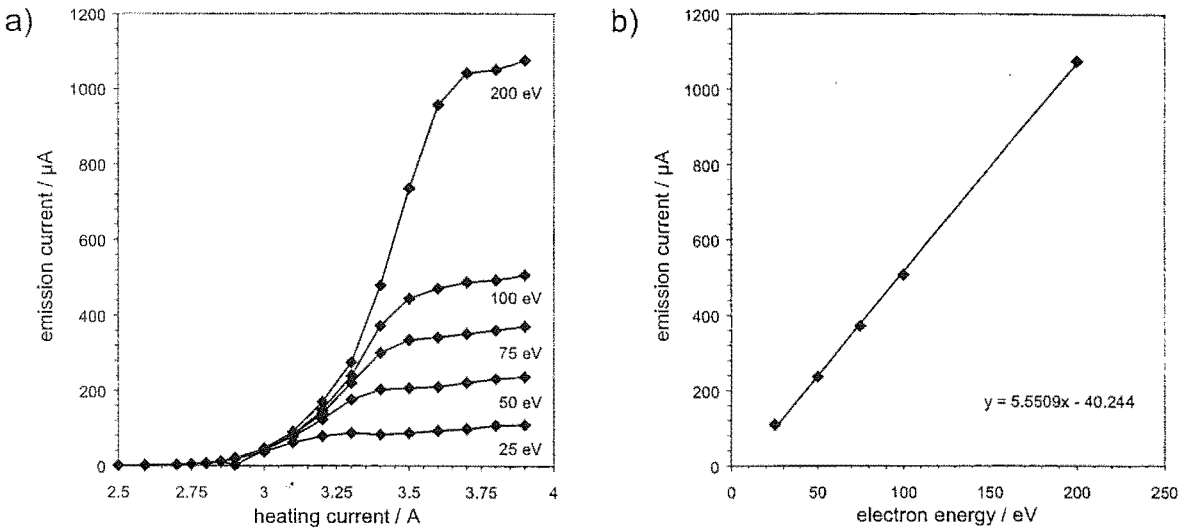

Figure 10.4: a) Total emission curves for Pierce electron gun as a function of filament heating current at electron energies ranging from 20 to 200 eV; b) Dependence of plateau emission on electron energy.

Phosphor screen detector

One of the principal requirements for carrying out a successful crossed beam experiment is a well focused electron or ion beam. Adjusting the electrostatic lenses to maximise the electron current reaching a Faraday plate detector should result in a reasonably focused beam. However, a detector which images the beam profile would be useful not only in focusing the beam, but also in aligning the beam axis to the centre of the crossing region. A small detector based on a cathodoluminescent phosphor was developed to fulfil these requirements. Initially, a modified commercial vacuum tube image intensifier was tested for the purpose, but it was found that the configuration of lens elements within the device resulted in the beam always being focused to the axis, giving a bright spot in the center of the phosphor. The detector design which was finally implemented is shown in Figure 10.5.

The detector is based around a circular glass plate which is fitted into a thin walled stainless steel tube and Torr sealed in place. The front face of the plate is coated with ZnS phosphor (BDH Laboratory Chemicals Group) and then aluminized by vacuum deposition. The phosphor is deposited by filling the small well formed by the rim of the steel tube with a suspension of ZnS powder in ethanol and allowing the solvent to evaporate. The aluminium forms a conducting layer over the phosphor, allowing an electrostatic potential to be applied. This is necessary in order to accelerate electrons towards the detector so that they strike with

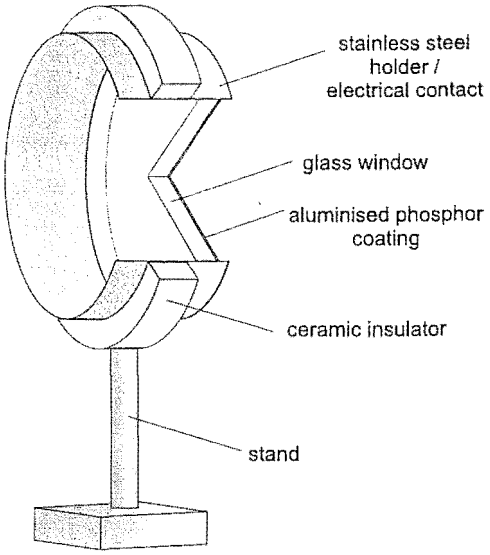

Figure 10.5: Phosphor screen detector designed for electron beam imaging.

enough energy to excite the phosphor.

The detector is mounted on the base of the scattering chamber in the path of the electron beam and positioned so that the phosphor can be viewed through a window in a $2\frac{3}{4}''$ ConFlat flange. In order to image the electron beam a potential of around 1–2 kV is applied to the phosphor until the beam spot becomes visible. The electrostatic lenses for the electron gun can then be adjusted to focus the spot and maximise its intensity and the gun can be translated to centre the beam to the axis. The width of the electron beam based on the size of the beam spot is approximately 2-3 mm after the beam has been focused. In principle the phosphor detector could also be used to image the ion beam, though in the case of ions mass sensitive detection is normally preferable and a quadrupole mass spectrometer is the detector of choice.

10.2.3 Beam crossing region

The scattering region for the crossed beam experiment was designed to meet the electric field requirements for production of an oriented molecular beam and extraction of product ions to the imaging detector situated above the crossing center, perpendicular to the scattering plane. The primary geometrical constraints were provision of a fairly weak homogeneous field parallel to the ion beam axis for orienting the molecular beam and a stronger field perpendicular to the plane defined by the two beams to direct product ions towards the

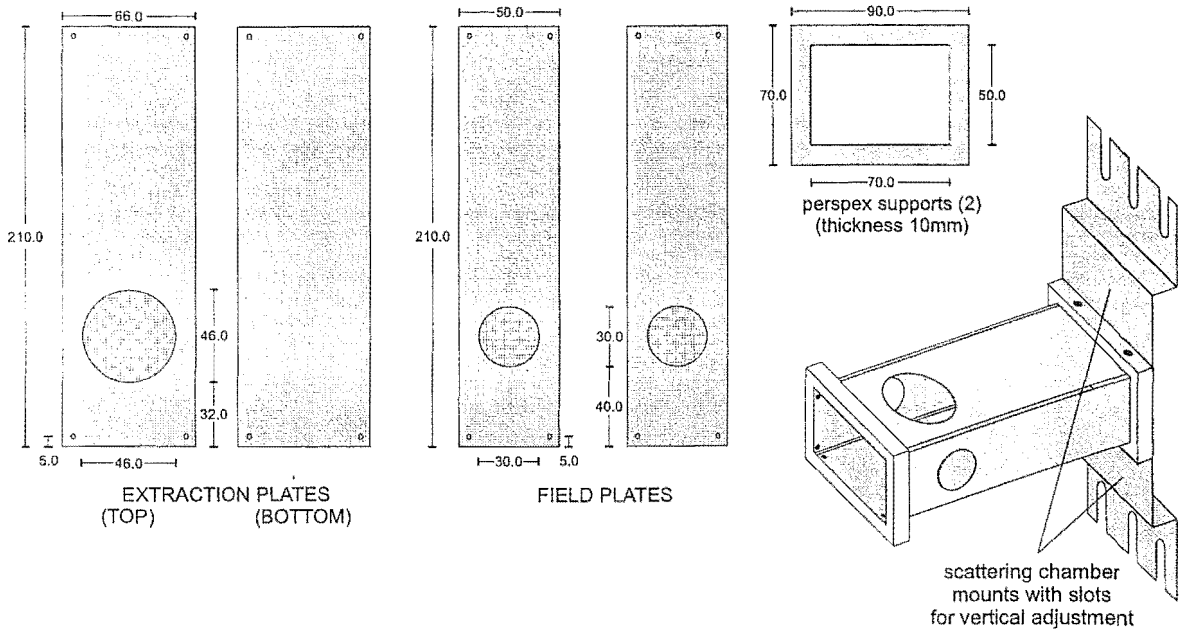

Figure 10.6: Field plate assembly designed for the beam crossing region.

microchannel plates of the ion imaging detection system.

These requirements are satisfied by two pairs of plane electrostatic lens elements which form the sides of an open ended box through which the molecular beam passes. All four plates are made of stainless steel sheet and are fixed to a pair of square perspex mounts which support the assembly and also provide electrical isolation for the elements. A pair of steel elbow mounts connected to the top and bottom of one of the perspex mounts bolt onto the inside of the scattering chamber wall to position the assembly. Slots in the top and bottom of the mounts allow the field plates to be centred in the vertical direction. The ion beam enters and exits the crossing region through sections of 90% transmitting nickel mesh (Buckbee Mears) in the homogeneous field plates. The top extraction plate incorporates a larger section of mesh through which ions are extracted to the detector. A short flight tube mounted on the top extraction plate provides a field free region for the ions as they travel towards the microchannel plates. The field plate assembly is shown in Figure 10.6. The separations of the homogeneous field plates and extraction plates were optimised by modelling the electric field lines within the region using SIMION6.0.[32] During the time when the molecular beam is being oriented between the homogeneous field plates the extraction plates are held at ground potential. At small plate separations edge effects due to field lines terminating on the grounded surfaces distort the field along the molecular beam axis. The

same considerations hold for the field between the extraction plates when the homogeneous field plates are grounded. Separations of 50 mm for the extraction plates and 70 mm for the homogeneous field plates were chosen to minimise these effects.

10.2.4 Scattering chamber lid

The existing lid for the scattering chamber cannot be used for the crossed beam experiments since the geometry does not allow for the ion imaging detector to be mounted directly above the collision region. A second lid, shown in Figure 10.7 was designed and fabricated for these experiments.

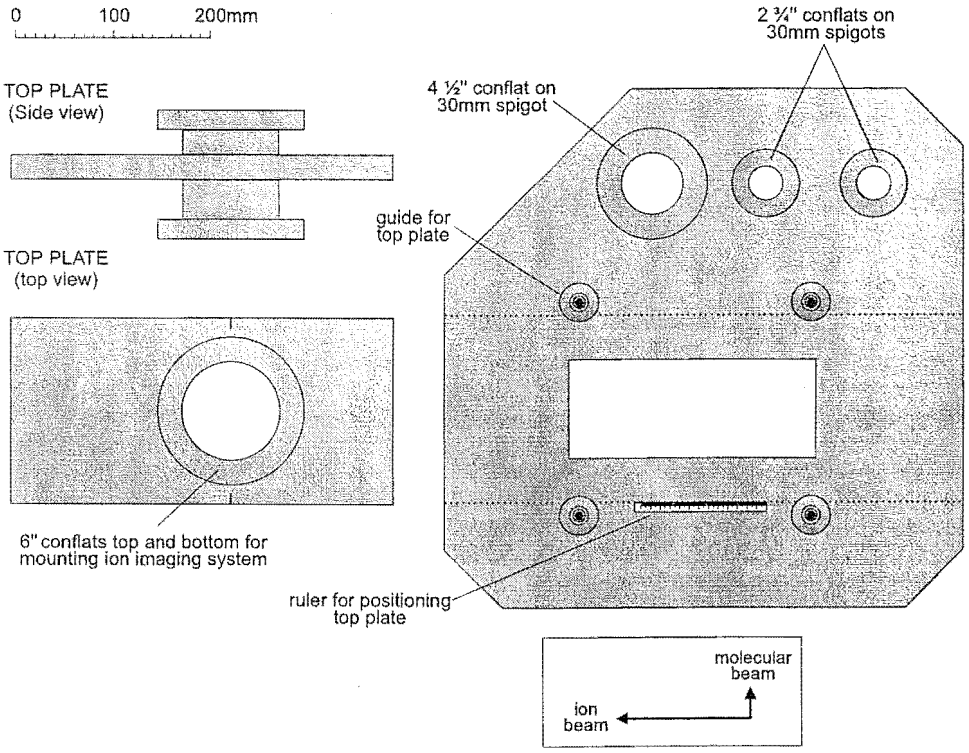

Figure 10.7: The new scattering chamber lid, designed to allow translation of the ion imaging detector off the molecular beam axis.

The new lid is in two sections, a base and a rectangular plate onto which the ion imaging detection system is mounted. The plate can slide on an O–ring seal over a large slit in the base of the lid to allow the detector to be translated along the axis of the ion or electron beam. In the study of ion–molecule collisions this translation is required so that the detector position can be adjusted to correct for the centre of mass velocity of the reacting system, which will lie predominantly along the ion beam axis due to the high velocity of the accelerated ion beam

compared to the molecular beam velocity. If required, the molecular beam velocity can be corrected for by horizontal translation of the ion source using the xyz translator. The base of the lid is fitted with one $4\frac{1}{2}''$ and two $2\frac{3}{4}''$ ConFlat flanges mounted on short spigots used to mount an ion gauge and electrical feedthroughs.

The sliding plate was initially designed with a short spigot terminating in a $6''$ flange welded into the top, to which the $6''$ flange carrying the microchannel plate (MCP) assembly of the ion imaging system is fitted. The plate was later modified to allow the flight length from the crossing region to the detector to be shortened for preliminary experiments in order to optimise the ion detection efficiency. For this purpose a second spigot and $6''$ flange were welded into the base of the plate. In the short flight path configuration the top face of the MCP flange seals to the ConFlat flange on a Viton O-ring. The flight length from the center of the crossing region to the microchannel plates is either 75 mm or 235 mm, depending on which configuration is used.

10.2.5 Pulse sequences and electronics

The time-of-flight nature of ion imaging detection means that in order to carry out the crossed beam experiments a series of fast switching pulsed electric fields are required. The pulse sequence is shown in Figure 10.8. The experiment is initiated when a pulse of electrons or ions is allowed to enter the collision region by switching a gating potential on the final ion lens to ground potential. Immediately before the pulse is released, the homogeneous field plates between which the molecular beam is oriented are also switched to ground so that the collision region is field free as the pulse of charged particles enters. After a short delay, during which the two beams collide and the product ion cloud starts to expand from the scattering center, the extraction plates are energised to propel ionic products of the collision towards the detector.

In practice the molecular beam is also pulsed in order to allow higher nozzle stagnation pressures to be used, maximising the particle density in the molecular beam. The piezo-electric nozzle is typically run at a frequency of 500 Hz with an open time of 60 μs. The nozzle driver provides a TTL output pulse with a variable delay of 0-5 ms from the nozzle opening; this pulse is used as the master trigger for the pulse sequence described above. A delay of around 3 ms is required to allow for the flight time of the molecular beam pulse from the nozzle to the crossing region. The electronics used to pulse the electron/ion beam,

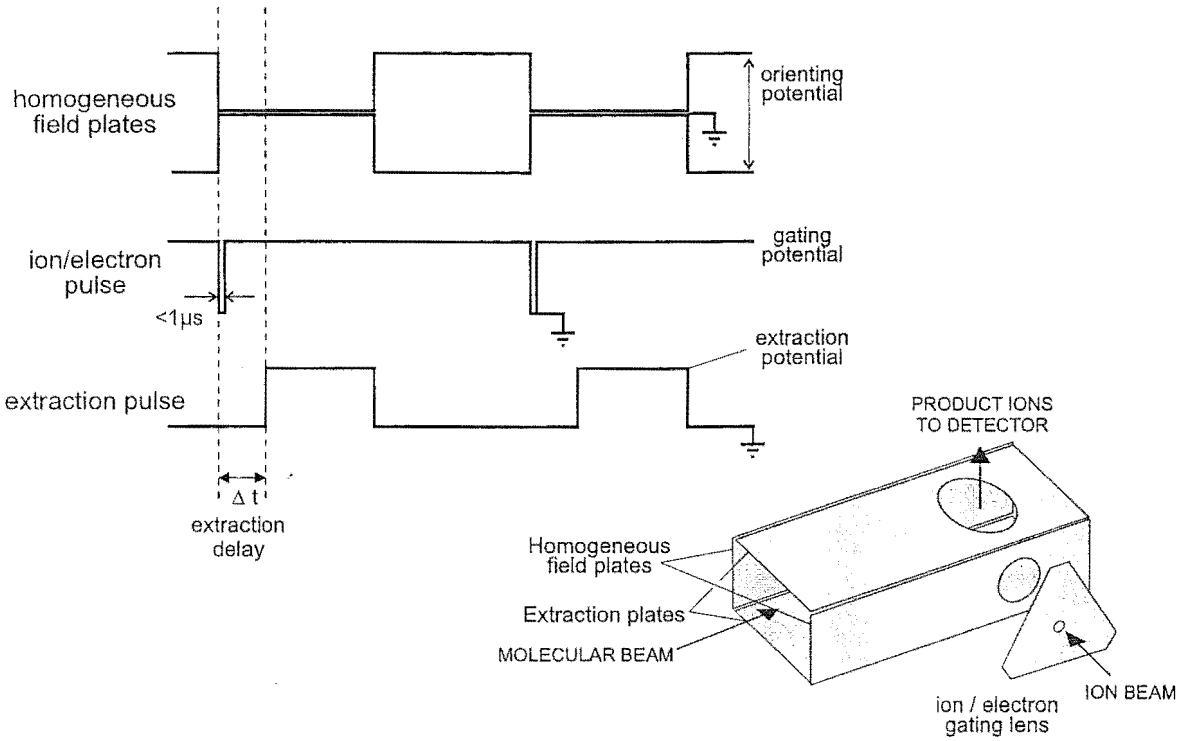

Figure 10.8: Pulse sequence for crossed beam ion/electron–molecule experiments.

homogeneous field plates and extraction plates were all designed and built in the department's Electronics workshop. The system consists of a master pulse generator together with two fast transistor switch units and associated power supplies. The potentials for the homogeneous field plates are supplied to the master unit from a separate power supply. On receiving a trigger from the piezoelectric nozzle driver the unit switches the homogeneous field plates to ground and provides a TTL trigger to the first transistor switch unit which gates the electron/ion beam. The switching circuit is based around a BUZ92 transistor switch driven by a HCPL–3150 optoisolating high speed FET driver. The pulse width is variable from ~0.1 up to 3 μs. A second TTL pulse, with variable delay up to 40 μs and variable width up to 100 μs, triggers the second transistor switch unit, which pulses the extraction field. The extraction field is controlled by a pair of Eurotech HTS–81 transistor switches rated to switch up to 8000 V with a rise time of less than 10 ns. After the extraction field is returned to ground the homogeneous field plates are switched on to orient the molecular beam ready for the next cycle.

10.2.6 Product ion detection

Ion imaging system

Ions are detected using a custom built ion imaging system supplied by Photonic Science Ltd. The first stage of the system consists of a pair of 40 mm diameter microchannel plates in a chevron configuration mounted on the face of a 6″ ConFlat flange. Potentials can be applied to the front and back faces of the MCP assembly and also to the face at which the two channel plates are joined. For detection of positive ions a potential of around -1.4 kV is applied to the front 'MCP in' connection from a Glassman Series EL 0-5000 V power supply and the back 'MCP out' connection is grounded. The 'MCP intermediate' lead is usually left floating between the two potentials. The second stage of the detector is a phosphor screen coated onto the front face of a fibreoptic bundle, which forms the vacuum interface. Secondary electrons exiting the MCP's are accelerated by a potential of around 3 kV from a Spellman HV power supply applied to a fine grid situated in front of the phosphor screen. These electrons excite the phosphor and form an image which is transmitted through the fibreoptic bundle and captured using a gated intensified CCD camera. The camera is a low light level, high resolution system which can be operated at wavelengths through the visible region and down to 250 nm. The image intensifier can be gated on to image only those ions arriving at the MCP's during the interval of interest. The gate width and delay can be incremented in steps of 10 ns up to a maximum of 10 ms using a fast pulse generator which is controlled by the same trigger as the ion/electron beam gating pulse unit. Both the intensifier gain and video gain can be varied from the camera controller unit to optimise the image obtained.

Time of flight detection

A perspex light pipe is fitted alongside the camera lens to direct light from the fibreoptic bundle through to a CV 337 KB/E photomultiplier tube coupled to an Extranuclear Laboratories 032–3 pulse counting preamplifier. When the photomultiplier output is connected to an oscilloscope the time of flight mass spectrum of ions reaching the MCP's can be viewed and used to determine the gate width and delay required for the image intensifier in order to image only ions corresponding to the peak of interest.

10.2.7 Data analysis software

The large number of machine parameters involved in the crossed beam experiments for which the current system has been designed, together with the fact that there is no guarantee that the product distribution will have an axis of symmetry, means that the inverse Abel transform method of image analysis is unsuitable. Instead, two different types of forward simulation software have been developed. Both are included in Appendix F as Fortran code.

Analysis package 1

The techniques described in Chapter 9, in which experimentally measured Doppler profiles are fitted to a set of basis functions in order to extract the product differential cross section and translational energy distribution, can be readily adapted to the analysis of ion images. The approach used is entirely analagous to that described in Section 9.1.2 and the procedure returns a differential cross section and translational energy distribution as a linear combination of Legendre polynomials*. The basis functions are simulations of the ion images which would be obtained if the differential cross section and product translational energy distribution were each described by a Legendre polynomial. If each distribution is to be fitted to a linear expansion of three Legendre polynomials this gives rise to a 3×3 array of basis functions. Such a set of basis functions for the reaction $CH_3Cl+Br^- \rightarrow CH_3Br+Cl^-$, generated by the program `imagebas` (Appendix F), is illustrated in Figure 10.9. As input, the program requires the reagent and product masses†, the reaction exoergicity, and the time of flight of the product ion to the detector after the collision takes place. The program uses a Monte Carlo procedure to calculate the spatial distribution of the product ions, which are binned into an array of 'pixels' to generate the simulated image. It should be noted that the basis functions do not take account of the product ion centre of mass velocity, which would cause the entire image to be shifted from the origin. This simply requires experimentally measured images to be centred to the origin before being analysed.

A non-linear least squares fitting program based on the Levenberg–Marquardt algorithm[190] described in Chapter 8 is used to fit the experimental image to a linear combination

* It should be noted that the fitting coefficients cannot be related back to an established theory of the reactive scattering process in these experiments as they can for the laser pump probe experiments described in Chapter 9.

† At present the program is limited to reactions of the type A+B→C+D, but could be modified to include other cases.

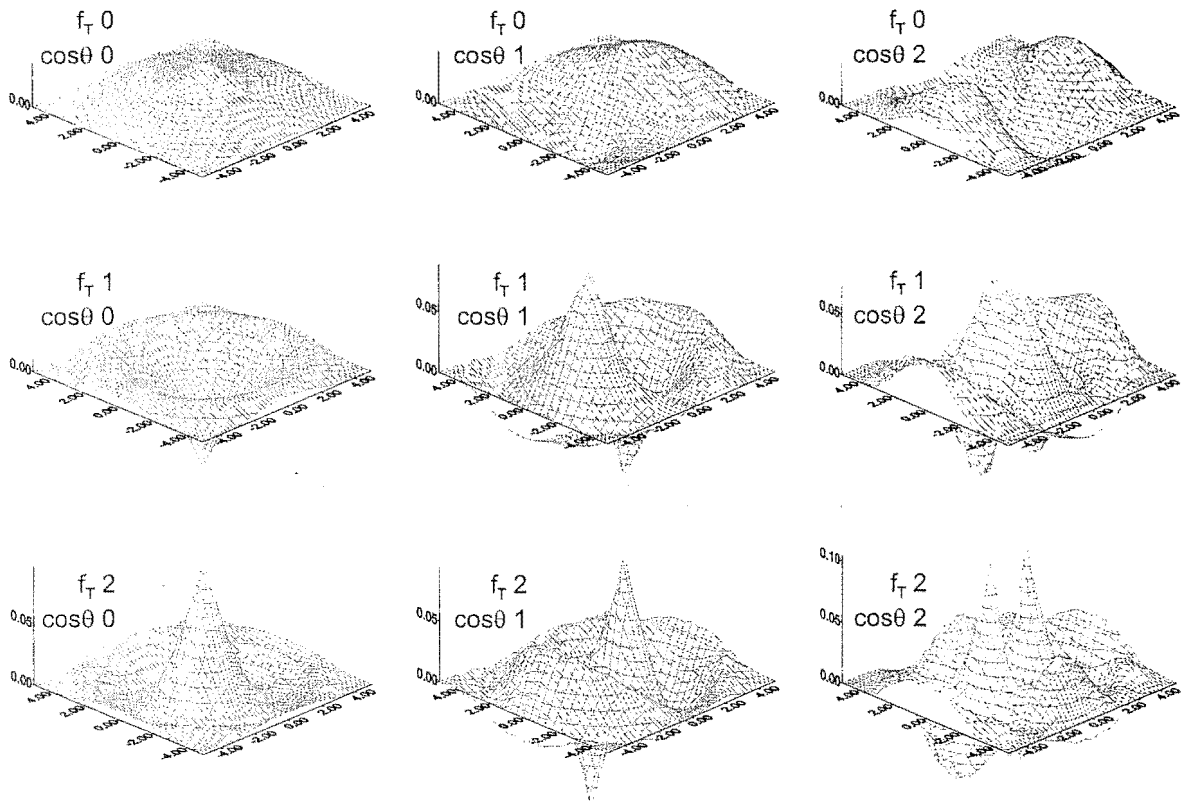

Figure 10.9: 3×3 basis set of ion images for the $Br^- + CH_3Cl$ reaction generated using the program `imagebas` listed in Appendix F.

of the basis functions. To test the capabilities of the method a modified version of the basis function program was written to produce a simulated ion image from a user specified differential cross section and translational energy distribution, which was then fitted to a set of image basis functions. An example of the fit obtained for a case where the product is forward scattered with approximately a third of the available energy released as product translation, similar to the expected product scattering for the S_N2 reaction, is shown in Figure 10.10. The functions used as the input differential cross section and $P(f_T)$ distribution to produce the simulated image were generated from a linear combination of two Gaussians and are functionally independent of the Legendre polynomials to which they are fitted. In order to obtain the fit shown, a basis set of dimension 4×8 was required. The fit is almost exact.

The programs were equally successful at fitting simulated images corresponding to other types of scattering. Based on these results it would seem that this technique is viable as a method of extracting data from ion images. Unfortunately, there is a very real problem associated with using the method for analysing experimental data. For the simulations described

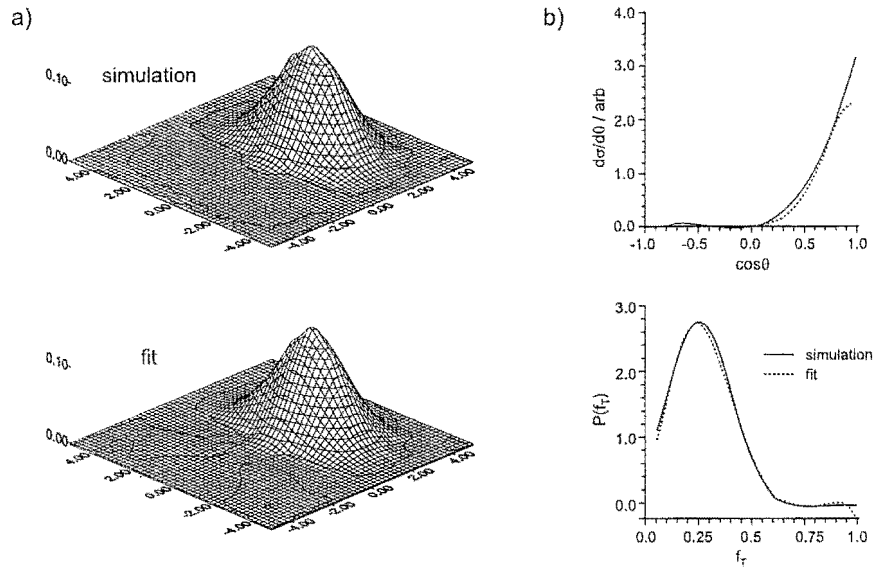

Figure 10.10: a) Simulated and fitted images for the $Br^- + CH_3Cl$ reaction obtained using the programs `imagebas` and `imagefit` listed in Appendix F; b) input and returned differential cross section and $P(f_T)$ distributions.

above the images and basis functions are made up of a 10×10 array of points, and run times for the basis function program are already significant. Much larger arrays would be needed to realistically model experimental data collected on the 753×576 pixel array of the CCD sensor in the ion imaging system, making the analysis prohibitively time consuming since the run time of the programs scales with the array dimensions. Fitting of experimental profiles was therefore abandoned at this point and efforts were concentrated on writing an improved simulation package which would produce ion images for direct comparison with experiment.

Analysis package 2

Because the kinematics are slightly different for the ion–molecule and electron–molecule experiments, two separate programs (`ionsim` and `eisim` of Appendix F) were written to simulate the images obtained from each process. The aim was to carry out a full simulation of the entire experiment, taking as many machine parameters into account as possible, in order to accurately model the experimental images. Assuming the programs model the system faithfully it should be possible to extract dynamical information from experimental data by varying the trial differential cross section and translational energy distribution to obtain the best agreement with the experimental images.

In addition to the trial functions for the differential cross section and translational energy distribution, input to the program consists of details of the energetics of the reaction to be imaged, used in determining the available product translational energy, timings for the pulse sequence described in Section 10.2.5, the extraction voltage, and various parameters used in setting up the distributions from which the Monte Carlo procedure samples. The mean flow velocity and parallel translational temperature of the molecular beam are used in calculating the beam velocity distribution, using Equation 4.15 of Chapter 4 from which to sample the velocity of the molecular reagent. The reagent ion velocity is selected from a Gaussian beam energy distribution specified by the ion energy and full width at half maximum (FWHM) of the distribution. The initial spatial coordinates of the two reagents are sampled from Gaussian beam profiles with widths defined by a user specified FWHM for each beam.

Each trajectory through the system follows a series of steps. An ion (or electron) is released from the ion source (or electron gun) at a time randomly selected from within the specified pulse width with a position and velocity sampled from the Gaussian distributions mentioned above. After sampling a molecular velocity and position the flight time of the ion before the collision takes place is determined and the reagent relative velocity, velocity of the centre of mass and collision energy are calculated. Next the total energy release for the reaction is determined from the collision energy, reaction threshold (or ionization potential in the case of the electron–molecule experiments) and product internal energies specified in the input. Product ion scattering angles θ and ϕ are sampled and the centre of the mass frame product velocity is calculated. After transformation to the lab frame the product velocity, reagent ion flight time and extraction pulse delay are used to determine the position of the product ion when the extraction plates are switched on. The flight time of the ion to the detector is determined from the extraction potential and the z component of its lab frame velocity, and the position of the ion as it strikes the detector can now be calculated. Each ion trajectory is weighted according to the trial differential cross section and translational energy distribution and binned into a 'pixel' as it strikes the detector. Ion strikes accumulate as the simulation proceeds to build up the final image.

In addition to being used in the analysis of experimental data, the simulation program will also be very useful in the optimization of experimental conditions. As an example, the effect of the extraction delay, extraction voltage, and ion pulse width on the simulated images for the CH_3^+ ion product from the reaction of K^+ ions with CH_3Cl at an ion energy of

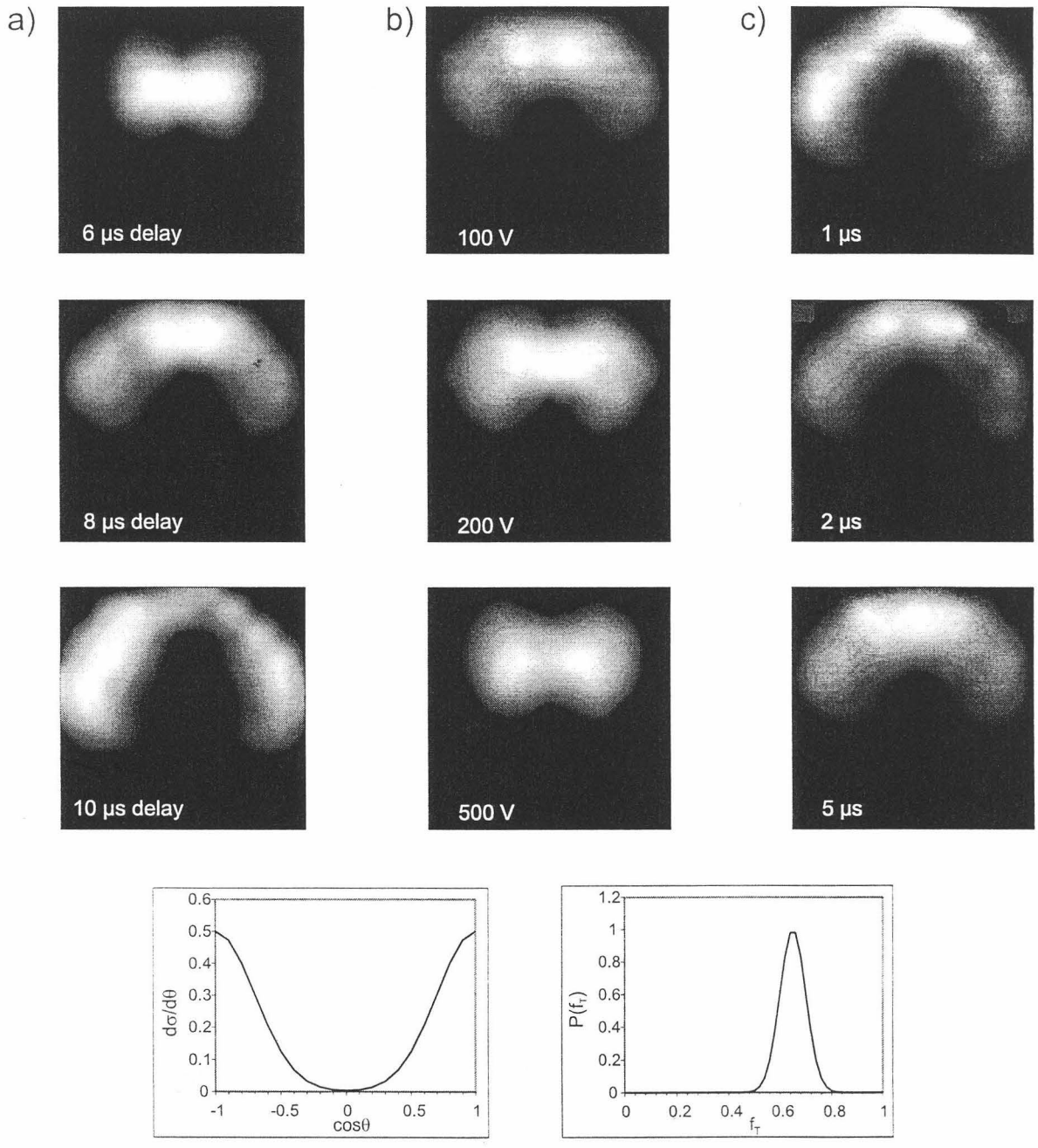

Figure 10.11: Simulated ion images for the CH_3^+ product of the $K^+ + CH_3Cl$ reaction at an ion energy of 15 eV: a) effect of extraction pulse delay on image at an extraction voltage of 1000 V; b) effect of extraction voltage on image with a pulse delay of 6 μs; and c)effect of ion pulse width with an extraction pulse delay of 10 μs and an extraction voltage of 1000 V. The trial differential cross section and translational energy distribution are inset.

15 eV is shown in Figure 10.11. The dynamics of this reaction are likely to be similar to the spectator stripping mechanism of the neutral K+CH_3I reaction, with the CH_3^+ product backscattered relative to the K^+ velocity vector. However, for the purposes of these simulations an arbitrary differential cross section with scattering over a wide range of angles was chosen, together with a trial translational energy distribution function for which around 60% of the available energy appears as product translation. Changing the delay between release of the ion pulse and extraction of the product has a marked effect on the images, since it controls the amount of time for which the product ions are allowed to spread before being directed towards the detector. Longer expansion times allow greater differentiation between product ions with different velocities and scattering angles and therefore greater resolution in the resulting image. The effect is similar to that of increasing the extraction voltage at a constant delay, and the two methods of controlling the expansion of the product ion sphere should be interchangeable. These effects have been observed in preliminary experiments in which background ions produced from collisions with beam electrons have been imaged. Increasing the width of the ion pulse has the expected effect of blurring the image, since temporal resolution of the collision event, and therefore spatial resolution of the product ions when they are extracted to the detector, is reduced.

10.2.8 Preliminary experiments and future work

The ion imaging system was initially tested before the field plate assembly was installed by using an electrostatic mirror to direct a Cl^- ion beam from the ion source up to the microchannel plates. The images obtained for a nominally 1 eV Cl^- ion beam as a function of the potential applied to the electrostatic mirror are shown in Figure 10.12. When a positive potential is applied the ions are accelerated towards the mirror and are scattered off the metal surface, leading to a diffuse image. As the potential applied to the mirror is decreased the ion beam is no longer scattered and is deflected at a sharper and sharper angle towards the MCP's; this is visible as the 'tail' of the bright ion spot in the images swinging round as the reflection angle becomes closer to 90°. When the applied potential is equal to the ion energy the deflection angle is 90° and the ion beam strikes the detector head on. This appears to occur at around -2 eV in the current experiment. The diameter of the beam spot is less than 2 mm, indicating a well focused ion beam even at low energies. As the potential becomes more negative than the ion energy the image quickly fades as ions are repelled back towards

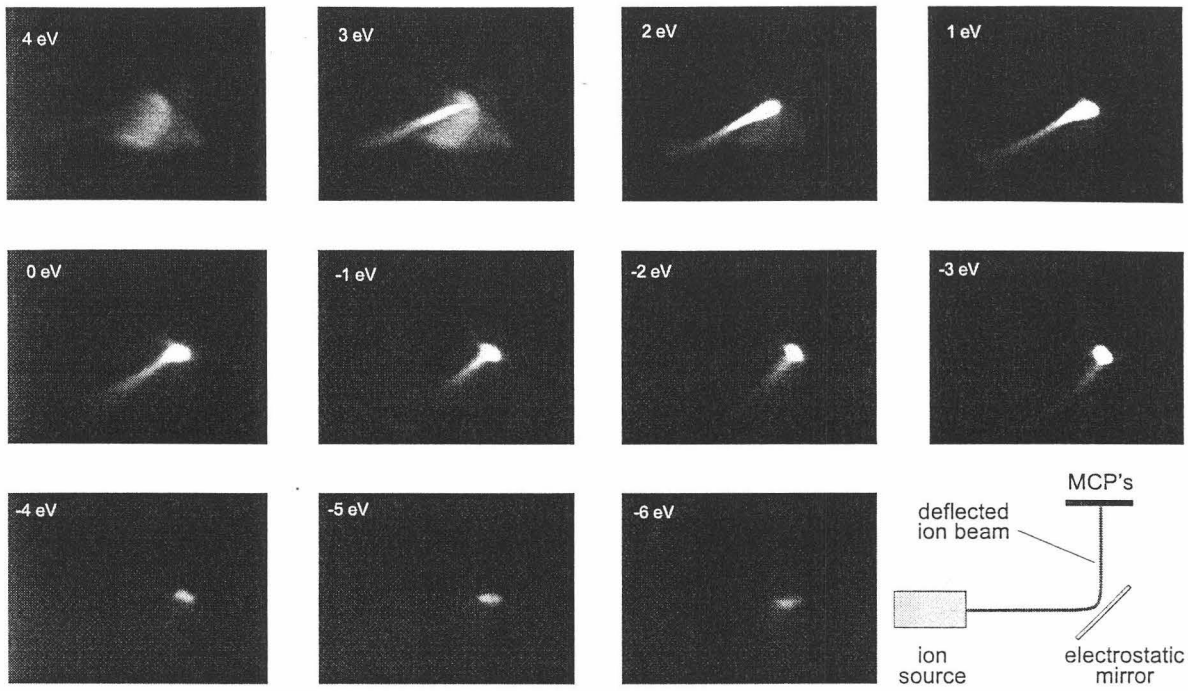

Figure 10.12: Images of a 1 eV Cl^- ion beam as a function of the potential applied to the electrostatic mirror.

the source.

After installation of the field plate assembly the complete system was tested by imaging pulses of ions from the ion source and checking that the images obtained, and also the time of flight peaks measured using the photomultiplier, respond correctly to changes in parameters such as the ion pulse width, extraction voltage and delay. Similar experiments have also been carried out with the electron gun in place, imaging ions from electron impact ionization of background gas. Additional peaks in the time of flight spectrum have been observed when a scattering gas is added to the chamber. However, attempts to observe products from crossed beam collisions have so far proved unsuccessful. The major problems which need to be solved appear to be high levels of background ion signals and poor resolution in the time of flight measurements. This is illustrated by an example of a time of flight signal obtained from electron impact ionization of background gas by an electron pulse, shown in Figure 10.13. The 40 eV electron pulse was 1 μs wide and there was no delay between passage of the electron beam through the chamber and extraction of product ions. The voltage applied to the extraction plates was $\pm$110 V. The first, sharp peaks correspond to ions formed within the crossing region which are extracted to the detector when the extraction plates are energised.

The resolution is very poor, with the two peaks spanning a mass range of around 100 mass units and making it impossible to isolate individual ions in the signal. The large 'hump' in the time of flight signal is thought to be the result of ions formed outside the crossing region which slowly leak in and are extracted to the detector over a wide range of times. Despite these problems, which will be discussed further below, the observation of time of flight peaks does indicate the system is working correctly. As expected, the peaks move to shorter time as the extraction voltage is increased, and to longer time as the delay between the electron pulse and extraction pulse is increased.

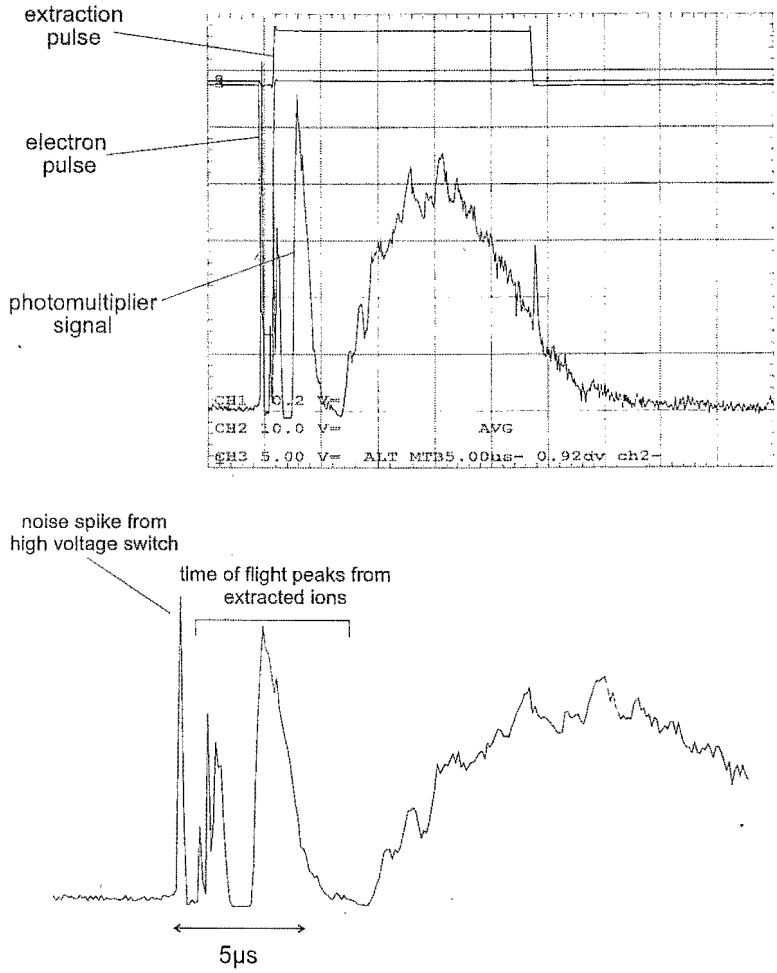

Figure 10.13: Time of flight signal of ions formed in collisions between electrons and background gas striking the ion imaging detector.

The ion imaging experiments described in Section 8.1 all depend on laser photoionization for production of the ions to be imaged. In some cases the ionic products are imaged directly, as in the case where a neutral product is ionized and detected, while in others the photoion

reacts to form a new ionic product which is imaged. In either case, the only point at which ions are formed is at the scattering center. The experiments for which the apparatus described in Section 10.2 has been developed are rather different. In these experiments an ion or electron beam is crossed with a molecular beam and attempts are made to extract the primary ionic products formed. This presents some special difficulties. In the electron–molecule experiments electron impact ionization of background gas leaves a trail of ions along the electron path, even at chamber pressures well below 10^{-7} Torr. When the extraction pulse is switched on, these ions are directed to the detector along with any ions formed from collisions with the molecular beam. Even though the particle density in the beam should be considerably higher than the background, the path length of the electron beam through the molecular beam is only around 2 mm, compared to the 70 mm between the field plates for which background gas ions can be extracted to the detector. In addition, the masses, and therefore the flight times to the detector, of the background ions are similar to those of the expected collision products, further reducing the chances of observing product ion peaks in the mass spectrum. In ion–molecule experiments any background ion signal is due to stray ions from the ion source, since the reagent ions do not react with the background gas. The principle problem in this case is that the primary ion beam must be allowed to clear the extraction region before the extraction plates can be energised, introducing a delay of around 15 μs between the beams colliding and extraction of products. Reactions which are to be studied must be chosen carefully to ensure that the velocity of the centre of mass is sufficiently different from the ion beam velocity that the product ions can be spatially separated from the primary ion beam. A second, related problem is the poor resolution of the time of flight spectrum measured using the photomultiplier. In previous ion imaging experiments, in which a laser pulse is used to initiate ion production, ions are only formed over the interval of the laser pulse, typically a few tens of nanoseconds. The ion pulse width in the current experiments is limited to the width of the gating pulse used for the ion/electron beam, which at present has a lower limit of around 150 ns. The short flight tube further limits temporal resolution since the short time between ion extraction and detection means that ions of widely differing masses are spaced apart by only a few microseconds. Clearly the experimental design must be modified somewhat in order to solve these problems and increase the chances of success.

The first and probably most important requirement is to decrease the background level of

ions reaching the detector and eliminate the need for a lengthy delay between beam crossing and ion extraction in the case of the ion–molecule experiments. It is hoped that the field plate assembly can be modified so that the ion beam is shielded from the extraction field along most of its flight path through the scattering chamber. However, some experimentation will be required to achieve this without affecting the uniformity of both the extraction and orienting fields. It may also be necessary to adopt the technique used by Bontuyan *et al*[181] in their inelastic scattering experiments (Section 8.1), in which the molecular beam is modulated and difference images are accumulated. This approach should allow at least partial cancelling of the background signal, but will require some modifications to the electronics which control the experiment.

Resolution can be improved by increasing the length of the flight tube between the top extraction plate and the detector. Provision was made for this in the design of the new lid for the scattering chamber (Section 10.2.4). Moving the microchannel plate flange to the top of the sliding plate on the lid should increase the resolution by about a factor of three. A new flight tube assembly is currently being constructed in the department's Mechanical Workshop.

It is envisaged that the problems discussed above should be overcome and the experiment operational within the next six to twelve months.

BIBLIOGRAPHY

[1] A. J. Dempster, *Phys. Rev.* **11**, 316 (1918).

[2] J. L. Franklin, J. G. Dillard, H. M. Rosenstock, and J. T. Heron, Technical report, U.S. Natl. Bur. Stand. (unpublished).

[3] R. D. Levin and S. G. Lias, Technical report, U.S. Natl. Bur. Stand. (unpublished).

[4] S. G. Lias, J. E. Bartmess, J. F. Lievman, J. L. Holmes, R. D. Levin, and W. G. Mallard, Technical report, U.S. Natl. Bur. Stand. (unpublished).

[5] M. J. McKewan, in *Advances in Gas Phase Ion Chemistry Vol. 1*, edited by N. J. Adams and L. M. Babcock (J. A. I. Press, Grenwich, CT, London, 1995).

[6] C. G. Aitken, D. A. Blunt, and P. W. Harland, *Int. J. Mass Spectrom. Ion. Procs.* **149/150**, 279 (1995).

[7] C. G. Aitken, Ph.D. thesis, Department of Chemistry, University of Canterbury, 1995.

[8] D. A. Blunt, Ph.D. thesis, Department of Chemistry, University of Canterbury, 1995.

[9] *Electron impact ionization*, edited by T. D. Märk and G. H. Dunn (Springer-Verlag, Wien, New York, 1985).

[10] F. H. Field and J. L. Franklin, *Electron Impact Phenomena and the Properties of Gaseous Ions* (Academic Press Inc., New York., 1957).

[11] D. D. Briglia and D. Rapp, *J. Chem. Phys.* **42**, 3201 (1965).

[12] K. T. Compton and C. C. V. Voorhis, *Phys. Rev.* **26**, 436 (1925).

[13] J. T. Tate and P. T. Smith, *Phys. Rev.* **36**, 1293 (1930).

[14] P. T. Smith, *Phys. Rev.* **37**, 808 (1931).

[15] J. T. Tate and P. T. Smith, *Phys. Rev.* **39**, 270 (1932).

[16] D. Rapp and P. Englander-Golden, *J. Chem. Phys.* **43**, 1464 (1965).

[17] H. S. W. Massey and E. H. S. Burhop, *Electronic and Ionic Impact Phenomena, 2nd Edn* (Oxford, Clarendon, 1969), p187.

[18] J. T. Tate and W. W. Lozier, *Phys. Rev.* **35**, 1285 (1930).

[19] B. A. Tozer, *J. Electron. Control* **4**, 149 (1958).

[20] T. D. Märk and.F. Egger, *J. Chem. Phys.* **67**, 2629 (1977).

[21] D. Rapp, P. Englander-Golden, and D. D. Briglia, *J. Chem. Phys.* **42**. 4081 (1965).

[22] J. Schutten, F. J. de Heer, H. R. Moustafa, A. J. H. Boerboom, and J. Kistemaker, *J. Chem. Phys.* **44**, 3924 (1966).

[23] T. D. Märk and F. Egger, *Int. J. Mass Spectrom. Ion Phys.* **20**, 89 (1976).

[24] M. E. Bell, *Phys. Rev.* **55**, 201 (1939).

[25] W. B. Nottingham, *Phys. Rev.* **55**, 203 (1939).

[26] H. Bethe, *Z. Physik* **76**, 293 (1932).

[27] T. Graf, *J. Phys. Radium.* **10**, 513 (1939).

[28] G. W. McClure, *Phys. Rev.* **90**, 796 (1953).

[29] F. F. Rieke and W. Prepejchal, *Phys. Rev.* **A6**, 1507 (1972).

[30] R. L. F. Boyd and G. W. Green, *Proc. Phys. Soc. (London)* **71**, 351 (1958).

[31] W. L. F. Fite and R. T. Brackman, *Phys. Rev.* **112**, 1141 (1948).

[32] I. N. E. L. Lockheed Martin Idaho Technologies, SIMION6.0, 1995.

[33] K. Stephan, H. Helm, and T. D. Märk, *J. Chem. Phys.* **73**, 3763 (1980).

[34] R. G. Montague, M. F. A. Harrison, and A. C. H. Smith, *J. Phys. B* **17**, 3295 (1984).

[35] R. C. Wetzel, F. A. Baiocchi, T. R. Hayes, and R. S. Freund, *Phys. Rev. A* **35**, 559 (1987).

[36] H. C. Straub, B. G. Renault, B. G. Lindsay, K. A. Smith, and R. F. Stebbings, *Phys. Rev. A* **52**, 1115 (1995), and references therein.

[37] K. Stephan, H. Helm, and T. D. Märk, *J. Chem. Phys.* **81**, 3116 (1984).

[38] *Theoretical Methods in Controlled Thermonuclear Fusion*, edited by M. R. C. McDowell and A. M. Ferendeci (Plenum Press, New York, 1980).

[39] L. D. Fadeev, *Sov. Phys. J.E.T.P.* **12**, 1014 (1961).

[40] G. Peach, *Proc. Phys. Soc.* **87**, 375,381 (1966).

[41] G. Peach, *J. Phys. B.* **2**, 1088 (1968).

[42] G. Peach, *J. Phys. B.* **3**, 328 (1970).

[43] G. Peach, *J. Phys. B* **4**, 1670 (1971).

[44] E. J. McGuire, *Phys. Rev. A* **3**, 267 (1971).

[45] E. J. McGuire, *Phys. Rev. A* **16**, 62,72 (1977).

[46] E. J. McGuire, *Phys. Rev. A* **20**, 445 (1979).

[47] D. L. Moores, *J. Phys. B* **11**, L403 (1978).

[48] D. L. Moores and H. Nussbaumer, *J. Phys. B* **3**, 161 (1970).

[49] Blaha and Davis, *Electron Ionization Cross Sections in the Distorted Wave Approximation. N.R.L. Memorandum Report 4245* (Naval Research Laboratory, Washington D.C., 1980).

[50] E. Trefftz, *Proc. Roy. Soc. London* **A271**, 379 (1962).

[51] E. Stingl, *J. Phys. B* **5**, 1160 (1972).

[52] S. M. Younger, *Phys. Rev. A* **22**, 111, 1425 (1980).

[53] S. M. Younger, *Phys. Rev. A* **23**, 1138 (1981).

[54] S. M. Younger, *Phys. Rev. A* **24**, 1272, 1278 (1981).

[55] S. M. Younger, *Phys. Rev. A* **25**, 3396 (1982).

[56] S. M. Younger, *Phys. Rev. A* **26**, 3177 (1982).

[57] R. K. Peterkop, *Theory of Ionization of Atoms by Electron Impact* (Colorado Associated University Press, Boulder, Colorado, 1977).

[58] M. R. H. Rudge and S. B. Schwartz, *Proc. Roy. Soc. London* **88**, 563 (1966).

[59] K. Butler and D. L. Moores, in *XII International Conference on the Physics of Electronic and Atomic Collisions*, edited by S. Datz (I. O. P. Publishing Ltd., 1981).

[60] K. J. Laggatuta and Y. Hahn, *Phys. Rev. A* **24**, 2273 (1981).

[61] M. R. H. Rudge, *Revs. Mod. Phys.* **40**, 564 (1968).

[62] D. N. Tripathi and D. K. Rai, *Ind. J. Pure Appl. Phys.* **10**, 185 (1972).

[63] J. J. Thomson, *Phil. Mag.* **23**, 449 (1912).

[64] H. Bethe, *Ann. Physik* **5**, 325 (1930).

[65] W. Lotz, *Z. Physik* **206**, 205 (1967).

[66] W. Lotz, *Z. Physik* **216**, 241 (1968).

[67] W. Lotz, *Z. Physik* **232**, 101 (1970).

[68] K. L. Bell, H. B. Gilbody, J. G. Hughes, A. E. Kingston, and F. J. Smith, *J. Phys. Chem. Ref. Dat.* **12**, 891 (1983).

[69] J. W. Otvos and D. P. Stevenson, *J. Am. Chem. Soc.* **78**, 546 (1956).

[70] M. Bobeldijk, W. J. V. der Zande, and P. G. Kistemaker, *Chem. Phys.* **179**, 125 (1994).

[71] M. Grysinski, *Phys. Rev. A* **138**, 305 (1965).

[72] L. Vriens, *Phys. Rev.* **141**, 88 (1966).

[73] S. Frage, J. Karwovski, and K. M. S. Saxena, *Handbook of Atomic Data* (Elsevier, Amsterdam, 1976).

[74] D. Margreiter, H. Deutsch, and T. D. Märk, *Contrib. Plasma phys.* **30**, 487 (1990).

[75] D. Margreiter, H. Deutsch, and T. D. Märk, *Int. J. Mass Spectrom. Ion. Proc.* **139**, 127 (1994).

[76] A. Szabo and N. S. Ostlund, *Modern Quantum Chemistry - Introduction to Advanced Electronic Structure Theory* (Macmillan Publishing Co. Ltd., New York. 1982), p151.

[77] Y. K. Kim and M. E. Rudd, *Phys. Rev. A* **50**, 3954 (1994).

[78] N. F. Mott. *Proc. Roy. Soc. London Ser. A* **126**, 259 (1930).

[79] *Case Studies in Atomic Physics, Vol1*, edited by E. W. McDaniel and M. R. C. McDowell (North-Holland Amsterdam, 1969), p335.

[80] *Atomic and Molecular Processes*, edited by R. D. Bates (Academic Press, London, 1962), p124.

[81] W. Hwang, Y. K. Kim, and M. E. Rudd, *J. Chem. Phys.* **104**. 2956 (1996).

[82] Y. K. Kim, W. Hwang, N. M. Weinberger, M. A. Ali, and M. E. Rudd. *J. Chem. Phys* **106**, 1026 (1997).

[83] D. K. Jain and S. P. Khare, in *Proc. 9th ICPEAC, Seattle*, ICPEAC (I. O. P. Publishing Ltd., 1975), p. 484.

[84] D. K. Jain and S. P. Khare, *J. Phys. B* **9**, 1429 (1976).

[85] W. F. Miller and R. L. Platzman, *Proc. Roy. Soc. London* **A70**, 299 (1957).

[86] S. P. Khare, *Planet. Space Sci.* **17**, 1257 (1969).

[87] C. B. Opal, E. C. Beaty, and W. K. Peterson, *Atomic Data* **4**, 209 (1972).

[88] M. J. Frisch, G. W. Trucks, H. B. Schlegel, P. M. W. Gill, B. G. Johnson, M. A. Robb, J. R. Cheeseman, T. A. Keith, G. A. Petersson, J. A. Montgomery, K. Raghavachari, M. A. Al-Laham, V. G. Zakrzewski, J. V. Ortiz, J. B. Foresman, J. Cioslowski, B. B. Stefanov, A. Nanayakkara, M. Challacombe, C. Y. Peng, P. Y. Ayala, W. Chem, M. Wong, J. L. Andres, E. S. Replogle, R. Comperts, R. L. Martin, D. J. Fox, J. S. Binkley, D. J. Defrees, J. Baker, J.P.Stewart, M. Head-Gordon, C. Gonzalez, and J. Pople, *Gaussian94 (Revision A.1.)* (Gaussian Inc., Pittsburgh PA, 1995).

[89] P. W. Harland, R. G. A. R. Maclagan, and C. Vallance, *J. Phys. Chem.* **100**, 15021 (1996).

[90] F. W. Lampe, J. L. Franklin, and F. H. Field, *J. Am. Chem. Soc.* **79**, 6129 (1957).

[91] J. E. Bartmess and J. E. Geordiadis, *Vacuum* **33**, 149 (1983).

[92] H. Nishimura and H. Tawara, *J. Phys. B* **27**, 2063 (1994).

[93] P. W. Harland and C. Vallance, *Int. J. Mass Spectrom. Ion Proc.* **171**, 173 (1997).

[94] *C.R.C. Handbook of Chemistry and Physics, 77th Edn, 1996-97*, edited by D. R. Lide (C.R.C. Press Inc., 1996).

[95] N. L. Djuric, I. M. Kadez, and M. V. Kurepa, *Int. J. Mass Spectrom. Ion Proc.* **83**, R7 (1988).

[96] O. J. Orient and S. K. Srivastava, *J. Phys. B.* **20**, 3923 (1987).

[97] S. A. Harris, J. E. Hudson, P. W. Harland, and C.Vallance, *J. Phys. B* **30**, 2465 (1997).

[98] C. Vallance. *Honours Part II Research Project* (Department of Chemistry, University of Canterbury, Christchurch, New Zealand, 1996).

[99] P. W. Harland, R. G. A. R. Maclagan, and C. Vallance, *J. Phys. Chem. A* **101(19)**, 3505 (1997).

[100] B. L. Schram, F. J. de Heer, M. J. van der Wiel, and J. Kistemaker, *Physica* **31**, 94 (1965).

[101] S. K. Srivastava and E. Krishnakumar, *Int. J. Mass Spectrom. Ion Proc.* **113**, 1 (1992).

[102] R. S. Freund and R. C. Wetzel, *Phys. Rev. A* **41**, 5861 (1990).

[103] E. Hille and T. D. Märk, *J. Chem. Phys.* **69**, 4600 (1978).

[104] S. K. Srivastava and M. V. V. S. Rao, *J. Geophys. Res.* **96(E2)**, 17563 (1991).

[105] S. P. Khare and M. J. Meath, *J. Phys. B* **20**, 2101 (1987).

[106] K. Bedereski, L. Wójcik, and B. Adamczyk, *Int. J. Mass Spectrom. Ion Phys.* **35**, 171 (1980).

[107] A. Crowe and J. W. McConkey, *Int. J. Mass Spectrom. Ion Phys.* **24**, 181 (1977).

[108] G. S. Inc., *Surfer for Windows* (Golden, CO 80401-1866, USA, 1993-95).

[109] D. A. Blunt, S. A. Harris, W. P. Hu, and P. W. Harland, *J. Phys. Chem. A* **102**, 1482 (1998).

[110] B. R. Cameron, Ph.D. thesis, Department of Chemistry, University of Canterbury, 1993.

[111] B. R. Cameron, C. G. Aitken, and P. W. Harland, *J. Chem. Soc. Faraday Trans.* **90**, 935 (1994).

[112] S. A. Harris, Ph.D. thesis, Department of Chemistry, University of Canterbury, 1997.

[113] R. B. Bernstein, *Chemical Dynamics via Molecular Beam and Laser Techniques* (Oxford University Press, 1982).

[114] *Atomic and Molecular Beam Methods Vol. I*, edited by G. Scoles (Oxford University Press, 1988).

[115] J. G. King and J. R. Zacharias, in *Advances in Electronics and Electron Physics, Volume VIII*, edited by L. Marton (Academic Press, New York, 1956), p. 1.

[116] K. Bier and B. Schmidt, *Z. Angew. Phys.* **13**, 1493 (1961).

[117] W. R. Gentry and C. F. Giese, *Rev. Sci. Instrum.* **46**, 104 (1975).

[118] I. N. Levine, *Quantum Chemistry Volume II: Molecular Spectroscopy* (Allyn and Bacon, Inc., 470 Atlantic Avenue, Boston, 1970).

[119] I. N. Levine, *Quantum Chemistry Volume I: Quantum mechanics and molecular electronic structure* (Allyn and Bacon, Inc., 470 Atlantic Avenue, Boston, 1970).

[120] C. H. Townes and A. L. Schawlow, *Microwave Spectroscopy* (McGraw–Hill Book Company Inc, 1955).

[121] S. D. Wiediger, P. W. Harland, J. R. Holt, and P. R. Brooks, *J. Phys. Chem. A* **102**, 1112 (1998).

[122] T. Oka, *Adv. Atomic Mol. Phys.* **9**, 127 (1973).

[123] J. M. Johns, A. R. W. McKellar, T. Oka, and M. Römheld, *J. Chem. Phys.* **62**, 1488 (1973).

[124] C. Vallance, W.-P. Hu, and P. W. Harland, *J. Phys. Chem.* **103(6)**, 665 (1999).

[125] P. R. Brooks. E. R. Jones, and K. Smith, *J. Chem. Phys.* **51**, 3073 (1969).

[126] S. Kaesdorf. G. Schönhense, and U. Heinzmann, *Phys. Rev. Lett* **54**. 885 (1985).

[127] S. R. Ghandi and R. B. Bernstein, *Z. Phys. D* **10**, 179 (1988).

[128] S. R. Ghandi and R. B. Bernstein, *J. Chem. Phys.* **93**, 4024 (1990).

[129] K. Bahloul. M. Irac-Astaud, E. Ilisca, and P. L. Chapovsky, *J. Phys. B.* **31**, 73 (1998).

[130] J. Bulthuis. J. B. Milan, M. H. M. Janssen, and S. Stolte, *J. Chem. Phys.* **94(11)**, 7181 (1991).

[131] P. W. Harland, W. p. Hu, and C. Vallance, unpublished results (unpublished).

[132] J. P. Toennies, *Faraday Discuss. Chem. Soc.* **33**, 96 (1962).

[133] J. P. Toennies, *Zeitschrift für Physik* **182**, 257 (1965).

[134] J. P. Toennies, *Zeitschrift für Physik* **193**, 76 (1966).

[135] H. G. Bennewitz, K. H. Kramer, W. Paul, and J. P. Toennies, *Zeitschrift für Physik* **177**, 84 (1964).

[136] U. Borkenhagen, H. Malthan, and J. P. Toennies, *Chem. Phys. Lett.* **41**, 222 (1976).

[137] U. Borkenhagen, H. Malthan, and J. P. Toennies, *J. Chem. Phys.* **71**, 1722 (1979).

[138] W.-P. Hu. S. A. Harris, P. W. Harland, and L. F. Phillips, *Int. J. Quantum Chem.* **71**, 75 (1999).

[139] N. Kashihira and E. Vietzke, Technical Report No. Jül-1032-NC, Kernforschungsanlage Jülich, Institut für Nuklearchemie (unpublished).

[140] N. Kashihira, E. Vietzke, and G. Zellerman, *Chem. Phys. Lett.* **39**, 316 (1976).

[141] E. Vietzke and G. Zellerman, *Radiochimica Acta* **50**, 107 (1990).

[142] J. M. Lafferty, *J. Appl. Phys.* **22**, 299 (1951).

[143] K. N. Leung, P. A. Pincosy, and K. W. Ehlers, *Rev. Sci. Instrum.* **55**, 1064 (1984).

[144] T. Fujii and H. Arimoto, *Anal. Chem.* **57**, 490 (1985).

[145] D. M. Goebel, Y. Hirooka, and T. A. Sketchley, *Rev. Sci. Instrum.* **56**, 1717 (1985).

[146] E. L. Kerley, C. D. Hanson, and D. H. Russell, *Anal. Chem.* **62**, 409 (1990).

[147] P. Loschialpo and C. A. Kapetanakos, *J. Appl. Phys.* **63**, 2552 (1988).

[148] H. M. Rosenstock, K. Draxl, B. W. Steiner, and J. T. Herron, *J. Phys. Chem. Ref. Dat.* **6, Suppl 1**, I (1977).

[149] K. Oláh, A. Szóke, and Z. Vajta, *J. Chromatogr. Sci.* **17**, 497 (1979).

[150] P. B. Moon, *Proc. Cambridge Philos. Soc.* **28**, 490 (1932).

[151] V. V. Brazhnikov, M. V. Gurev, and K. I. Sakodynsky, *Chromatogr. Rev.* **12**, 1 (1980).

[152] NIST Standard Reference Database Number 69, November 1988 release, NIST Chemistry Webbook - http://webbook.nist.gov/chemistry/.

[153] A. Holst, *The Best of Alison Holst* (Hodder Moa Beckett Publishing, 1998).

[154] B. F. Billing, *Thermocouples: Their Instrumentation, Selection and Use* (Monograph 64/1, Institution of Engineering Inspection, 1964).

[155] J. A. Simpson and C. E. Kuyatt, *Rev. Sci. Instr.* **34**, 265 (1963).

[156] H. B. Haskell, O. Heinz, and D. C. Lorents, *Rev. Sci. Instr.* **37**, 607 (1966).

[157] R. N. Zare and P. J. Dagdigian, *Science* **185**, 739 (1974).

[158] J. L. Kinsey, *Ann. Rev. Phys. Chem.* **28**, 349 (1977).

[159] N. Shafer and R. Bersohn, *J. Chem. Phys.* **94**, 4817 (1991).

[160] J. J. Valentini, *Spectrometric Techniques* (Academic Press, London, 1985).

[161] P. M. Johnson and C. E. Otis, *Ann. Rev. Phys. Chem.* **32**, 139 (1981).

[162] M. N. R. Ashfold, *Mol. Phys.* **58**, 1 (1986).

[163] M. N. R. Ashfold and J. D. Howe, *Ann. Rev. Phys. Chem.* **45**, 57 (1994).

[164] J. W. Hepburn, in *Atomic and molecular beam methods*, edited by G. Scoles (Oxford University Press, New York, 1992), p. 261.

[165] R. O. Loo, H.-P. Haerri, G. E. Hall, and P. L. Houston, *J. Chem. Phys.* **90**, 4222 (1989).

[166] H. J. Krautwald, L. Schneider, K. H. Welge, and M. N. R. Ashfold, *Faraday Discuss. Chem. Soc.* **82**, 99 (1986).

[167] T. A. Spiglanin and D. W. Chandler, *Int. J. Mass Spectrom. Ion Process.* **131**, 265 (1987).

[168] H. J. Hwangi, J. Griffiths, and M. A. El-Sayed, *J. Chem. Phys.* **131**, 265 (1994).

[169] J. Griffiths and M. A. El-Sayed, *J. Chem. Phys.* **100**, 4910 (1994).

[170] T. A. Hertz and J. A. Syage, *J. Chem. Phys.* **100**, 9265 (1994).

[171] M. N. R. Ashfold, I. R. Lambert, D. H. Mordaunt, G. P. Morley, and C. M. Western, *J. Phys. Chem.* **96**, 2938 (1992).

[172] C. Jaques, L. Valachovic, S. Ionov, E. Bömer, and Y. Wen, *J. Chem. Soc. Faraday Trans.* **89**, 1419 (1993).

[173] L. Schneider, W. Meier, K. W. Welge, M. N. R. Ashfold, and C. M. Western, *J. Chem. Phys.* **92**, 7027 (1990).

[174] J. Solomon, *J. Chem. Phys.* **47**, 889 (1967).

[175] C. Jonah, P. Chandra, and R. Bersohn, *J. Chem. Phys.* **55**, 1903 (1971).

[176] J. Solomon, C. Jonah, P. Chandra, and R. Bersohn, *J. Chem. Phys.* **55**, 1908 (1971).

[177] *Research in Chemical Kinetics, Volume 1*, edited by R. G. Compton and G. Hancock (Elsevier Science Publishers, 1993).

[178] A. J. R. Heck and D. W. Chandler, *Annu. Rev. Phys. Chem.* **46**, 335 (1995).

[179] C. W. Walter, K. A. Smith, and F. B. Dunning, *J. Chem. Phys.* **90(3)**, 1652 (1989).

[180] C. W. Walter, B. G. Lindsay, K. A. Smith, and F. B. Dunning, *Chem. Phys. Lett.* **154(5)**, 409 (1989).

[181] L. S. Bontuyan, A. G. Suits, P. L. Houston, and B. J. Whitaker, *J. Phys. Chem.* **97**, 6342 (1993).

[182] M. A. Buntine, D. A. Baldwin, R. N. Zare, and D. W. Chandler, *J. Chem. Phys.* **94**, 4672 (1991).

[183] T. N. Kitsopoulos, M. A. Buntine, D. P. Baldwin, R. N. Zare, and D. W. Chandler, *SPIE* **1858**, 2 (1993).

[184] T. N. Kitsopoulos, M. A. Buntine, D. P. Baldwin, R. N. Zare, and D. W. Chandler, *Science* **260**, 1605 (1993).

[185] L. M. Smith, D. R. Keefer, and S. I. Sudharsanan, *J. Quant. Spectrosc. Radiat. Transfer* **39**, 367 (1988).

[186] E. Entemann and E. Herschbach, *J. Chem. Phys.* **55**, 4872 (1971).

[187] R. T. Pack, *J. Chem. Phys.* **81**, 1841 (1984).

[188] R. E. Continetti, B. A. Balko, and Y. T. Lee, *J. Chem. Phys.* **93**, 5719 (1993).

[189] R. Y. Rubinstein, *Simulation and the Monte Carlo Method* (John Wiley and Sons Inc, 1981).

[190] W. H. Press, S. A. Teukolsky, W. T. Vetterling, and B. P. Flannery, *Numerical Recipes in Fortran. 2nd ed.* (Cambridge University Press, 1992).

[191] S. K. Park and K. W. Miller, *Communications of the ACM* **31**, 1192 (1988).

[192] I. M. Sobol, *USSR Computational Mathematics and Mathematical Physics* **7**, 86 (1967).

[193] J. P. Lambert, *NATO ASI Series C, Mathematical and Physical Sciences* **203**, 193 (1987).

[194] D. W. Marquardt, *J. Soc. Indust. Appl. Math.* **11(2)**, 431 (1963).

[195] G. W. Booth, G. E. P. Box, M. E. Muller, and T. I. Peterson, *Forecasting by Generalized Regression Methods, Nonlinear Estimation* (Princeton – IBM International Business Machines Corp., Mimeo., 1959), iBM Share Program No. 687 WL NL1.

[196] H. O. Hartley, *Technometrics* **3(2)**, 269 (1961).

[197] H. M. Cartwright, *Applications of Artificial Intelligence in Chemistry* (Oxford University Press, 1993).

[198] S. J. Greenland, Master's thesis, Brasenose College,University of Oxford, 1997.

[199] G. H. Dieke and H. M. Crosswhite, *J. Quant. Spectrosc. Radiat. Transfer* **2**, 97 (1961).

[200] R. N. Dixon, *J. Chem. Phys.* **85**, 1866 (1986).

[201] N. E. Shafer, A. J. Orr-Ewing, and R. N. Zare, *J. Phys. Chem.* **99**, 7591 (1995).

[202] S. P. Rayner, Ph.D. thesis, Wadham College,University of Oxford, 1996.

[203] J. Warnatz, *Combustion Chemistry* (Springer, 1984).

[204] G. C. Schatz and H. Elgersma, *J. Phys. Chem.* **88**, 2971 (1984).

[205] J. C. Polanyi, *Acc. Chem. Res.* **5**, 161 (1972).

[206] J. C. Polanyi and W. H. Wong, *J. Chem. Phys.* **51**, 1439 (1969).

[207] D. H. Zhang and J. C. Light, *J. Chem. Soc. Faraday Trans.* **93**, 691 (1997).

[208] G. Nyman and D. C. Clary, *J. Chem. Phys.* **99**, 7774 (1993).

[209] J. Palma, J. Echave, and D. C. Clary, *J. Chem. Soc. Faraday Trans.* **93(5)**, 841 (1997).

[210] S. K. Pogvebnya, J. Echave, and D. C. Clary, *J. Chem. Phys.* **107**, 8975 (1997).

[211] M. Alagia, N. Balucani, P. Casavecchia, D. Stranges, G. G. Volpi, D. C. Clary, A. Cliesch, and H. J. Werner, *Chemical Physics* **207**, 389 (1996).

[212] I. W. M. Smith and R. Zellner, *J. Chem. Soc. Faraday Trans. 2* **70**, 1045 (1974).

[213] A. R. Ravishankara, J. M. Nicovich, R. L. Thompson, and F. P. Tully, *J. Phys. Chem.* **85**, 2498 (1981), and references therein.

[214] K. K. Taluhdar, T. Gierczak, L. Goldfarb, Y. Rudich, B. S. M. Rao, and A. R. Ravishankara, *J. Phys. Chem.* **100**, 3037 (1996).

[215] K. Kleinermanns and J. Wolfrum, *Appl. Phys. B.* **34**, 5 (1984).

[216] A. Jacobs, H. R. Volpp, and J. Wolfrum, *24th International Symposium on Combustion* (The Combustion Institute, Pittsburgh. PA., 1992), p. 605.

[217] K. Honda, M. Takayanagi, T. Nishiya, H. Ohoyama, and I. Hanazaki, *Chem. Phys. Lett.* **180**, 321 (1991).

[218] K. Kessler and K. Kleinermanns, *Chem. Phys. Lett.* **190**, 145 (1992).

[219] M. J. Bronikowski, W. R. Simpson, and R. N. Zare, *J. Phys. Chem.* **97**, 2194 (1993).

[220] A.Sihna, M. C. Hsiao, and F. F. Crim, *J. Chem. Phys.* **92**, 6333 (1990).

[221] A. Sihna, *J. Phys. Chem.* **94**, 4391 (1990).

[222] F. F. Crim, M. C. Hsiao, J. L. Scott, A. Sinha, and R. L. V. der Wal, *Philos. Trans.Roy. Soc. London A* **332**, 259 (1990).

[223] M. C. Hsiao, A. Sihna, and F. F. Crim, *J. Phys. Chem.* **95**, 8263 (1991).

[224] M. J. Bronikowski, W. R. Simpson, B. Girard, and R. N. Zare, *J. Chem. Phys.* **95**, 8647 (1991).

[225] M. J. Bronikowski, W. R. Simpson, and R. N. Zare, *J. Phys. Chem.* **97**, 2194 (1993).

[226] D. E. Adelman, S. V. Filseth, and R. N. Zare, *J. Chem. Phys.* **98**, 4636 (1993).

[227] K. Kudla and G. C. Schatz, *Chem. Phys. Lett* **193**, 507 (1992).

[228] K. Kudla and G. C. Schatz, *J. Chem. Phys.* **98**, 4644 (1993).

[229] D. C. Clary, *Chem. Phys. Lett.* **192**, 34 (1992).

[230] J. L. Bowman and D. Wang, *J. Chem. Phys.* **96**, 7852 (1992).

[231] M. Brouard, I. Burak, G. A. J. Markillie, K. McGrath, and C. Vallance, *Chem. Phys. Lett.* **281**, 97 (1997).

[232] G. C. Schatz, personal communication (unpublished).

[233] A. J. Alexander, F. J. Aoiz, L. Banares, M. Brouard, J. Short, and J. P. Simons, *J. Phys. Chem.* **101**, 7544 (1997).

[234] F. J. Aoiz, M. Brouard, and P. A. Enriquez, *J. Chem. Phys.* **105**, 4964 (1996).

[235] W.-P. Hu and D. H. Truhlar, *J. Phys. Chem.* **98(4)**, 1049 (1994).

[236] B. D. Wladowski, W. D. Allen, and J. I. Brauman, *J. Phys. Chem.* **98**, 13532 (1994).

[237] H. Wang, L. Zhu, and W. L. Hase, *J. Phys. Chem.* **98**, 1608 (1994).

[238] H. Wang and W. L. Hase, *Chem. Phys.* **212**, 247 (1996).

[239] Z. Shi and R. Boyd, *J. A. C. S.* **113(7)**, 2433 (1990).

[240] Z. Shi and R. Boyd, *J. A. C. S.* **112(19)**, 6789 (1990).

[241] R. Vetter and L. Zülicke, *J. A. C. S.* **112(13)**, 5136 (1990).

[242] F. Keil and R. Ahlrichs, *J. A. C. S.* **98(16)**, 4787 (1976).

[243] A. Dedieu and A. Veillard, *J. A. C. S.* **94(19)**, 6730 (1972).

[244] A. J. Duke and R. F. W. Bader, *Chem. Phys. Lett.* **10(5)**, 631 (1971).

[245] H. B. Schlegel and K. Mislow, *Theoret. Chim. Acta.* **44**, 245 (1977).

[246] W. L. Hase, *Science* **266**, 998 (1994).

[247] G. H. Peslherbe, H. Wang, and W. L. Hase, *J. A. C. S.* **118**, 2257 (1996).

[248] S. R. V. Linde and W. L. Hase, *J. Phys. Chem.* **94**, 2778 (1990).

[249] W. L. Hase and D. M. Wardlaw, in *Bimolecular Collisions*, edited by M. N. R. Ashfold and J. E. Baggot (Royal Society of Chemistry, London, 1989), p. 171.

[250] A. A. Viggiano, R. A. Morris, J. S. Paschkewitz, and J. F. Paulson, *J. A. C. S.* **114**, 10477 (1992).

[251] T. Su, R. A. Morris, A. A. Viggiano, and J. F. Paulson, *J. Phys. Chem.* **94(22)**, 8426 (1990).

[252] C. H. Depuy, S. Gronert, A. Mullin, and V. M. Bierbaum, *J. A. C. S.* **112(24)**, 8651 (1990).

[253] C. Li, P. Ross, J. E. Szulejko, and T. B. McMahon, *J. A. C. S.* **118**, 9369 (1996).

[254] V. F. DeTuri, P. A. Hintz, and K. M. Ervin, *J. Phys. Chem. A.* **101**, 5969 (1997).

[255] G. Zellerman and E. Vietzke, *Radiochimica Acta* **50**, 107 (1996).

[256] D. E. Case and D. R. Herschbach, *Mol. Phys.* **30**, 1537 (1975).

[257] J. G. M. McClelland and D. R. Herschbach, *J. Phys. Chem.* **83**, 1145 (1979).

[258] J. D. Barnwell, J. G. Loeser, and D. R. Herschbach, *J. Phys. Chem.* **87**, 281 (1983).

[259] J. Aoiz, M. Brouard, P. A. Enriquez, and R. Sayos, *J. Chem. Soc. Faraday Trans.* **89**, 1427 (1993).

[260] N. E. Shafer, A. J. Orr-Ewing, W. R. Simpson, H. Xu, and R. N. Zare, *Chem. Phys. Lett.* **212**, 155 (1993).

[261] A. J. Orr-Ewing and R. N. Zare, *Ann. Rev. Phys. Chem.* **45**, 315 (1994).

[262] L. C. Biederharn, in *Nuclear Spectroscopy, Part B*, edited by F. Azjenberselove (Wiley, New York, 1998).

[263] D. M. Brink and G. R. Satchler, *Angular momentum, 3rd Ed.* (Wiley, New York, 1988).

[264] A. Messiah, *Quantum Mechanics* (North Holland, Amsterdam, 1975).

[265] J. I. Cline, C. A. Taatjes, and S. R. Leone, *J. Chem. Phys.* **93**, 6543 (1990).

APPENDICES

A. THEORETICAL DATA FOR CALCULATION OF ELECTRON IMPACT IONIZATION CROSS SECTIONS

A.1 *Data for* ab initio *calculations*

Table A.1: Optimized geometries, ionization potentials and critical energies at HF/6-31G* level for electrostatic model calculations of maximum molecular electron impact ionization cross sections. Experimental values for the ionization potential (in eV) are shown in parentheses.

Molecule	Geometry / Å & degrees	Ionization Potential / Hartrees	Ionization Potential / eV	Target Energy / Hartrees
H_2	HH = 0.73012	0.56226	15.300 (15.427)	-1.68908
N_2	NN = 1.07837	0.66384	18.064 (15.576)	-109.60780
O_2	OO = 1.16772	0.47327	12.878 (12.063)	-150.09117
CO	CO = 1.11378	0.47245	12.856 (14.013)	-113.21033
	CM = 0.63644 from C			
NO	NO = 1.14698	0.35824	9.748 (9.25)	-129.60612
	CM = 0.60106 from N			
NO_2	NO = 1.17388	0.31949	8.694 (9.79)	-204.29000
	CM on N			
H_2O	OH = 0.94732	0.37669	10.250 (12.6)	-76.38744
	HOH = 52.74584			
	CM = 0.11469 from O			
CO_2	CO = 1.14326	0.44679	12.158 (13.769)	-188.08097
	CM on C			
NH_3	NH = 1.00251	0.30322	8.251 (10.2)	-56.48758
	HNX = 111.67621			
	CM = 0.11087 from N			
CH_4	CH = 1.08366	0.44512	12.112 (12.6)	-40.64029
	HCH = 109.47097			
	CM on C			
CH_3F	CF = 1.36458	0.40955	11.144	-139.44416
	CH = 1.08185			

	HCF = 109.09040			
	CM = 0.74126 from F			
CH_3Cl	CCl = 1.78452	0.34062	9.269 (11.22)	-499.43377
	CH = 1.07787			
	HCCl = 108.46085			
	CM = 1.12742 from C			
CH_3Br	CBr = 1.94761	0.31410	8.547	-2609.81477
	CH = 1.07642			
	HCBr = 107.68872			
	CM = 0.47068 from Br			
$CHCl_3$	CH = 1.07133	0.42196	11.482	-1417.29
	CCl = 1.76268			
	ClCH = 107.57865			
	CM = 1.52097 from H			

Table A.2: Results of *ab initio* calculations for maximum electron impact ionization cross section as a function of molecular orientation for several small molecules using calculated and experimental ionization potentials.

Molecule	Direction	Calculated Ionization Pot.			Experimental Ionization Pot.		
		r_{th} / Å	σ_{max} / Å^2	Mean σ_{max} / Å^2	r_{th} / Å	σ_{max} / Å^2	Mean σ_{max} / Å^2
H_2	Z	0.805	2.04		0.804	2.03	
	X	0.357	0.40	0.95	0.355	0.40	0.94
N_2	Z	1.227	4.73		1.258	4.97	
	X	0.627	1.23	2.40	0.673	1.43	2.61
O_2	Z	1.344	5.68		1.360	5.81	
	X	0.681	1.46	2.87	0.702	1.55	2.97
CO	+Z(O)	1.206	4.57		1.238	4.82	
	-Z(C)	1.429	6.41		1.409	6.23	
	X	0.718	1.62	2.91	0.691	1.50	2.84
NO	+Z(O)	1.327	5.53		1.388	5.62	
	-Z(N)	1.439	6.51		1.451	6.61	
	X	0.822	2.12	3.42	0.840	2.22	3.52
CO_2	Z	1.887	11.19		1.861	10.88	
	X	0.949	2.83	5.62	0.906	2.58	5.35
NO_2	Z	2.028	12.93		2.004	12.62	
	X	1.054	3.49	6.63	1.018	3.26	6.38
H_2O	+Z (H's)	0.763	1.83		0.702	1.55	

	-Z (O)	0.840	2.22		0.808	2.05	
	X (in plane)	1.065	3.56		0.978	3.01	
	Y	0.731	1.68	2.42	0.698	1.53	2.11
NH_3	+Z (N)	0.869	2.37		0.841	2.22	
	-Z (H's)	0.793	1.98		0.745	1.74	
	+X (H_2)	1.469	6.78		1.404	6.19	
	-X (H_1, H_3)	0.930	2.72		0.873	2.39	
	±Y	1.103	3.82	3.58	1.016	3.24	3.17

Table A.3: Results of *ab initio* calculations for maximum electron impact ionization cross section as a function of molecular orientation for a series of CX_3Y molecules using calculated and experimental ionization potentials.

Molecule	Direction	Calculated Ionization Pot.			Experimental Ionization Pot.		
		r_{th} / Å	σ_{max} / Å^2	Mean σ_{max} / Å^2	r_{th} / Å	σ_{max} / Å^2	Mean σ_{max} / Å^2
CH_4	+Z (H_1)	1.580	7.84		1.571	7.75	
	-Z (H_2, H_3), H_4)	0.860	2.32		0.851	2.28	
	+X (H_2)	1.338	5.62		1.326	5.52	
	-X (H_3, H_4)	0.858	2.31		0.849	2.27	
	±Y	0.917	2.64	3.90	0.904	2.57	3.83
CH_3F	+Z (F)	1.467	6.76		–	–	
	-Z (H's)	1.550	7.55		–	–	
	+X (H_1)	0.702	1.55		–	–	
	-X (H_2, H_3)	0.694	1.52		–	–	
	±Y	0.698	1.53	3.41	–	–	–
CH_3Cl	+Z (Cl)	1.793	10.10		1.735	9.46	
	-Z (H's)	2.129	14.24		2.064	13.38	
	+X (H_1)	0.925	2.60		0.833	2.18	
	-X (H_2, H_3)	0.914	2.62		0.838	2.21	
	±Y	0.968	2.95	5.89	0.836	2.19	5.27
CH_3Br	+Z (Br)	1.708	9.17		–	–	
	-Z (H's)	2.565	20.68		–	–	
	+X (H_1)	1.144	4.11		–	–	
	-X (H_2, H_3)	1.142	4.10		–	–	
	±Y	1.142	4.11	7.71	–	–	–
$CHCl_3$	+Z (H)	2.092	13.73		–	–	
	-Z (Cl's)	0.580	1.06		–	–	
	+X (Cl_1)	2.775	24.19		–	–	

	-X (Cl_2,Cl_3	0.971	2.96		–	–	
	±Y	2.031	12.96	11.31	–	–	–

Table A.4: Effect of changing basis set and level of theory on the maximum electron impact ionization cross section of CO calculated using the *ab initio* model

Level of theory	I.P. eV	Direction	r_{th} / Å	σ_{max} / Å^2	Mean σ_{max} / Å^2
HF/6-31G*	12.856	+Z	1.206	4.57	
		–Z	1.429	6.41	
		X	0.718	1.62	2.91
HF/6-311G**	12.875	+Z	1.193	4.47	
		–Z	1.437	6.48	
		X	0.728	1.66	2.93
MP2/6-31G*	14.016	+Z	1.162	4.24	
		–Z	1.423	6.36	
		X	0.699	1.53	2.79
MP2/6-311G**	14.164	+Z	1.157	4.20	
		–Z	1.436	6.48	
		X	0.699	1.56	2.82
MP4/6-311G**	14.163	+Z	1.155	4.19	
		–Z	1.436	6.48	
		X	0.702	1.55	2.81
QCISD(T)/6-311G**	13.690	+Z	1.164	4.25	
		–Z	1.448	6.59	
		X	0.715	1.61	2.88

Table A.5: Effect of basis set and level of theory used on the maximum *ab initio* electron impact ionization cross section of H_2O.

Level of theory	I.P. eV	Direction	r_{th} / Å	σ_{max} / Å^2	Mean σ_{max} / Å^2
HF/6-31G*	10.250	+Z	0.763	1.83	
		–Z	0.840	2.22	
		±X	1.065	3.56	
		±Y	0.731	1.68	2.42
HF/6-311G**	10.285	+Z	0.770	1.86	
		–Z	0.833	2.18	

		±X	1.087	3.72	
		±Y	0.737	1.70	2.48
MP4/6-311G*	11.602	+Z	0.734	1.69	
		-Z	0.830	2.16	
		±X	1.047	3.45	
		±Y	0.723	1.64	2.34
CCSD(T)/6-311G**	11.568	+Z	0.734	1.69	
		-Z	0.831	2.17	
		±X	1.048	3.45	
		±Y	0.724	1.65	2.34
QCISD(T)/6-311G**	11.570	+Z	0.734	1.69	
		-Z	0.831	2.17	
		±X	1.048	3.45	
		±Y	0.724	1.65	2.34
QCISD(T)/6-311G**(2df)	11.772	+Z	0.737	1.71	
		-Z	0.837	2.20	
		±X	1.043	3.42	
		±Y	0.727	1.66	2.35
QCISD(T)/6-311G**(3df)	11.772	+Z	0.736	1.70	
		-Z	0.840	2.22	
		±X	1.040	3.40	
		±Y	0.729	1.67	2.34

A.2 Data for DM calculations

Table A.6: Mulliken population analyses, atomic orbital mean square radii, weighting factors and overall molecular orbital scaling factors for a DM cross section calculation on H_2.

Molecular level	E_{in} / eV	Atomic shell	N_{nl}	r_{nl} / Å	g_{nl}	$\pi N_{nl} r_{nl}^2 g_{nl}$	Scaling factor
$1\sigma_g$	16.05838	H 1s	1.0	0.52918	3.67647	3.23436	
		H 1s	1.0	0.52918	3.67647	3.23436	6.46871

Table A.7: Mulliken population analyses, atomic orbital mean square radii, weighting factors and overall molecular orbital scaling factors for a DM cross section calculation on N_2.

Molecular level	E_{in} / eV	Atomic shell	N_{nl}	r_{nl} / Å	g_{nl}	$\pi N_{nl} r_{nl}^2 g_{nl}$	Scaling factor
$2\sigma_g$	38.32781	N 1s	0.00528	0.08	0.17370	1.84×10^{-5}	
		N 2s	0.76188	0.52	0.98377	0.6367	
		N $2p_z$	0.23286	0.52	2.06469	0.40842	
		N 1s	0.00528	0.08	0.17370	1.84×10^{-5}	
		N 2s	0.76188	0.52	0.98377	0.6367	
		N $2p_z$	0.23286	0.52	2.06469	0.40842	2.09028
$2\sigma_u$	19.79726	N 1s	0.00422	0.08	0.17370	1.47×10^{-5}	
		N 2s	0.75422	0.52	0.98377	0.63055	
		N $2p_z$	0.24116	0.52	2.06469	0.42298	
		N 1s	0.00422	0.08	0.17370	1.47×10^{-5}	
		N 2s	0.75422	0.52	0.98377	0.63055	
		N $2p_z$	0.24116	0.52	2.06469	0.42298	2.10709
$1\pi_u$	14.92856	N $2p_{x,y}$	2.00000	0.52	2.06469	3.50786	
		N $2p_{x,y}$	2.00000	0.52	2.06469	3.50786	7.01572
$3\sigma_g$	14.42922	N 1s	0.00054	0.08	0.17370	1.89×10^{-6}	
		N 2s	0.23254	0.52	0.98377	0.19433	
		N $2p_z$	0.76698	0.52	2.06469	1.34523	
		N 1s	0.00054	0.08	0.17370	1.89×10^{-6}	
		N 2s	0.23254	0.52	0.98377	0.19433	
		N $2p_z$	0.76698	0.52	2.06469	1.34523	3.07913

Table A.8: Mulliken population analyses, atomic orbital mean square radii, weighting factors and overall molecular orbital scaling factors for a DM cross section calculation on O_2.

Molecular level	E_{in} / eV	Atomic shell	N_{nl}	r_{nl} / Å	g_{nl}	$\pi N_{nl} r_{nl}^2 g_{nl}$	Scaling factor
$2\sigma_g$ α	43.85612	O 1s	0.00243	0.07	0.13011	4.87×10^{-6}	
		O 2s	0.43819	0.46	0.70225	0.20456	
		O $2p_z$	0.05937	0.43	2.20264	0.07598	
		O 1s	0.00243	0.07	0.13011	4.87×10^{-6}	
		O 2s	0.43819	0.46	0.70225	0.20456	
		O $2p_z$	0.05938	0.43	2.20264	0.07598	0.56107
$2\sigma_u$ α	29.72133	O 1s	0.00266	0.07	0.13011	5.33×10^{-6}	
		O 2s	0.45414	0.46	0.70225	0.21201	
		O $2p_z$	0.04320	0.43	2.20264	0.05527	
		O 1s	0.00266	0.07	0.13011	5.33×10^{-6}	
		O 2s	0.45414	0.46	0.70225	0.21201	
		O $2p_z$	0.04320	0.43	2.20264	0.05527	0.53457
$1\pi_u$ α	19.36350	O $2p_y$	0.50000	0.43	2.20264	0.63974	
		O $2p_y$	0.50000	0.43	2.20264	0.63974	1.27947
$1\pi_u$ α	19.36350	O $2p_x$	0.50000	0.43	2.20264	0.63974	
		O $2p_x$	0.50000	0.43	2.20264	0.63974	1.27947
$3\sigma_g$ α	16.46084	O 1s	0.00022	0.07	0.13011	4.41×10^{-7}	
		O 2s	0.05915	0.46	0.70225	0.02761	
		O $2p_z$	0.44058	0.43	2.20264	0.56371	
		O 1s	0.00022	0.07	0.13011	4.41×10^{-7}	
		O 2s	0.05915	0.46	0.70225	0.02761	
		O $2p_z$	0.44064	0.43	2.20264	0.56379	1.18272
$1\pi_g$ α	11.30533	O $2p_y$	0.50000	0.43	2.20264	0.63974	
		O $2p_y$	0.50000	0.43	2.20264	0.63974	1.27947
$1\pi_g$ α	11.30533	O $2p_x$	0.50000	0.43	2.20264	0.63974	
		O $2p_x$	0.50000	0.43	2.20264	0.63974	1.27947
$2\sigma_g$ β	40.28269	O 1s	0.00215	0.07	0.13011	4.31×10^{-6}	
		O 2s	0.42162	0.46	0.70225	0.19682	
		O $2p_z$	0.07623	0.43	2.20264	0.09753	
		O 1s	0.00215	0.07	0.13011	4.31×10^{-6}	
		O 2s	0.42162	0.46	0.70225	0.19682	
		O $2p_z$	0.07623	0.43	2.20264	0.09753	0.58873
$2\sigma_u$ β	24.47602	O 1s	0.00223	0.07	0.13011	4.47×10^{-6}	
		O 2s	0.43115	0.46	0.70225	0.20127	

		O $2p_z$	0.06663	0.43	2.20264	0.08525	
		O 1s	0.00223	0.07	0.13011	4.47×10^{-6}	
		O 2s	0.43115	0.46	0.70225	0.20127	
		O $2p_z$	0.06663	0.43	2.20264	0.08525	0.57306
$3\sigma_g$ β	15.03495	O 1s	0.00026	0.07	0.13011	5.21×10^{-7}	
		O 2s	0.07598	0.46	0.70225	0.03547	
		O $2p_z$	0.42377	0.43	2.20264	0.54220	
		O 1s	0.00026	0.07	0.13011	5.21×10^{-7}	
		O 2s	0.07598	0.46	0.70225	0.03547	
		O $2p_z$	0.42377	0.43	2.20264	0.54220	1.15534
$1\pi_u$ β	11.93991	O $2p_y$	0.50000	0.43	2.20264	0.63974	
		O $2p_y$	0.50000	0.43	2.20264	0.63974	1.27947
$1\pi_u$ β	11.93991	O $2p_x$	0.50000	0.43	2.20264	0.63974	
		O $2p_x$	0.50000	0.43	2.20264	0.63974	1.27947

Table A.9: Mulliken population analyses, atomic orbital mean square radii, weighting factors and overall molecular orbital scaling factors for a DM cross section calculation on CO.

Molecular level	E_{in} / eV	Atomic shell	N_{nl}	r_{nl} / Å	g_{nl}	$\pi N_{nl} r_{nl}^2 g_{nl}$	Scaling factor
3σ	39.32811	C 1s	0.00320	0.09	0.24306	1.98×10^{-5}	
		C 2s	0.28503	0.65	1.20555	0.45609	
		C $2p_z$	0.14306	0.65	2.66430	0.50592	
		O 1s	0.00782	0.07	0.13011	1.57×10^{-5}	
		O 2s	1.36982	0.46	0.70225	0.63947	
		O $2p_z$	0.14154	0.43	2.20264	0.18110	1.78261
4σ	18.96186	C 1s	0.00468	0.09	0.24306	2.89×10^{-5}	
		C 2s	0.53066	0.65	1.20555	0.84914	
		C $2p_z$	0.00504	0.65	2.66430	0.01782	
		O 1s	0.00218	0.07	0.13011	4.37×10^{-6}	
		O 2s	0.46744	0.46	0.70225	0.21821	
		O $2p_z$	1.00004	0.43	2.20264	0.127952	2.36473
1π	14.69236	C $2p_{x,y}$	1.13572	0.65	2.6643	4.01635	
		O $2p_{x,y}$	2.86432	0.43	2.20264	3.66481	7.68116
5σ	12.11270	C 1s	0.00340	0.09	0.24306	2.1×10^{-5}	
		C 2s	0.85886	0.65	1.20555	1.37431	
		C $2p_z$	0.79300	0.65	2.66430	2.80435	
		O 2s	0.00680	0.46	0.70225	0.00317	

		O $2p_z$	0.33790	0.43	2.20264	0.43233	4.61419

Table A.10: Mulliken population analyses, atomic orbital mean square radii, weighting factors and overall molecular orbital scaling factors for a DM cross section calculation on NO.

Molecular level	E_{in} / eV	Atomic shell	N_{nl}	r_{nl} / Å	g_{nl}	$\pi N_{nl} r_{nl}^2 g_{nl}$	Scaling factor
$3\sigma_g$ α	37.78521	N 1s	0.00207	0.08	0.17370	7.21×10^{-6}	
		N 2s	0.39225	0.52	0.98377	0.32780	
		N $2p_z$	0.07482	0.52	2.06469	0.13122	
		O 1s	0.00242	0.07	0.13011	4.84×10^{-6}	
		O 2s	0.47466	0.46	0.70225	0.22158	
		O $2p_z$	0.05351	0.43	2.20264	0.06846	0.74908
$4\sigma_g$ α	24.76174	N 1s	0.00353	0.08	0.17370	1.23×10^{-5}	
		N 2s	0.48700	0.52	0.98377	0.40699	
		N $2p_z$	0.03838	0.52	2.06469	0.06732	
		O 1s	0.00215	0.07	0.13011	4.3×10^{-6}	
		O 2s	0.40756	0.46	0.70225	0.19026	
		O $2p_z$	0.06184	0.43	2.20264	0.07912	0.74369
1π α	16.93732	N $2p_x$	0.57290	0.52	2.06469	1.00482	
		O $2p_x$	0.42740	0.43	2.20264	0.54685	1.55166
2π α	14.36310	N $2p_y$	0.90292	0.52	2.06469	1.58365	
		O $2p_y$	0.09710	0.43	2.20264	0.12424	1.70789
$5\sigma_g$ α	12.11270	N 1s	0.00019	0.08	0.17370	6.64×10^{-7}	
		N 2s	0.06881	0.52	0.98377	0.05750	
		N $2p_z$	0.44320	0.52	2.06469	0.77734	
		O 1s	0.00022	0.07	0.13011	4.31×10^{-7}	
		O 2s	0.05909	0.46	0.70225	0.02758	
		O $2p_z$	0.42843	0.43	2.20264	0.54816	1.41058
3π α	9.61140	N $2p_x$	0.42741	0.52	2.06469	0.74964	
		O $2p_x$	0.57260	0.43	2.20264	0.73262	1.48226
$3\sigma_g$ β	38.59748	N 1s	0.00046	0.08	0.17370	1.59×10^{-6}	
		N 2s	0.12994	0.52	0.98377	0.10859	
		N $2p_z$	0.06384	0.52	2.06469	0.11197	
		O 1s	0.00419	0.07	0.13011	8.39×10^{-6}	
		O 2s	0.76136	0.46	0.70225	0.35542	
		O $2p_z$	0.04000	0.43	2.20264	0.05118	0.62717
$4\sigma_g$ β	21.51839	N 1s	0.00306	0.08	0.17370	1.07×10^{-5}	
		N 2s	0.51986	0.52	0.98377	0.43444	

		N $2p_z$	0.00076	0.52	2.06469	0.00132	
		O 1s	0.00105	0.07	0.13011	2.09×10^{-6}	
		O 2s	0.18440	0.46	0.70225	0.08608	
		O $2p_z$	0.29274	0.43	2.20264	0.37455	0.89376
1π β	16.14355	N $2p_x$	0.06885	0.52	2.06469	0.12076	
		O $2p_x$	0.93115	0.43	2.20264	1.19138	1.31214
2π β	13.66213	N $2p_y$	0.10226	0.52	2.06469	0.17936	
		O $2p_y$	0.89773	0.43	2.20264	1.14863	1.32798
$5\sigma_g$ β	13.12089	N 1s	0.00094	0.08	0.17370	3.28×10^{-6}	
		N 2s	0.25582	0.52	0.98377	0.21379	
		N $2p_z$	0.39990	0.52	2.06469	0.70140	
		O 1s	0.00000	0.07	0.13011	0.00000	
		O 2s	0.01088	0.46	0.70225	0.00508	
		O $2p_z$	0.33241	0.43	2.20264	0.42531	1.34588

Table A.11: Mulliken population analyses, atomic orbital mean square radii, weighting factors and overall molecular orbital scaling factors for a DM cross section calculation on H_2O.

Molecular level	E_{in} / eV	Atomic shell	N_{nl}	r_{nl} / Å	g_{nl}	$\pi N_{nl} r_{nl}^2 g_{nl}$	Scaling factor
$2A_1$	34.70840	O 1s	0.00856	0.07	0.13011	1.71×10^{-5}	
		O 2s	1.57130	0.46	0.70225	0.73352	
		O $2p_z$	0.04894	0.43	2.20264	0.06262	
		H 1s	0.18558	0.53	3.67647	0.60023	
		H 1s	0.18558	0.53	3.67647	0.60023	1.99662
$1B_2$	16.15976	O $2p_y$	1.07308	0.43	2.20264	1.37298	
		H 1s	0.46348	0.53	3.67647	1.49906	
		H 1s	0.46348	0.53	3.67647	1.49906	4.37110
$3A_1$	12.51001	O 1s	0.00130	0.07	0.13011	2.6×10^{-6}	
		O 2s	0.26440	0.46	0.70225	0.12343	
		O $2p_z$	1.36174	0.43	2.20264	1.74231	
		H 1s	0.18628	0.53	3.67647	0.60250	
		H 1s	0.18528	0.53	3.67647	0.60250	3.07073
$1B_1$	10.68374	O $2p_x$	2.00000	0.43	2.20264	2.55895	2.55895

Table A.12: Mulliken population analyses, atomic orbital mean square radii, weighting factors and overall molecular orbital scaling factors for a DM cross section calculation on CO_2.

Molecular level	E_{in} / eV	Atomic shell	N_{nl}	r_{nl} / Å	g_{nl}	$\pi N_{nl} r_{nl}^2 g_{nl}$	Scaling factor
$3\sigma_g$	38.98957	C 2s	0.00513	0.65	1.20555	0.00821	
		O 2s	0.54998	0.46	0.70225	0.25675	
		O $2p_z$	0.00353	0.43	2.20264	0.00452	
		O 2s	0.64549	0.46	0.70225	0.30133	
		O $2p_z$	0.07393	0.43	2.20264	0.09459	0.66540
$2\sigma_u$	37.23278	C $2p_z$	0.52136	0.65	2.66430	1.84373	
		O 1s	0.00412	0.07	0.13011	8.25×10^{-6}	
		O 2s	0.69117	0.46	0.70225	0.32266	
		O $2p_z$	0.04404	0.43	2.20264	0.05635	
		O 1s	0.00412	0.07	0.13011	8.25×10^{-6}	
		O 2s	0.69117	0.46	0.70225	0.32266	
		O $2p_z$	0.04404	0.43	2.20264	0.05635	2.60176
$4\sigma_g$	18.53139	C 1s	0.00430	0.09	0.24306	2.66×10^{-5}	
		C 2s	0.44289	0.65	1.20555	0.70869	
		O 1s	0.00153	0.07	0.13011	3.06×10^{-6}	
		O 2s	0.30478	0.46	0.70225	0.14228	
		O $2p_z$	0.47014	0.43	2.20264	0.60153	
		O 1s	0.00153	0.07	0.13011	3.06×10^{-6}	
		O 2s	0.30478	0.46	0.70225	0.14228	
		O $2p_z$	0.47014	0.43	2.20264	0.60153	2.19635
$1\pi_u$	16.89286	C $2p_y$	0.85541	0.65	2.66430	3.02506	
		O $2p_y$	0.57230	0.43	2.20264	0.73224	
		O $2p_y$	0.57230	0.43	2.20264	0.73224	4.48954
$1\pi_u$	16.89286	C $2p_x$	0.85541	0.65	2.66430	3.02506	
		O $2p_x$	0.57230	0.43	2.20264	0.73224	
		O $2p_x$	0.57230	0.43	2.20264	0.73224	4.48954
$3\sigma_u$	15.86888	C $2p_z$	0.32531	0.65	2.66430	1.15042	
		O 1s	0.00080	0.07	0.13011	1.6×10^{-6}	
		O 2s	0.20922	0.46	0.70225	0.09767	
		O $2p_z$	0.62732	0.43	2.20264	0.80264	
		O 1s	0.00080	0.07	0.13011	1.6×10^{-6}	
		O 2s	0.20922	0.46	0.70225	0.09767	
		O $2p_z$	0.62732	0.43	2.20264	0.80264	2.95104
$2\pi_u$	10.54920	O $2p_y$	1.00000	0.43	2.20264	1.27947	

		O $2p_y$	1.00000	0.43	2.20264	1.27947	2.55894
$2\pi_u$	10.54920	O $2p_x$	1.00000	0.43	2.20264	1.27947	
		O $2p_x$	1.00000	0.43	2.20264	1.27947	2.55894

Table A.13: Mulliken population analyses, atomic orbital mean square radii, weighting factors and overall molecular orbital scaling factors for a DM cross section calculation on NO_2.

Molecular level	E_{in} / eV	Atomic shell	N_{nl}	r_{nl} / Å	g_{nl}	$\pi N_{nl} r_{nl}^2 g_{nl}$	Scaling factor
$3\sigma_g$ α	41.11700	N 1s	0.00266	0.08	0.17370	9.29×10^{-6}	
		N 2s	0.45370	0.52	0.98377	0.37916	
		O 1s	0.00127	0.07	0.13011	2.54×10^{-6}	
		O 2s	0.23883	0.46	0.70225	0.11149	
		O $2p_z$	0.03172	0.43	2.20264	0.04059	
		O 1s	0.00127	0.07	0.13011	2.54×10^{-6}	
		O 2s	0.23883	0.46	0.70225	0.11149	
		O $2p_z$	0.03172	0.43	2.20264	0.04059	0.68333
$2\sigma_u$ α	37.20234	N $2p_z$	0.24797	0.52	2.06469	0.43492	
		O 1s	0.00201	0.07	0.13011	4.03×10^{-6}	
		O 2s	0.35773	0.46	0.70225	0.16700	
		O $2p_z$	0.01628	0.43	2.20264	0.02083	
		O 1s	0.00201	0.07	0.13011	4.03×10^{-6}	
		O 2s	0.35773	0.46	0.70225	0.16700	
		O $2p_z$	0.01628	0.43	2.20264	0.02083	0.81059
$4\sigma_g$ α	22.97748	N 1s	0.00193	0.08	0.17370	6.74×10^{-6}	
		N 2s	0.29477	0.52	0.98377	0.24634	
		O 1s	0.00134	0.07	0.13011	2.68×10^{-6}	
		O 2s	0.24574	0.46	0.70225	0.11472	
		O $2p_z$	0.10450	0.43	2.20264	0.13371	
		O 1s	0.00134	0.07	0.13011	2.68×10^{-6}	
		O 2s	0.24574	0.46	0.70225	0.11472	
		O $2p_z$	0.10450	0.43	2.20264	0.13371	0.74320
$1\pi_u$ α	19.94338	N $2p_x$	0.62393	0.52	2.06469	1.09433	
		O $2p_x$	0.18803	0.43	2.20264	0.24058	
		O $2p_x$	0.18803	0.43	2.20264	0.24058	1.57549
$2\pi_u$ α	17.34522	N $2p_y$	0.53315	0.52	2.06469	0.93511	
		O $2p_y$	0.23343	0.43	2.20264	0.29867	
		O $2p_y$	0.23343	0.43	2.20264	0.29867	1.53244
$3\sigma_u$ α	16.60343	N $2p_z$	0.27255	0.52	2.06469	0.47803	

		O 1s	0.00048	0.07	0.13011	9.61×10^{-7}	
		O 2s	0.10743	0.46	0.70225	0.05001	
		O $2p_z$	0.25612	0.43	2.20264	0.32770	
		O 1s	0.00048	0.07	0.13011	9.61×10^{-7}	
		O 2s	0.10743	0.46	0.70225	0.05001	
		O $2p_z$	0.25612	0.43	2.20264	0.32770	1.23345
$1\pi_g$	α	13.65913	O $2p_x$	0.50000	0.43	2.20264	0.63974
			O $2p_x$	0.50000	0.43	2.20264	0.63974	1.27947
$2\pi_g$	α	9.87128	O $2p_y$	0.50000	0.43	2.20264	0.63974
			O $2p_y$	0.50000	0.43	2.20264	0.63974	1.27947
$3\pi_u$	α	8.11232	N $2p_x$	0.37606	0.52	2.06469	0.65958
			O $2p_x$	0.31197	0.43	2.20264	0.39916
			O $2p_x$	0.31197	0.43	2.20264	0.39916	1.45790
$3\sigma_g$	β	39.76458	N 1s	0.00216	0.08	0.17370	7.54×10^{-6}
			N 2s	0.38876	0.52	0.98377	0.32489
			O 1s	0.00142	0.07	0.13011	2.84×10^{-6}
			O 2s	026994	0.46	0.70225	0.12602
			O $2p_z$	0.03319	0.43	2.20264	0.04247
			O 1s	0.00142	0.07	0.13011	2.84×10^{-6}
			O 2s	0.26994	0.46	0.70225	0.12602
			O $2p_z$	0.03319	0.43	2.20264	0.04247	0.66186
$2\sigma_u$	β	36.64777	N $2p_z$	0.24872	0.52	2.06469	0.43624
			O 1s	0.00198	0.07	0.13011	3.97×10^{-6}
			O 2s	0.35598	0.46	0.70225	0.16618
			O $2p_z$	0.01771	0.43	2.20264	0.022266
			O 1s	0.00197	0.07	0.13011	3.97×10^{-6}
			O 2s	0.35598	0.46	0.70225	0.16618
			O $2p_z$	0.01769	0.43	2.20264	0.02263	0.81390
$4\sigma_g$	β	21.28437	N 1s	0.00186	0.08	0.17370	6.5×10^{-6}
			N 2s	0.28702	0.52	0.98377	0.23986
			O 1s	0.00111	0.07	0.13011	2.22×10^{-6}
			O 2s	0.20974	0.46	0.70225	0.09791
			O $2p_z$	0.14472	0.43	2.20264	0.18517
			O 1s	0.00111	0.07	0.13011	2.22×10^{-6}
			O 2s	0.20974	0.46	0.70225	0.09791
			O $2p_z$	1.14472	0.43	2.20264	1.46464	2.0855
$1\pi_u$	β	16.54302	N $2p_y$	0.44168	0.52	2.06469	0.77468
			O $2p_y$	0.27916	0.43	2.20264	0.35718
			O $2p_y$	0.27916	0.43	2.20264	0.35718	1.48903

$3\sigma_u$ β	16.49322	N $2p_z$	0.24452	0.52	2.06469	0.42287	
		O 1s	0.00046	0.07	0.13011	9.21×10^{-7}	
		O 2s	0.10538	0.46	0.70225	0.04919	
		O $2p_z$	0.27190	0.43	2.20264	0.34789	
		O 1s	0.00047	0.07	0.13011	9.21×10^{-7}	
		O 2s	0.10538	0.46	0.70225	0.04919	
		O $2p_z$	0.27190	0.43	2.20264	0.34789	0.87515
$2\pi_u$ β	15.57102	N $2p_x$	0.41382	0.52	2.06469	0.72581	
		O $2p_x$	0.29308	0.43	2.20264	0.37499	
		O $2p_x$	0.29308	0.43	2.20264	0.37499	1.47579
$1\pi_g$ β	0.42368	O $2p_y$	0.50000	0.43	2.20264	0.63974	
		O $2p_y$	0.50000	0.43	2.20264	0.63974	1.27947
$2\pi_g$ β	9.82230	O $2p_x$	0.50000	0.43	2.20264	0.63974	
		O $2p_x$	0.50000	0.43	2.20264	0.63974	1.27947

Table A.14: Mulliken population analyses, atomic orbital mean square radii, weighting factors and overall molecular orbital scaling factors for a DM cross section calculation on NH_3.

Molecular level	E_{in} / eV	Atomic shell	N_{nl}	r_{nl} / Å	g_{nl}	$\pi N_{nl} r_{nl}^2 g_{nl}$	Scaling factor
$2A_1$	29.57075	N 1s	0.00810	0.08	0.17370	2.83×10^{-5}	
		N 2s	1.35878	0.52	0.98377	0.13553	
		N $2p_z$	0.06393	0.52	2.06469	0.11213	
		H 1s	0.18973	0.53	3.67647	0.61365	
		H 1s	0.18973	0.53	3.67647	0.61365	
		H 1s	0.18973	0.53	3.67647	0.61365	3.08865
1E	15.28040	N $2p_y$	1.05565	0.52	2.06469	1.85154	
		H 1s	0.62956	0.53	3.67647	2.03622	
		H 1s	0.15738	0.53	3.67647	0.50902	
		H 1s	0.15738	0.53	3.67647	0.50902	4.90580
1E	15.28040	N $2p_x$	1.05565	0.52	2.06469	1.85154	
		H 1s	0.47216	0.53	3.67647	1.52713	
		H 1s	0.47216	0.53	3.67647	1.52713	4.90580
$3A_1$	9.75534	N 1s	0.00110	0.08	0.17370	3.84×10^{-6}	
		N 2s	0.25004	0.52	0.98377	0.20896	
		N $2p_z$	1.64501	0.52	2.06469	2.88523	
		H 1s	0.03461	0.53	3.67647	0.11194	
		H 1s	0.03461	0.53	3.67647	0.11194	

		H 1s	0.03461	0.53	3.67647	0.11194	3.43002

Table A.15: Mulliken population analyses, atomic orbital mean square radii, weighting factors and overall molecular orbital scaling factors for a DM cross section calculation on CH_4.

Molecular level	E_{in} / eV	Atomic shell	N_{nl}	r_{nl} / Å	g_{nl}	$\pi N_{nl} r_{nl}^2 g_{nl}$	Scaling factor
$2A_1$	24.81943	C 1s	0.00880	0.09	0.24306	5.44×10^{-5}	
		C 2s	1.16728	0.65	1.20555	1.86783	
		H 1s	0.20602	0.53	3.67647	0.66634	
		H 1s	0.20602	0.53	3.67647	0.66634	
		H 1s	0.20602	0.53	3.67647	0.66634	
		H 1s	0.20602	0.53	3.67647	0.66634	4.53325
$1T_2$	14.16337	C $2p_{x,y,z}$	3.08274	0.65	2.66430	10.90176	
		H 1s	0.72912	0.53	3.67647	2.35823	
		H 1s	0.72912	0.53	3.67647	2.35823	
		H 1s	0.72912	0.53	3.67647	2.35823	
		H 1s	0.72912	0.53	3.67647	2.35823	20.33470

Table A.16: Mulliken population analyses, atomic orbital mean square radii, weighting factors and overall molecular orbital scaling factors for a DM cross section calculation on CH_3F.

Molecular level	E_{in} / eV	Atomic shell	N_{nl}	r_{nl} / Å	g_{nl}	$\pi N_{nl} r_{nl}^2 g_{nl}$	Scaling factor
$3A_1$	40.30328	F 1s	0.00894	0.06	0.101	1.02×10^{-5}	
		F 2s	1.74304	0.41	0.528	0.48603	
		F $2p_z$	0.02140	0.38	1.722	0.01672	
		C 1s	0.00084	0.09	0.243	5.19×10^{-6}	
		C 2s	0.13416	0.65	0.206	0.03668	
		C $2p_z$	0.08162	0.65	2.664	0.28861	
		H 1s	0.00316	0.53	3.676	0.01021	
		H 1s	0.00316	0.53	3.676	0.01021	
		H 1s	0.00316	0.53	3.676	0.01021	0.85869
$4A_1$	24.32247	F 1s	0.00068	0.06	0.101	7.77×10^{-7}	
		F 2s	0.11410	0.41	0.528	0.03182	
		F $2p_z$	0.12020	0.38	1.722	0.09390	
		C 1s	0.00766	0.09	0.243	4.74×10^{-5}	

		C 2s	1.03588	0.65	0.206	0.28324	
		C $2p_z$	0.05272	0.65	2.664	0.18642	
		H 1s	0.22288	0.53	3.676	0.72029	
		H 1s	0.22288	0.53	3.676	0.72029	
		H 1s	0.22288	0.53	3.676	0.72029	2.75629
1E	16.35517	F $2p_y$	0.59342	0.38	1.722	0.46357	
		C $2p_y$	0.82928	0.65	2.664	2.93232	
		H 1s	0.38492	0.53	3.676	1.24396	
		H 1s	0.09624	0.53	3.676	0.31102	
		H 1s	0.09624	0.53	3.676	0.31102	5.26190
1E	16.35517	F $2p_x$	0.59342	0.38	1.722	0.46357	
		C $2p_x$	0.82928	0.65	2.664	2.93232	
		H 1s	0.28868	0.53	3.676	0.93294	
		H 1s	0.28868	0.53	3.676	0.93294	5.26177
$5A_1$	14.58102	F 1s	0.00038	0.06	0.101	4.34×10^{-7}	
		F 2s	0.09696	0.41	0.528	0.02146	
		F $2p_z$	1.11134	0.38	1.722	0.86816	
		C 1s	0.00006	0.09	0.243	3.71×10^{-7}	
		C 2s	0.00438	0.65	0.206	0.00120	
		C $2p_z$	0.65664	0.65	2.664	2.32187	
		H 1s	0.04934	0.53	3.676	0.15945	
		H 1s	0.04934	0.53	3.676	0.15945	
		H 1s	0.04934	0.53	3.676	0.15945	3.68865
1E	11.37814	F $2p_y$	1.38096	0.38	1.722	1.07878	
		C $2p_y$	0.20600	0.65	2.664	0.72841	
		H 1s	0.27274	0.53	3.676	0.88143	
		H 1s	0.06820	0.53	3.676	0.22041	
		H 1s	0.06820	0.53	3.676	0.22041	3.12943
1E	11.37814	F $2p_x$	1.38096	0.38	1.722	1.07878	
		C $2p_x$	0.20998	0.65	2.664	0.74249	
		H 1s	0.20456	0.53	3.676	0.66109	
		H 1s	0.20456	0.53	3.676	0.66109	3.14343

Table A.17: Mulliken population analyses, atomic orbital mean square radii, weighting factors and overall molecular orbital scaling factors for a DM cross section calculation on CH_3Cl.

Molecular level	E_{in} / eV	Atomic shell	N_{nl}	r_{nl} / Å	g_{nl}	$\pi N_{nl} r_{nl}^2 g_{nl}$	Scaling factor

$5A_1$	28.84947	Cl 1s	0.00021	0.03	0.025	1.46×10^{-8}	
		Cl 2s	0.01189	0.19	0.072	9.71×10^{-5}	
		Cl $2p_z$	0.00038	0.16	0.145	7.93×10^{-6}	
		Cl 3s	1.12578	0.67	0.570	0.90496	
		Cl $3p_z$	0.06771	0.75	1.696	0.20293	
		C 1s	0.00386	0.09	0.243	2.39×10^{-5}	
		C 2s	0.56195	0.65	0.206	0.15365	
		C $2p_z$	0.03013	0.65	2.664	0.10654	
		H 1s	0.06594	0.53	3.676	0.21310	
		H 1s	0.06594	0.53	3.676	0.21310	
		H 1s	0.06594	0.53	3.676	0.21310	2.00751
$6A_1$	23.68607	Cl 2s	0.00818	0.19	0.072	6.68×10^{-5}	
		Cl 3s	0.71004	0.67	0.570	0.57077	
		Cl $3p_z$	0.02232	0.75	1.696	0.06690	
		C 1s	0.00480	0.09	0.243	2.97×10^{-5}	
		C 2s	0.63776	0.65	0.206	0.17438	
		C $2p_z$	0.11120	0.65	2.664	0.39320	
		H 1s	0.16862	0.53	3.676	0.54494	
		H 1s	0.16862	0.53	3.676	0.54494	
		H 1s	0.16862	0.53	3.676	0.54494	2.84015
2E	16.16478	Cl $2p_y$	0.00131	0.16	0.145	1.53×10^{-5}	
		Cl $3p_y$	0.14575	0.75	1.696	0.43682	
		C $2p_y$	1.01576	0.65	2.664	3.59172	
		H 1s	0.55772	0.53	3.676	1.80241	
		H 1s	0.13945	0.53	3.676	0.45067	
		H 1s	0.13945	0.53	3.676	0.45067	6.73230
2E	16.16478	Cl $2p_x$	0.00131	0.16	0.145	1.53×10^{-5}	
		Cl $3p_x$	0.14575	0.75	1.696	0.43682	
		C $2p_x$	1.01550	0.65	2.664	3.5908	
		H 1s	0.41872	0.53	3.676	1.35320	
		H 1s	0.41872	0.53	3.676	1.35320	6.73403
$7A_1$	13.16824	Cl 2s	0.00092	0.19	0.072	7.51×10^{-6}	
		Cl $2p_z$	0.01220	0.16	0.145	0.00014	
		Cl 3s	0.09862	0.67	0.570	0.07928	
		Cl $3p_z$	1.12676	0.75	1.696	3.37699	
		C 2s	0.00670	0.65	0.206	0.00183	
		C $2p_z$	0.64700	0.65	2.664	2.28778	
		H 1s	0.03591	0.53	3.676	0.11605	
		H 1s	0.03591	0.53	3.676	0.11605	

		H 1s	0.03591	0.53	3.676	0.11605	6.09419
3E	10.35048	Cl $2p_y$	0.01973	0.16	0.145	0.00023	
		Cl $3p_y$	1.82574	0.75	1.696	5.47189	
		C $2p_y$	0.04944	0.65	2.664	0.17482	
		H 1s	0.07083	0.53	3.676	0.22890	
		H 1s	0.01771	0.53	3.676	0.05723	
		H 1s	0.01771	0.53	3.676	0.05723	5.99031
3E	10.35048	Cl $2p_x$	0.01973	0.16	0.145	0.00023	
		Cl $3p_x$	1.82574	0.75	1.696	5.47189	
		C $2p_x$	0.04972	0.65	2.664	0.17581	
		H 1s	0.05240	0.53	3.676	0.16934	
		H 1s	0.05240	0.53	3.676	0.16934	5.98661

Table A.18: Mulliken population analyses, atomic orbital mean square radii, weighting factors and overall molecular orbital scaling factors for a DM cross section calculation on CH_3Br.

Molecular level	E_{in} / eV	Atomic shell	N_{nl}	r_{nl} / Å	g_{nl}	$\pi N_{nl} r_{nl}^2 g_{nl}$	Scaling factor
2E	187.1138	Br $2p_y$	0.01453	0.07	0.01909	4.27×10^{-6}	
		Br $3p_y$	1.96078	0.25	0.11476	0.04418	
		Br $4p_y$	0.02469	0.88	1.56118	0.09378	0.13796
2E	187.1138	Br $2p_x$	0.01453	0.07	0.01909	4.27×10^{-6}	
		Br $3p_x$	1.96078	0.25	0.11476	0.04418	
		Br $3d_{+1}$	0.00004	0.24	0.17801	1.29×10^{-6}	
		Br $4p_x$	0.02469	0.88	1.56118	0.09378	
		C $2p_x$	0.00004	0.65	2.66430	0.00014	0.13782
$7A_1$	61.12312	Br 3s	0.00001	0.27	0.05344	1.22×10^{-7}	
		Br $3p_z$	0.00003	0.25	0.11476	6.76×10^{-7}	
		Br $3d_0$	1.99793	0.24	0.17801	0.06436	
		C 1s	0.00001	0.09	0.24306	3.71×10^{-8}	
		C 2s	0.00111	0.65	1.20555	0.00178	
		C $2p_z$	0.00115	0.65	0.22643	0.00407	0.06997
3E	60.99222	Br $3p_y$	0.00004	0.25	0.11476	9.01×10^{-7}	
		Br $3d_{-1}$	1.99981	0.24	0.17801	0.06422	
		C $2p_y$	0.00018	0.65	2.66430	0.00064	0.06506
3E	60.99222	Br $3p_x$	0.00004	0.25	0.11476	9.01×10^{-7}	
		Br $3d_{+1}$	1.99981	0.24	0.17801	0.06422	
		C $2p_x$	0.00018	0.65	2.66430	0.00064	0.06506
4E	60.63419	Br $3d_{+2}$	2.00000	0.24	0.17801	0.06442	0.06442

4E	60.63419	Br $3d_{-2}$	2.00000	0.24	0.17801	0.06442	0.06442
$8A_1$	26.79361	Br 1s	0.00001	0.02	0.00519	6.52×10^{-11}	
		Br 2s	0.00069	0.09	0.01192	2.09×10^{-7}	
		Br $2p_z$	0.00001	0.07	0.01909	2.94×10^{-9}	
		Br 3s	0.00321	0.27	0.05344	3.93×10^{-5}	
		Br $3p_z$	0.00085	0.25	0.11476	1.92×10^{-5}	
		Br $3d_0$	0.00043	0.24	0.17801	1.39×10^{-5}	
		Br 4s	0.55563	0.78	0.42017	0.44622	
		Br $4p_z$	0.07250	0.88	1.56118	0.27536	
		C 1s	0.00661	0.09	0.24306	4.09×10^{-5}	
		C 2s	0.93733	0.65	1.20555	1.49987	
		C $2p_z$	0.00848	0.65	0.22643	0.02999	
		H 1s	0.13808	0.53	3.67647	0.44660	
		H 1s	0.13808	0.53	3.67647	0.44660	
		H 1s	0.13808	0.53	3.67647	0.44660	3.59135
$9A_1$	21.57328	Br 1s	0.00002	0.02	0.00519	1.3×10^{-10}	
		Br 2s	0.00172	0.09	0.01192	5.22×10^{-7}	
		Br 3s	0.00728	0.27	0.05344	8.91×10^{-5}	
		Br 4s	1.22204	0.78	0.42017	0.98140	
		Br $4p_z$	0.00031	0.88	1.56118	0.00118	
		C 1s	0.00211	0.09	0.24306	1.31×10^{-5}	
		C 2s	0.25775	0.65	1.20555	0.41244	
		C $2p_z$	0.18981	0.65	0.22643	0.67124	
		H 1s	0.10632	0.53	3.67647	0.34388	
		H 1s	0.10632	0.53	3.67647	0.34388	
		H 1s	0.10632	0.53	3.67647	0.34388	3.09799
5E	15.48480	Br $3p_y$	0.00089	0.25	0.11476	2.01×10^{-5}	
		Br $3d_{-1}$	0.00011	0.24	0.17801	3.54×10^{-6}	
		Br $4p_y$	0.08598	0.88	1.56118	0.32656	
		C $2p_x$	1.08281	0.65	2.66430	3.82923	
		H 1s	0.58984	0.53	3.67647	1.90775	
		H 1s	0.14746	0.53	3.67647	0.47694	
		H 1s	0.14746	0.53	3.67647	0.47694	7.01745
5E	15.48480	Br $2p_x$	0.00001	0.07	0.01909	2.94×10^{-9}	
		Br $3p_x$	0.00089	0.25	0.11476	2.01×10^{-5}	
		Br $3d_{+1}$	0.00011	0.24	0.17801	3.54×10^{-6}	
		Br $4p_x$	0.08598	0.88	1.56118	0.32656	
		C $2p_x$	1.08281	0.65	2.66430	3.82923	
		H 1s	0.44238	0.53	3.67647	1.43082	

		H 1s	0.44238	0.53	3.67647	0.43082	6.82436
$10A_1$	11.83867	Br 2s	0.00021	0.09	0.01192	6.37×10^{-8}	
		Br $2p_z$	0.00022	0.07	0.01909	6.47×10^{-8}	
		Br 3s	0.00070	0.27	0.05344	8.57×10^{-6}	
		Br $3p_z$	0.01285	0.25	0.11476	0.00029	
		Br $3d_0$	0.00031	0.24	0.17801	9.99×10^{-6}	
		Br 4s	0.14814	0.78	0.42017	0.11897	
		Br $4p_z$	1.02079	0.88	1.56118	3.87708	
		C 1s	0.00013	0.09	0.24306	8.04×10^{-7}	
		C 2s	0.02015	0.65	1.20555	0.03324	
		C $2p_z$	0.69724	0.65	0.22643	2.46571	
		H 1s	0.03309	0.53	3.67647	0.10703	
		H 1s	0.03309	0.53	3.67647	0.10703	
		H 1s	0.03309	0.53	3.67647	0.10703	6.81539

B. SOLUTION OF THE SCHRODINGER EQUATION FOR A SYMMETRIC TOP MOLECULE

This appendix outlines the solution of the Schrödinger wave equation for a freely rotating symmetric top molecule in order to determine the energy levels and rotational quantum numbers. The solutions for a symmetric top molecule in the presence of an electric field are usually obtained by including the Stark energy $-\mu \cdot \mathbf{E}$ into the rotational Hamiltonian and using perturbation theory. From Equation 4.30 of Chapter 4, the Schrodinger equation $(\hat{H}_0 - E_0)\psi = 0$ is:

$$\frac{\partial^2\psi}{\partial\theta^2} + \frac{\cos\theta}{\sin\theta}\frac{\partial\psi}{\partial\theta} + \csc^2\theta\frac{\partial^2\psi}{\partial\phi^2} + \left(\frac{I_B}{I_C} + \cot^2\theta\right)\frac{\partial^2\psi}{\partial\chi^2} - 2\cot\theta\csc\theta\frac{\partial^2\psi}{\partial\phi\partial\chi} + \frac{2I_B E_0}{\hbar^2}\psi = 0 \tag{B.1}$$

This may be solved by separation of variables using the following trial solution.

$$\psi = \Theta(\theta)e^{iM\phi}e^{iK\chi} \tag{B.2}$$

On substituting Equation B.2 into Equation B.1 separability is attained and on dividing through by $e^{iM\phi}e^{iK\chi}$, an equation is obtained which depends only on $\Theta(\theta)$ and its derivatives.

$$\frac{d^2\Theta}{d\theta^2} + \frac{\cos\theta}{\sin\theta}\frac{d\Theta}{d\theta} - \left[\frac{M^2}{\sin^2\theta} + \left(\frac{I_B}{I_C} + \cot^2\theta\right)K^2 - 2\cot\theta\csc\theta KM - \frac{2I_B E_0}{\hbar^2}\right] = 0 \tag{B.3}$$

This differential equation must be transformed into a different form which can be solved by conventional methods. A change of variables is introduced:

$$\begin{aligned} x &= \frac{1}{2}(1-\cos\theta) \\ \Theta(\theta) &= x^{\frac{1}{2}|K-M|}(1-x)^{\frac{1}{2}|K+M|}F(x) \end{aligned} \tag{B.4}$$

The derivatives involved may be determined in terms of the new variables using the chain rule.

$$\begin{aligned} \frac{d\Theta}{d\theta} &= \frac{d\Theta}{dx}\frac{dx}{d\theta} \\ \frac{d^2\Theta}{d\theta^2} &= \frac{dx}{d\theta}\frac{d}{dx}\left(\frac{d\Theta}{dx}\frac{dx}{d\theta}\right) \end{aligned} \tag{B.5}$$

When these expressions are substituted into Equation B.3 the transformed equation has the form of the hypergeometric equation, which can be solved using a power series expansion.

$$x(1-x)\frac{d^2F}{dx^2} + (\alpha - \beta x)\frac{dF}{dx} + \gamma F = 0 \tag{B.6}$$

where

$$\begin{aligned}
\alpha &= |K-M|+1 \\
\beta &= |K+M|+|K-M|+2 \\
\gamma &= \frac{2I_B E_0}{\hbar^2} - \frac{I_B}{I_C}K^2 + K^2 - \left(\frac{1}{2}|K+M| + \frac{1}{2}|K-M|\right)\left(\frac{1}{2}|K+M| + \frac{1}{2}|K-M|+1\right)
\end{aligned}$$

Any well behaved function may be expressed as a power series expansion. Solution of the above differential equation then corresponds to a determination of the coefficients of such an expansion. The generic solution and its derivatives are:

$$\begin{aligned}
F(x) &= \sum_{k=0}^{\infty} A_k x^k \\
\frac{dF}{dx} &= \sum_{k=0}^{\infty} k A_k x^{k-1} \\
\frac{d^2F}{dx^2} &= \sum_{k=0}^{\infty} k(k-1) A_k x^{k-2}
\end{aligned} \tag{B.7}$$

Substituting these into Equation B.6 gives

$$\sum_{k=0}^{\infty} k(k-1)A_k x^{k-1} - \sum_{k=0}^{\infty} k(k-1)A_k x^k + \alpha \sum_{k=0}^{\infty} k A_k x^{k-1} - \beta \sum_{k=0}^{\infty} k A_k x^k + \gamma \sum_{k=0}^{\infty} A_k x^k = 0 \tag{B.8}$$

Collecting terms in x^k and x^{k-1} gives,

$$\sum_{k=0}^{\infty}[k(k-1)+\alpha k]A_k x^{k-1} + \sum_{k=0}^{\infty}[-k(k-1)-\beta k+\gamma]A_k x^k = 0 \tag{B.9}$$

In order to make both terms in x^{k-1} the dummy index of summation k in the second term can be changed to $k-1$ without changing the sum.

$$\sum_{k=0}^{\infty}[k(k-1)+\alpha k]A_k x^{k-1} + \sum_{k=1}^{\infty}[-(k-1)(k-2)-\beta(k-1)+\gamma]A_{k-1} x^{k-1} = 0 \tag{B.10}$$

The $k=0$ term is equal to zero, and the two summations may be combined to give,

$$\sum_{k=1}^{\infty}[(k(k-1)+\alpha k)A_k + (-(k-1)(k-2)-\beta(k-1)+\gamma)A_{k-1}]x^{k-1} = 0 \tag{B.11}$$

In order for the above expression to be true for all x, all the coefficients must be equal to zero.

$$[k(k-1)+\alpha k]A_k + [-(k-1)(k-2)-\beta(k-1)+\gamma]A_{k-1} = 0 \tag{B.12}$$

Rearranging the above equation yields a recursion relation for the coefficients of the series expansion.

$$A_k = \left[\frac{(k-1)(k-2)+\beta(k-1)-\gamma}{k(k-1)+\alpha k}\right] A_{k-1} \tag{B.13}$$

or, as it is more commonly written (substituting $k+1$ for k)

$$A_{k+1} = \left[\frac{k(k-1)+\beta k-\gamma}{(k+\alpha)(k+1)}\right] A_k \tag{B.14}$$

The wavefunctions for a freely rotating symmetric top are therefore:

$$\psi = e^{iM\Phi}e^{iK\chi}(\frac{1}{2}-\frac{1}{2}\cos\theta)^{\frac{1}{2}|K-M|}(\frac{1}{2}+\frac{1}{2}\cos\theta)^{\frac{1}{2}|K+M|}\sum_{k=0}^{\infty}A_k(\frac{1}{2}-\frac{1}{2}\cos\theta)^k \tag{B.15}$$

where the A_k are given* by Equation B.14.

For ψ to be a normalizable wave function, the series must terminate and become a finite polynomial. This requirement allows an expression for the rotational energy E_0 to be determined.

The definition of γ can be rearranged to give,

$$\frac{2I_BE_0}{\hbar^2} = \gamma + \frac{I_B}{I_C}K^2 - K^2 + \left(\frac{1}{2}|K+M|+\frac{1}{2}|K-M|\right)\left(\frac{1}{2}|K+M|+\frac{1}{2}|K-M|+1\right) \tag{B.16}$$

or in terms of rotational constants $B = \frac{h}{8\pi^2 I_B}$ *etc* rather than moments of inertia,

$$\frac{E_0}{h} = B\left[\gamma + \left(\frac{1}{2}|K+M|+\frac{1}{2}|K-M|\right)\left(\frac{1}{2}|K+M|+\frac{1}{2}|K-M|+1\right)\right] + (C-B)K^2 \tag{B.17}$$

From the recurrence relation (Equation B.14)

$$\gamma = k(k-1)+\beta k-(k+1)(k+\alpha)\frac{A_{k+1}}{A_k} \tag{B.18}$$

* The summation is from $k=0$ rather than $k=1$ as in Equation B.11 due to the change of dummy variable used to convert Equation B.13 to Equation B.14

Assuming a finite sum, there will be some value $k_{\max}$ of k, corresponding to the final term in the summation, for which $A_{k+1} = 0$. The expression for γ is then

$$\gamma = k_{\max}(k_{\max} - 1) + \beta k_{\max} \tag{B.19}$$

Substituting this into Equation B.17 gives

$$\begin{aligned}
\frac{E_0}{h} &= B\left[k_{\max}^2 - k_{\max} + \beta k_{\max} + \left(\frac{1}{2}|K+M| + \frac{1}{2}|K-M|\right)\left(\frac{1}{2}|K+M| + \frac{1}{2}|K-M| + 1\right)\right] + (C-B)K^2 \\
&= B\left(k_{\max} + \frac{1}{2}|K+M| + \frac{1}{2}|K-M|\right)\left(k_{\max}\frac{1}{2}|K+M| + \frac{1}{2}|K-M| + 1\right) + (C-B)K^2 \\
&= BJ(J+1) + (C-B)K^2
\end{aligned} \tag{B.20}$$

in which

$$J = k_{\max} + \frac{1}{2}|K+M| + \frac{1}{2}|K-M| \tag{B.21}$$

In order for ψ to be normalised and to give wavefunction phases (signs) consistent with the Condon and Shortley convention, the first term of the series, A_0, which can be thought of as a normalisation and phase factor for the wavefunction, must be

$$A_0 = e^{\frac{i\pi}{2}|K-M|}\left[\frac{(2J+1)(J+\frac{1}{2}|K+M|+\frac{1}{2}|K-M|)!(J-\frac{1}{2}|K+M|+\frac{1}{2}|K-M|)^{\frac{1}{2}}}{8\pi^2(J-\frac{1}{2}|K+M|+\frac{1}{2}|K-M|)!|K-M|!(J+\frac{1}{2}|K+M|-\frac{1}{2}|K-M|)^{\frac{1}{2}}}\right]^{\frac{1}{2}} \tag{B.22}$$

From Equation B.21 J must be a positive integer which is greater than or equal to $|K|$ or $|M|$. i.e.

$$\begin{aligned}
J &= 0, 1, 2, ... \\
K &= 0, \pm 1, \pm 2, ... \pm J \\
M &= 0, \pm 1, \pm 2, ... \pm J
\end{aligned} \tag{B.23}$$

By application of the appropriate operators it can be shown that $J(J+1)\hbar$ is the square of the total angular momentum, $K\hbar$ is its projection on the molecular axis, and $M\hbar$ its projection on the space fixed axis.

C. THEORY OF PHOTOINITIATED BIMOLECULAR REACTION DYNAMICS

Semiclassically, the dynamics of a reaction may be characterised by a probability density function which gives the relative orientations of the linear and angular momenta of the reagents and products (i.e. the vectors $\mathbf{k}$, $\mathbf{k}'$ and $\mathbf{j}'$) known as the $\mathbf{k} - \mathbf{k}' - \mathbf{j}'$ distribution. This distribution is in turn described by double and triple vector correlations between the individual vectors.[256–258]

Measurements are carried out in the lab frame, but the required quantities are the vector correlations in the centre of mass (CM) frame. This creates the requirement for a reliable lab→CM frame transformation method. Several different approaches have been developed for this purpose. The theory has its origins in the semiclassical bipolar moment expansion formalism developed by Dixon[200] to describe the correlation between the translational and rotational motion of the products of photodissociation processes. This scheme has subsequently been extended by Aoiz *et al*[259] for application to photoinitiated bimolecular reactions, in which the first step in the reaction is the photodissociation of a precursor molecule. An alternative approach, developed by Shafer-Ray *et al*[201,260] and closely related to the method of Zare and Orr-Ewing[261] expands the CM angular momentum distribution in a series of spherical harmonics. In this formalism the expansion coefficients are known as the polarization dependent differential cross sections (PDDCS's) and provide a convenient link between the CM frame properties and the corresponding lab frame quantities.

This Appendix will describe the theories used to extract information on CM vector correlations from Doppler profiles measured in the lab frame. It should be noted that the theory is entirely general and may be adapted for use in the analysis of crossed beam experiments. The following description applies to the state resolved probing of the diatomic AB fragments from a triatomic A+BC reaction, though it is fairly straightforward to extend the theory to describe atom – polyatomic molecule reactions by accounting for the spread of product energies due to varying levels of internal excitation in the molecular coproduct. It is based on the recent paper by Aoiz *et al*,[234] which brings together the various approaches mentioned

above to provide a unified description of the current theory of photoinitiated bimolecular reactions.

C.1 Vector correlations

C.1.1 The CM frame $\mathbf{k} - \mathbf{k}' - \mathbf{j}'$ distribution

For the reaction between an atom and a diatomic molecule the centre of mass frame product velocity $\mathbf{w_i}$ for a given product state is determined by energy conservation. The angular distribution function for this product state can be written

$$\begin{aligned} P(\omega_t, \omega_r, w) &= \delta(w - w_i) P(\omega_t, \omega_r) \\ &= \frac{1}{\sigma} \frac{d^2\sigma}{d\omega_t d\omega_r} \delta(w - w_i) \end{aligned} \tag{C.1}$$

where w is the CM frame product speed and w_i its value for a state i at a given total energy. The CM frame z axis is defined to be along the reagent relative velocity vector $\mathbf{k}$. The angles $\omega_t = \theta_t, \phi_t$ and $\omega_r = \theta_r, \phi_r$ give the coordinates of the unit vectors $\mathbf{k}'$ and $\mathbf{j}'$, the product relative velocity and rotational angular momentum as shown in Figure C.1. In terms of the reagent and product CM velocities the reagent and product relative velocities are $\mathbf{k} = \mathbf{v_A} - \mathbf{v_{BC}}$ and $\mathbf{k}' = \mathbf{v_{AB}} - \mathbf{v_C}$

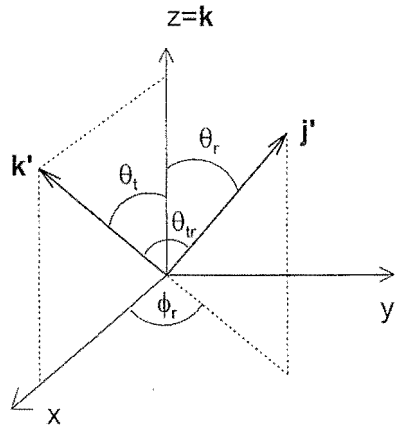

Figure C.1: Centre of mass frame coordinate system

The moments of an angular distribution transform under rotation in the same way as the modified spherical harmonics $C_{kq}(\theta, \phi)$ and these functions can be used as a basis set in which to expand any function of the angles θ and ϕ. The probability density function above is a double angular distribution. A suitable basis in which to expand this function is the set

of bipolar harmonics, which form a complete set in the space spanned by ω_t and ω_r. The bipolar harmonics are related to the spherical harmonics by

$$\begin{aligned} B_{KQ}(k_1,k_2;\omega_t,\omega_r) &= \sum_{q_1q_2}\langle KQ|k_1k_2q_1q_2\rangle C_{k_1q_1}(\theta_t,\phi_t)C_{k_2q_2}(\theta_r,\phi_r) \\ &= \sum_{q_1q_2}(-1)^{K-Q}[K]^{1/2}\begin{pmatrix} k_1 & K & k_2 \\ q_1 & -Q & q_2 \end{pmatrix} \\ &\quad \times C_{k_1q_1}(\theta_t,\phi_t)C_{k_2q_2}(\theta_r,\phi_r) \end{aligned} \tag{C.2}$$

where $[K] = 2K + 1$. The indices K, Q denote the total angular momentum and projection of the total angular momentum, while the indices k_1, q_1 and k_2, q_2 denote the contributions from the product relative velocity vector and rotational angular momentum vector.

In terms of the basis set of bipolar harmonics, the probability distribution function is given by

$$P(\omega_t,\omega_r) = \frac{1}{16\pi^2}\sum_{KQ}\sum_{k_1k_2}[k_1][k_2]h_{KQ}(k_1k_2)B_{KQ}(k_1,k_2;\omega_t\omega_r) \tag{C.3}$$

The coefficients h_{KQ} in the above expansion are the CM frame bipolar moments. These bipolar moments are just the expectation values of the bipolar harmonics which characterise the $\mathbf{k} - \mathbf{k}' - \mathbf{j}'$ triple vector correlation.

$$h_{KQ}(k_1,k_2) = \int B_{KQ}(k_1,k_2;\omega_t,\omega_r)^* P(\omega_t,\omega_r)d(\cos\theta_t)d(\cos\theta_r)d\phi_t d\phi_r \tag{C.4}$$

The CM xz plane is defined as the plane which contains the product relative velocity vector $\mathbf{k}'$, so that $\phi_t = 0$. This choice means that for $P(\omega_t, \omega_r)$ to be real, Q must be zero, and also the bipolar moments must satisfy the relationship

$$h_{K0}(k_1,k_2) = (-1)^{K+k_1+k_2}h_{K0}(k_1,k_2)^* \tag{C.5}$$

This implies that $h_{K0}(k_1, k_2)$ is real when $K + k_1 + k_2$ is even, and pure imaginary when it is odd. Applying these restrictions, the expression for the probability distribution becomes

$$P(\omega_t,\omega_r) = \frac{1}{16\pi^2}\sum_{KQ}\sum_{k_1k_2}[k_1][k_2]h_{K0}(k_1k_2)B_{K0}(k_1,k_2;\omega_t\omega_r) \tag{C.6}$$

Several groups have expanded the probability distribution in basis sets other than the bipolar harmonics used here. Herschbach and coworkers used an expansion in Biederharn polynomials[262] with a simple phase and scaling factor relating the moments of the expansion

to the bipolar moments described here. Shafer Ray *et al*[201] expanded in modified spherical harmonics C^*_{kq} with the PDDCS's as expansion coefficients. In this expansion the first coefficient is proportional to the differential cross section and the higher order moments give its dipolar dependence, quadrupolar dependence and so on.

The modified spherical harmonics differ from the standard spherical harmonics by the factor $(4\pi/[k])^{1/2}$. In the present coordinate system this expansion is of the form

$$P(\omega_t, \omega_r) = \sum_{kq} \frac{[k]}{4\pi} \frac{1}{\sigma} \frac{d\sigma_{kq}}{d\omega_t} C_{kq}(\theta_r, \phi_r)^* \tag{C.7}$$

The PDDCS's are obtained by multiplying both sides of Equation C.7 through by $C_{kq}(\theta_r, \phi_r)$ and integrating over the solid angle ω_r.

$$\frac{1}{\sigma} \frac{d\sigma_{kq}}{d\omega_t} = \int C_{kq}(\theta_r, \phi_r) P(\omega_t, \omega_r) d\omega_r \tag{C.8}$$

and the modified spherical harmonics are

$$C_{kq}(\theta, \phi) = (-1)^q \left[\frac{(k-q)!}{(k+q)!}\right]^{1/2} P_k^q(\cos\theta) \exp(im\phi) \tag{C.9}$$

with the associated Legendre functions $P_k^q(\cos\theta)$ given by

$$P_{kq}(x) = \frac{(1-x^2)^{q/2}}{2^k k!} \frac{d^{k+q}}{dx^{k+q}} (x^2-1)^k \tag{C.10}$$

Taking the complex conjugate of Equation C.8 shows that the PDDCS's have the same symmetry with respect to conjugation as the spherical harmonics, since the probability distribution $P(\omega_t, \omega_r)d\omega_r$ must be real, namely

$$\frac{1}{\sigma} \frac{d\sigma^*_{kq}}{d\omega_t} = (-1)^q \frac{1}{\sigma} \frac{d\sigma_{k,-q}}{d\omega_t} \tag{C.11}$$

Substituting Equation C.6, describing $P(\omega_t, \omega_r)$ as a linear combination of bipolar harmonics, into Equation C.8, gives a relation between the CM frame bipolar moments and the PDDCS's

$$\begin{aligned} \frac{1}{\sigma} \frac{d\sigma_{kq}}{d\omega_t} &= \frac{1}{4\pi} \sum_{K,k_1} (-1)^K [k_1][K]^{1/2} \begin{pmatrix} k_1 & K & k \\ q & 0 & -q \end{pmatrix} h_{K0}(k_1, k) C_{k_1,-q}(\theta_t, 0) \\ &= \frac{1}{4\pi} \sum_{K,k_1} (-1)^K [k_1] S^{k_1}_{kq} C_{k_1,-q}(\theta_t, 0) \end{aligned} \tag{C.12}$$

where

$$S^{k_1}_{kq} = \sum_K (-1)^K [K]^{1/2} \begin{pmatrix} k_1 & K & k \\ q & 0 & -q \end{pmatrix} h_{K0}(k_1, k) \tag{C.13}$$

C.1.2 Consequences of reflection symmetry in the scattering plane

The scattering of the probed product molecule will be symmetric above and below the scattering plane, with the only assumption being that the photon initiated reaction process is achiral. Using the set of axes defined above, the scattering plane, defined as the plane in which both the initial and final relative velocity vectors lie, is the xz plane. The distribution of internuclear axes of the AB product is therefore invariant to reflection in this plane, leading to a number of simplifications. The product rotational angular momentum $\mathbf{j}'$ behaves as a pseudovector. Unlike normal vectors a pseudovector does not change sign under inversion of all its spatial coordinates. The x and z components of $\mathbf{j}'$ change sign under reflection of the nuclear coordinates in the xz plane, but the y component is invariant to the reflection. This can be expressed as follows.

$$P(\omega_t, \omega_r) \equiv P(\theta_t, \theta_r, \phi_r) = P(\theta_t, \pi - \theta_r, \pi - \phi_r) \tag{C.14}$$

Combining this with Equation C.6 gives the result that

$$\frac{1}{\sigma}\frac{d\sigma_{kq}}{d\omega_t} = (-1)^{k+q}\frac{1}{\sigma}\frac{d\sigma_{k,-q}}{d\omega_t} = (-1)^k\frac{1}{\sigma}\frac{d\sigma^*_{kq}}{d\omega_t} \tag{C.15}$$

where the second equality follows from Equation C.11 after multiplying on both sides by $(-1)^k$. Using Equation C.11 this gives the following results for the various cases of k and q odd or even, ensuring that the distribution function is real. In the following expressions further 'sum and difference' PDDCS's are defined.

$$\frac{1}{\sigma}\frac{d\sigma_{k0}}{d\omega_t} = 0$$

k odd

$$\begin{aligned}
\frac{1}{\sigma}\frac{d\sigma_{kq+}}{d\omega_t} &= \frac{1}{\sigma}\frac{d\sigma_{kq}}{d\omega_t} + \frac{1}{\sigma}\frac{d\sigma_{k,-q}}{d\omega_t} \\
&= (-1)^{k+q}\frac{1}{\sigma}\frac{d\sigma_{k,-q}}{d\omega_t} + \frac{1}{\sigma}\frac{d\sigma_{k,-q}}{d\omega_t} \\
&= [(-1)^{k+q} + 1]\frac{1}{\sigma}\frac{d\sigma_{k,-q}}{d\omega_t} \\
&= 0
\end{aligned}$$

k even, q odd or k odd, q even

$$\begin{aligned}\frac{1}{\sigma}\frac{d\sigma_{kq-}}{d\omega_t} &= \frac{1}{\sigma}\frac{d\sigma_{kq}}{d\omega_t} - \frac{1}{\sigma}\frac{d\sigma_{k,-q}}{d\omega_t} \\ &= [(-1)^{k+q}-1]\frac{1}{\sigma}\frac{d\sigma_{k,-q}}{d\omega_t} \\ &= 0\end{aligned} \tag{C.16}$$

k even, q even or k odd, q odd.

Substituting the index $kq\pm$ for kq into Equation Equation C.12 allows the PDDCS's to be written in a shorter form as

$$\frac{1}{\sigma}\frac{d\sigma_{kq\pm}}{d\omega_t} = \sum_{k_1}\frac{[k_1]}{4\pi}S^{k_1}_{kq\pm}C_{k_1,-q}(\theta_t,0) \tag{C.17}$$

in which

$$S^{k_1}_{kq\pm} = \sum_K (-1)^K [K]^{1/2}\begin{pmatrix} k_1 & K & k \\ q & 0 & -q\end{pmatrix}\frac{[1\pm(-1)^{K+k_1+k+q}]}{1+\delta_{q0}}h_{K0}(k_1,k) \tag{C.18}$$

An expectation value expression may be formulated to evaluate the above equation.

$$S^{k_1}_{kq\pm} = \langle C_{k_1 q}(\theta_t,0)C_{kq}(\theta_r,0)[(-1)^q\exp(iq\phi_r)\pm\exp(-iq\phi_r)]\rangle \tag{C.19}$$

C.1.3 The moments of the $\mathbf{k}-\mathbf{k}'$ *distribution*

If the angular distribution function of Equation C.6 is integrated over the $\mathbf{j}'$ angular coordinates ω_t, removing the dependence of the distribution on this parameter, the moments of the $\mathbf{k}-\mathbf{k}'$ distribution are obtained. These correspond to the $h_{K0}(k_1,k_2)$ moments with $k_2=0$ (no dependence on the spherical harmonic in θ_r,ϕ_r of the bipolar harmonic basis function). The $\mathbf{k}-\mathbf{k}'$ distribution is usually known as the angular differential cross section, and is given by

$$\begin{aligned}\frac{1}{\sigma}\frac{d\sigma_{00}}{d\omega_t} &\equiv P(\omega_t) \\ &= \frac{1}{4\pi}\sum_{k_1}[k_1]S^{k_1}_{00}C_{k_1 0}(\theta_t,0) \qquad \text{(fromEquationC.12)} \\ &= \frac{1}{4\pi}\sum_{k_1}[k_1]h_{k_1 0}(k_1,0)P_{k_1}(\cos\theta_t)\end{aligned} \tag{C.20}$$

From this it can be seen that the bipolar moments $h_{k_1 0}(k_1,0)$ are the expectation values of an expansion of the differential cross section in Legendre polynomials.

$$S^k_{00} = h_{k0}(k_1,0) = \langle P_k(\cos\theta_t)\rangle \tag{C.21}$$

C.1.4 The moments of the $\mathbf{k} - \mathbf{j}'$ distribution

The moments describing the correlation between the initial relative velocity and final rotational angular momentum are determined in a similar way to the moments of the $\mathbf{k} - \mathbf{k}'$ distribution above by integrating the full distribution (Equation C.6) over the product relative velocity vector coordinates $\omega_t = \theta_t, \phi_t$.

$$\begin{aligned} P(\theta_r, \phi_r) &\equiv \frac{1}{\sigma}\frac{d\sigma}{d\omega_r} \\ &= \int P(\omega_t, \omega_r) d\omega_t \\ &= \int \sum_{kq} \frac{[k]}{4\pi}\frac{1}{\sigma}\frac{d\sigma_{kq}}{d\omega_t} C^*_{kq}(\theta_r, \phi_r) d\omega_t \qquad \text{(fromEquationC.7)} \\ &= \sum_{kq} \frac{[k]}{4\pi} C^*_{kq}(\theta_r, \phi_r) 2\pi \int_{-1}^{1} \frac{1}{\sigma}\frac{d\sigma_{kq}}{d\omega_t} d(\cos\theta_t) \qquad \text{(integrating over } \phi_t\text{)} \\ &= \frac{1}{2}\sum_{kq} [k] C^*_{kq}(\theta_r, \phi_r) \int_{-1}^{1} \frac{1}{\sigma}\frac{d\sigma_{kq}}{d\omega_t} \end{aligned} \tag{C.22}$$

The quantity $\frac{1}{\sigma}\frac{d\sigma}{d\omega_r}$ is the rotational solid angle differential cross section, the rotational angular momentum equivalent of the differential cross section, expressing the distribution of orientations of the product rotational angular momentum rather than the product relative velocity vector relative to the reagent relative velocity. The rotational solid angle differential cross section can be rewritten in terms of the polarization parameters a^k_q defined by Shafer Ray *et al.* These polarization parameters are the integrals of the PDDCS's over the $\mathbf{k}'$ coordinates ω_t.

$$a^k_q = 2\pi \int_{-1}^{1} \frac{1}{\sigma}\frac{d\sigma_{kq}}{d\omega_t} d(\cos\theta_t) \tag{C.23}$$

Sum and difference polarization parameters are defined analagously to the sum and difference PDDCS's in Equation C.16.

$$a^k_{q\pm} = 2\pi \int_{-1}^{1} \left(\frac{1}{\sigma}\frac{d\sigma_{kq}}{d\omega_t} \pm \frac{1}{\sigma}\frac{d\sigma_{k,-q}}{d\omega_t}\right) d(\cos\theta_t) \tag{C.24}$$

$$\begin{aligned} a^k_{q+} &= 0 \qquad \text{k even, q odd or k odd, q even} \\ a^k_{q-} &= 0 \qquad \text{k, q both even or both odd} \\ a^k_0 &= 0 \qquad \text{k odd} \end{aligned}$$

As was the case with the PDDCS's $a^k_{0\pm} \equiv a^k_0$.

The rotational solid angle differential cross section can then be written in terms of these polarization parameters as

$$\begin{aligned} \frac{1}{\sigma}\frac{d\sigma}{d\omega_r} &= \frac{1}{4\pi}\sum_{kq}[k]a_q^k C_{kq}^*(\theta_r,\phi_r) \\ &= \frac{1}{4\pi}\sum_k\sum_{q\geq 0}[k][a_{q\pm}^k\cos(q\phi_r) - a_{q\mp}^k i\sin(q\phi_r)]C_{kq}(\theta_r,0) \end{aligned} \tag{C.25}$$

In the sum over q in the second line of the above equation, the upper sign in the index of the polarization parameters applies when q is even and the lower sign when q is odd. By integrating Equation C.17 over ω_t and using the expectation value expression for $S_{q\pm}^{k_1}$ the relationship between the polarization parameters $a_{q\pm}^k$ and the CM frame bipolar moments $S_{q\pm}^{k_1}$ is obtained.

$$\begin{aligned} a_{q\pm}^k &= \sum_{k_1}\frac{[k_1]}{2}S_{kq\pm}^{k_1}\int_{-1}^{+1}C_{k_1-q}(\theta_t,0)\mathrm{d}(\cos\theta_t) \\ &= \langle C_{k_1|q|}(\theta_t,0)2\cos q\phi_r\rangle \quad k \text{ even} \\ &= i\langle C_{k_1|q|}(\theta_t,0)2\sin q\phi_r\rangle \quad k \text{ odd} \end{aligned} \tag{C.26}$$

When $q = 0$ this reduces to

$$a_0^k = h_0^k(0,k) \tag{C.27}$$

In order to determine the preferential orientation of the product angular momentum with respect to the scattering plane experimentally, measurements of polarization parameters (or equivalently, PDDCS's) with k odd are required, since examination of the above equations shows that only these terms show a $\sin\phi_r$ dependence. Terms with k even can give information on alignment of the rotational angular momentum, but not on its orientation.

The $\mathbf{k}-\mathbf{j}'$ correlation is obtained in terms of $a_0^{k_1}$ by integrating Equation C.26 over the angle ϕ_r.

$$\begin{aligned} P(\theta_r) &= \int_{-1}^{+1}P(\theta_r,\phi_r)d\phi_r \\ &= \frac{1}{4\pi}\int_0^{2\pi}\sum_{kq}[k]a_q^k C_{kq}^*(\theta_r,\phi_r)d\phi_r \\ &= \frac{1}{2}\sum_k[k]a_0^k P_k(\cos\theta_r) \end{aligned} \tag{C.28}$$

in which the coefficients are the expectation values of the Legendre polynomial expansion of the $\mathbf{k}-\mathbf{j}'$ distribution in $\cos\theta_r$, where θ_r is the angle between the vectors $\mathbf{k}$ and $\mathbf{j}$.

$$a_0^k = h_0^k(0,k) = \langle P_k(\cos\theta_r)\rangle. \tag{C.29}$$

It has already been shown in Equations C.16 and C.25 that all the terms in the above expansion for $P(\theta_r)$ with k odd are zero, so that the distribution must be even.

The distribution of dihedral angles for the $\mathbf{k}-\mathbf{j}'$ correlation can be found by integrating Equation C.26 over the $\cos\theta_r$ angle.

$$P(\phi_r) = \frac{1}{4\pi}\sum_k \sum_{q\geq 0}[k][a^k_{q\pm}\cos(q\phi_r) - a^k_{q\mp} i\sin(q\phi_r)]\int_{-1}^{1} C_{kq}(\theta_r, 0) \tag{C.30}$$

The integrals over the spherical harmonics disappear for those functions which are odd with respect to $\cos\theta_r$ (i.e. the spherical harmonics for which $k+q$ is odd). Apart from the case ($k=0,\ q=0$), in which the integral is equal to 2, they also vanish when $q=0$. When combined with the rules for the polarization parameters presented in Equation C.25, this has several implications for the dihedral angular distribution. Since only terms with $k+q$ even survive, k and q must either be both odd or both even, so that all a^k_{q-} terms vanish and only a^k_{q+} terms are involved in the distribution. The $P(\phi_r)$ distribution can therefore be expressed as a Fourier series with only odd terms in sines and only even terms in cosines, in which the Fourier coefficients a_n and b_n are themselves sums over even $k \geq n$ and odd $k \geq n$ terms respectively, with only $k, q+$ contributions.

$$P(\phi_r) = \frac{1}{2\pi}[1 + \sum_{\text{even}n\geq 2} a_n\cos(n\phi_r) + \sum_{\text{odd}n\geq 2} b_n\sin(n\phi_r) \tag{C.31}$$

C.1.5 The moments of the $\mathbf{k}'-\mathbf{j}'$ *distribution*

The distribution of the angle between the product relative velocity vector and rotational angular momentum vectors $P(\theta_{tr})$ can be found by forming the tensor product in Equations C.3 and C.6 when $K=0$, which means that $k_1 = k_2 = k$.

$$P(\theta_{tr}) = \frac{1}{2}\sum_k [k]^{\frac{3}{2}} h_{00}(k,k)\sum_q C_{kq}(\theta_t, 0)C_{kq}(\theta_r, \phi_r)^*. \tag{C.32}$$

The product of the two spherical harmonics can be evaluated using the spherical harmonic addition theorem,[263] which states

$$\sum_q C_{kq}(\theta_t, 0)C^*_{kq}(\theta_r, \phi_r) = P_k(\cos\theta_{tr}) \tag{C.33}$$

giving

$$P(\theta_{tr}) = \frac{1}{2}\sum_k [k]^{\frac{3}{2}} h_{00}(k,k)P_k(\cos\theta_{tr}). \tag{C.34}$$

From this it is seen that the $h_{00}(k,k)$ centre of mass frame bipolar moments are proportional to the expectation values of the Legendre polynomials in $\cos\theta_{tr}$

$$h_0^0(k,k) = \frac{1}{[k]^{\frac{1}{2}}}\langle P_k(\cos\theta_{tr})\rangle \tag{C.35}$$

The planar symmetry constraints considered earlier for achiral systems mean that these moments are zero if k is odd, so that the distribution of θ_{tr} is even for these systems.

C.1.6 Other moments

If only the projections of the product relative velocity and rotational angular momentum vectors onto the initial relative velocity vector $\mathbf{k}' \cdot \mathbf{k}$ and $\mathbf{j}' \cdot \mathbf{k}$ are measured, the joint θ_t, θ_r distribution can be obtained. This is calulated from Equation C.6 by integrating over ϕ_r and the scattering plane azimuthal angle.

$$\begin{aligned}
P(\theta_t,\theta_r) &= 2\pi \int P(\omega_t,\omega_r)d\phi_r \qquad (C.36)\\
&= \frac{1}{8\pi}\sum_K \sum_{k_1,k_2}[k_1][k_2]h_{K0}(k_1,k_2)\int B_{K0}(k_1,k_2;\omega_t,\omega_r)d\phi_r \\
&= \frac{1}{8\pi}\sum_K \sum_{k_1,k_2}[k_1][k_2]h_{K0}(k_1,k_2) \\
&\quad \times \int \sum_{q_1,q_2}(-1)^K[K]^{1/2}\begin{pmatrix} k_1 & K & k_2 \\ q_1 & 0 & q_2\end{pmatrix} C_{k_10}(\theta_t,0)C_{k_20}(\theta_r,\phi_r)d\phi_r \\
&= \frac{1}{4}\sum_K \sum_{k_1,k_2}(-1)^K[K]^{\frac{1}{2}}[k_1][k_2]h_{K0}(k_1,k_2)\begin{pmatrix} k_1 & K & k_2 \\ 0 & 0 & 0\end{pmatrix} \\
&\quad \times P_{k_1}(\cos\theta_t)P_{k_2}(\cos\theta_r).
\end{aligned}$$

This can be rewritten in terms of the $S_{k_20}^{k_1}$ coefficients defined previously, and finally written in terms of the PDDCS $\frac{1}{\sigma}\frac{d\sigma_{k_20}}{d\omega_t}$.

$$\begin{aligned}
P(\theta_t,\theta_r) &= \frac{1}{4}\sum_{k_1,k_2}[k_1][k_2]S_{k_20}^{k_1}P_{k_1}(\cos\theta_t)P_{k_2}(\cos\theta_r) \qquad (C.37)\\
&= 2\pi\sum_{k_2}\frac{[k_2]}{2}\frac{1}{\sigma}\frac{d\sigma_{k_20}}{d\omega_t}P_{k_2}(\cos\theta_r) \qquad \text{(fromEquationC.17)}
\end{aligned}$$

The moments of the distribution are given by

$$S_{k_20}^{k_1} = \langle P_{k_1}(\cos\theta_t)\cdot P_{k_2}(\cos\theta_r)\rangle \tag{C.38}$$

If Equations C.12 and C.38 are compared it is seen that these $S^{k_1}_{k_20}$ coefficients are the expansion coefficients for the PDDCS which has $q = 0$. i.e.

$$\frac{1}{\sigma}\frac{d\sigma_{k0}}{d\omega_t} = \frac{1}{4\pi}\sum_{k_1}[k_1]S^{k_1}_{k0}P_{k_1}(\cos\theta_t) \tag{C.39}$$

The definitions of the various polarization dependent differential cross sections given in Equation C.16 showed that if k is odd then the PDDCS with $q = 0$ is zero. This means that in the above expansion only $S^{k_1}_{k_20}$ coefficients with k_2 even are non zero. From Equation C.39 $S^{k_1}_{k0}$ can also be expressed as

$$S^{k_1}_{k0} = 2\pi\int_{-1}^{+1}\frac{1}{\sigma}\frac{d\sigma_{k0}}{d\omega_t}P_{k_1}(\cos\theta_t)d(\cos\theta_t). \tag{C.40}$$

For the case where $k_1 = 0$ the Legendre polynomial has a value of unity over the entire range of $\cos\theta_t$ and the S^0_{k0} coefficients are given by

$$\begin{aligned} S^0_{k0} &= a^k_0 \\ &= 2\pi\int_{-1}^{+1}\frac{1}{\sigma}\frac{d\sigma_{k0}}{d\omega_t}d(\cos\theta_t) \\ &= h_{k0}(0,k) \\ &= \langle P_k(\cos\theta_r)\rangle \qquad \text{(fromEquationC.21)} \end{aligned} \tag{C.41}$$

where the a^k_0 are the rotational alignment parameters.

C.2 The lab frame angular distribution

Expressions have now been formulated for several probability distributions in terms of an expansion in either the polarization dependent differential cross sections, or the polarization parameters a^k_q. Because experimental measurements cannot be carried out in the CM frame, it is not possible to determine these distributions directly. A reliable method of transforming between the CM and lab frames is required so that CM frame quantities can be extracted from lab frame measurements.

A good approximation to the full 3D treatment of the transformation problem is to assume that the target molecule velocity $\mathbf{v_2}$ lies along the hot atom velocity vector $\mathbf{v_1}$. This leads to a degree of simplification since the relative velocity $\mathbf{k}$ is now parallel to $\mathbf{v_1}$ and its magnitude v_r is just equal to $v_1 \pm v_2$. This 1D approximation leads to equations which can be fairly easily compared with those obtained previously by other groups such as Shafer-Ray *et al*,[201]

who assumed that the motion of both the photolysis precursor and the target molecule could be ignored in their analysis.

For experiments in which the photolysis precusor and molecular target are coexpanded in a molecular beam the approximation becomes essentially exact since the transverse velocity components in a molecular beam are very small. However, in general $\mathbf{v_1}$ and $\mathbf{v_2}$ are not parallel, and analysis of experimental results obtained using bulb type experiments benefits from the full 3D treatment.

In order to carry out the transformation from the CM to the lab frame, a new reference frame—the v_1 frame—is defined, with axes X, Y, Z. The v_1 frame Z axis is parallel to the hot atom velocity $\mathbf{v_1}$ and its X axis is in the $\mathbf{v_1} - \mathbf{v_2}$ plane, so that the reactant relative velocity vector $\mathbf{k}$ lies in the XZ plane, making an angle θ_k with the Z axis. The CM scattering plane (xz plane) makes an angle ϕ_t with the v_1 frame XZ plane, this angle being defined so that $\phi_t \to \phi_v$ when $\theta_k \to 0$. The relationship between the frames is shown in the diagram below.

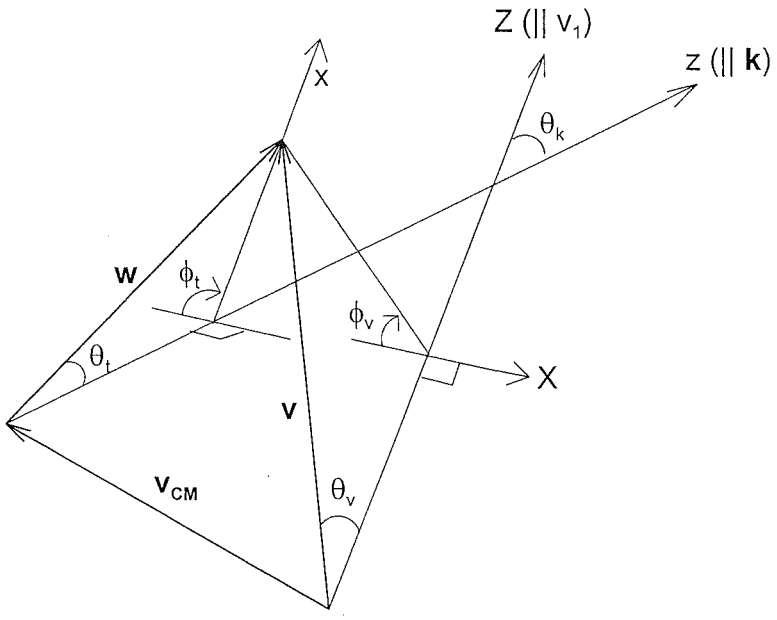

Figure C.2: Coordinates involved in the CM to v_1 frame transformation

If it is assumed that no collisional relaxation has occurred during the interval between formation of the nascent product and detection, which in practice means short delay times between the photolysis and probe lasers, the differential flux into a given product channel i in the v_1 frame is proportional to the AB_i number density. For particular hot atom and target

velocities $\mathbf{v_1}$ and $\mathbf{v_2}$ this flux may be written as

$$\mathrm{I}(\theta_v, \omega_r; v, v_1, v_2) = \mathrm{R}\sigma v_r \, P(\omega_t, \omega_r)\delta(w - w_i) \frac{\partial(w, \theta_t)}{\partial(v, \theta_v)} \tag{C.42}$$

where v is the magnitude of the product lab frame velocity vector $\mathbf{v}$, θ_v is its angular coordinate ($\phi_v = \phi_t = 0$), and R is a factor which accounts for the number densities of the reagents and also for the reaction volume.

The unit vector $\mathbf{k}$, in the direction of the initial relative velocity, has cartesian coordinates $\mathbf{r}^{\mathbf{v_1}} = (-\sin\theta_k, 0, \cos\theta_k)$ in the v_1 frame and $\mathbf{r}^{\mathrm{CM}} = (0, 0, 1)$ in the CM frame (since $\mathbf{k}$ lies along the z axis of this frame). The XZ plane of the v_1 frame forms an angle ϕ_t with the xz plane of the CM frame, so that the cartesian coordinates of the CM frame x axis in the v_1 frame are $\mathbf{r}^{\mathbf{v_1}} = (\cos\theta_k \cos\phi_t, \sin\phi_t, \sin\theta_k \cos\phi_t)$. Both of these pairs of coordinates may be related by a unitary rotation matrix.

$$\mathbf{r}^{\mathbf{v_1}} = \mathrm{R}(\alpha\beta\gamma)^{-1}\mathbf{r}^{\mathrm{CM}} \tag{C.43}$$

where the Euler angles α,β and γ and the direction cosine rotation matrix $\mathrm{R}(\alpha\beta\gamma)$ are defined as follows.[264]

The CM cartesian axis system xyz is obtained by rotation of the v_1 frame axes. A vector $\mathbf{u}$ is defined which is perpendicular to the zZ plane. The Euler angles are defined as $\alpha = \angle(\mathbf{yu})$, $\beta = \angle(\mathbf{Zz})$ and $\gamma = \angle(\mathbf{uY})$, as shown in Figure C.3.

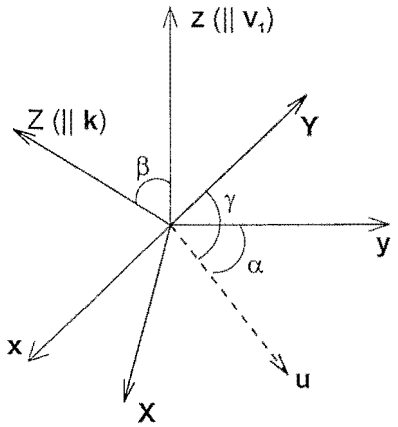

Figure C.3: Definition of the Euler angles for the CM to v_1 frame transformation

The rotation is as follows:

1. Rotation by angle α about $\mathbf{z}$, $\mathrm{R}_z(\alpha)$, maps $\mathbf{y}$ onto $\mathbf{u}$.

2. Rotation by angle β about **u**, $R_u(\beta)$, maps **z** onto **Z**.

3. Rotation by angle γ about **Z**, $R_Z(\gamma)$, maps **u** onto **Y**.

The combination of these three rotations maps the two coordinate systems onto each other*.

$$\begin{aligned} R(\alpha\beta\gamma) &= R_Z(\gamma)R_u(\beta)R_z(\alpha) \\ &= \begin{pmatrix} c\gamma c\beta c\alpha - s\gamma s\alpha & -s\gamma c\beta c\alpha - c\gamma s\alpha & s\beta c\alpha \\ c\gamma c\beta s\alpha + s\gamma c\alpha & -s\gamma c\beta s\alpha - c\gamma c\alpha & s\beta s\alpha \\ -c\gamma s\beta & s\gamma s\beta & c\beta \end{pmatrix} \end{aligned} \tag{C.44}$$

By applying this matrix to the transformations for the x and z axes the Euler angles for this system can be determined. For the transformation of the CM z axis:

$$\begin{pmatrix} \sin\theta_k \\ 0 \\ \cos\theta_k \end{pmatrix} = \begin{pmatrix} c\gamma c\beta c\alpha - s\gamma s\alpha & -s\gamma c\beta c\alpha - c\gamma s\alpha & s\beta c\alpha \\ c\gamma c\beta s\alpha + s\gamma c\alpha & -s\gamma c\beta s\alpha - c\gamma c\alpha & s\beta s\alpha \\ -c\gamma s\beta & s\gamma s\beta & c\beta \end{pmatrix} \begin{pmatrix} 0 \\ 0 \\ 1 \end{pmatrix} \tag{C.45}$$

This system of linear equations can be solved to give the two solutions ($\beta = \theta_k$, $\gamma = 0$) or ($\beta = -\theta_k$, $\gamma = \pi$). Substituting these sets of angles in for the transformation ofthe CM x axis gives $\alpha = -\phi_t$ or $\alpha = \pi - \phi_t$. The Euler angles defining the CM to v_1 frame rotation are therefore

$$(\alpha, \beta, \gamma) = (-\phi_t, \theta_k, 0) \text{ or } (\pi - \phi_t, -\theta_k, \phi) \tag{C.46}$$

When dealing with angular momentum vectors $|kq\rangle$, the $2k+1$ eigenvalues of an angular momentum operator, the rotation matrices are

$$\begin{aligned} D^k_{qq'}(\alpha\beta\gamma) &\equiv \langle kq|R(\alpha\beta\gamma)|kq\rangle \\ &\equiv \langle kq|e^{-i\alpha k_z}\ e^{-i\beta k_y}\ e^{-i\gamma k_z}|kq\rangle \\ &\equiv e^{-i\alpha q}\ d^k_{qq'}(\beta)\ e^{-i\gamma q} \end{aligned} \tag{C.47}$$

where

$$d^k_{qq'}(\beta) = \langle kq|e^{-i\beta k_y}|kq\rangle \tag{C.48}$$

* In the following equations cos and sin are abbreviated to c and s.

Using these definitions, the v_1 frame product differential flux becomes

$$\begin{aligned} \mathrm{I}(\omega_v, \omega_j; v, v_1, v_2) &= \mathrm{R}\sigma v_r P(\omega_t, \omega_r) \frac{d(w, \theta_t)}{d(v, \theta_v)} \\ &= \mathrm{R}\sigma v_r \sum_{kq} \frac{[k]}{4\pi} \frac{1}{\sigma} \frac{d\sigma_{kq'}}{d\omega_t} C^*_{kq}(\theta_j, \phi_j) \frac{d(w, \theta_t)}{d(v, \theta_v)} \\ &= \mathrm{R}\sigma v_r \sum_{kq} \frac{[k]}{4\pi} \sum_{q'} \mathrm{D}^k_{q'q}(-\phi_t, \theta_k, 0) \frac{1}{\sigma} \frac{d\sigma_{kq'}}{d\omega_t} C^*_{kq}(\theta_j, \phi_j) \\ &\quad \times \delta(\cos\theta_v - \cos\theta_v^i) \left| \frac{d(\cos\theta_v)}{dw_i} \right| \frac{v^2}{w_i^2} \end{aligned} \tag{C.49}$$

where in the second line $P(\omega_t, \omega_r)$ has been substituted for using Equation C.7. The quantities ω_v and ω_j are the angular coordinates of $\mathbf{v}$ and $\mathbf{j}$ in the v_1 frame and the Jacobian is defined below.

$$\left| \frac{d(\cos\theta_v)}{dw_i} \right|^{-1} = \left| \frac{v_{CM} v}{w_i} \left(\frac{\cos\theta_v}{\sin\theta_v} \cos\phi_v \sin\theta_{CM}^{v_1} - \cos\theta_{CM}^{v_1} \right) \right| \tag{C.50}$$

where $\theta_{CM}^{v_1}$ is the angle between the CM velocity vector $\mathbf{v_{CM}}$ and $\mathbf{v_1}$.

This flux can also be expressed as a linear expansion in v_1 frame bipolar harmonics $B_{KQ}(k_1, k_2; \omega_v, \omega_j)$.

$$\mathrm{I}(\omega_v, \omega_j; v, v_1, v_2) = \frac{1}{16\pi^2} \sum_{KQ} \sum_{k_1, k_2} [k_1][k_2] b_{KQ}(k_1, k_2; v) B_{KQ}(k_1, k_2; \omega_v, \omega_j) \tag{C.51}$$

The set of v_1 frame bipolar harmonics are given by

$$\begin{aligned} B_{KQ}(k_1, k_2; \omega_v, \omega_j) &= \sum_{q'} (-1)^{K-Q} [K]^{1/2} \begin{pmatrix} k_1 & K & k_2 \\ q_1 & -Q & q_2 \end{pmatrix} \\ &\quad \times C_{k_1 q_1}(\theta_v, \phi_v) C_{k_2 q_2}(\theta_j, \phi_j) \end{aligned} \tag{C.52}$$

and their corresponding bipolar moments by

$$b_{KQ}(k_1, k_2; v) = \int B^*_{KQ}(k_1, k_2 : \omega_v, \omega_j) \mathrm{I}(\omega_v, \omega_j; v, v_1, v_2) d\omega_v d\omega_j \tag{C.53}$$

Substitution of Equations C.53 and C.50 for B_{KQ} and I into Equation C.53 gives

$$\begin{aligned} b_{KQ}(k_1, k_2; v) &= \mathrm{R}\sigma v_r \int\int \sum_{q_1} (-1)^{K-Q} [K]^{1/2} \begin{pmatrix} k_1 & K & k_2 \\ q_1 & -Q & q_2 \end{pmatrix} \\ &\quad \times C^*_{k_1 q_1}(\theta_v, \phi_v) (-1)^{q_2} C_{k_2, -q_2}(\theta_j, \phi_j) \\ &\quad \times \sum_{kq} \frac{[k]}{4\pi} \sum_{q'} \mathrm{D}^k_{q'q}(-\phi_t, \theta_k, 0) \frac{1}{\sigma} \frac{d\sigma_{kq'}}{d\omega_t} C^*_{kq}(\theta_j, \phi_j) \\ &\quad \times \delta(\cos\theta_v - \cos\theta_v^i) \times \left| \frac{d(\cos\theta_v)}{dw_i} \right| \frac{v^2}{w_i^2} d\omega_v d\omega_j \end{aligned} \tag{C.54}$$

Carrying out the integration over ω_j and θ_v gives

$$\begin{aligned} b_{KQ}(k_1,k;v) &= \mathrm{R}\sigma v_r \int \sum_{q_1} (-1)^K [K]^{1/2} \begin{pmatrix} k_1 & K & k \\ q_1 & -Q & q \end{pmatrix} \\ &\times C_{k_1,-q_1}(\theta_v^i,0) \sum_{q'} \mathrm{d}^k_{q'q}(\theta_k) \mathrm{e}^{-iq_1\phi_v} \ \mathrm{e}^{iq'\phi_t} \\ &\times \frac{1}{\sigma}\frac{d\sigma_{kq'}}{d\omega_t} \left|\frac{d(\cos\theta_v^i)}{dw_i}\right| \frac{v^2}{w_i^2} d\phi_v \end{aligned} \tag{C.55}$$

As was the case in the CM frame the v_1 frame probability distribution has a plane of symmetry, so that $k_1 + K$ must be even. Applying the above equation to the case where $Q = 0$ gives

$$\begin{aligned} b_{K0}(k_1,k;v) &= \mathrm{R}\sigma v_r \int \sum_{q_1} (-1)^K [K]^{1/2} \begin{pmatrix} k_1 & K & k \\ q & 0 & q \end{pmatrix} \\ &\times C_{k_1,-q_1}(\theta_v^i,0) \sum_{q'} \mathrm{d}^k_{q'q}(\theta_k) \mathrm{e}^{-iq_1\phi_v} \ \mathrm{e}^{(iq'\phi_t)} \\ &\times \frac{1}{\sigma}\frac{d\sigma_{kq'}}{d\omega_t} \left|\frac{d(\cos\theta_v^i)}{dw_i}\right| \frac{v^2}{w_i^2} d\phi_v \end{aligned} \tag{C.56}$$

When the indices of the bipolar moments are even, Equation C.57 can be expressed in a more explicit form as

$$\begin{aligned} b_{K0}(k_1,k;v) &= \mathrm{R}\sigma v_r \int \sum_{q\geq 0} (-1)^K [K]^{1/2} \begin{pmatrix} k_1 & K & k \\ q & 0 & q \end{pmatrix} C_{k_1,-q_1}(\theta_v^i,0) \\ &\times \sum_{q'\geq 0} \frac{\mathrm{d}^k_{q'q}(\theta_k)\cos(q'\phi_t - q\phi_v) + (-1)^{q'}\mathrm{d}^k_{-q'q}(\theta_k)\cos(q'\phi_t + q\phi_v)}{(1+\delta_{q0})} \\ &\times \frac{1}{\sigma}\frac{d\sigma_{kq'\pm}}{d\omega_t} \left|\frac{d(\cos\theta_v^i)}{dw_i}\right| \frac{v^2}{w_i^2} d\phi_v \end{aligned} \tag{C.57}$$

In the above expression the plus sign in the PDDCS applies when q' is even, and the minus sign when it is odd. As before $\frac{1}{\sigma}\frac{d\sigma_{k0\pm}}{d\omega_t} = \frac{1}{\sigma}\frac{d\sigma_{k0}}{d\omega_t}$.

In order to obtain the differential flux in the lab frame all that is required is to integrate the v_1 frame flux over the lab distributions of v_1 and v_2. This corresponds to integrating over all the possible orientations of the v_1 frame with respect to the lab frame. After carrying out this integration the final expression for the lab frame angular distribution is

$$\begin{aligned} \mathrm{I}(v,\Omega_v\Omega_j) &= \frac{1}{16\pi^2} \sum_k [k]^2 \overline{b_{00}(k,k;v)} B_{00}(k,k;\Omega_v,\Omega_j) \\ &+ \frac{\beta}{5} \sum_{k_1 k_2} [k_1][k_2] \overline{b_{20}(k_1,k_2;v)} B_{20}(k_1,k_2;\Omega_v,\Omega_j)) \end{aligned} \tag{C.58}$$

where β is the translational anisotropy of the reagent atom A in the CM frame. This equation, describing the product flux from a bimolecular reaction, is very similar to that obtained for molecular photodissociation. The presence of β ensures that for this application the bipolar moments are referenced to the reagent atom velocity $\mathbf{v_1}$ and not the electronic transition moment of the precursor, as would be the case in a photodissociation study. Ω_v and Ω_j are the angular coordinates of $\mathbf{v}$ and $\mathbf{j}$ in the lab frame as shown in Figure C.2.

The bars over the bipolar moments indicate that these moments have now been averaged over the velocities $\mathbf{v_1}$ and $\mathbf{v_2}$. These averaged moments are given by

$$\overline{b_{K0}(k_1,k_2;v)} = \int\int\int\int f_k(v_1)g(v_2)b^*_{K0}(k_1,k_2;v)v_1^2v_2^2dv_1dv_2d\Omega_{v_2} \qquad \text{(C.59)}$$

where $f_k(v_1)$ is the lab frame speed distribution of reagent atom velocities $\mathbf{v_1}$ and $g(v_2)$ is the lab speed distribution of target molecule velocities $\mathbf{v_2}$.

C.2.1 The reagent velocity distributions

For bulb type experiments, in which the target molecule is present in a bulk sample of gas at room temperature, $g(v_2)$ is simply a Maxwell-Boltzmann distribution,

$$g(v_2) = 4\pi v_2^2\left(\frac{M}{2\pi kT}\right)^{3/2} e^{-\frac{Mv_2}{2kT}} \qquad \text{(C.60)}$$

where M is the mass of the target molecule and k is the Boltzmann constant.

The velocity distribution for the hot atom is somewhat more complicated, and is dependent on not only the identity of the atom, but also the precursor and method of preparation.

If the photolysis is carried out on a sample of stationary parent molecules the distribution has cylindrical symmetry and can be expressed as an expansion in Legendre polynomials[265]

$$f'_k(v) = \sum_n c_n f_n(v)P_n(\cos\theta) \qquad \text{(C.61)}$$

where the $f_n(v)$ are normalized CM speed distribution functions and c_n are expansion coefficients. A symmetry constraint is introduced by the fact that the hot atoms are prepared by one photon photolysis using linearly polarized light, so that only the coefficients c_0 and c_2 are non zero.

The thermal velocity of the parent molecules can now be accounted for by convoluting the above distribution with the isotropic Maxwell Boltzmann distribution G_v of the parent

molecules, which has the same form as the distribution in Equation C.60.

$$f_k(v_1) = \int f'_v G_(|v_1 - v|)dv \tag{C.62}$$

The solution to this integral has the form

$$f_k(v_1) = \frac{1}{4\pi}[f_0(v_1) + f_2(v)\beta P_2(\cos\theta)] \tag{C.63}$$

where

$$\begin{aligned} f_0(v_1) &= \sqrt{\frac{\gamma}{\pi}} \int_0^\infty \frac{v}{v_1} f(v)(\exp(-\gamma(v_1 - v)^2) \\ &\quad \exp(-\gamma(v_1 + v)^2))dv \\ f_2(v_1) &= f_0(v_1) + \frac{3}{2}\sqrt{\frac{\gamma}{\pi}}\frac{1}{\gamma v^2}\int_0^\infty f(v)\,[\,(\frac{1}{2\gamma v_1 v} - 1)\,\exp(-\gamma(v_1 - v)^2) \\ &\quad -(\frac{1}{2\gamma v_1 v} + 1)\,\exp(-\gamma(v_1 + v)^2)\,]dv \end{aligned} \tag{C.64}$$

in which $\gamma = \frac{M}{2kT}$ and $f(v)$ is the centre of mass frame speed distribution.

D. COMPOSITE DOPPLER PROFILES

The projection $\mathbf{k_a} \cdot \mathbf{v}$ of the product velocity vector $\mathbf{v}$ onto the laser propagation axis $\mathbf{k}$ can be used in conjunction with the lab frame product velocity distribution (Equation C.59 of Appendix C) to give the line shape function of the Doppler profile. In [1+1] LIF detection the lineshape function is dominated by a fairly small number of the bipolar moments $b_{KQ}(k_1, k_2)$. The relationships between these v_1 frame bipolar moments and the PDDCS's are shown in Table D.1. Note that the bipolar moments appearing in the table are the more commonly used 'rescaled bipolar moments' as defined below, and require multiplication by the factor $\mathrm{R}\sigma v_r \frac{v^2}{w_i^2} |\frac{d\cos\theta_v}{dw_i}|$ to obtain normalization.

$$\begin{aligned}
\beta_{00}(0,0) &\equiv b_{00}(0,0) \\
\beta_{20}(2,0) &\equiv b_{20}(2,0) \\
\beta_{02}(0,2) &\equiv b_{20}(0,2) \\
\beta_{00}(2,2) &\equiv \sqrt{5} b_{00}(2,2) \\
\beta_{20}(2,2) &\equiv \sqrt{\frac{7}{2}} b_{20}(2,2) \\
\beta_{20}(4,2) &\equiv \sqrt{\frac{7}{2}} b_{20}(4,2)
\end{aligned} \tag{D.1}$$

The lineshape function is usually expressed in terms of the Doppler shift, x, which is related to the product speed v_p by the expression

$$x = \frac{c}{v_p} \frac{\nu_0 - \nu}{\nu} \tag{D.2}$$

in which c is the speed of light, ν_0 is the line centre of the transition or 'Doppler free' frequency, and ν is the Doppler shifted frequency which corresponds to a shift of magnitude x.

Equations C.59, C.59 and 9.2 lead to the following expression[259,260] for the lineshape as a function of the velocity projection v_p

$$D(v_p) = \int_{v=|v_p|}^{\infty} \frac{1}{2v} \left[\sum_{L=0}^{4} g_L(v) P_L(\frac{v_p}{v}) \right] dv \tag{D.3}$$

Bipolar Moments	Coefficients			
	$\frac{1}{\sigma}\frac{d\sigma_{00}}{d\omega_t}$	$\frac{1}{\sigma}\frac{d\sigma_{20}}{d\omega_t}$	$\frac{1}{\sigma}\frac{d\sigma_{21-}}{d\omega_t}$	$\frac{1}{\sigma}\frac{d\sigma_{22+}}{d\omega_t}$
$\beta_0^0(0,0)$	1	0	0	0
$\beta_0^2(2,0)$	$C_{20}(\theta_v^i,0)$	0	0	0
$\beta_0^2(0,2)$	0	$d^2_{0\,0}(\theta_k)$	$\cos\phi_t d^2_{1\,0}(\theta_k)$	$\cos 2\phi_t d^2_{2\,0}(\theta_k)$
$\beta_0^0(2,2)$	0	$\sum_{q\geq 0} C_{2q}(\theta_v^i,0)\cos q\phi_v \times \frac{2\,d^2_{0\,q}(\theta_k)}{1+\delta_{q\,0}}$	$\sum_{q\geq 0} C_{2q}(\theta_v^i,0) \times \frac{1}{1+\delta_{q\,0}}[d^2_{1\,q}(\theta_k)\cos(\phi_t-q\phi_v)- d^2_{-1\,q}(\theta_k)\cos(\phi_t+q\phi_v)]$	$\sum_{q\geq 0} C_{2q}(\theta_v^i,0) \times \frac{1}{1+\delta_{q\,0}}[d^2_{2\,q}(\theta_k)\cos(2\phi_t-q\phi_v)+ d^2_{-2\,q}(\theta_k)\cos(2\phi_t+q\phi_v)]$
$\beta_0^2(2,2)$	0	$\sum_{q\geq 0}\left(\frac{q^2-2}{2}\right)C_{2q}(\theta_v^i,0) \times\cos(q\phi_v)\frac{2\,d^2_{0\,q}(\theta_k)}{1+\delta_{q\,0}}$	$\sum_{q\geq 0}\left(\frac{q^2-2}{2}\right)C_{2q}(\theta_v^i,0) \times\frac{1}{1+\delta_{q\,0}}[d^2_{1\,q}(\theta_k)\cos(\phi_t-q\phi_v)- d^2_{-1\,q}(\theta_k)\cos(\phi_t+q\phi_v)]$	$\sum_{q\geq 0}\left(\frac{q^2-2}{2}\right)C_{2q}(\theta_v^i,0) \times\frac{1}{1+\delta_{q\,0}}(d^2_{2\,q}(\theta_k)\cos(2\phi_t-q\phi_v)+ d^2_{-2\,q}(\theta_k)\cos(2\phi_t+q\phi_v))$
$\beta_0^2(4,2)$	0	$\sum_{q\geq 0}\frac{1}{12}\left[(16-q^2)(9-q^2)\right]^{\frac{1}{2}} \times C_{4q}(\theta_v^i,0) \times\cos(q\phi_v)\frac{2\,d^2_{0\,q}(\theta_k)}{1+\delta_{q\,0}}$	$\sum_{q\geq 0}\frac{1}{12}\left[(16-q^2)(9-q^2)\right]^{\frac{1}{2}} C_{4q}(\theta_v^i,0)\frac{1}{1+\delta_{q\,0}} \times[d^2_{1\,q}(\theta_k)\cos(\phi_t-q\phi_v)- d^2_{-1\,q}(\theta_k)\cos(\phi_t+q\phi_v)]$	$\sum_{q\geq 0}\frac{1}{12}\left[(16-q^2)(9-q^2)\right]^{\frac{1}{2}} C_{4q}(\theta_v^i,0)\frac{1}{1+\delta_{q\,0}} \times[d^2_{2\,q}(\theta_k)\cos(2\phi_t-q\phi_v)+ d^2_{-2\,q}(\theta_k)\cos(2\phi_t+q\phi_v)]$

Table D.1: The relationship between commonly determined 3D v_1 frame bipolar moments and the PDDCS's.

where

$$
\begin{aligned}
g_0(v) &= b_0\overline{\beta_{00}(0,0;v)} + b_1\frac{\beta}{2}\overline{\beta_{20}(0,2;v)} \\
g_2(v) &= b_2\frac{\beta}{2}\overline{\beta_{20}(2,0;v)} + b_3\overline{\beta_{00}(2,2;v)} + b_4\beta 2\overline{\beta_{20}(2,2;v)} \\
g_4(v) &= b_6\frac{\beta}{2}\overline{\beta_{20}(4,2;v)}
\end{aligned}
\tag{D.4}
$$

The b_j coefficients depend on the rotational branch of the transition being probed and also on the relative spatial orientation of the photolysis and probe laser beams and their polarizations. By recording Doppler profiles in several different experimental geometries and taking suitable linear combinations, it is possible to construct 'composite Doppler profiles', which project out the individual bipolar moment terms of Equations D.3 and D.5. It is not possible to completely separate the $\beta_{20}(4,2)$ moment from the lower order moments, and corrections need to be made for this moment when attempting to simulate experimental profiles. Higher moments with k_2 equal to 4 or 6 make a negligible contribution to the Doppler profiles since the b_i coefficients on which they depend have extremely small magnitudes. The g_1 and g_3

terms omitted from Equations D.3 and D.5 contain information on orientation, rather than just alignment, of the product velocity and rotational angular momentum vectors. It is not possible to measure these orientation moments with linearly polarized photolysis, so that for the present experiments the above sum is restricted to moments with even values of k_1.

Initially, the individual experimental profiles recorded at each experimental geometry are normalised to an intensity of unity. Weighted sums of these profiles can then be formed to give the various composite Doppler profiles. The three geometries used are known as 'Case A', 'Case B' and 'Case D' and are shown in Figure 9.2. Either the g_0 or g_2 term can be eliminated as required by summing profiles for Q and P or R branch transitions.[202] This procedure is summarised in Table D.2

Profile	Geometry	Rotational Branch		Resulting Lineshape Function
		Q	P/R	$f = q_2^{(Q)} q_0^{(P/R)} - q_2^{(P/R)} q_0^{(Q)} : \chi = \frac{v_p}{v}$
Ia	$\frac{1}{3}(A+B+D)$	$-q_2^{(P/R)}$	$q_2^{(Q)}$	$f \int \frac{1}{2v} \overline{\beta_{00}(0.0;v)} dv$
Ib	$\frac{1}{3}(A+B+D)$	$-q_0^{(P/R)}$	$q_0^{(Q)}$	$f \int \frac{1}{2v} \overline{\beta_{00}(2,2;v)} P_2(\chi) dv$
IIa	$A-D$	$q_2^{(P/R)}$	$-q_2^{(Q)}$	$\frac{3}{2} f\beta \int \frac{1}{2v} \overline{\beta_{20}(2,0;v)} P_2(\chi) dv$
IIb	$A-D$	$q_0^{(P/R)}$	$-q_0^{(Q)}$	$\frac{3}{5} f\beta \int \frac{1}{2v} \overline{\beta_{20}(0,2;v)} dv$
IIIa	$D-B$	$q_2^{(P/R)}$	$-q_2^{(Q)}$	$-\frac{3}{2} f\beta \int \frac{1}{2v} \overline{\beta_{20}(2,0;v)} P_2(\chi) dv$
IIIb	$D-B$	$q_0^{(P/R)}$	$-q_0^{(Q)}$	$\frac{6}{7} f\beta \int \frac{1}{2v} \overline{\beta_{20}(2,2;v)} P_2(\chi) dv$

Table D.2: Construction of composite Doppler profiles by summing Doppler profiles according to rotational branch and experimental geometry

E. THE SAGA OF THE COPPER LENS

The water cooled copper lens was not part of the original design of the ion source, yet it caused more problems than every other part combined.

Initially the circulating water was direct from the mains water supply. This was found to be unsatisfactory since a constant potential could not be maintained on the lens due to current leakage through the liquid. Christchurch water is apparently a fairly good electrical conductor. To solve this problem chilled nitrogen gas was tried as a coolant, with the result that the lens overheated and zinc from the easiflow weld vaporised and deposited on the inside of the ceramic insulators of the water feedthrough, which seriously compromised their insulating properties Several hours of scrubbing the inside of the feedthroughs with various solvents and eventually concentrated nitric acid failed to remedy the problem and the feedthrough was redesigned to preclude a repeat performance. The next coolant to be used was methanol. An ancient methanol circulator and its refrigeration unit were resurrected from the basement of the chemistry department and installed beneath the scattering chamber of the molecular beam machine. It was quite a challenge to get the ageing pump initially circulating the methanol, generally requiring stringing plastic water lines halfway across the lab from the sink to a small water pump to prime the methanol pump. Once it was started, the pump would sometimes keep going, unless you happened to be in the middle of an important experiment using the ion source, in which case it would suddenly cut out, necessitating immediate switching off of the ion source in order to prevent the copper lens from overheating. The unreliability of the pump on the methanol circulator eventually led to the return of this piece of history to the basement.

It was then decided to try using water again with the now redesigned feedthrough. This seemed to work reasonably well until it was discovered that the excellent conduction properties of the water were causing a partial short circuit between the lens and the tip of the ion source via the water cooling lines on the high current feedthroughs supplying the heating current to the tip. This meant that the voltages on the tip and the first lens could not be varied

independently, which was slightly inconvenient considering extraction of ions from the source depends rather heavily on the potential difference maintained between these two elements.

The solution to this seemed simple; just use a separate reservoir of cooling water for the lens. All that was needed was a pump capable of circulating this coolant. Another senior citizen of pumps was revived from the mechanical workshop for this purpose, cleaned up and connected to the system. The problem of the short circuit was solved, but relief was short lived since it soon became clear that though old, this pump did not lack in enthusiasm, and appeared to have missed its true calling as a fountain. One of its favourite tricks was to wait until there was noone in the room and then blow its outlet line off, directing the flow vertically upwards onto the underside of the molecular beam machine and consequently depositing the contents of the water reservoir all over the floor. As well as this meaning the water was no longer being pumped through the lens, it also meant that the occupants of the lab below started complaining about the frequent rain showers as the water followed the call of gravity and went through the floor. Several attempts at anchoring the outlet line more and more firmly to the pump, using an elaborate system of wires and hose clamps, failed, but it was soon found that running the pump through a step down transformer dropped the pumping speed to a more reasonable level. The only problem with the pump now was that it had the tendency to turn the water brown. Once it had been taken apart for cleaning it was discovered that it was impossible to put it back together again so that it didn't leak, and another pump was placed back into retirement. Obviously a new pump was needed and this led to the purchase of a small submersible pump, which delivered an ideal water flow. There were a few moments of consternation when it was found that there was still current leakage from the lens to ground via the pump, but running the pump through an isolation transformer eliminated this problem. The current leakage problem was solved at last!

However, it was soon replaced by water leakage problems. First the water feedthrough started to leak. Once it was determined that simply placing a beaker underneath it and emptying it at regular intervals was not going to be a satisfactory solution, this was remedied by a generous application of Torr seal and Araldite. Unfortunately this did not turn out to be a permanent solution, and soon feedthrough mark III was designed, constructed and installed. Having eliminated any reasonable chance of a water leak outside the vacuum chamber, the leaks relocated to inside the vacuum system, which was a rather more serious problem. These varied from tiny leaks, which were remedied by simply tightening the pipe fittings inside the

scattering chamber, to major floods which required panic, copious quantities of paper towels, the pulling of diffusion pumps and turbo pumps off the machine to empty litres of water out of the gate valves, and the replacement of five mechanical pumps worth of emulsified pump oil to fix. The lens leaked for the last time when the Teflon ferrules, which formed part of the seal to the flexible stainless steel bellows between the feedthrough and the lens inside the vacuum chamber, melted. This effectively destroyed the ends of the bellows, and caused the operator of the ion source to admit defeat completely and give up on the copper lens for good. A quick bit of research into high temperature materials led to the fabrication of a lens from molybdenum, which has a melting point of 2617°C, over 1000 degrees higher than the operating temperature of the ion source. The problems appear to be solved!

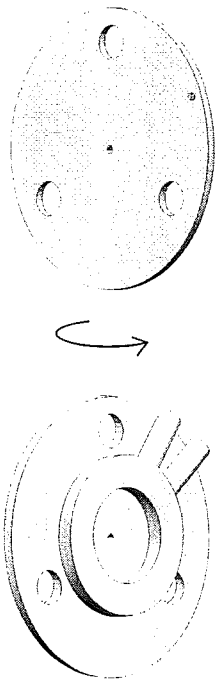

F. COMPUTER PROGRAMS

F.1 Programs used in beam characterisation experiments

F.1.1 beamvel - Beam velocity fitting program

```
c Program to simulate falling edge of signal from a chopped molecular beam
c for use in fitting beam velocity measurements.

      program beamvel

      implicit double precision(a-h,o-z)
      double precision mass, ionvel, ionenergy
      parameter(nout=300,num=1000000)
      dimension time(nout),sig(nout),v(nout),vprob(nout)
      character*20 title1,outfile

c num=number of points to include in Monte Carlo integration.
c nout=number of points to output.

      external ran1

      e=1.602d-19       !electron charge
      Avog=6.022d23     !Avogadro's number
      R=8.314d0         !gas constant
      temp=298.0d0      !beam stagnation temperature
      iseed=-27         !seed for random number generator
      spread=200.0d0    !velocity range
      quadlength = 0.4087d0  !length of quadrupole

      open(unit=2,file='beamvel.inp',status='old')

c  Set mexpt to 1 if you want to normalise data to an experimental
c  curve.  Make sure the experimental data set is in the same directory!

      read(2,*) mexpt
        if (mexpt.eq.1) then
          anorm=0.0d0
          read(2,*) title1
          open(unit=4,file=title1,status='old')
            do i=1,50
              read(4,*) dum1,dum2,value
              anorm=anorm+value/50.0d0
            enddo
          close(4)
        endif
      read(2,*) outfile

c title1 is a data file containing the mass spec signal as a function of
c time.  Used to normalise the simulation to experimental data for fitting.

      read(2,*) dist       !Distance from chopper to mass spec ion source
      read(2,*) mass       !mass of beam molecule
      read(2,*) ionenergy  !ion energy setting on mass spec
      read(2,*) tparr      !parallel translational temperature / K
      read(2,*) tmin,tmax  !time range to calculate for / s

      close(2)

c  Working out flow velocity of beam.

      gamma=5.0d0/3.0d0
      gammafac=gamma/(gamma-1.0d0)
      mass=mass/1000.0d0
      flowvel=dsqrt(2.0d0*R*temp*gammafac/mass)
      tofav=1.0d6*dist/flowvel

      sumnorm=0.0d0

      do i=1,num

c  Picking a random velocity in the range (flowvel-spread) to
c  (flowvel+spread) and calculating flight time from chopper to detector
c  (in s).

        vel=2.0d0*spread*ran1(iseed)-spread+flowvel
        tof=(dist/vel)*1.0d6
```

```
c  Add correction factor for time of flight through quadrupole.

        ionvel = dsqrt(2.0d0*e*ionenergy*Avog/mass)
        corr = quadlength*1.0d6/ionvel
        tof = tof + corr

c  Calculate weighting factor for tof from velocity distribution and
c  calculate normalization factor for distribution.

        argum=-mass*(vel-flowvel)**2/(2.0d0*R*tparr)
        tofweight=(vel**2)*dexp(argum)
        sumnorm=sumnorm+tofweight

c  velocity distribution for output

        dblek=(vel-flowvel+spread)*nout/(2.0d0*spread)
        k=int(dblek)
        vprob(k)=vprob(k)+tofweight

c  Pick a random time in the interval tmin to tmax and bin for output.
        t=(tmax-tmin)*ran1(iseed)+tmin
        dblen=nout*(t-tmin)/(tmax-tmin)
        n=dint(dblen)

        if(t.lt.tof) then      !signal measured at the detector is equal
           plot=1.0d0          !to 1 if t < tof and 0 if t > tof.
        else
           plot=0.0d0
        endif

        sig(n)=sig(n)+tofweight*plot

      enddo

      open(unit=8,file=outfile,status='unknown')
      write(8,*) "    ","v / ms-1","           ","Prob","            ",
     1  "time / s","         ","Signal"

c  Normalising for velocity distribution

      do n=1,nout-1
        v(n)=flowvel-spread+dble(n)*2.0d0*spread/dble(nout)
        vprob(n)=vprob(n)/sumnorm
        time(n)=dble(n)*(tmax-tmin)/dble(nout)+tmin
        sig(n)=sig(n)/sumnorm
        if (mexpt.ne.1) then
          write(8,180) v(n),vprob(n),time(n),sig(n)
        endif
      enddo

c  Normalising to experimental signal amplitude if required.

      if (mexpt.eq.1) then
        enorm=0.0d0
        do i=1,50
          enorm=enorm+sig(i)/50.0d0
        enddo

        do n=1,nout-1
          sig(n)=sig(n)*anorm/enorm
          write(8,180) v(n),vprob(n),time(n),sig(n)
        enddo
      endif

 180  format(4(1pe15.7,2x))
      close(4)

      end

c ----------------------------------------
      double precision function ran1(idum)
c ----------------------------------------
c  Random number generator

      implicit double precision (a-h,o-z)
      integer idum,ia,im,iq,ir,ntab,ndiv
      parameter (ia=16807,im=2147483647,iq=127773,ir=2836,
     *ntab=32,ndiv=1+(im-1)/ntab)
      parameter (am=1.0d0/dble(im),eps=1.2d-7,rnmx=1.0d0-eps)
      integer j,k,iv(ntab),iy
      save iv,iy
      data iv /ntab*0/, iy /0/

      if ((idum.le.0) .or. (iy.eq.0)) then
         idum = max0(-idum,1)
         do 11 j=ntab+8,1,-1
            k = idum/iq
            idum = ia*(idum-k*iq)-ir*k
            if (idum .lt. 0) idum = idum+im
            if (j .le. ntab) iv(j) = idum
 11      continue
```

```
        iy=iv(i)
      endif
      k = idum/iq
      idum = ia*(idum-k*iq)-ir*k
      if (idum .lt. 0) idum = idum+im
      j = 1+iy/ndiv
      iy = iv(j)
      iv(j) = idum
      ran1 = dmin1(am*dble(iy),rnmx)

      return
      end
```

F.1.2 enhance - Monte Carlo simulation of hexapole enhancements

```
      program enhance

c  Calculates the composition of the molecular beam at various points
c  along the trajectory (end of A, C and B fields and detector) with the
c  C field on or off.  Also outputs hexapole enhancements for the two cases.
c  NB: 1. Check that the variable vspread defined near the
c  beginning of the program is large enough to include the entire velocity
c  distribution.  Trajectories are picked with velocities from
c  vflow-vspread to vflow+vspread
c      2. Long output (mode 0) outputs everything, short output (mode 1) is
c  limited to hexapole enhancements for each state.

      implicit double precision (a-h,o-z)
      character*20 outfile
      external velpick
      double precision counts(0:1),totcounts(0:1,0:1),spin(8),
     >                 spinweight(8)
      double precision fJK(20,-20:20)
      double precision kB,kTrot

      common /dim/ dbmstop,rbmstop,dnozskim,hexrad,rskim,exitap
      common /fields/ dABfield,dCfield
      common /detect/ dhexms,rdetect
      common /velocity/ vflow
      common/omegafac/factor
      common/countup/nup,nupA,nupB,nupC,nupdet
      common/countlow/nlow,nlowA,nlowB,nlowC,nlowdet
      common/countzero/nzero,nzeroA,nzeroB,nzeroC,nzerodet
      common/countall/ncount,ncountA,ncountB,ncountC

      data rg/8.314d0/                !gas constant
      data avogadro/6.02214d23/       !Avogadro's number
      kB = 1.3806d-23                 !Boltzmann's constant
      h=6.626d-34                     !Planck's constant
      c=2.998d10                      !speed of light in cm/s
      data pi/3.14159265d0/           !pi
      data convert/3.3356d-30/        !converts Debyes to Cm
      vspread=350.0d0                 !spread of molecular velocities

      dnozskim = 0.110d0        !nozzle-skimmer distance
      rskim = 0.75d-3           !radius of skimmer orifice
      dbmstop = 0.535d0         !distance from beginning of hexapole to beamstop
      hexrad = 4.74d-3          !hexapole inscribed radius
      dhexms = 0.265d0          !distance from end of hexapole to mass spec
      rdetect = 3.0d-3          !radius of mass spec entrance aperture
      dABfield = 0.53d0         !length of A and B fields
      dCfield = 0.15d0          !length of C field

c  Input data

      open(unit=5, file='enhance.inp', status='old')
      read(5,*) jmax              !maximum J value
      read(5,*) outfile           !output filename
      read(5,*) mode              !long(0) or short(1) output.
      read(5,*) smass             !mass of seed gas (g/mol)
      read(5, *) cmass            !mass of carrier gas (g/mol)
      read(5,*) seedfrac          !fraction of seed
      if(seedfrac.gt.1.0d0) then
        write(*,*) 'seed fraction input error'
        goto 1000
      endif
      read(5,*) tsource           !stagnation temperature (~298K)
      read(5,*) Tpar              !beam parallel translational T (K)
      read(5,*) gammaseed         !Gamma = Cp/Cv for seed and carrier gases
      read(5,*) gammacarr
      read(5,*) dipole            !dipole moment (Debyes)
      dipole=convert*dipole
      read(5,*) A,B               !rotational constants
      A=h*c*A
      B=h*c*B
      read(5,*) Trot              !rotational temperature
      kTrot=kB*Trot
        read(5,*) spinx,spiny     !spin quantum numbers for nuclei X and Y in CX3Y
      read(5,*) exitap            !radius of hexapole exit aperture (m)
```

```
      read(5,*) rbmstop           !radius of beamstop
      read(5,*) hexvolts          !hexapole voltage
      read(5,*) ntraj             !number of trajectories

      close(5)

      open(unit=7, file=outfile, status='unknown')
      write(7,*) 'ntraj= ',ntraj
      write(7,'(a20,f10.0,a2)') 'hexapole voltage = ',hexvolts, ' V'

      alphmin=rbmstop/(dnozskim+dbmstop)  !minimum and maximum angles for trajectories defined
      alphmax=datan(rskim/dnozskim)       !by beam stop and second skimmer aperture size.

c  Calculating beam velocity using equation for isenthalpic expansion of
c  a supersonic beam

      smass=smass/1000.0d0                              !convert masses to kg/mol
      cmass=cmass/1000.0d0
      avmass=seedfrac*smass+(1.0d0-seedfrac)*cmass      !average mass of beam molecules
      gamma=seedfrac*gammaseed+(1.0d0-seedfrac)*gammacarr !average gamma
      gammafac=gamma/(gamma-1.0d0)
      vflow=sqrt(2.0d0*rg*gammafac*tsource/avmass)      !most probable velocity

c  Experimentally measured flow velocity for neat CH3F.  Comment out this
c  line to use a calculated value or change for a different gas.
c      vflow=690.0d0

      write(7,'(a40,f6.2)') "Average mass of beam gases (g/mol)",
     >                      avmass*1000.0d0
      write(7,'(a40,f6.2)') "Average gamma", gamma
      write(7,'(a40,f6.2)') "Most probable velocity (m/s)", vflow

c  Statistical weighting factors for JKM states
c  NB: For a molecule CX3Y with X and Y both having spin there are 8
c  possible spin combinations (some will be the same if X and Y have the
c  same spin).  These are: 3x+y, 3x-y, -3x+y, -3x-y (each with weight of 1)
c  and x+y, x-y, -x+y, -x-y (each with a weight of 3).  The following
c  calculation finds the average fJK over all these possibilities.

      spin(1)=3.0d0*spinx+spiny       !calculating the possible spin
      spin(2)=3.0d0*spinx-spiny       !combinations.
      spin(3)=-3.0d0*spinx+spiny
      spin(4)=-3.0d0*spinx-spiny
      spin(5)=spinx+spiny
      spin(6)=spinx-spiny
      spin(7)=-spinx+spiny
      spin(8)=-spinx-spiny

      do i=1,8                        !weighting factor for each spin combination
        if(i.le.4) then
           spinweight(i) = 1.0d0/16.0d0
        else
           spinweight(i)=3.0d0/16.0d0
        endif
      enddo

      q=0.0d0                         !calculation of partition function
      do j=1,50
        do 5 k=-j,j
          Ezero=B*dble(j*(j+1))+(A-B)*dble(k**2)
          expfac=dexp(-Ezero/kTrot)
          do ispin=1,8
            if(k.eq.0) then
              SIK=4.0d0*spin(ispin)*(spin(ispin)+1.0d0)+3.0d0
            else if (3*(k/3).eq.k) then
              SIK=2.0d0*(4.0d0*spin(ispin)**2+4.0d0*
     >             spin(ispin)+3.0d0)
            else
              SIK=8.0d0*spin(ispin)*(spin(ispin)+1.0d0)
            endif
            q=q+spinweight(ispin)*SIK*(2.0d0*j+1.0d0)*expfac
          enddo
 5      continue
      enddo

      do j=1,jmax                                   !calculation of matrix of
        do 6 k=-j,j                                 !statistical weighting
          Ezero=B*dble(j*(j+1))+(A-B)*dble(k**2)    !factors for the rotational
          expfac=dexp(-Ezero/kTrot)                 !states
          do ispin=1,8
            if(k.eq.0) then
              SIK=4.0d0*spin(ispin)*(spin(ispin)+1.0d0)+3.0d0
            else if (3*k/3.eq.k) then
              SIK=2.0d0*(4.0d0*spin(ispin)**2+4.0d0*
     >             spin(ispin)+3.0d0)
            else
              SIK=8.0d0*spin(ispin)*(spin(ispin)+1.0d0)
            endif
            fJK(j,k)=spinweight(ispin)*SIK*expfac/q

          enddo
          write(16,'(2i3,f10.5)') j,k,fJK(j,k)
```

```
6      continue
      enddo

      do 10 j=1,jmax
        do 20 k=-j,j,1
          do 30 m=-abs(k),abs(k),1

         write(7,*) ' '
         write(7,*) 'Rotational state = |',j,k,m,'>'

      do 100 ncfield=0,1        !LOOP OVER C FIELD ON OR OFF
        do 150 ihex=0,1         !LOOP OVER HEXAPOLE ON OR OFF

          if (ihex.eq.1) then  !hexapole voltage
             hexv=hexvolts
          else
             hexv=0.0d0
          endif

          iseed=13              !seed for random number generator

            ncount=0            !zeroing counters for successful trajectories
            ncountA=0           !at each point along track
            ncountB=0
            ncountC=0

            nup=0               !zeroing counters for beam composition at
            nupA=0              !each point along trajectory
            nupC=0
            nupB=0
            nupdet=0
            nlow=0
            nlowA=0
            nlowC=0
            nlowB=0
            nlowdet=0
            nzero=0
            nzeroA=0
            nzeroC=0
            nzeroB=0
            nzerodet=0

            counts(ihex)=0.0d0

          do 200 nt=1,ntraj         !LOOP OVER TRAJECTORIES

          jstate=j                  !JKM state and omega
          kstate=k
          if(ihex.eq.1) then
            mstate=m
            rho = dble(mstate*kstate)/dble(jstate*(jstate+1))
            factor=6.0d0*dipole*hexv/((smass/avogadro)*hexrad**3)
            omega=sqrt(dabs(factor*rho))
          else
            mstate=0
          endif


          vel=vflow+(vflow+spread)*ran2(iseed)-2.0d0*vspread     !sample and weight beam
          arg=mass*(vel-vflow)**2/(2.0d0*kB*Tpar)                !velocity
          velweight=(vel**2)*dexp(-arg)

          alpha=alphmax*ran2(iseed)-alphmin      !sample alpha (nozzle exit angle)

c  Trajectory calculation

             call traject(vel,alpha,omega,iseed,ncfield,ihex,
     >          jstate,kstate,mstate,iflag)

             if(iflag.eq.1) then                        !calculate weighted sum of
                counts(ihex)=counts(ihex)+velweight     !trajectories for hexapole
             endif                                      !enhancement

 200       continue

c  Calculating percentage of beam in each state at end of A, C and B fields
c  and at detector.

           if(mode.eq.0) then
             write(7,*) ' '
             if (ncfield.eq.1) then
               write(7,*) '###  BEAM COMPOSITION - C field on  ###'
             else
               write(7,*) '###  BEAM COMPOSITION - C field off  ###'
             endif
             if (ihex.eq.0) then
               write(7,*) 'Hexapole off'
             else
               write(7,*) 'Hexapole voltage ',hexv,'V'
             endif
             write(7,*) ' '
             write(7,'(a15,4a10)') ' ','Upper', 'Lower', 'M=0',
```

```
     >         'traj %'

               fupA=100.0d0*dble(nupA)/dble(ncountA)          !end of first hexapole
               flowA=100.0d0*dble(nlowA)/dble(ncountA)
               fzeroA=100.0d0*dble(nzeroA)/dble(ncountA)
               write(7,'(a15,4f10.2)') 'A field',fupA,flowA,fzeroA,
     >           100.0d0*dble(ncountA)/dble(ntraj)

               if (ncountC.eq.0) then                         !end of C field
                  fupC=0.0d0
                  flowC=0.0d0
                  fzeroC=0.0d0
               else
                 fupC=100.0d0*dble(nupC)/dble(ncountC)
                 flowC=100.0d0*dble(nlowC)/dble(ncountC)
                 fzeroC=100.0d0*dble(nzeroC)/dble(ncountC)
               endif
               write(7,'(a15,4f10.2)') 'C field',fupC,flowC,fzeroC,
     >           100.0d0*dble(ncountC)/dble(ntraj)

               if(ncountB.eq.0) then                          !end of second hexapole
                 fupB=0.0d0
                 flowB=0.0d0
                 fzeroB=0.0d0
               else
                 fupB=100.0d0*dble(nupB)/dble(ncountB)
                 flowB=100.0d0*dble(nlowB)/dble(ncountB)
                 fzeroB=100.0d0*dble(nzeroB)/dble(ncountB)
               endif
               write(7,'(a15,4f10.2)') 'B field',fupB,flowB,fzeroB,
     >           100.0d0*dble(ncountB)/dble(ntraj)

               if(ncount.eq.0) then                           !detector
                 fupdet=0.0d0
                 flowdet=0.0d0
                 fzerodet=0.0d0
               else
                 fupdet=100.0d0*dble(nupdet)/dble(ncount)
                 flowdet=100.0d0*dble(nlowdet)/dble(ncount)
                 fzerodet=100.0d0*dble(nzerodet)/dble(ncount)
                 endif
                 write(7,'(a15,4f10.2)') 'Detector',fupdet,flowdet,
     >    fzerodet,100.0d0*dble(ncount)/dble(ntraj)

c  % of total trajectories reaching detector in each state
                 fup=100.0d0*dble(nupdet)/dble(ntraj)
                 flow=100.0d0*dble(nlowdet)/dble(ntraj)
                fzero=100.0d0*dble(nzerodet)/dble(ntraj)
                write(7,'(a15,3f10.2)') 'total percent',fup,flow,fzero

              if(mode.eq.0) write(7,*) ' '
            endif

 150     continue

         enhancement=counts(1)/counts(0)     !HEXAPOLE ENHANCEMENT

         if(ncfield.eq.1) then
            write(7,'(a35,f5.2)') 'hexapole enhancement (C field on)',
     >          enhancement
         else
            write(7,'(a35,f5.2)') 'hexapole enhancement (C field off)',
     >          enhancement
         endif

         totcounts(ncfield,1)=totcounts(ncfield,1)+fJK(j,k)*counts(1)
         totcounts(ncfield,0)=totcounts(ncfield,0)+fJK(j,k)*counts(0)

 100   continue
 30    continue
 20    continue
 10    continue

         totEnon=totcounts(1,1)/totcounts(1,0)      !AVERAGE HEXAPOLE ENHANCEMENT
         totEnoff=totcounts(0,1)/totcounts(0,0)

          write(7,*) ' '
          write(7,*) '*** AVERAGE HEXAPOLE ENHANCEMENT ***'
          write(7,'(a16,f8.3)') '   C field on', totEnon
          write(7,'(a16,f8.3)') '   C field off', totEnoff

c  Outputting
          write(7,*) ' '
          write(7,*) 'total unscaled signal hexapole on'
          write(7,'(a16,e15.3)') 'C field on', totcounts(1,1)/1.0d6
          write(7,'(a16,e15.3)') 'C field off', totcounts(0,1)/1.0d6

       close(7)
 1000  end
```

```
c-----------------------------------------------
      double precision function ran2(iseed)
c-----------------------------------------------
c  Long period (>2.0d18) random number generator of L'Ecuyer with
c  Bays-Durham shuffle and added safeguards.  Returns a uniform
c  random deviate between 0.0 and 1.0 (exclusive of the endpoints).  Call
c  with iseed a negative integer to initialize.  Do not alter iseed
c  between successive deviates in a sequence.  RNMX should approximate the
c  largest floating value that is <1.

      implicit double precision (a-h,o-z)

      parameter(im1=2147483563,im2=2147483399,imm1=im1-1,ia1=40014,
     1          ia2=40692,iq1=53668,iq2=52774,ir1=12211,ir2=3791,
     2          ntab=32,ndiv=1+imm1/ntab)
      parameter(am=dble(1.0d0/im1),eps=1.2d-7,rnmx=1.0d0-eps)
      dimension iv(ntab)
      save iv,iy,idum2
      data idum2/123456789/,iv/ntab*0/,iy/0/

c  Initialize (ensure iseed.ne.0)

      if (iseed.le.0) then
        iseed=max(-iseed,1)
        idum2=iseed
        do 11 jj=ntab+8,1,-1
          kk=iseed/iq1
          iseed=ia1*(iseed-kk*iq1)-kk*ir1
          if (iseed.lt.0) iseed=iseed+im1
          if (jj.le.ntab) iv(jj)=iseed
 11     continue
        iy=iv(1)
      endif

      kk=iseed/iq1
      iseed=ia1*(iseed-k*iq1)-kk*ir1
      if (iseed.lt.0) iseed=iseed+im1
      kk=idum2/iq2
      idum2=ia2*(idum2-k*iq2)-kk*ir2
      if(idum2.lt.0) idum2=idum2+im2
      jj=1+iy/ndiv
      iy=iv(jj)-idum2
      iv(jj)=iseed
      if (iy.lt.1) iy=iy+imm1
      ran2=min(am*iy,rnmx)
      return
      end

c-------------------------------------------------------------
      subroutine traject(vel,alpha,omega,iseed,icfield,ihexap,
     >          jj,kk,mm,iflag)
c-------------------------------------------------------------
c  Flies molecules through the hexapole and C field regions.  Determines
c  the Stark state composition of the beam at the end of the A, C and B
c  field regions and at the detector.

      implicit double precision (a-h,o-z)
      common/dim/dbmstop,rbmstop,dnozskim,hexrad,rskim,exitap
      common/omegafac/factor
      common/fields/dABfield,dCfield
      common/detect/dhexms,rdetect
      common/countup/nup,nupA,nupB,nupC,nupdet
      common/countlow/nlow,nlowA,nlowB,nlowC,nlowdet
      common/countzero/nzero,nzeroA,nzeroB,nzeroC,nzerodet
      common/countall/ncount,ncountA,ncountB,ncountC

      iflag=0

c  Radial distance and radial velocity on entering hexapole.

      rin=dnozskim*dtan(alpha)    !radial distance and radial velocity on
      rdotin=vel*sin(alpha)       !entering hexapole

      thex1=dABfield/vel          !omega*t for flight through first hexapole
      beta3=omega*thex1

      if (mm*kk.eq.0) then
        rAC = rin + rdotin*(dABfield/vel)      !radial distance and velocity at end
        rdotAC = rdotin                        !of A field
      else if (mm*kk.lt.0) then
        rAC = rin*dcos(beta3) + (rdotin/omega)*dsin(beta3)
        rdotAC = -rin*omega*dsin(beta3) + rdotin*cos(beta3)
      else
        rAC = 0.5d0*(rin+rdotin/omega)*dexp(beta3)+
     1        0.5d0*(rin-rdotin/omega)*dexp(-beta3)
        rdotAC = 0.5d0*(rin*omega+rdotin)*dexp(beta3)-
     1        0.5d0*(rin*omega-rdotin)*dexp(-beta3)
       endif

       if (rAC.lt.hexrad) then      !Determine number of upper Stark states, lower Stark
          ncountA=ncountA+1         !states and KM=0 states making it through first hexapole
          if (mm*kk.gt.0) then
```

```
            nlowA=nlowA+1
         else if (mm*kk.lt.0) then
             nupA=nupA+1
         else
             nzeroA=nzeroA+1
         endif
      else
         return
      endif

      if (icfield.eq.1) then       !C field on or off?  If on molecule stays in
         goto 15                   !same state; if off it scrambles.
      else
         if (ihexap.eq.0) goto 15
         test=ran2(iseed)
         mdegen=2*abs(kk)+1
         frac=1.0d0/dble(mdegen)
         mtest=int(test/frac)+1
         mm=mtest-(abs(kk)+1)
         rho = dble(mm*kk)/dble(jj*(jj+1))
         omega=sqrt(dabs(factor*rho))
         beta3=omega*thex1
      endif

15    rCB = rAC + rdotAC*(dCfield/vel)     !radial distance and velocity at end of
      rdotCB = rdotAC                      !C field (constant radial velocity)

      if (rCB.lt.hexrad) then              !Counting states entering B field
         ncountC=ncountC+1
         if (mm*kk.gt.0) then
            nlowC=nlowC+1
         else if (mm*kk.lt.0) then
             nupC=nupC+1
         else
             nzeroC=nzeroC+1
         endif
      else
         return
      endif

      if (mm*kk.lt.0) then                 !radial distance and velocity at end of B field
        rout = rCB*dcos(beta3) + (rdotCB/omega)*dsin(beta3)
        rdotout = -rCB*omega*dsin(beta3) + rdotCB*cos(beta3)
      else if (mm*kk.eq.0) then
        rout = rCB - rdotCB*(dABfield/vel)
        rdotout = rCBdot
      else
        rout = 0.5d0*(rCB+rdotCB/omega)*dexp(beta3)+
     >        0.5d0*(rCB-rdotCB/omega)*dexp(-beta3)
        rdotout = 0.5d0*(rCB*omega+rdotCB)*dexp(beta3)-
     >        0.5d0*(rCB*omega-rdotCB)*dexp(-beta3)
      endif

      if (dabs(rout).le.exitap) then       !count trajectories getting through exit aperture
         ncountB=ncountB+1
         if (mm*kk.gt.0) then
            nlowB=nlowB+1
         else if (mm*kk.lt.0) then
             nupB=nupB+1
         else
             nzeroB=nzeroB+1
         endif
      else
         return
      endif

      rend = rout + rdotout*(dhexms/vel)   !radial distance at detector

      if (dabs(rend).lt.rdetect) then      !see if trajectory is detected
         ncount=ncount+1
         iflag=1
         if (mm*kk.gt.0) then
            nlowdet=nlowdet+1
         else if (mm*kk.lt.0) then
             nupdet=nupdet+1
         else
             nzerodet=nzerodet+1
         endif
      else
         return
      endif

      return
      end
```

F.2 Analysis software for ion imaging experiments

These programs are described in Chapter 10

F.2.1 imagebas - Basis function program

```
      program imagebas

c  Program to make a set of basis functions in Legendre polynomials for
c fitting ion images.  Each basis function is the image which would be
c obtained with a differential cross section and P(fT) distribution set to a
c Legendre polynomial.

c  m1 is the molecular reagant and m2 is the ionic reagent.  m1p is the
c  detected ion and m2p is the partner product.

c  The single parameter mpt governs the convergence of the simulation and
c  corresponds to the number of ions in the image.  Check that increasing
c  mpt doesn't change the simulation.

c  The lab frame is defined with the x axis along the molecular beam and the
c  y axis along the ion beam.  The z axis is up to the detector.  The CM
c  frame has the X axis along the reagent relative velocity vector, the Z
c  axis up to the detector and the Y axis lying in the lab frame xy plane.

      implicit double precision (a-h,o-z)
      double precision m1,m2,m1p,m2p,jac
      character*30 title1
      parameter(nxpix=10,nypix=10)
      parameter(net=1,nplcm=4,nplq=4)

c   nxpix and nypix = number of pixels in image in x and y dimensions.
c        NB: The program assumes that the MCP image fits into the CCD and
c            touches the edges.
c   net, nplcm, nplq are the number of Legendre moments in energy, coscm
c     and fT

      dimension aimage(net,nplq,nplcm,
     i             -(nxpix/2):(nxpix/2),-(nypix/2):(nypix/2))
      dimension weight(net,nplq,nplcm)
      dimension v1(3),v2(3),x1(50),x2(50)
      common /dat/ e0
      external pft,cmang,sigma,ran2

c  READING INPUT

      open(unit=5,file='imagebas.inp',status='old')

      read(5,*) title1   ! basis set output file

      open(unit=10,file=title1,status='unknown')
      open(unit=12,file='imagebas.out',status='unknown')

      data conv/1.0364132d-08/  !converts (m/s)**2 to eV
      data rg/8.31451d0/        !gas constant
      data rmcp/0.02d0/         !radius of MCP (2cm)
      pi = dacos(-1.0d0)

      read(5,*) mpt                    !number of points in simulation
      read(5,*) m1,m2,m1p,m2p          !masses of reactants and products (g/mol)
       if ((m1+m2).ne.(m1p+m2p)) then
          write(*,*) 'Check masses'
       endif
      read(5,*) qmax     !Reaction exoergicity
                         !qmax=Eint(reactants)-deltaH(T=0)-Eint(products)
      read(5,*) tof      !Flight time from reaction to hitting MCP.
      read(5,*) e0       !Excitation function threshold

      close(5)

c  Writing input data

      write(12,10000) nxpix,nypix,mpt
      write(12,11000) m1,m2,m1p,m2p

c  INPUT FINISHED

c  Mass relations.  NB These are only correct for the case where only two
c  products are formed.  Otherwise need to change rmp and epc.

      rm = m1*m2/(m1+m2)
      rmp = m1p*m2p/(m1p+m2p)
      uc = rm*conv/2.0d0
      epc = 5.0d-01*m1p*(m1p+m2p)*conv/m2p

c  Initializing parameters for calculating relative mean velocity,mean
c  squared velocity, average kinetic energy, and standard deviation of
c  collision energy.
```

```
      vrmin = 1.0d6
      vrmax = 0.0d0

c  Initializing sums over velocities
      sumnorm=0.0d0
      sumvr = 0.0d0
      sumvrsq = 0.0d0
      sumcm = 0.0d0
      ndiscard = 0

      iseed=-13     !seed for random number generator


c  LOOPING OVER MPT (number of integration steps)

      do 130 n=1,mpt

       call v1pick(iseed,v1)                    !molecular reagent velocity
       v1mag=dsqrt(v1(1)**2+v1(2)**2+v1(3)**2)

       call v2pick(iseed,v2)                    !ionic reagent velocity
       v2mag=dsqrt(v2(1)**2+v2(2)**2+v2(3)**2)

      phit=2.0d0*pi*ran2(iseed)                 !setting up fT, coscm
      coscm=2.0d0*ran2(iseed)-1.0d0             !and phi values for Monte
      ft=ran2(iseed)                            !Carlo integration

      vxr = v1(1)-v2(1)                         !calculating relative
      vyr = v1(2)-v2(2)                         !velocity
      vzr = v1(3)-v2(3)
      vr = dsqrt(vxr*vxr+vyr*vyr+vzr*vzr)
      if (vr .gt. vrmax) vrmax=vr
      if (vr .lt. vrmin) vrmin=vr

      vxcm = (m1*v1(1)+m2*v2(1))/(m1+m2)   !Velocity of CM (in lab frame).
      vycm = (m1*v1(2)+m2*v2(2))/(m1+m2)   !This is the vector connecting
      vzcm = (m1*v1(3)+m2*v2(3))/(m1+m2)   !the origins of CM and lab frames.
      vcm = dsqrt(vxcm**2+vycm**2+vzcm**2)

      sumnorm=sumnorm+v1mag*v2mag          !Integrals to get average properties
      sumvrsq = sumvrsq+vr*vr*v1mag*v2mag  !(calculated after mpt loop)
      sumvr = sumvr+vr*v1mag*v2mag
      sumcm = sumcm+vcm*v1mag*v2mag

      theta=dacos(coscm)
      sincm = dsin(dacos(coscm))
      cosphit=dcos(phit)
      sinphit=dsin(phit)

      e=uc*vr*vr                    !Collision energy

      epmx = ft*(e+qmax)            !E release into translation
      if (epmx.lt.0.0d0) then
        write(*,*) 'Discarding trajectory - negative energy'
        goto 130
      endif

      wp = dsqrt(epmx/epc)          !mlp product velocity in CM frame

      wxcm = wp*coscm             !x,y,z components of CM frame product
      wycm = wp*sincm*cosphit     !velocity (x along initial relative velocity
      wzcm = wp*sincm*sinphit     !vector, z up to detector)

      rxcm = wxcm*tof   !Convert velocities to radial displacements by
      rycm = wycm*tof   !multiplying by flight time.  tof includes time
      rzcm = wzcm*tof   !delay between ion formation and switching on
      rcm = wp*tof      !extraction plates and time to reach detector after
                        !switching.

      fracx=rxcm/rmcp   !Determine which pixel this corresponds to.  This
      fracy=rycm/rmcp   !automatically integrates over z direction.
      nx=nint(fracx*dble(nxpix/2))
      ny=nint(fracy*dble(nypix/2))

      if(abs(nx).gt.(nxpix/2).or.abs(ny).gt.(nypix/2)) then
         ndiscard = ndiscard+1
c         write(*,'(a21,i5,a26)') 'Discarding trajectory',n,
c     &' - product ion missing MCP'
         goto 130
      endif

     do ne=1,net           !Weight the pixel according to the DCS and
       sig=sigma(ne,e)     !P(fT) distribution.
       do nf=1,nplq
         pxt=pft(nf,ft)
         do nc=1,nplcm
           dcs=cmang(nc,coscm)
           weight(ne,nf,nc)=sig*pxt*dcs*(1.0d0/2.0d0*pi)
           aimage(ne,nf,nc,nx,ny)=aimage(ne,nf,nc,nx,ny) +
     1             weight(ne,nf,nc)
       enddo
      enddo
```

```
      enddo

 130  continue

c  Calculating average properties:
      vravr = sumvr/sumnorm    !relative mean velocity
      vcmavr = sumcm/sumnorm   !average CM velocity
      vr2av = sumvrsq/sumnorm !mean squared velocity
      vrms = dsqrt(vr2av)      !root mean squared velocity
      ea = uc*vr2av            !average kinetic energy

      emin = uc*(vrmin**2)     !min and max collision energies
      emax = uc*(vrmax**2)

      write(12,15000) vravr,vr2av,vrms,vcmavr,ea
      write(12,15500) emin
      write(12,15600) emax
      write(*,*) 'Number of discarded trajectories =',ndiscard
      percent=100.0d0*(dble(ndiscard)/dble(mpt))
      write(*,'(a12,f8.2)') 'Percentage =',percent
      write(12,'(a38,f3.2)') 'Percentage of trajectories discarded ='
     &,percent

      delta=(rmcp/dble(nxpix))**2     !Normalising image intensity
      do ne=1,net                  ,   !(delta is the pixel area)
        do nf=1,nplq
          do nc=1,nplcm
            do nx=-nxpix/2,nxpix/2
              do ny=-nypix/2,nypix/2
c               sumimage = sumimage+aimage(ne,nf,nc,nx,ny)*delta
                sumimage = sumimage+aimage(ne,nf,nc,nx,ny)
              enddo
            enddo
          enddo
        enddo
      enddo

      write(*,*) 'sumnorm',sumnorm
      write(*,*) 'sumimage',sumimage

      do 194 ne=1,net
        do 193 nf=1,nplq
          do 192 nc=1,nplcm
            do 191 nx=-nxpix/2,nxpix/2
              do 190 ny=-nypix/2,nypix/2
                aimage(ne,nf,nc,nx,ny) = aimage(ne,nf,nc,nx,ny)/sumimage
 190          continue
 191          continue
 192        continue
 193      continue
 194  continue

c Output basis functions

      do ne=1,net
        do nf=1,nplq
          do nc=1,nplcm
            do nx=-nxpix/2,nxpix/2
              do ny=-nypix/2,nypix/2
                write(10,'(2i5,f15.8)') nx,ny,aimage(ne,nf,nc,nx,ny)
              enddo
            enddo
          enddo
        enddo
      enddo


c  FORMATS

10000 format(t10,'Integration parameters',/
     &'nxpix =',i4/,'nypix =',i4/ 'mpt=',i10/)
11000 format(/t10,'Masses of reactants and products',/
     &'m1 =',f5.1,5x,'m2 =',f5.1,5x,'m1p =',f5.1,5x,'m2p =',f5.1/)
15000 format(//5x,'Mean relative velocity (m/s) =',1pe12.5/
     &5x,'Mean square velocity (m**2/s**2) =',1pe12.5/
     &5x,'Root mean square velocity (m/s) =',1pe12.5/
     &5x,'Mean CM velocity (m/s) =',1pe12.5/
     &5x,'Mean collision energy (ev) =',1pe12.5/)
15500 format(/t5,'Emin =',1pe12.5/)
15600 format(/t5,'Emax =',1pe12.5/)

      close(10)

      close(12)

      end

c-------------------------------------------
      double precision function ran2(iseed)
c-------------------------------------------
c  Long period (>2.0d18) random number generator of L'Ecuyer with
c  Bays-Durham shuffle and added safeguards.  Returns a uniform
```

```
c  random deviate between 0.0 and 1.0 (exclusive of the endpoints).  Call
c  with iseed a negative integer to initialize.  Do not alter iseed
c  between successive deviates in a sequence.  RNMX should approximate the
c  largest floating value that is <1.

      implicit double precision (a-h,o-z)

      parameter(im1=2147483563,im2=2147483399,imm1=im1-1,ia1=40014,
     1          ia2=40692,iq1=53668,iq2=52774,ir1=12211,ir2=3791,
     2          ntab=32,ndiv=1+imm1/ntab)
      parameter(am=dble(1.0d0/im1),eps=1.2d-7,rnmx=1.0d0-eps)
      dimension iv(ntab)
      save iv,iy,idum2
      data idum2/123456789/,iv/ntab*0/,iy/0/

c  Initialize (ensure iseed.ne.0)

      if (iseed.le.0) then
        iseed=max(-iseed,1)
        idum2=iseed
        do 11 j=ntab+8,1,-1
          k=iseed/iq1
          iseed=ia1*(iseed-k*iq1)-k*ir1
          if (iseed.lt.0) iseed=iseed+im1
          if (j.le.ntab) iv(j)=iseed
 11     continue
        iy=iv(1)
      endif

      k=iseed/iq1
      iseed=ia1*(iseed-k*iq1)-k*ir1
      if (iseed.lt.0) iseed=iseed+im1
      k=idum2/iq2
      idum2=ia2*(idum2-k*iq2)-k*ir2
      if(idum2.lt.0) idum2=idum2+im2
      j=1+iy/ndiv
      iy=iv(j)-idum2
      iv(j)=iseed
      if (iy.lt.1) iy=iy+imm1
      ran2=min(am*iy,rnmx)
      return
      end

c-------------------------------------------
      subroutine v1pick(iseed,vv1)
c-------------------------------------------
c  Generates molecular velocities.

      implicit double precision (a-h,o-z)
      dimension vv1(3)

      vv1(1)=603.0d0
      vv1(2)=0.0d0
      vv1(3)=0.0d0

      return
      end

c-------------------------------------------
      subroutine v2pick(iseed,vv2)
c-------------------------------------------
c  Generates ion velocities.

      implicit double precision (a-h,o-z)
      dimension vv2(3)

      vv2(1)=0.0d0
      vv2(2)=7424.76d0
      vv2(3)=0.0d0

      return
      end

c -----------------------------------------
      double precision function pl(l,x)
c -----------------------------------------
c  Legendre Polynomials.
      implicit double precision (a-h,o-z)

      if (dabs(x).gt.1.) pause 'bad arguments'
      pmm = 1.0d0
      if (l.eq.0) then
 pl = pmm
      else
 pmmp1 = x*pmm
 if (l.eq.1) then
    pl = pmmp1
 else
    do 12 ll = 2,l
  pll = (x*dble(2*ll-1)*pmmp1-dble(ll-1)*pmm)/dble(ll)
       pmm = pmmp1
       pmmp1 = pll
```

```
12          continue
    pl = pll
 endif
      endif
c
      return
      end

c-------------------------------------------------
      double precision function cmang(nc,coscmn)
c-------------------------------------------------
c    Differential cross section as a sum of Legendre polynomials
      implicit double precision (a-h,o-z)
      external pl

      if (coscmn.lt.-1.0d0) coscmn=-1.0d0
      if (coscmn.gt.1.0d0) coscmn=-1.0d0
      cmang=(2.0d0*dble(nc-1)+1.0d0)*pl(nc-1,coscmn)
c      cmang=pl(nc-1,coscmn)

      return
      end

c-------------------------------------------------
      double precision function pft(nf,ftm)
c-------------------------------------------------
c   P(fT) distribution as a sum of Legendre polynomials
      implicit double precision (a-h,o-z)
      external pl

c  transforming ft to lie in the range -1 to 1

      ftn=2.0d0*ftm-1.0d0
      if (ftn.lt.-1.0d0) ftn = -1.0d0
      if (ftn.gt.1.0d0) ftn = 1.0d0
      pft=(2.0d0*dble(nf-1)+1.0d0)*pl(nf-1,ftn)
c      pft=pl(nf-1,ftn)

      return
      end

c -------------------------------------------------
      double precision function sigma(ne,en)
c -------------------------------------------------
c
c  Excitation function - often set to unity.
c
      implicit double precision (a-h,o-z)
      common /dat/ e0,emax,net
      external pl

      if (en .gt. e0) then
         sigma=1.0d0
      else
        sigma = 0.0d0
      endif

      return
      end
```

F.2.2 *imagefit - non-linear least squares fitting program*

```
      program imagefit

c  Non linear  fitting  program for ion images based on numerical recipes.

      implicit double precision (a-h,o-z)
      double precision max,min
      character*30 title1,title2
      integer ord
      external pl
      external funct

      parameter(npl=2000,nxexpt=10,nyexpt=10,nxpix=10,
     &nypix=10,maa=11,nmmax=28)

c  npl=number of points to use in finding max and min values for a(n)
c  maa = number of fitting parameters
c  nmmax = number of contracted basis functions = (nplcm)(nplq)
c  nxexpt,nyexpt = number of pixels in image in x and y dimensions.
c  nxpix,nypix = number of pixels used to make the basis functions.

      dimension amax(maa),amin(maa),plpt(npl),x(npl)
      dimension xpos(-nxexpt/2:nxexpt/2),ypos(-nyexpt/2:nyexpt/2),
     &z(-nxexpt/2:nxexpt/2,-nyexpt/2:nyexpt/2),a(maa),
     & ia(maa),coa(maa,maa),alpha(maa,maa),gues(maa),dum(maa)
      dimension aimage(nmmax,-nxpix/2:nxpix/2,-nypix/2:nypix/2)
      common/const/pi,sqpi
      common/dat/nplcm,nplq
```

```
      common/data/aimage,mode
      common/data1/nangpl,nftpl,modec
      common/data2/sum,sumacos,sumbft,cmcos,ft
      common/data3/fmax,delft,ftmin,delcm,cosmin
      common/pos/x,dx
      common/vp/vpmin,vpmax
      common/delta/delxexpt,delyexpt,delxbas,delybas

      pi = dacos(-1.0d0)
      sqpi = dsqrt(pi)
      c=2.997925d8
      dmcp=0.04       !diameter of MCP's

c  Reading input parameters

      open(unit=5,file='imagefit.inp',status='old')
      open(unit=9,file='data.out',status='unknown')

      read(5,*) title1  !data file
      read(5,*) title2  !basis functions
      read(5,*) mode    !separable or non separable fitting
      read(5,*) nplcm   !number of Legendre expansion terms for DCS
      read(5,*) nplq    !number of Legendre expansion terms for P(fT)
      read(5,*) fmin,fmax  !min and max fT (usually 0 and 1)
      do 10 i=1,maa
         read(5,*) gues(i) !Initial guesses for fitting coefficients
 10   continue
      close(5)

c  Pixel size in basis functions - used in subroutine funct to interpolate
c  the basis functions to the experimental data.
      delxexpt=dmcp/dble(nxexpt+1)    !Pixel size in basis functions
      delyexpt=dmcp/dble(nyexpt+1)
      delxbas=dmcp/dble(nxpix+1)
      delybas=dmcp/dble(nypix+1)

      if (mode .eq. 1.or.mode.eq.2) then            !Checking parameter
        if (nplcm+nplq .ne. maa) then               !inputs
  write(*,*) 'Check parameter input - maa1'
  goto 999
        endif
if (nmmax .ne. (nplcm)*(nplq)) then
  write(*,*)  'Check parameter input - nmmax'
  goto 999
        endif
      else
        if (nplcm*nplq .ne. maa) then
        write(*,*) 'Check parameter input - maa2'
  goto 999
        endif
        if (nmmax .ne. (nplcm)*(nplq)) then
          write(*,*)  'Check parameter input - nmmax'
          goto 999
        endif
      endif

      modec=mode
      nangpl=nplcm
      nftpl=nplq

      open(unit=5,file=title2,status='old')    !Reading in basis functions
      do 20 nm=1,nmmax
do 30 nx=-nxpix/2,nxpix/2
        do 35 ny=-nypix/2,nypix/2
    read(5,*) dummy,dummy,aimage(nm,nx,ny)
 35       continue
 30     continue
 20   continue
      close(5)

c      open(unit=7,file='param.out',status='unknown')
      open(unit=8,file=title1,status='old')
      open(unit=11,file='fit.dat',status='unknown')
        do nx=-nxexpt/2,nxexpt/2          !Reading in experimental data
          do ny=-nyexpt/2,nyexpt/2
             read(8,*) xpos(nx),ypos(ny),z(nx,ny)
          enddo
        enddo

      sig=1.0d0    !Assume noiseless profiles so standard deviation is unity.

      close(8)
      close(10)

      mfit = maa   !number of fitting parameters

      do i=1,maa           !Initializing fitting coeff's
 a(i)=gues(i)
      enddo

      do 100 i=1,mfit      !Program only fits parameter a(i) if ia(i) is
        ia(i) = 1          !non-zero.  To fix parameter put ia(i)=0.
```

```
 100  continue
        ia(1)=0
        ia(5)=0

      xmin=-1.0d0+1.0d0/dble(npl)      !Setting up constraints on max and
      xmax=1.0d0-1.0d0/dble(npl)       !min values of fitting coeff's to
      dx=(xmax-xmin)/dble(npl)         !keep within allowed boundaries of
      do i=1,npl                       !(2n+1)Pnmax and (2n+1)Pnmin (Pnmax
        x(i)=xmin+dble(i-1)*dx         !and Pnmin are the max and min values
      enddo                            !of the nth Legendre polynomial in
                                       !the interval -1 to 1).
      do 13 n=1,maa
 if (n.le.nplcm) then
            ord=n-1
         else
            ord=n-1-nplcm
         endif

         max=0.0d0
         min=0.0d0
         do 11 j=1,npl
            plpt(j)=pl(ord,x(j))
            if (plpt(j).gt.max) then
               max=plpt(j)
            endif
            if (plpt(j).lt.min) then
               min=plpt(j)
            endif
 11      continue
         amax(n)=(2.0d0*dble(ord)+1.0d0)*max
         amin(n)=(2.0d0*dble(ord)+1.0d0)*min
 13   continue

c   initial call to fitting routine.  mrqmin does one iteration to return
c   new set of coefficients and chisq.

      alamda = -1.0d0
      call mrqmin(xpos,ypos,z,sig,nxexpt,nyexpt,a,ia,mfit,coa,
     1           alpha,maa,chisq,funct,alamda,amax,amin)
      k = 1
      itst = 0

c  Loop over minimization of chisq

 101  write(9,1000) k,chisq,alamda
      write(9,1010)
      write(9,1020) (a(i),i=1,maa)

      k = k+1
      ochisq = chisq

      call mrqmin(xpos,ypos,z,sig,nxexpt,nyexpt,a,ia,mfit,coa,alpha,
     1        maa,chisq,funct,alamda,amax,amin)

      if (chisq .gt. ochisq) then
        itst = 0
      else
        if (dabs(ochisq-chisq) .lt. 1.0d-04) then
 itst = itst + 1
        endif
      endif
      if (itst .lt. 20) then
goto 101
      endif

c  final call to minimization routines. alamda set to 0 so covar returns
c  the covariance matrix and al the curvature matrix.

      alamda = 0.0d0
      call mrqmin(xpos,ypos,z,sig,nxexpt,nyexpt,a,ia,mfit,coa,alpha,
     1         maa,chisq,funct,alamda,amax,amin)

c  Calculation of the final fitted distribution.  Funct constructs the
c  final fitted profiles, res are the residuals.

 113  continue
      do 120 i=-nxexpt/2,nxexpt/2
        do 125 j=-nyexpt/2,nyexpt/2
  call funct(xpos(i),ypos(j),a,fit,dum,maa)
  res = z(i,j)-fit
  write (11,'(4(1pe13.3))') xpos(i),ypos(j),fit,res
 125    continue
 120  continue
c
      write(9,*) ' Final coefficients and uncertainties'
      write(9,*) ' chisq  = ',chisq
      do 130 j=1,maa
        aa = dsqrt(dabs(coa(j,j)))
write(9,1030) a(j),aa
 130  continue

      do i=1,maa
```

```
         write(9,6789)(coa(i,j),j=1,maa)      !output covariance matrix
       enddo

       call distgen(a)      !Generates fT and angular distributions and outputs
                            !to files 'ft.dat' and 'CM.dat'

c  Formats

1000  format(1x,'iteration # =',i2,t20,'chi-squared =',1pe12.4,
     #         t48,'alamda =',1pe9.2)
c1010  format(1x,t7,'a(1)',t19,'a(2)',t31,'a(3)',t43,'a(4)',
c     #          t55,'a(5)',t67,'a(6)',t79,'a(7)')
1010  format(10x,'the coefficients')
1020  format(1x,13(1pe12.4))
1030  format(1pe12.4,3x,'+/-',3x,1pe12.4)
1040  format(1pe12.4,3x,'+/-',3x,1pe12.4)
6789  format(7f10.4)
 999  close(6)
       close(13)
       close(7)
       close(11)
       close(12)

       end

c -------------------------------------------------------
       subroutine funct(xp,yp,a,zfit,dzfitda,na)
c -------------------------------------------------------
c  Sum of Basis functions - trial solution

       implicit double precision (a-h,o-z)
       parameter(nxpix=10,nypix=10,maa=11,nmmax=28)
       dimension a(na),dzfitda(na),anm(maa,maa)
       dimension aimage(nmmax,-nxpix/2:nxpix/2,-nypix/2:nypix/2)
       common/dat/nplcm,nplq
       common/data/aimage,mode
       common/delta/delxexpt,delyexpt,delxbas,delybas

c  Interpolating basis functions to experimental data using weighted
c  average.
c       dkx = xp/delxbas
c       dky = yp/delybas

c  When using test data from basis function program so that actually
c  reading in indices for x and y not distances.
       dkx=xp*delxexpt/delxbas
       dky=yp*delyexpt/delybas

       kx = idint(dkx)
       ky = idint(dky)
       fracx = dkx-dble(kx)
       fracy = dky-dble(ky)

       zfit = 0.0d0
       do 10 j = 1,na
 dzfitda(j) = 0.0d0
 10    continue

c  For separable fitting:
       if (mode .eq. 1) then
do 40 m=1,nplq
  mmo = m-1
  do 50 n=1,nplcm
    nmo = n-1
    nm = mmo*nplcm+n
    npm = m+nplcm
c Interpolating basis functions
        term=(1.0d0-fracx)*(1.0d0-fracy)*aimage(nm,kx,ky)+fracx*
     0    (1.0d0-fracy)*aimage(nm,kx+1,ky)+fracx*fracy*
     0    aimage(nm,kx+1,ky+1)+(1.0d0-fracx)*fracy*aimage(nm,kx,ky+1)

        if (nm.eq.1) write(16,'(3f15.7)') dkx,dky,term

c  Sum of basis functions
c   Zeroth order fT moment so fT coefficient is unity.
           zfit = zfit+a(n)*a(npm)*term
    dzfitda(n) = dzfitda(n)+a(npm)*term
    dzfitda(npm) = dzfitda(npm)+a(n)*term
 50       continue
 40      continue

c  For non-separable fitting:
      else
 do 70 n=1,nplcm
    do 80 m=1,nplq
       nm = (m-1)*nplcm+n
       anm(n,m) = a(nm)
 80         continue
 70      continue
 do 100 n=1,nplcm
    do 110 m=1,nplq
       nm = (m-1)*nplcm+n
```

```
c  Interpolation
        term=(1.0d0-fracx)*(1.0d0-fracy)*aimage(nm,kx,ky)+fracx*
     @     (1.0d0-fracy)*aimage(nm,kx+1,ky)+fracx*fracy*
     @     aimage(nm,kx+1,ky+1)+(1-fracx)*fracy*aimage(nm,kx,ky+1)

c  Sum of basis functions.
       zfit = zfit+anm(n,m)*term
       dzfitda(nm) = dzfitda(nm)+term
 110         continue
 100      continue
      endif

      return
      end

c ---------------------------------------------------------------
      subroutine mrqmin(xp,yp,z,sig,nx,ny,a,ia,mf,co,al,nc,chisq,
     @                  funcs,alamda,amax,amin)
c ---------------------------------------------------------------
c  Levenberg-Marquardt method, attempting to reduce the value of chisq
c  of a fit between a set of data points xp,yp,z with individual standard
c  deviations sigma and a nonlinear function dependent on maa coefficients
c  a.  Returns current best fit values for the parameters a and chisq.

      implicit double precision (a-h,o-z)
      parameter (maa=11)
      external funcs
      dimension a(mf),ia(mf),co(nc,nc),al(nc,nc),atry(maa),b(maa),
     @     xp(-nx/2:nx/2),yp(-ny/2:ny/2),z(-nx/2:nx/2,-ny/2:ny/2),
     @     da(maa),amax(nc),amin(nc)
      common/dat/nplcm,nplq
      save ihit
c
      if (alamda .lt. 0.0d0) then
 ihit = 0
 do 11 k=1,mf
    if (ia(k) .ne. 0) ihit = ihit+1
 11      continue
 alamda = 2.0d0

c  Calculate gradient (beta vector), Hessian (alpha) matrix, and chisq.
 call mrqcof(xp,yp,z,sig,nx,ny,a,ia,mf,al,b,nc,chisq,funcs)
 ochisq = chisq
 do 12 j=1,mf
    atry(j) = a(j)
 12      continue
      endif
      j=0
      do 14 l=1,mf
 if(ia(l).ne.0)then
    j=j+1
    k=0
    do 13 m=1,mf
       if(ia(m).ne.0)then
 k=k+1
 co(j,k) = al(j,k)
       endif
 13         continue
    co(j,j) = al(j,j)*(1.0d0+alamda)
    da(j) = b(j)
 endif
 14   continue

c  Gauss-Jordan elimination to find increments by which to alter coeff's
c  for next iteration.
      call gaussj(co,ihit,nc,da,1,1)

c  Sort alpha matrix to true order of fitting coeff's and set variances
c  and all covariances to zero in alpha for any frozen variables.
      if (alamda .eq. 0.0d0) then
 call covsrt(co,nc,mf,ia,ihit)
 return
      endif
      j=0
      do 15 l=1,mf
 if(ia(l).ne.0)then
    j=j+1

c  Incrementing trial coeff's for next iteration
    atry(l)=a(l)+da(j)
 endif

c   Constraining coeffs to lie within allowed range
c         if (atry(l).gt.amax(l)) then
c           atry(l)=amax(l)
c         endif
c         if (atry(l).lt.amin(l)) then
c           atry(l)=amin(l)
c         endif
 15   continue
      call mrqcof(xp,yp,z,sig,nx,ny,atry,ia,mf,co,da,nc,chisq,
     1          funcs)
```

```
      if (chisq .lt. ochisq) then
 alamda = 0.1d0*alamda
 ochisq = chisq
 j=0
 do 18 l=1,mf
    if(ia(l).ne.0)then
       j=j+1
       k=0
       do 17 m=1,mf
  if(ia(m).ne.0)then
     k=k+1
     al(j,k) = co(j,k)
  endif
 17            continue
       b(j) = da(j)
       a(l) = atry(l)
    endif
 18      continue
      else
 alamda = 1.0d1*alamda
 chisq = ochisq
      endif

      return
      end

c -------------------------------------------------------------
      subroutine mrqcof(xp,yp,z,sig,nx,ny,a,ia,mf,al,b,na,
     1                  chisq,funcs)
c -------------------------------------------------------------
c  Computes alpha matrix and beta vector.

      implicit double precision (a-h,o-z)
      external funcs
      parameter (maa=11)
      dimension al(na,na),b(mf),dzda(maa),ia(mf),a(mf),
     1 xp(-nx/2:nx/2),yp(-ny/2:ny/2),z(-nx/2:nx/2,-ny/2:ny/2)

      common/pos/x,dx
c
      ihit=0
      do 11 j=1,mf
 if(ia(j).ne.0)ihit=ihit+1
 11   continue
      do 13 j=1,ihit
 do 12 k=1,j
    al(j,k) = 0.0d0
 12      continue
 b(j) = 0.0d0
 13   continue
      chisq = 0.0d0
      sig2i = 1.0d0/(sig*sig)
      do 16 i=-nx/2,nx/2
        do 17 jj=-ny/2,ny/2
 call funcs(xp(i),yp(jj),a,zmod,dzda,mf)
 dz = z(i,jj)-zmod
 j=0
 do 15 l=1,mf
    if(ia(l).ne.0)then
       j=j+1
       wt = dzda(l)*sig2i
       k=0
       do 14 m=1,l
  if(ia(m).ne.0)then
     k=k+1
     al(j,k) = al(j,k)+wt*dzda(m)
  endif
 14            continue
       b(j) = b(j)+dz*wt
    endif
 15      continue
 chisq = chisq+dz*dz*sig2i
 17     continue
 16   continue

      do 18 j=2,mf
 do 19 k=1,j-1
    al(k,j) = al(j,k)
 19      continue
 18   continue
c
      return
      end

c --------------------------------------
      subroutine gaussj(a,n,np,b,m,mp)
c --------------------------------------
c  Solves matrix equation (alpha)(da)=beta to find increments to change
c  fitting coeff's by for next iteration.

      implicit double precision (a-h,o-z)
```

```
      parameter (mmax=100)
      dimension a(np,np),b(np,mp),ipiv(mmax),indxr(mmax),indxc(mmax)

      do 11 j=1,n
 ipiv(j) = 0
 11   continue
      do 22 i=1,n
 big = 0.0d0
 do 13 j=1,n
    if (ipiv(j) .ne. 1) then
       do 12 k=1,n
  if (ipiv(k) .eq. 0) then
     if (dabs(a(j,k)) .ge. big) then
big = dabs(a(j,k))
irow = j
icol = k
     endif
  else if (ipiv(k) .gt. 1) then
     pause 'singular matrix'
  endif
 12            continue
    endif
 13      continue
 ipiv(icol) = ipiv(icol)+1
 if (irow .ne. icol) then
    do 14 l=1,n
       dum = a(irow,l)
       a(irow,l) = a(icol,l)
       a(icol,l) = dum
 14          continue
    do 15 l=1,m
       dum1 = b(irow,l)
       b(irow,l) = b(icol,l)
       b(icol,l) = dum
 15          continue
 endif
 indxr(i) = irow
 indxc(i) = icol
 if (a(icol,icol) .eq. 0.0d0) pause 'singular matrix.'
 pivinv = 1.0d0/a(icol,icol)
 a(icol,icol) = 1.0d0
 do 16 l=1,n
    a(icol,l) = a(icol,l)*pivinv
 16      continue
 do 17 l=1,m
    b(icol,l) = b(icol,l)*pivinv
 17      continue
 do 21 ll=1,n
    if (ll .ne. icol) then
       dum = a(ll,icol)
       a(ll,icol) = 0.0d0
       do 18 l=1,n
  a(ll,l) = a(ll,l)-a(icol,l)*dum
 18            continue
       do 19 l=1,m
  b(ll,l) = b(ll,l)-b(icol,l)*dum
 19            continue
    endif
 21      continue
 22   continue
      do 24 l=n,1,-1
 if (indxr(l) .ne. indxc(l)) then
    do 23 k=1,n
       dum = a(k,indxr(l))
       a(k,indxr(l)) = a(k,indxc(l))
       a(k,indxc(l)) = dum
 23          continue
 endif
 24   continue

      return
      end

c -----------------------------------------------
      subroutine covsrt(co,nc,mf,ia,ihit)
c -----------------------------------------------
      implicit double precision (a-h,o-z)
      dimension co(nc,nc),ia(mf)

      do 12 i=ihit+1,mf
 do 11 j=1,i
    co(i,j) = 0.0d0
    co(j,i) = 0.0d0
 11      continue
 12   continue
      k=ihit
      do 15 j=mf,1,-1
 if(ia(j).ne.0)then
    do 13 i=1,mf
       swap=co(i,k)
       co(i,k)=co(i,j)
       co(i,j)=swap
```

```
 13         continue
    do 14 i=1,mf
       swap=co(k,i)
       co(k,i)=co(j,i)
       co(j,i)=swap
 14         continue
    k=k-1
 endif
 15   continue
c
      return
      end

c ------------------------------------------
      double precision function pl(l,x)
c ------------------------------------------
c  Legendre Polynomials.
      implicit double precision (a-h,o-z)

      if (dabs(x).gt.1.) pause 'bad arguments'
      pmm = 1.0d0
      if (l.eq.0) then
 pl = pmm
      else
 pmmp1 = x*pmm
 if (l.eq.1) then
    pl = pmmp1
 else
    do 12 ll = 2,l
  pll = (x*dble(2*ll-1)*pmmp1-dble(ll-1)*pmm)/dble(ll)
       pmm = pmmp1
       pmmp1 = pll
12          continue
    pl = pll
 endif
      endif
c
      return
      end

c----------------------------------------
      subroutine distgen(a)
c----------------------------------------
c  Generates differential cross section and P(fT) distribution.
      implicit double precision (a-h,o-z)
      parameter (maa=11,nplcm=4,nplq=4,ncmft=20)
      dimension a(maa)
      dimension ft(ncmft),cm(ncmft),pft(ncmft),dcs(ncmft)

      delta=1.0d0/dble(ncmft)
      do i=1,ncmft
        cm(i)=2.0d0*(dble(i)/dble(ncmft))-1.0d0
        ft(i)=cm(i)
      enddo

      do i=1,ncmft
        dcs(i)=0.0d0
        do n=1,nplcm
          dcs(i)=dcs(i)+a(n)*dble(2*(n-1)+1)*pl(n-1,cm(i))/2.0d0
        enddo
      enddo
      do i=1,ncmft
        pft(i)=0.0d0
        do n=nplcm+1,maa
          pft(i)=pft(i)+a(n)*dble(2*(n-1-nplcm)+1)*pl(n-1-nplcm,ft(i))
        enddo
        ft(i)=0.5d0*(ft(i)+1.0d0)
       enddo

      open(unit=3,file='cm.dat',status='unknown')
      open(unit=4,file='ft.dat',status='unknown')

      do i=1,ncmft
        write(3,'(2f15.6)') cm(i),dcs(i)
        write(4,'(2f15.6)') ft(i),pft(i)
      enddo

      return
      end
```

F.2.3 *eisim - Image simulation program for electron impact ionization experiments*

```
      program eisim

c  Program to simulate an ion image resulting from electron impact
c  ionization of a molecular beam given a differential cross section
c  and P(fT) distribution.  The distributions are made up of a sum of
c  two gaussians and a baseline.  Change coeff's ci-7 in functions
```

```
c  dcs and pft to get the desired functions.  Otherwise put in a function
c  of your choice in place of these functions.

c  Includes spatial distribution (beam profiles) for electron and molecular
c  beam and velocity distributions along the beam axis for each beam.
c  Transverse velocity distributions are not included (this would be easy
c  to modify by including them in the subroutines epick and molpick).

c  mmol is the mass of the molecular reagent and mion (and mneut) are the
c  masses of the product ion (and neutral if fragmetation occurs) formed. me
c  is the electron mass.

c  The single parameter mpt governs the convergence of the simulation and
c  corresponds to the number of ions in the image.  Check that increasing
c  mpt doesn't change the simulation.

c  The lab frame is defined with the x axis along the molecular beam and the
c  y axis along the ion beam.  The z axis is up to the detector.  The CM
c  frame has the X axis along the reagent relative velocity vector, the Z
c  axis up to the detector and the Y axis lying in the lab frame xy plane.

c  NB: Normalised distributions for DCS and P(fT) are not required.

      implicit double precision (a-h,o-z)
      double precision mmol,mion,mneut,me,ip,kB,mbwidth
      character*30 title1
      parameter(nxpix=10,nypix=10)

c   nxpix and nypix = number of pixels in image in x and y dimensions.
c        NB: The program assumes that the MCP image fits into the CCD and
c            touches the edges.

      dimension aimage(-(nxpix/2):(nxpix/2),-(nypix/2):(nypix/2))

      common /consts/ me,qe,kB,Av
      common /mb/ mbwidth,Tpar,flowvel,dgunscat,mmol,velwidth
      common /elec/ pwidth,ee,ewidth,EEwidth
      external pft,epick,molpick,dpick,dcs1,sigma,ran1,gasdev,
     @   xygauss

c ***Constants***
      qe=1.602d-19     !electronic charge
      kB=1.3806d-23    !Boltzmann's constant
      me=9.102d-31     !electron mass
      Av=6.022d23      !Avogadro's number
      temp=298.0d0     !nozzle stagnation temperature
      convmass=1.0d0/(1000.0d0*Av)   !converts g/mol to kg
      pi = dacos(-1.0d0)

c  ***Beam characteristics***
      ewidth=3.0d-3    !FWHM of electron beam
      mbwidth=2.0d-3   !FWHM of molecular beam
      EEwidth=0.7d0    !FWHM of electron energy distribution // axis

c  ***Machine geometry***
      rmcp=2.0d-2       !radius of MCP's.
      dgunscat=8.0d-2   !distance from electron source to scattering centre.
      dscatext=2.5d-2   !distance from scattering centre to extraction plates.
      dscatfp=3.5d-2    !distance from scattering centre to field plates.
      rmesh=2.3d-2      !radius of mesh in top extraction plate.
      dscatmcp=7.5d-2


c  READING INPUT

      open(unit=5,file='eisim.inp',status='old')
      read(5,*) title1      !output file

      open(unit=10,file=title1,status='unknown')
      open(unit=12,file='eisim.out',status='unknown')

      read(5,*) mpt         !number of points to simulate (=no. of ions)

      read(5,*) mmol,mion,mneut    !mass of beam molecule, product ion and
      mmol=mmol*convmass           !neutral in g/mol (program allows for
      mion=mion*convmass           !fragmentation in which an ion and neutral
      mneut=mneut*convmass         !are produced.  If looking at molecular
      if (mmol.ne.(mion+mneut)) then     !ion put mneut=0.0d0
        write(*,*) "Check masses"
        stop
      endif

c  Molecular beam flow velocity and width of velocity distribution (this
c  gives the limits between which velocities are selected for the simulation
c  so make sure you cover the entire distribution - can check this by
c  getting the program to output the beam velocity distribution and checking
c  it isn't cut off at the edges.)

      read(5,*) flowvel, velwidth

      read(5,*) Tpar  !parallel translational temperature of molecular beam.
      read(5,*) ip    !molecular ionization potential / eV
```

```
      read(5,*) efrag !fragmentation energy / eV
      read(5,*) ee    !electron energy / eV
      read(5,*) p1int,p2int   !product internal energies (reagent internal
        pintE=p1int1+p2int    !E's assumed to be kT)

      read(5,*) pwidth    !width of electron beam pulse / s
      read(5,*) tdelay    !delay between electron pulse and extraction pulse / s
      read(5,*) extractV  !voltage applied to each extraction plate

      read(5,*) mode        !mode=1 for gated intensifier, 0 for ungated (camera
      if (mode.eq.1) then   !always on)
        read(5,*) mcpdelay  !delay for image intensifier / s
        read(5,*) mcpwidth  !gate width of image intensifier / s
        mcpoff=mcpdelay+mcpwidth
      endif

      close(5)

c  Writing input data

      write(12,10000) nxpix,nypix,mpt
      write(12,11000) mmol,mion,mneut

c  INPUT FINISHED

      rm = mmol*me/(mmol+me) !reduced mass of reactants.

c  Need to work out CM velocity to superimpose on product ion velocities.

c  Mass factor for fraction of total available product translational energy
c  into each fragment (from conservation of momentum the fragments travel
c  in opposite directions P=0=p1+p2).  These are the factors to multiply the
c  available product translation energy by to get the squares of the
c  individual ion and neutral velocities

      if (mneut.eq.0.0d0) then
         fion=1.0d0
         fneut=0.0d0
      else
         fion=2.0d0*mion/(mneut*mmol)
         fneut=2.0d0*mneut/(mion*mmol)
      endif

        vrmin = 1.0d6
        vrmax = 0.0d0
        iseed=13     !seed for random number generator

       nplates=0   !zeroing counters for lost ions that hit field plates or
       nmiss=0     !extraction plates, miss MCP's or fall outside detection
       ngate=0     !gate.

       tmin=1000.0d0
       tmax=0.0d0

c  LOOPING OVER MPT (number of integration steps)

       do 130 n=1,mpt

c Release an electron from the electron gun.  Position is defined by the
c electron beam profile and electron energy (->velocity) from the energy
c distribution.  Electrons are released over a time from 0 to pwidth
c seconds during the gating pulse applied to the cathode.

  10     call epick(iseed,ex,ez,vex,vey,vez,etime)
         vemag2=vex**2+vey**2+vez**2
         vemag=dsqrt(vemag2)

c  Assumes a Gaussian beam profile for the electron beam and ignores
c  transverse velocity component.

c Ionization occurs after the electron has covered the flight path from the
c filament to the crossing region.  This distance is dependent on the
c molecular beam profile.

         call dpick(iseed,ez,diony,dist,iflag)
         if (iflag.eq.1) goto 10
         tof = dist/vey

c  Molecular reagent velocity.
         call molpick(iseed,vmolx,vmoly,vmolz,vprob)
         vmolmag=dsqrt(vmolx**vmolx+vmoly**vmoly+vmolz**vmolz)

        vxr = vmolz-vex      !Calculating relative velocity.
        vyr = vmoly-vey
        vzr = vmolz-vez
        vr = dsqrt(vxr**2+vyr**2+vzr**2)
        if (vr .gt. vrmax) vrmax=vr
        if (vr .lt. vrmin) vrmin=vr

        vxcm = (mmol*vmolx+me*vex)/(mmol+me)      !lab frame velocity of
        vycm = (mmol*vmoly+me*vey)/(mmol+me)      !center of mass (vector
        vzcm = (mmol*vmolz+me*vez)/(mmol+me)      !connecting CM and lab
```

```
      vcm = dsqrt(vxcm**2+vycm**2+vzcm**2)       !frame origins)

      ecoll=0.5d0*rm*vr*vr/qe      !Collision energy / eV

      ft=ran1(iseed)             !Calculating energy release into translation.
      epmx = ft*(ecoll+(kB*temp/qe)-ip-efrag-pintE)
      if (epmx.lt.0.0d0) then
        write(*,*) 'Discarding trajectory - negative energy'
        goto 130
      endif
      epmx=epmx*qe     !Convert to Joules

      if (mneut.eq.0.0d0) then            !Product velocites in CM frame.
        wion = dsqrt(2.0d0*epmx/mion)
      else
        wion=dsqrt(epmx*fion)
        wneut=dsqrt(epmx*fneut)
      endif

       theta=2.0d0*pi*ran1(iseed)  !Product scattering angle.  Theta is
       phi=pi*ran1(iseed)          !the angle anticlockwise from the
       costh=dcos(theta)           !positive x axis (MB direction) in the
       sinth=dsin(theta)           !scattering plane.  phi is the angle
       cosphi=dcos(phi)            !between the product velocity vector
       sinphi=dsin(phi)            !wion and the z axis.

      weight=pft(ft)*dcs(costh)*vprob    !Weighting factor for each ion.

      wionx = wion*sinphi*costh    !components of product ion velocity in
      wiony = wion*sinphi*sinth    !CM frame (same axes as lab frame,
      wionz = wion*cosphi          !positive direction in beam direction)

      vionx=wionx+vxcm      !Transform to lab frame (add CM velocity)
      viony=wiony+vycm
      vionz=wionz+vzcm

      tfly=tdelay-tof-etime     !Time to go before extraction plates
      if(tfly.lt.0.0d0) then    !switched on.
         write(*,*) 'Extraction began before ions were formed'
         goto 130
      endif

      dionx=ex+vionx*tfly           !xyz position of product ion wrt origin
      diony=diony+viony*tfly        !at center of scattering region when
      dionz=ez+vionz*tfly           !extraction plates switch.
      rionxy=dsqrt(dionx**2+diony**2)

      if (dabs(dionz).gt.dscatext.or.dabs(diony).gt.dscatfp) then
         nplates=nplates+1
         goto 130                         !Eliminating ions which hit
      else if(rionxy.gt.rmesh) then       !extraction/field plates or
         nplates=nplates+1                !don't make it through mesh.
         goto 130
      endif

      dplate=dscatext-dionz               !z component of ion velocity after
      fracgap=dplate/(2.0d0*dscatext)     !extraction plates switch on.
      Eion=2.0d0*extractV*fracgap
      velext=dsqrt(2.0d0*qe*Eion/mion)
      vionz=vionz+velext

      ddetect=dscatmcp-dionz      !Flight time to detector (assuming no
      tdetect=ddetect/vionz       !field penetration from MCP's)
      ttot=tdelay+tdetect

      if(ttot.gt.tmax) tmax=ttot  !find range of times at which ions
      if(ttot.lt.tmin) tmin=ttot  !hit detector.

      dionx=dionx+tdetect*vionx     !x,y positions of ions at detector.
      diony=diony+tdetect*viony
      rionxy=dsqrt(dionx**2+diony**2)

      if(rionxy.gt.rmcp) then    !eliminate ions which miss MCP's
        nmiss=nmiss+1
        goto 130
      endif

      fracx=dionx/rmcp           !Work out which pixel ion hit corresponds
      fracy=diony/rmcp           !to on CCD chip.
      nx=nint(fracx*dble(nxpix/2))
      ny=nint(fracy*dble(nypix/2))

c  To get an ion image need to integrate over the z direction (since
c  image is flattened onto detector), weighting each velocity vector
c  according to the DCS and P(fT) distribution.  Effectively just bin the
c  vectors into pixels.

      if(mode.eq.0) then
        aimage(nx,ny)=aimage(nx,ny) + weight
      else if (mode.eq.1) then
        if(tdetect.gt.mcpdelay.and.tdetect.lt.mcpoff) then
          aimage(nx,ny)=aimage(nx,ny) + weight
```

```
        else
          ngate=ngate+1
        endif
      endif

130   continue

      fracplates=dble(nplates)/dble(mpt)      !Fractions of ions that didn't
      fracmiss=dble(nmiss)/dble(mpt)          !make it to detector.
      fracgate=dble(ngate)/dble(mpt)
      fraclost=fracmiss+fracplates+fracgate

      emin = 0.5d0*rm*(vrmin**2)     !Min and max collision energies.
      emax = 0.5d0*rm*(vrmax**2)

      write(12,15500) emin
      write(12,15600) emax

      write(*,'(a18,f6.2,a4,f6.2,a3)' ) 'Ion arrival from ',
     @  tmin*1.0e6,' to ',tmax*1.0e6,' s'
      write(12,'(a18,f6.2,a4,f6.2,a3)' ) 'Ion arrival from ',
     @  tmin*1.0e6,' to ',tmax*1.0e6,' s'
      write(12,'(a12,f6.2,a3)') 'interval = ', (tmax-tmin)*1.0d6,' s'

      write(12,'(a38,f6.2)') '% of trajectories to field plates',
     @  100.0d0*fracplates
      if(mode.eq.1) write(12,'(a38,f6.2)') '% of trajectories
     @  missing gate ', 100.0d0*fracgate
      write(12,'(a38,f6.2)') '% of trajectories missing MCPs',
     @  100.0d0*fracmiss
      write(12,'(a38,f6.2)') 'total % of trajectories lost',
     @  100.0d0*fraclost

      write(*,'(a38,f6.2)') '% of trajectories to field plates',
     @  100.0d0*fracplates
      if(mode.eq.1) write(*,'(a38,f6.2)') '% of trajectories
     @  missing gate ', 100.0d0*fracgate
      write(*,'(a38,f6.2)') '% of trajectories missing MCPs',
     @  100.0d0*fracmiss
      write(*,'(a38,f6.2)') 'total % of trajectories lost',
     @  100.0d0*fraclost


      aimax=0.0d0                  !Normalising image intensity
      do nx=-nxpix/2,nxpix/2
        do ny=-nypix/2,nypix/2
          if(aimage(nx,ny).gt.aimax) then
            aimax=aimage(nx,ny)
          endif
        enddo
      enddo

      do nx=-nxpix/2,nxpix/2
        do ny=-nypix/2,nypix/2
          if (aimage(nx,ny).ne.aimax) then
            sumimage = sumimage+aimage(nx,ny)
          endif
        enddo
      enddo

      write(*,*) 'sumimage',sumimage

      do 190 nx=-nxpix/2,nxpix/2
        do 191 ny=-nypix/2,nypix/2
          aimage(nx,ny) = aimage(nx,ny)/sumimage
191     continue
190   continue


c Output image

       aimax=aimax/sumimage
       do nx=-nxpix/2,nxpix/2
         do ny=-nypix/2,nypix/2
           if(aimage(nx,ny).ne.aimax) then
             write(10,'(2i5,f15.8)') nx,ny,aimage(nx,ny)
           endif
         enddo
       enddo


c  FORMATS

10000 format(t10,'Integration parameters',/
     @'nxpix =',i4/,'nypix =',i4/ 'mpt=',i10/)
11000 format(/t10,'Masses of reactants and products',/
     @'mmol =',f5.1,5x,'mion =',f5.1)
15000 format(//5x,'Mean relative velocity (m/s) =',1pe12.5/
     @5x,'Mean square velocity (m**2/s**2) =',1pe12.5/
     @5x,'Root mean square velocity (m/s) =',1pe12.5/
     @5x,'Mean CM velocity (m/s) =',1pe12.5/
     @5x,'Mean collision energy (ev) =',1pe12.5/)
```

```
15500 format(/t5,'Emin =',1pe12.5/)
15600 format(/t5,'Emax =',1pe12.5/)

      close(10)

      close(12)

      end

c ------------------------------------------------
      double precision function sigma(ee)
c ------------------------------------------------

c  Ionization efficiency curve

      implicit double precision (a-h,o-z)

      sigma(ee)=1.0d0

      return
      end

c-------------------------------------------
      double precision function ran2(iseed)
c-------------------------------------------
c  Long period (>2.0d18) random number generator of L'Ecuyer with
c  Bays-Durham shuffle and added safeguards.  Returns a uniform
c  random deviate between 0.0 and 1.0 (exclusive of the endpoints).  Call
c  with iseed a negative integer to initialize.  Do not alter iseed
c  between successive deviates in a sequence.  RNMX should approximate the
c  largest floating value that is <1.

      implicit double precision (a-h,o-z)

      parameter(im1=2147483563,im2=2147483399,imm1=im1-1,ia1=40014,
     1          ia2=40692,iq1=53668,iq2=52774,ir1=12211,ir2=3791,
     2          ntab=32,ndiv=1+imm1/ntab)
      parameter(am=dble(1.0d0/im1),eps=1.2d-7,rnmx=1.0d0-eps)
      dimension iv(ntab)
      save iv,iy,idum2
      data idum2/123456789/,iv/ntab*0/,iy/0/

c  Initialize (ensure iseed.ne.0)

      if (iseed.le.0) then
        iseed=max(-iseed,1)
        idum2=iseed
        do 11 j=ntab+8,1,-1
          k=iseed/iq1
          iseed=ia1*(iseed-k*iq1)-k*ir1
          if (iseed.lt.0) iseed=iseed+im1
          if (j.le.ntab) iv(j)=iseed
 11     continue
        iy=iv(1)
      endif

      k=iseed/iq1
      iseed=ia1*(iseed-k*iq1)-k*ir1
      if (iseed.lt.0) iseed=iseed+im1
      k=idum2/iq2
      idum2=ia2*(idum2-k*iq2)-k*ir2
      if(idum2.lt.0) idum2=idum2+im2
      j=1+iy/ndiv
      iy=iv(j)-idum2
      iv(j)=iseed
      if (iy.lt.1) iy=iy+imm1
      ran2=min(am*iy,rnmx)
      return
      end

c-------------------------------------------
      double precision function gauss(iseed)
c-------------------------------------------

      implicit double precision (a-h,o-z)

 1    r1=ran2(iseed)
      r2=ran2(iseed)
      if (r1.le.2.0d0/3.0d0) then
        gauss=1.5d0*r1
        w=0.5d0*gauss**2
      else
        gauss=1.0d0-0.5d0*dlog(3.0d0-3.0d0*r1)
        w=0.5d0*(gauss-2.0d0)**2
      endif

      if ((1.0d0-r2).gt.w) goto 12
      if ((1.0d0/r2)-1.0d0.le.w) goto 1
      if (-1.0d0*dlog(r2).le.w) goto 1
 12   r3=ran2(iseed)
      if (r3.ge.0.5d0) gauss=-1.0d0*gauss
```

```
      return
      end

c-------------------------------------------
      subroutine molpick(iseed,vx,vy,vz,prob)
c-------------------------------------------
c  Generates molecular velocities and probabilities.  Currently only
c  includes parallel velocity from equation Brett Cameron's thesis and
c  assumes zero for transverse components.

      implicit double precision (a-h,o-z)
      double precision kB,me,mmol,mbwidth
      common /consts/ me,qe,kB,Av
      common /mb/ mbwidth,Tpar,flowvel,dgunscat,mmol,velwidth

      vx = flowvel + velwidth*rani(iseed)-velwidth/2.0d0
      arg = mmol*(vx-flowvel)**2/(2.0d0*kB*Tpar)
      prob=vx*vx*dexp(-arg)

      vy=0.0d0
      vz=0.0d0

      return
      end

c-----------------------------------------------------------
      subroutine epick(iseed,x,z,vx,vy,vz,etime)
c-----------------------------------------------------------
c  Generates electron parameters (velocity, position and release time)

      implicit double precision (a-h,o-z)
      double precision me,kB
      common /consts/ me,qe,kB,Av
      common /elec/ pwidth,ee,ewidth,EEwidth
      external xygauss,gasdev

      etime=pwidth*rani(iseed)    !time at which electron is released from
                                  !filament (inside gate width pwidth).

      call xygauss(iseed,x,z)     !offsets from beam axis, assumes a 2D
      x=(ewidth/2.0d0)*x          !Gaussian beam profile with FWHM=ewidth
      z=(ewidth/2.0d0)*z

      vx=0.0d0                          !electron velocity distribution, uses
      elecE=ee+EEwidth*gasdev(iseed)    !a Gaussian energy distribution of
      vy=dsqrt(2.0d0*qe*elecE/me)       !width EEwidth for parallel velocity.
      vz=0.0d0                          !Perpendicular velocity not included.

      return
      end


c-----------------------------------------------------------
      subroutine dpick(idum,z,ycomp,d,iflag)
c-----------------------------------------------------------
c  Distance from electron beam source until electron hits a beam molecule.
      implicit double precision(a-h,o-z)
      double precision mbwidth,mmol
      common /mb/ mbwidth,Tpar,flowvel,dgunscat,mmol,velwidth

c Picks the radius from the axis of a molecule in the beam according to a
c Gaussian distribution, then determines the y component at the z position
c of the electron in order to get d, the distance the electron flies from
c the filament before a collision. Randomly puts the molecule on one side of
c the beam or the other.  Exits if electron misses molecular beam.

      iflag=0
      rad = (mbwidth/2.0d0)*gasdev(idum)
      arg=rad**2-z**2
      if (arg.lt.0.0d0) then
        iflag=1
        return
      endif
      ycomp = dsqrt(arg)
      pick=2.0d0*rani(idum)-1.0d0
      picksign=pick/dabs(pick)
      ycomp = ycomp*picksign
      d = dgunscat-ycomp

      return
      end

c     ------------------------------------------------
      double precision function dcs(coscm)
c     ------------------------------------------------
c  Model differential cross section made up of two Gaussians and a baseline
c  c1,c2 are weights of Gaussians (c1+c2=1), c3,c4 are their centres and
c  c5,c6 are the widths.  c7 is the baseline. coscm is the cosine of
c  the CM scattering angle.

      implicit double precision (a-h,o-z)
```

```
      c1=1.0d0
      c2=0.0d0
      c3=1.0d0
      c4=0.0d0
      c5=0.3d0
      c6=0.3d0
      c7=0.0d0
c
      pi = dacos(-1.0d0)
      ap=-0.5d0

      oso1 = ((c3-coscm)/c5)      !Setting up arguments of the exponential in
      oso2 = ((c4-coscm)/c6)      !the Gaussians.
      roso1=ap*oso1*oso1
      roso2=ap*oso2*oso2

c The Gaussians...
      if (roso1 .lt. -2.2d2) then
 tmp1=0.0d0
      else
 tmp1=c1*dexp(roso1)
      endif
      if (roso2.lt.-2.2d2) then
 tmp2=0.0d0
      else
 tmp2=c2*dexp(roso2)
      end if
      dcs=tmp1+tmp2+c7

      return
      end
c   ------------------------------------------------------
      double precision function pft(ftm)
c   ------------------------------------------------------
c  Model P(fT) made up of two Gaussians and a baseline
c  c1,c2 are weights of Gaussians (c1+c2=1), c3,c4 are their centres and
c  c5,c6 are the widths.  c7 is the baseline.

      implicit double precision (a-h,o-z)

      ftn=2.0d0*ftm-1.0d0

      c1=1.0d0
      c2=0.0d0
      c3=-0.95d0
      c4=0.0d0
      c5=0.01d0
      c6=0.2d0
      c7=0.0d0

      pi = dacos(-1.0d0)
      ap=-0.5d0

      oso1 = ((c3-ftn)/c5)    !Setting up the arguments of the exponential
      oso2 = ((c4-ftn)/c6)    !in the Gaussians.
      roso1=ap*oso1*oso1
      roso2=ap*oso2*oso2

c  The Gaussians...
      if (roso1 .lt. -2.2d2) then
 tmp1=0.0d0
      else
 tmp1=c1*dexp(roso1)
      endif
      if (roso2.lt.-2.2d2) then
 tmp2=0.0d0
      else
 tmp2=c2*dexp(roso2)
      end if
      pft=tmp1+tmp2+c7

      return
      end

c ----------------------------------------
      double precision function ran1(idum)
c ----------------------------------------
c  Random number generator

      implicit double precision (a-h,o-z)
      integer idum,ia,im,iq,ir,ntab,ndiv
      parameter (ia=16807,im=2147483647,iq=127773,ir=2836,
     *ntab=32,ndiv=1+(im-1)/ntab)
      parameter (am=1.0d0/dble(im),eps=1.2d-7,rnmx=1.0d0-eps)
      integer j,k,iv(ntab),iy
      save iv,iy
      data iv /ntab*0/, iy /0/

      if ((idum.le.0) .or. (iy.eq.0)) then
         idum = max0(-idum,1)
         do 11 j=ntab+8,1,-1
            k = idum/iq
```

```
            idum = ia*(idum-k*iq)-ir*k
            if (idum .lt. 0) idum = idum+im
            if (j .le. ntab) iv(j) = idum
 11       continue
          iy=iv(1)
        endif
        k = idum/iq
        idum = ia*(idum-k*iq)-ir*k
        if (idum .lt. 0) idum = idum+im
        j = 1+iy/ndiv
        iy = iv(j)
        iv(j) = idum
        ran1 = dmin1(am*dble(iy),rnmx)

        return
        end

c -------------------------------------------------
        subroutine xygauss(iseed,dev1,dev2)
c -------------------------------------------------
c  Generates a 2 dimensional Gaussian distribution, 2 points between -1 and
c  +1.
        implicit double precision (a-h,o-z)
        external ran1

c  Generates 'velocity components' for molecular reactant on interval -1
c  to +1 using a random number generator.
  1     v1=2.0d0*ran1(iseed)-1.0d0
        v2=2.0d0*ran1(iseed)-1.0d0
        rsq=v1**2+v2**2
        if(rsq.ge.1.0d0.or.rsq.eq.0.0d0)goto 1

c  Transforms from random velocities in range -1,1 to a Gaussian distribution
c  of full width wdth.
        fac=dsqrt(-2.0d0*dlog(rsq)/rsq)
        dev1=v1*fac
        dev2=v2*fac
        return
        end

c-------------------------------------------------
        double precision function gasdev(idum)
c-------------------------------------------------
c  Picks a random number from a Gaussian distribution between -1 and 1
        implicit double precision(a-h,o-z)
        save iset,gset
        data iset/0/
        if(iset.eq.0) then
 1        v1=2.0d0*ran1(idum)-1.0d0
          v2=2.0d0*ran1(idum)-1.0d0
          rsq=v1**2+v2**2
          if(rsq.ge.1.0d0.or.rsq.eq.0.0d0) goto 1
          fac=dsqrt(-2.0d0*dlog(rsq)/rsq)
          gset=v1*fac
          gasdev=v2*fac
          iset=1
        else
          gasdev=gset
          iset=0
        endif
        return
        end
```

F.2.4 `ionsim` - Image simulation program for ion–molecule experiments

```
        program ionsim

c  Program to simulate an ion image resulting from a crossed beam
c  ion-molecule reaction given a differential cross section and P(fT)
c  distribution.  The distributions are made up of a sum of
c  two gaussians and a baseline.  Change coeff's c1-7 in functions
c  dcs and pft to get the desired functions.  Otherwise put in a function
c  of your choice in place of these functions.

c  Includes spatial distribution (beam profiles) for ion and molecular
c  beam and velocity distributions along the beam axis for each beam.
c  Transverse velocity distributions are not included (this would be easy
c  to modify by including them in the subroutines ionpick and molpick).

c  mmol and mion are the masses of the molecular and ionic reagents and
c  mmolp and mionp, the masses of the products

c  The single parameter mpt governs the convergence of the simulation and
c  corresponds to the number of ions in the image.  Check that increasing
c  mpt doesn't change the simulation.

c  The lab frame is defined with the x axis along the molecular beam and the
c  y axis along the ion beam.  The z axis is up to the detector.  The CM
```

```
c  frame has the X axis along the reagent relative velocity vector, the Z
c  axis up to the detector and the Y axis lying in the lab frame xy plane.

c  NB: Normalised distributions for DCS and P(fT) are not required.

c                       Claire Vallance 22/9/98

      implicit double precision (a-h,o-z)
      double precision mmol,mion,mmolp,mionp,mtot,kB,mbwidth
      double precision ionx,ionz,iontime,ionE,ionEE,ionwidth,ionEwidth
      character*30 title1
      parameter(nxpix=10,nypix=10)

c   nxpix and nypix = number of pixels in image in x and y dimensions.
c        NB: The program assumes that the MCP image fits into the CCD and
c            touches the edges.

      dimension aimage(-(nxpix/2):(nxpix/2),-(nypix/2):(nypix/2))

      common /consts/ mion,qe,kB,Av
      common /mb/ mbwidth,Tpar,flowvel,dgunscat,mmol,velwidth
      common /elec/ pwidth,ionE,ionwidth,ionEwidth
      external pft,ionpick,molpick,dpick,dcs1,sigma,ran1,gasdev,
     @   xygauss

c  ***Constants***
      qe=1.602d-19     !electronic charge
      kB=1.3806d-23    !Boltzmann's constant
      Av=6.022d23      !Avogadro's number
      temp=298.0d0     !nozzle stagnation temperature
      convmass=1.0d0/(1000.0d0*Av)  !converts g/mol to kg
      pi = dacos(-1.0d0)

c  ***Beam characteristics***
      ionwidth=3.0d-3    !FWHM of ion beam
      mbwidth=2.0d-3     !FWHM of molecular beam
      ionEwidth=1.0d0    !FWHM of ion energy distribution // axis

c  ***Machine geometry***
      rmcp=2.0d-2        !radius of MCP's
      dgunscat=4.0d-2    !distance from ion source L7 to scattering centre.
      dscatext=2.5d-2    !distance from scattering centre to extraction plates.
      dscatfp=3.5d-2     !distance from scattering center to field plates.
      rmesh=2.3d-2       !radius of mesh in top extraction plate.
      dscatmcp=7.5d-2


c  READING INPUT
      open(unit=5,file='ionsim.inp',status='old')
      read(5,*) title1       !output filename

      open(unit=10,file=title1,status='unknown')
      open(unit=12,file='eisim.out',status='unknown')

      read(5,*) mpt                     !number of points for Monte Carlo integration
      read(5,*) mmol,mion,mmolp,mionp  !masses of reagents and products / g/mol
      write(*,*) (mmol+mion),(mmolp+mionp)
      if((mmol+mion).ne.(mmolp+mionp)) then
         write(*,*) "Check masses"
         stop
      endif
      mmol=mmol*convmass
      mion=mion*convmass
      mmolp=mmolp*convmass
      mionp=mionp*convmass
      mtot=mmol+mion

c  Molecular beam flow velocity and width of velocity distribution (this
c  gives the limits between which velocities are selected for the simulation
c  so make sure you cover the entire distribution - can check this by
c  getting the program to output the beam velocity distribution and checking
c  it isn't cut off at the edges.)

      read(5,*) flowvel, velwidth

      read(5,*) Tpar     !parallel translational temperature of molecular beam
      read(5,*) Ethresh  !threshold energy for reaction (positive for endoergic)
      read(5,*) ionE     !ion beam energy
      read(5,*) pint,p2int  !product internal energies (reagent energy assumed to
        pintE=pint1+p2int   !be kT)

      read(5,*) pwidth    !width of ion beam pulse / s
      read(5,*) tdelay    !delay between ion pulse and extraction pulse / s
      read(5,*) extractV  !voltage to each extraction plate.

      read(5,*) mode        !mode=1 for gated intensifier, 0 for ungated (camera always on)
      if (mode.eq.1) then
        read(5,*) mcpdelay  !delay and gate width for image intensifier / s
        read(5,*) mcpwidth  !(measured from ion pulse)
        mcpoff=mcpdelay+mcpwidth
      endif
```

```
      close(5)

      write(12,10000) nxpix,nypix,mpt          !writing input data
      write(12,11000) mmol,mion,mmolp,mionp

c  INPUT FINISHED

      rm = mmol*mion/(mmol+mion)  !reduced mass of reagents

        fmolp=2.0d0*mionp/(mmolp*mtot)    !mass factors for fraction of total available
        fionp=2.0d0*mmolp/(mionp*mtot)    !product translational E into each fragment
                                          !(used to calculate CM frame product velocities)
        vrmin = 1.0d6
        vrmax = 0.0d0

        iseed=13  !seed for random number generator

       nplates=0     !zeroing counters for ions lost through hitting field
       nmiss=0       !plates, missing the detector or arriving outside the
       ngate=0       !intensifier gate.

       tmin=1000.0d0
       tmax=0.0d0

c  LOOPING OVER MPT (number of integration steps)

       do 130 n=1,mpt

c Release an ion from the ion gun.  Position is defined by the
c ion beam profile and ion energy (->velocity) from the energy
c distribution.  Ions are released over a time from 0 to pwidth
c seconds during the gating pulse applied to the final ion lens.

  10     call ionpick(iseed,ionx,ionz,vionx,viony,vionz,iontime)
         vionmag2=vionx**2+viony**2+vionz**2
         vionmag=dsqrt(vionmag2)

c Collision occurs after the ion has covered the flight path from the
c filament to the crossing region.  This distance is dependent on the
c molecular beam profile.

         call dpick(iseed,ionz,diony,dist,iflag)
         if (iflag.eq.1) goto 10
         tof = dist/viony

c  Molecular reagent velocity.
         call molpick(iseed,vmolx,vmoly,vmolz,vprob)
         vmolmag=dsqrt(vmolx**vmolx+vmoly**vmoly+vmolz**vmolz)

        vxr = vmolx-vionx      !Calculating reagent relative velocity
        vyr = vmoly-viony
        vzr = vmolz-vionz
        vr = dsqrt(vxr**2+vyr**2+vzr**2)
        if (vr .gt. vrmax) vrmax=vr
        if (vr .lt. vrmin) vrmin=vr

        vxcm = (mmol*vmolx+mion*vionx)/(mmol+mion)  !Calculating lab frame velocity of the
        vycm = (mmol*vmoly+mion*viony)/(mmol+mion)  !centre of mass
        vzcm = (mmol*vmolz+mion*vionz)/(mmol+mion)
        vcm = dsqrt(vxcm**2+vycm**2+vzcm**2)

        ecoll=0.5d0*rm*vr*vr/qe       !collision energy / eV

        ft=ran1(iseed)
        epmx = ft*(ecoll+(kB*temp/qe)-Ethresh-pintE)     !energy release into translation
        if (epmx.lt.0.0d0) then
          write(*,*) 'Discarding trajectory - negative energy'
          goto 130
        endif
        epmx=epmx*qe    !convert to Joules

          wionp=dsqrt(epmx*fionp)    !product CM frame velocities
          wmolp=dsqrt(epmx*fmolp)

         theta=2.0d0*pi*ran1(iseed)     !product scattering angles.  Theta is
         phi=pi*ran1(iseed)             !the angle anticlockwise from the positive
         costh=dcos(theta)              !x axis (MB direction) in the scattering
         sinth=dsin(theta)              !plane.  phi is the angle between the product
         cosphi=dcos(phi)               !velocity vector wionp and the z axis.
         sinphi=dsin(phi)

        weight=pft(ft)*dcs(costh)*vprob  !weighting factor for each ion.

        wionx = wionp*sinphi*costh    !components of product CM frame velocity
        wiony = wionp*sinphi*sinth    !(same axes as lab frame, positive direction
        wionz = wionp*cosphi          !in beam direction)

        vionx=wionx+vxcm    !transform to lab frame (add CM velocity)
        viony=wiony+vycm
        vionz=wionz+vzcm
```

```
      tfly=tdelay-tof-iontime     !time to go before extraction
      if(tfly.lt.0.0d0) then
        write(*,*) 'Extraction began before ions were formed'
        goto 130
      endif

      dionx=ionx+vionx*tfly      !xyz position of product ion w.r.t. origin
      diony=diony+viony*tfly     !at centre of scattering region when
      dionz=ionz+vionz*tfly      !extraction plates switch.
      rionxy=dsqrt(dionx**2+diony**2)

      if (dabs(dionz).gt.dscatext.or.dabs(diony).gt.dscatfp) then
        nplates=nplates+1
        goto 130                      !eliminating ions which hit extraction
      else if(rionxy.gt.rmesh) then   !or field plates or don't make it
        nplates=nplates+1             !through mesh.
        goto 130
      endif

      dplate=dscatext-dionz             !z component of ion velocity after
      fracgap=dplate/(2.0d0*dscatext)   !extraction plates switch on.
      Eion=2.0d0*extractV*fracgap
      velext=dsqrt(2.0d0*qe*Eion/mionp)
      vionz=vionz+velext

      ddetect=dscatmcp-dionz  !flight time to detector (assuming no field
      tdetect=ddetect/vionz   !penetration from MCP's)
      ttot=tdelay+tdetect

      if(ttot.gt.tmax) tmax=ttot   !range of times over which ions hit
      if(ttot.lt.tmin) tmin=ttot   !detector

      dionx=dionx+tdetect*vionx    !x and y positions of ions at detector
      diony=diony+tdetect*viony
      rionxy=dsqrt(dionx**2+diony**2)

      if(rionxy.gt.rmcp) then      !eliminating ions which miss MCP's
        nmiss=nmiss+1
        goto 130
      endif

      fracx=dionx/rmcp             !working out which pixel hit corresponds
      fracy=diony/rmcp             !to on CCD chip.
      nx=nint(fracx*dble(nxpix/2))
      ny=nint(fracy*dble(nypix/2))

c  To get an ion image need to integrate over the z direction (since
c  image is flattened onto detector), weighting each velocity vector
c  according to the DCS and P(fT) distribution.  Effectively just bin the
c  vectors into pixels.

      if(mode.eq.0) then
        aimage(nx,ny)=aimage(nx,ny) + weight
      else if (mode.eq.1) then
        if(tdetect.gt.mcpdelay.and.tdetect.lt.mcpoff) then
          aimage(nx,ny)=aimage(nx,ny) + weight
        else
          ngate=ngate+1
        endif
      endif

 130  continue

      fracplates=dble(nplates)/dble(mpt)       !calculating fraction of ions
      fracmiss=dble(nmiss)/dble(mpt)           !which don't reach detector
      fracgate=dble(ngate)/dble(mpt)
      fraclost=fracmiss+fracplates+fracgate

      emin = 0.5d0*rm*(vrmin**2)               !min and max collision energies
      emax = 0.5d0*rm*(vrmax**2)

      write(12,15500) emin
      write(12,15600) emax

      write(*,'(a18,f6.2,a4,f6.2,a3)' ) 'Ion arrival from ',
     @  tmin*1.0e6,' to ',tmax*1.0e6,' s'
      write(12,'(a18,f6.2,a4,f6.2,a3)' ) 'Ion arrival from ',
     @  tmin*1.0e6,' to ',tmax*1.0e6,' s'
      write(12,'(a12,f6.2,a3)') 'interval = ', (tmax-tmin)*1.0d6,' s'

      write(12,'(a38,f6.2)') '% of trajectories to field plates',
     @  100.0d0*fracplates
      if(mode.eq.1) write(12,'(a38,f6.2)') '% of trajectories
     @  missing gate ', 100.0d0*fracgate
      write(12,'(a38,f6.2)') '% of trajectories missing MCPs',
     @  100.0d0*fracmiss
      write(12,'(a38,f6.2)') 'total % of trajectories lost',
     @  100.0d0*fraclost

      write(*,'(a38,f6.2)') '% of trajectories to field plates',
     @  100.0d0*fracplates
      if(mode.eq.1) write(*,'(a38,f6.2)') '% of trajectories
```

```
     @  missing gate ', 100.0d0*fracgate
      write(*,'(a38,f6.2)') '% of trajectories missing MCPs',
     @  100.0d0*fracmiss
      write(*,'(a38,f6.2)') 'total % of trajectories lost',
     @  100.0d0*fraclost

      aimax=0.0d0                          !normalising image
      do nx=-nxpix/2,nxpix/2
        do ny=-nypix/2,nypix/2
          if(aimage(nx,ny).gt.aimax) then
            aimax=aimage(nx,ny)
          endif
        enddo
      enddo

      do nx=-nxpix/2,nxpix/2
        do ny=-nypix/2,nypix/2
          if (aimage(nx,ny).ne.aimax) then
            sumimage = sumimage+aimage(nx,ny)
          endif
        enddo
      enddo

      write(*,*) 'sumimage',sumimage

c  Normalization

      do 190 nx=-nxpix/2,nxpix/2
        do 191 ny=-nypix/2,nypix/2
          aimage(nx,ny) = aimage(nx,ny)/sumimage
 191    continue
 190  continue


c Output image

       aimax=aimax/sumimage
       do nx=-nxpix/2,nxpix/2
         do ny=-nypix/2,nypix/2
           if(aimage(nx,ny).ne.aimax) then
             write(10,'(2i5,f15.8)') nx,ny,aimage(nx,ny)
           endif
         enddo
       enddo


c  FORMATS

10000 format(t10,'Integration parameters',/
     @'nxpix =',i4/,'nypix =',i4/ 'mpt=',i10/)
11000 format(/ti0,'Masses of reactants and products',/
     @'mmol =',f5.1,5x,'mion =',f5.1,5x,'mmolp =',f5.1,5x,
     @'mionp =',f5.1)
15000 format(//5x,'Mean relative velocity (m/s) =',1pe12.5/
     @5x,'Mean square velocity (m**2/s**2) =',1pe12.5/
     @5x,'Root mean square velocity (m/s) =',1pe12.5/
     @5x,'Mean CM velocity (m/s) =',1pe12.5/
     @5x,'Mean collision energy (ev) =',1pe12.5/)
15500 format(/t5,'Emin =',1pe12.5/)
15600 format(/t5,'Emax =',1pe12.5/)

      close(10)

      close(12)

      end

c ------------------------------------------------
      double precision function sigma(ee)
c ------------------------------------------------

c  Ionization efficiency curve

      implicit double precision (a-h,o-z)

      sigma(ee)=1.0d0

      return
      end

c-----------------------------------------
      double precision function ran2(iseed)
c-----------------------------------------
c  Long period (>2.0d18) random number generator of L'Ecuyer with
c  Bays-Durham shuffle and added safeguards.  Returns a uniform
c  random deviate between 0.0 and 1.0 (exclusive of the endpoints).  Call
c  with iseed a negative integer to initialize.  Do not alter iseed
c  between successive deviates in a sequence.  RNMX should approximate the
c  largest floating value that is <1.

      implicit double precision (a-h,o-z)
```

```
      parameter(im1=2147483563,im2=2147483399,imm1=im1-1,ia1=40014,
     1          ia2=40692,iq1=53668,iq2=52774,ir1=12211,ir2=3791,
     2          ntab=32,ndiv=1+imm1/ntab)
      parameter(am=dble(1.0d0/im1),eps=1.2d-7,rnmx=1.0d0-eps)
      dimension iv(ntab)
      save iv,iy,idum2
      data idum2/123456789/,iv/ntab*0/,iy/0/

c  Initialize (ensure iseed.ne.0)

      if (iseed.le.0) then
        iseed=max(-iseed,1)
        idum2=iseed
        do 11 j=ntab+8,1,-1
          k=iseed/iq1
          iseed=ia1*(iseed-k*iq1)-k*ir1
          if (iseed.lt.0) iseed=iseed+im1
          if (j.le.ntab) iv(j)=iseed
 11     continue
        iy=iv(1)
      endif

      k=iseed/iq1
      iseed=ia1*(iseed-k*iq1)-k*ir1
      if (iseed.lt.0) iseed=iseed+im1
      k=idum2/iq2
      idum2=ia2*(idum2-k*iq2)-k*ir2
      if(idum2.lt.0) idum2=idum2+im2
      j=1+iy/ndiv
      iy=iv(j)-idum2
      iv(j)=iseed
      if (iy.lt.1) iy=iy+imm1
      ran2=min(am*iy,rnmx)
      return
      end

c-------------------------------------------
      double precision function gauss(iseed)
c-------------------------------------------

      implicit double precision (a-h,o-z)

 1    r1=ran2(iseed)
      r2=ran2(iseed)
      if (r1.le.2.0d0/3.0d0) then
        gauss=1.5d0*r1
        w=0.5d0*gauss**2
      else
        gauss=1.0d0-0.5d0*dlog(3.0d0-3.0d0*r1)
        w=0.5d0*(gauss-2.0d0)**2
      endif

      if ((1.0d0-r2).gt.w) goto 12
      if ((1.0d0/r2)-1.0d0.le.w) goto 1
      if (-1.0d0*dlog(r2).le.w) goto 1
 12   r3=ran2(iseed)
      if (r3.ge.0.5d0) gauss=-1.0d0*gauss

      return
      end

c-----------------------------------------------
      subroutine molpick(iseed,vx,vy,vz,prob)
c-----------------------------------------------
c  Generates molecular velocities and probabilities.  Currently only
c  includes parallel velocity from equation Brett Cameron's thesis and
c  assumes zero for transverse components.

      implicit double precision (a-h,o-z)
      double precision kB,me,mmol,mbwidth,mion
      common /consts/ mion,qe,kB,Av
      common /mb/ mbwidth,Tpar,flowvel,dgunscat,mmol,velwidth

      vx = flowvel + velwidth*ran1(iseed)-velwidth/2.0d0
      arg = mmol*(vx-flowvel)**2/(2.0d0*kB*Tpar)
      prob=vx*vx*dexp(-arg)

      vy=0.0d0
      vz=0.0d0

      return
      end

c-------------------------------------------------------------
      subroutine ionpick(iseed,x,z,vx,vy,vz,iontime)
c-------------------------------------------------------------
c  Generates ion parameters (velocity, position and release time)

      implicit double precision (a-h,o-z)
      double precision kB,mion,ionE,ionEE,ionwidth,ionEwidth
      common /consts/ mion,qe,kB,Av
      common /elec/ pwidth,ionE,ionwidth,ionEwidth
```

```
      external xygauss,gasdev

      iontime=pwidth*ran1(iseed)    !time at which ion leaves L7

      call xygauss(iseed,x,z)        !offset from beam axis.  Beam profile
      x=(ionwidth/2.0d0)*x           !assumed to be 2D Gaussian with FWHM
      z=(ionwidth/2.0d0)*z           !equal to ionwidth

c Ion velocity distribution.  Uses a Gaussian energy distribution of
c width ionEwidth for parallel velocity.  Perpendicular velocity not
c included.

      vx=0.0d0                              !ion velocity distribution.  Uses a
      ionEE=ionE+ionEwidth*gasdev(iseed)    !Gaussian energy distribution of width
      vy=dsqrt(2.0d0*qe*ionEE/mion)         !ionEwidth for parallel velocity.
      vz=0.0d0                              !Perpendicular velocity not included.

      return
      end

c-------------------------------------------------------------
      subroutine dpick(idum,z,ycomp,d,iflag)
c-------------------------------------------------------------
c  Distance from electron beam source until electron hits a beam molecule.
      implicit double precision(a-h,o-z)
      double precision mbwidth,mmol
      common /mb/ mbwidth,Tpar,flowvel,dgunscat,mmol,velwidth

c Picks the radius from the axis of a molecule in the beam according to a
c Gaussian distribution, then determines the y component at the z position
c of the beam ion in order to get d, the distance the ion flies from
c the source before a collision.  Randomly puts the molecule on one side of
c the beam or the other.  Exits if ion misses molecular beam.

      iflag=0
      rad = (mbwidth/2.0d0)*gasdev(idum)
      arg=rad**2-z**2
      if (arg.lt.0.0d0) then
        iflag=1
        return
      endif
      ycomp = dsqrt(arg)
      pick=2.0d0*ran1(idum)-1.0d0
      picksign=pick/dabs(pick)
      ycomp = ycomp*picksign
      d = dgunscat-ycomp

      return
      end

c   ---------------------------------------------------
      double precision function dcs(coscm)
c   ---------------------------------------------------
c  Model differential cross section made up of two Gaussians and a baseline
c  c1,c2 are weights of Gaussians (c1+c2=1), c3,c4 are their centres and
c  c5,c6 are the widths.  c7 is the baseline. coscm is the cosine of
c  the CM scattering angle.

      implicit double precision (a-h,o-z)

      c1=0.5d0
      c2=0.5d0
      c3=1.0d0
      c4=-1.0d0
      c5=0.3d0
      c6=0.3d0
      c7=0.0d0
c
      pi = dacos(-1.0d0)
      ap=-0.5d0

c  Setting up the arguments of the exponential in the Gaussians
      oso1 = ((c3-coscm)/c5)
      oso2 = ((c4-coscm)/c6)
      roso1=ap*oso1*oso1
      roso2=ap*oso2*oso2

c  The Gaussians
      if (roso1 .lt. -2.2d2) then
 tmp1=0.0d0
      else
 tmp1=c1*dexp(roso1)
      endif
      if (roso2.lt.-2.2d2) then
 tmp2=0.0d0
      else
 tmp2=c2*dexp(roso2)
      end if
      dcs=tmp1+tmp2+c7

      return
      end
```

```
c   ------------------------------------------------
      double precision function pft(ftm)
c   ------------------------------------------------
c  Model P(fT) made up of two Gaussians and a baseline
c  c1,c2 are weights of Gaussians (c1+c2=1), c3,c4 are their centres and
c  c5,c6 are the widths.  c7 is the baseline.

      implicit double precision (a-h,o-z)

      ftn=2.0d0*ftm-1.0d0

      c1=1.0d0
      c2=0.0d0
      c3=0.3d0
      c4=0.0d0
      c5=0.1d0
      c6=0.0d0
      c7=0.0d0

      pi = dacos(-1.0d0)
      ap=-0.5d0

c  Setting up the arguments of the exponential in the Gaussians
      oso1 = ((c3-ftn)/c5)
      oso2 = ((c4-ftn)/c6)
      roso1=ap*oso1*oso1
      roso2=ap*oso2*oso2

c  The Gaussians
      if (roso1 .lt. -2.2d2) then
 tmp1=0.0d0
      else
 tmp1=c1*dexp(roso1)
      endif
      if (roso2.lt.-2.2d2) then
 tmp2=0.0d0
      else
 tmp2=c2*dexp(roso2)
      end if
      pft=tmp1+tmp2+c7

      return
      end


c ----------------------------------------
      double precision function ran1(idum)
c ----------------------------------------
c  Random number generator

      implicit double precision (a-h,o-z)
      integer idum,ia,im,iq,ir,ntab,ndiv
      parameter (ia=16807,im=2147483647,iq=127773,ir=2836,
     *ntab=32,ndiv=1+(im-1)/ntab)
      parameter (am=1.0d0/dble(im),eps=1.2d-7,rnmx=1.0d0-eps)
      integer j,k,iv(ntab),iy
      save iv,iy
      data iv /ntab*0/, iy /0/

      if ((idum.le.0) .or. (iy.eq.0)) then
         idum = max0(-idum,1)
         do 11 j=ntab+8,1,-1
            k = idum/iq
            idum = ia*(idum-k*iq)-ir*k
            if (idum .lt. 0) idum = idum+im
            if (j .le. ntab) iv(j) = idum
 11      continue
         iy=iv(1)
      endif
      k = idum/iq
      idum = ia*(idum-k*iq)-ir*k
      if (idum .lt. 0) idum = idum+im
      j = 1+iy/ndiv
      iy = iv(j)
      iv(j) = idum
      ran1 = dmin1(am*dble(iy),rnmx)

      return
      end

c ------------------------------------------------
      subroutine xygauss(iseed,dev1,dev2)
c ------------------------------------------------
c  Generates a 2 dimensional Gaussian distribution, 2 points between -1 and
c  +1.
      implicit double precision (a-h,o-z)
      external ran1

c  Generates 'velocity components' for molecular reactant on interval -1
c  to +1 using a random number generator.
  1   v1=2.0d0*ran1(iseed)-1.0d0
      v2=2.0d0*ran1(iseed)-1.0d0
```

```
      rsq=v1**2+v2**2
      if(rsq.ge.1.0d0.or.rsq.eq.0.0d0)goto 1

c  Transforms from random velocities in range -1,1 to a Gaussian distribution
c  of full width wdth.
      fac=dsqrt(-2.0d0*dlog(rsq)/rsq)
      dev1=v1*fac
      dev2=v2*fac
      return
      end

c-------------------------------------------------*-----
      double precision function gasdev(idum)
c-------------------------------------------------------
c  Picks a random number from a Gaussian distribution between -1 and 1
      implicit double precision(a-h,o-z)
      save iset,gset
      data iset/0/
      if(iset.eq.0) then
 1      v1=2.0d0*ran1(idum)-1.0d0
        v2=2.0d0*ran1(idum)-1.0d0
        rsq=v1**2+v2**2
        if(rsq.ge.1.0d0.or.rsq.eq.0.0d0) goto 1
        fac=dsqrt(-2.0d0*dlog(rsq)/rsq)
        gset=v1*fac
        gasdev=v2*fac
        iset=1
      else
        gasdev=gset
        iset=0
      endif
      return
      end
```